Modal acoustic velocimetry in a gas-filled rotating spheroid

Sylvie Su

THÈSE

Pour obtenir le grade de

DOCTEUR DE L'UNIVERSITE GRENOBLE ALPES

Spécialité : **Sciences de la Terre et de l'Univers et de l'Environnement (CESTUE)**

Arrêté ministériel : 25 mai 2016

Présentée par

Sylvie SU

Thèse dirigée par **Philippe CARDIN,** Directeur de Recherche, Communauté Université Grenoble Alpes, et
co-dirigée par **David CÉBRON,** Chargé de Recherche, Communauté Université Grenoble Alpes,

préparée au sein de l'**Institut des Sciences de la Terre**
dans l'École Doctorale **Terre Univers Environnement**

Vélocimétrie acoustique modale dans un sphéroïde gazeux en rotation

Modal acoustic velocimetry in a gas-filled rotating spheroid

Thèse soutenue publiquement le **4 février 2020**,
devant le jury composé de :

Mme. Séverine ROSAT
Chargée de Recherche, EOST, Université de Strasbourg, Rapportrice

M. Frank STEFANI
Chercheur, Helmholtz-Zentrum Dresden-Rossendorf, Rapporteur

Mme. Helle PEDERSEN
Physicienne CNAP, Université Grenoble Alpes, Présidente

M. Santiago Andres TRIANA
Docteur, Royal Observatory of Belgium, Examinateur

M. Philippe CARDIN
Directeur de Recherche, Université Grenoble Alpes, Directeur de thèse

M. David CÉBRON
Chargé de Recherche, Université Grenoble Alpes, Co-Directeur de thèse

Abstract

Zonal flows are expected to play a major role in the heat transfer mechanism of geophysical bodies such as the Earth's core or Jupiter's atmosphere. However due to the turbulent regime the systems are in, and the specific force balance, dominated by rotation, it is very hard to accurately model zonal flows. This causes their formation and dynamics to still not be well understood. Experimental studies propose a complementary approach where all scales of structures coexist. However most of the existing experimental set-ups remain far from the relevant regimes found in the natural systems.

We present a new laboratory experiment built to study zonal flows induced by thermal convection, called ZoRo. The originality of this new apparatus resides in the fact that all balances, forcings and geometry are closest to the geophysical bodies. In order to match those, ZoRo is a rapidly rotating spheroid (flattened sphere) filled with air.

In order to experimentally study zonal flows, all physical ingredients are reunited in the apparatus, and we measure the flow field. Since the working fluid is air (a gas), it is very challenging to accurately measure its velocity. To tackle to this problem, we implemented a new velocimetry technique based on acoustic resonances of the fluid cavity, the modal acoustic velocimetry (MAV). In order to isolate the velocity acoustic signature, we develop theoretical predictions that take into account the main relevant effects that influence the acoustic spectrum (cavity's geometry, fluid's diffusions, container elasticity, etc.). It is then possible to retrieve the flow field using acoustic frequencies through an inverse problem. MAV is a well-suited technique for measuring global azimuthal flows such as zonal flows. It is very sensitive to variations in the flow structure, down to a few centimetres. We were able to image the internal flow velocity with non-intrusive sensors thanks to MAV.

Résumé

Les vents zonaux sont une famille d'écoulement jouant un rôle majeur dans la transmission de la chaleur dans les systèmes géophysiques tels que le noyau de la Terre ou l'atmosphère de Jupiter. Cependant ces systèmes présentent des régimes turbulents dominés par la rotation, ce qui rend l'étude des vents zonaux difficile. De ce fait les méchanismes de leur formation et de leur dynamique sont encore mal compris. Les études expérimentales permettent une approche complémentaire où toutes les tailles de structures peuvent facilement coexister. Pour des raisons pratiques, la plupart des expériences existantes présentent des régimes différents de ceux des systèmes planétaires.

Nous présentons une nouvelle expérience de laboratoire appelée ZoRo pour étudier les vents zonaux. L'originalité de ce nouveau montage est qu'il se rapproche autant que possible des conditions présentes dans les systèmes planétaires. Pour ce faire, nous avons choisi de construire un sphéroïde (sphère aplatie) rempli d'air en rotation rapide.

Pour mesurer la vitesse des éoulements nous avons développé une nouvelle technique de mesure qui s'appuie sur les modes acoustiques de la cavité fluide. Cette technique est non-intrusive et particulièrement adaptée à la mesure d'écoulement azimuthaux de grande échelle. Nous avons testé cette méthode sur des cas synthétiques puis des écoulements réels mesurés dans ZoRo. Grâce à la résolution d'un problème inverse, il est possible de remonter au champ de vitesse à partir des fréquences des modes acoustiques.

Acknowledgements

I would first like to thank my committee for accepting to review my manuscript and to participate to the defense. Helle for her encouragements and for accepting to be the president of the committee, Santiago for his kindness, and the two referees Frank and Séverine who accepted the cumbersome task of reviewing my manuscript, and who read every single line of it with (scary) precision.

Cette aventure de trois années qu'a été cette thèse n'aurait pas existé sans mes directeurs Philippe, David et Henri-Claude. Je n'ai pas les mots pour exprimer ma reconnaissance envers tout ce qu'ils m'ont apporté.

Tout d'abord merci à David, pour ta présence et tes encouragements. Merci d'avor toujours pris le temps de répondre à mes questions même quand elles n'avaient aucun sens. Merci de m'avoir montré par l'exemple comment on peut faire de la belle science, avec notamment une bonne dose de pragmatisme. J'ai découvert les joies de chercher avec quelqu'un et l'émulation que ça engendre.

Philippe ensuite qui a été un véritable mentor. Merci pour ta disponibilité, je sais que tu es en permanence enseveli sous une quantité de travail monstrueuse, mais tu t'es toujours interrompu pour moi. Merci pour ta confiance, tu as toujours insisté pour que je fasse (et rate) par moi-même et pour que je sois impliquée au cœur du projet. Merci aussi pour ta franchise dont j'avais besoin mais que tu as pris soin de réguler devant moi. Merci enfin pour ton soutien et ton investissement, qui se sont entre autres traduits par ton souci de m'épargner tant que tu le pouvais, et je sais que sans ça cette thèse aurait pu virer au drame plus d'une fois.

Et enfin Henri-Claude, qui même s'il refuse toujours d'être considéré comme un de mes directeurs, ne dupe personne. Merci pour ta patience et les heures que tu as passé à répondre à mes questions. Merci aussi pour tout le travail d'organisation dans l'ombre qui a permis de jalonner le projet et sans lequel les étapes de synthèse auraient sans doute été un joyeux casse-tête. J'ai conscience la quantité de travail énorme que tu as fourni pour ZoRo, et à laquelle je dois une partie non-négligeable des résultats présentés dans ce manuscrit.

Merci à vous trois, pour m'avoir accueillie dans mes premiers pas de chercheure, pour m'avoir appris comment faire de la science, pour m'avoir guidée en me laissant faire. Mais ce que je retiens aussi au-delà de l'aventure scientifique, c'est la gentillesse et la bienveillance mutuelles qui ont été présentes à chaque instant et qui font d'eux des personnes humaines avant d'être des chercheurs. Merci de m'avoir donné un modèle à suivre, et merci de prouver au monde que c'est possible.

Avec eux on a formé la Team ZoRo, sans oublier les ingés sans qui ZoRo serait resté une patate immobile et ne parlons même pas des données qui sont maintenant d'une précision déconcertante. Je n'abandonne pas l'idée qu'un jour, si on s'ennuie, on ira s'attaquer à la constante de Boltzmann. Avec dans l'ordre d'apparition les mécaniciens Anthony et Max, qui a intégralement dessiné et supervisé la construction de ZoRo. Mais d'eux deux, je vais aussi retenir les discusions en salle de manip', ou tard dans le couloir, philosophiques, sociales, politiques... Yann sur l'instrumentation, le pilotage et l'électronique. Merci pour les soudures minuscules, les circuits et les codes Labview incompréhensibles (pour moi) mais qui marchent au doigt et à l'œil. J'ai souvent entendu pendant ces trois années que

l'expérimental c'est dur, qu'il y a toujours des aléas, c'est comme ça. Mais leur présence, leur savoir-faire et leur expertise ont tout changé. C'est d'un coup devenu possible, presque facile. Et j'ai conscience que je le dois à leur investissement, à leur temps et leur énergie qu'ils ont dépensés sans compter. Ils ont ouvert le champ des possibles et ont fait de ZoRo une manip' qu'on n'aurait pas pu imaginer et qui nous surprend encore et encore par sa qualité. Merci d'être là, d'aimer ZoRo autant que moi. Et aussi merci d'être patients avec ces chercheurs qui ne savent ni ce qu'ils cherchent ni ce qu'ils doivent trouver.

Je suis convaincue que cette Team ZoRo n'a pu exister que grâce à la grande famille qu'est l'équipe Géodynamo. Avec « de mon temps » : Dominique, Nathanaël, Nicolas, Franck, puis Renaud et Guillaume. Et les indestructibles Patrick et Jean-Paul. Merci pour ce lieu de bienveillance et de confiance inconditionnelle. Merci aussi à Jérémie, pour ton soutien, tes conseils, tes encouragements et ta présence, tu as été pour moi la preuve vivante que c'est possible. Merci aussi à Olivier, Felix et Thibaut avec qui on a été des doctorants esseulés parmi les géologues du laboratoire.

Merci aux copains doctorants (géologues ou pas) que j'ai croisé au laboratoire d'avoir fait du labo un lieu de vie et pas seulement de travail. En particulier mes co-bureau, le bureau des filles : Gaëlle, Louise et Judith. Il s'y est passé tellement de choses, on y a toutes réellement habité, je pense que ce bureau est le vrai témoin de mes années de thèse. On y a partagé les joies, les peines, les moments de stress, de frustration, de soulagement, de bonnes rigolades, les râleries, le chocolat (très important) et le café, notamment avec l'invité spécial, la dernière « fille » du bureau : Benjamin. Merci à Tobias, mon alter ego et âme sœur au labo. Merci d'avoir supporté mes longs monologues, mes multiples débarquements intempestifs dans le bureau. Merci d'avoir été là, d'avoir partagé cette expérience. Le seul fait d'avoir été là a été un soutien moral pour moi. Je tiens aussi à adresser une mention spéciale au groupe des délégués qui comprennent la douleur liée au mot « bureau », avec la génération 1 : Chloé, Jacques, Ariana, Tobias et Julien aussi dans la génération 2 avec Axel, Louise, Noélie et Dorian. Je vais oublier des noms, mais merci à : Arnaud, Margot, Amber, Philippe, Antoine, Sylvain, Marwan, Johannes, Capucine, Ahmed, Aya... Merci aussi aux copains de Lyon, doctorants (ou pas), parce que savoir qu'on n'est pas tout seul ça aide, merci à Florian, Bruno, Amélie, Toto, Pierre, Élie, Léo.

ISTerre est un labo de géologues et de géophysiciens, avec une ambiance conviviale et bienveillante, investi dans un nombre de projets scientifiques et humains impressionnant. Merci de m'avoir réconciliée avec la géologie que j'avais juré de ne plus côtoyer même en peinture. C'est aussi grâce à lui que j'ai pu m'essayer aux joies de l'enseignement et vivre des expériences intenses (de stress principalement). Merci aux étudiants que j'ai croisé pour ma première expérience, d'avoir été eux tout simplement. Je n'ai d'ailleurs toujours pas avoué aux L2 qu'ils étaient mes premiers élèves... Je garde précieusement dans un coin de ma mémoire toutes les situations caucasses ou touchantes, ça s'accumule vite !

C'est aussi en partie grâce à ISTerre que j'ai croisé la route des doctorants avec qui on a formé l'équipe d'organisation des Tribulations Savantes avec : Rosemary, Thibault, Cyril, Cruz, Julien, Cyprien et Jérôme. C'était une chouette expérience, mais surtout pour les super moments passés ensemble, que ce soit les réunions-apéros, les réunions-petitdéj, l'évènement bien sûr, ou juste sortir boire un verre, le tout toujours dans la bonne humeur.

Toujours dans la catégorie des choses hors-thèse que j'ai faites pendant ma thèse, et qui prouvent qu'une thèse est bien une expérience de vie, j'aimerais remercier l'équipe de « Ma Thèse en 180 secondes ». Ludo pour le coaching, Domitille pour ses petits soins,

Lisa et les masters de communication scientifique pour leur professionnalisme, les grands bonnets qui nous ont permis de nous prendre pour des stars l'espace d'un instant, et bien sûr les autres doctorants candidats : Lencka, Hélène, Marie, Arthur, Simon, Mohamed, Cindy, Gregory, Abderrahmane, Guillaume, Agata, Adrien, Flora et Romain. L'adversité rapproche comme on dit, mais la force des liens qui se sont tissés dans ce groupe et la vitesse à laquelle c'est arrivé est surréelle. Pour cette expérience incroyable, merci !

Un petit dernier, et les ArnHackers se reconnaîtront. Au produit pseudo-final VortexLab. À David, Jordan, Guyhème, Anthony et Théo. Merci pour Pewpew, le non-sommeil et les 43 heures de folie créative commune. Et merci à Marc pour son café.

Enfin, merci à mes parents pour leur confiance.
Merci à ma « belle-famille » pour leur soutien.
Et merci à Nicolas pour ta présence (et ton expertise TEX !).

Contents

1 Introduction

Alone we go faster, together we go further.

- African saying,

This thesis presents a first landmark towards new zonal jets laboratory experiments, where we focused on developing the Modal Acoustic Velocimetry (MAV) technique, building on the pioneering work of Triana et al. (2014). In this chapter, we present the motivations that gave birth to this work.

First we will present zonal flows in rotating planets, their observations and some of the methods used to try and understand them, including numerical modelling and laboratory reduced models.We will then present why we decided to build a new experiment (ZoRo), its originality and how it complements the existing studies.

Due to the specificities of the newly built experiment, we show that the usual flow measurements techniques are not suitable for ZoRo. We present the modal acoustic velocimetry method, first proposed by Triana et al. (2014), and how it fits the experimental constraints.

This newly developed velocimetry technique is based on acoustic normal modes, and how their frequency changes in presence of a velocity field. This methodology is widely used in seismology, helio-seismology and astero-seismology to retrieve the systems' rotation and internal structure. We present a brief overview of the existing studies that inspired the framework of this thesis.

Incidentally, acoustic normal modes are also used in metrology to determine gases properties. Due to the high precision measurements, metrologists developed very accurate theories to describe many experimental effects that may influence the acoustic spectrum. We will present a few studies that will later be useful. Finally we give a general outline of this thesis in §1.4.

1.1 Zonal flows

The observation of fluid dynamics in planetary layers brings out a very rich physical system that is not yet well understood (Ingersoll, 1990). One of the most striking direct observations are the very impressive bands visible on Jupiter's or Saturn's atmosphere (Figure 1.1, left) (Porco et al., 2003). Those bands have been proven to be the signature of strong alternating winds propagating parallel to the planet's equator, either east-wards or west-wards. Such azimuthal winds are called zonal flows (or zonal jets) and can be observed on the Earth as well (Galperin and Read, 2016), in the atmosphere and oceans as seen in Figure 1.1, right, but also in the outer core (Livermore et al., 2017).

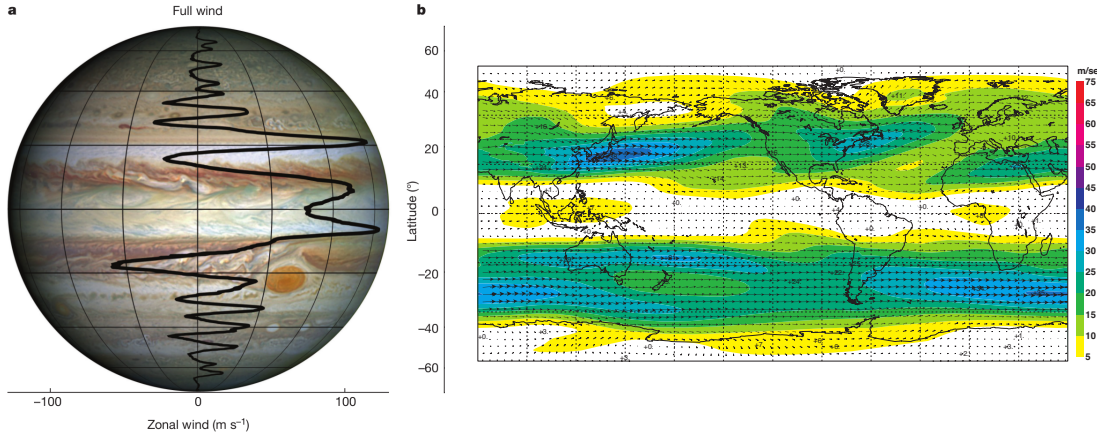

Figure 1.1: Left: Jupiter's atmosphere, an image of Jupiter taken by the Hubble wide field camera in 2014, with the cloud-level zonal flows (thick black line) as function of latitude as measured during Juno's 3rd perijove of Jupiter on December 11th 2016 (Tollefson et al., 2017). Longitudinal spread is 45°. From (Kaspi et al., 2018). Right: Earth's atmosphere, annual mean values of wind amplitude (in colour) and wind vectors (arrows) at 300hPa. From ERA40 Atlas. From Galperin and Read (2016).

Zonal flows are expected to be an important family of fluid motions in geophysical systems. Since most planets and stars are subject to rotation, that inherently changes the dynamics, and zonal flows are the only family of flows that is not destabilized by it (Vallis, 2017). The relative importance of rotational effects can be measured by the dimensionless Ekman number, that gives the ratio between viscous and Coriolis forces,

$$Ek = \frac{\nu}{\Omega a^2}, \tag{1.1}$$

where ν is the fluid viscosity, Ω the rotation rate and a a typical lengthscale of the system (e.g. radius of the planet).

To fully grasp the relative importance of rotational effects, it is useful to consider a complementary dimensionless number that gives the ratio between a rotation period and a typical advective time scale. That is the Rossby number, given by

$$Ro = \frac{U}{\Omega a}, \tag{1.2}$$

where U is a typical flow velocity.

Geophysical systems tend to have very low Rossby number ($\sim 10^{-7}$) and Ekman number ($10^{-7} \sim 10^{-15}$) hence their dynamics are expected to be mostly dominated by rotation (Pedlosky, 1987). In particular, in the low Rossby, low Ekman numbers limit, the momentum conservation equation reduces to a balance between Coriolis forces and the pressure gradient, called the geostrophic balance (Vallis, 2017), as

$$2\boldsymbol{\Omega} \times \boldsymbol{v} = -\frac{1}{\rho_0}\boldsymbol{\nabla} P, \tag{1.3}$$

where P is the pressure, $\boldsymbol{v}$ and $\boldsymbol{\Omega}$ the velocity and rotation vectors. Taking the curl of eq. (1.3), we see that if rotation dominates, the flows are expected to be invariant along the rotation axis, or the Taylor-Proudman theorem, which gives for $\boldsymbol{\Omega} = \Omega \boldsymbol{e_z}$,

$$\frac{\partial \boldsymbol{v}}{\partial z} = 0. \tag{1.4}$$

Zonal flows are thought to be an important factor in planetary dynamos as they can contribute to the heat transfer while verifying the geostrophy constraints (Heimpel et al., 2005; Heimpel and Pérez, 2011; Guervilly and Cardin, 2017). But the mechanisms that govern their formation and structures are still not well understood today (Dowling, 1995; Kong et al., 2018).

The main forcing is expected to be thermal convection, that transports heat in the radial direction. An interesting dimensionless number to consider is the Prandtl number, which gives the ratio between viscous and thermal diffusion,

$$Pr = \frac{\nu}{\kappa}, \tag{1.5}$$

where κ is the thermal diffusivity. In planetary systems, the Prandtl number is low ($10^{-2} \sim 10^{-4}$), which means the thermal gradients tend to smoother out mainly due to their thermal diffusion. This causes the thermal convection regimes to be much more turbulent than for higher Pr (Vallis, 2017). In such turbulent regimes, zonal flows are global planetary-scale structures that are steady in time (Yarom et al., 2013; Aurnou et al., 2015). The emergence of those global structures is expected to result from non-linear interactions (Rhines, 1975; Vallis and Maltrud, 1993).

In order to explore Jupiter's atmosphere, several spatial missions have been launched (Vasavada and Showman, 2005), including the recent *Juno* mission (Bolton and Team, 2010) from NASA (National Aeronautics and Space Administration). One of the main objectives of *Juno* is to determine the depth of the zonal jets, by using high-precision measurements of Jupiter's gravitational field (Kong et al., 2013, 2015; Zhang et al., 2015; Iess et al., 2018).

Parallel to those observation missions, in order to try and understand the physical mechanisms behind those flows, a number of numerical simulations have been performed, successfully reproducing their main features (e.g. Condie and Rhines (1994); Christensen (2002); Kaspi et al. (2009); Gastine et al. (2014); Guervilly and Cardin (2017); Cao and Stevenson (2017) or Heimpel et al. (2005), reproduced in Figure 1.2). However the relevant force balance is yet to be attained with numerical simulations (Schaeffer et al., 2017). Due to the vastly different length scales, from global zonal flows at planetary scale down to the turbulent eddies that can be a thousand times smaller, the computational cost needed to fully resolve the problem is huge. Hence the majority of the studies considers problems

that are more reasonably modelled. The historical approach is to alter the force balance (e.g. by increasing the Ekman number) into regimes that can be numerically modelled in a reasonable amount of time.

Due to the effects of rotation, zonal jets can form columnar quasi-geostrophic flows (Busse, 1994) with a concentric cylindrical shells structure (Kaspi et al., 2018; Kong et al., 2018). The invariance along the rotation axis allows to carry simplified bi-dimensional simulations, reducing the computational costs and allowing to explore regimes closer to the natural systems' (Guervilly and Cardin, 2017).

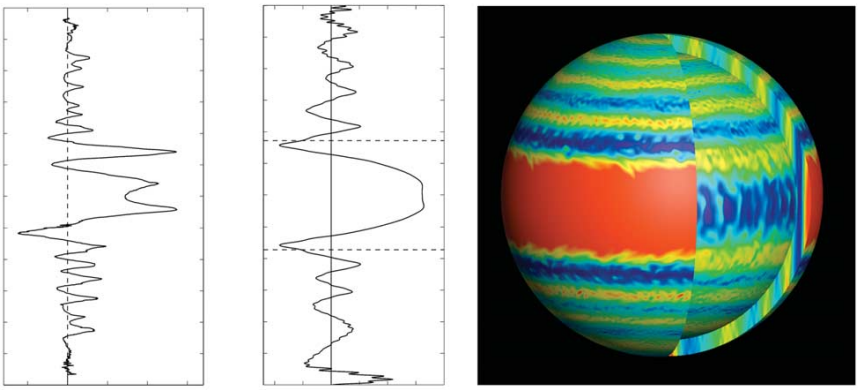

Figure 1.2: A snapshot of the longitudinal winds maintained on the outer and inner boundaries in a simulation of Jupiter using a Boussinesq, deep rotating convection model. Reds represent prograde winds; blues retrograde. Heimpel et al. (2005) adapted by Stanley and Glatzmaier (2010).

1.1.1 Experimental models

Turbulence and non-linear interactions are very difficult to accurately model numerically. In order to explore the parameter space and compare with the numerical results, several laboratory models have been developed. We present a few of the existing experimental set-ups used to model zonal flows, and why we decided to build a new apparatus.

Overview of existing experiments

Many laboratory experiments of various shapes and goals exist. We can separate them depending on the working fluid that can be electrically conductive fluids, using liquid metals (e.g. Gillet et al. (2007); Aurnou and Olson (2001)) and non-conductive fluids (e.g. Manneville and Olson (1996); Cabanes et al. (2017)), the experiment geometry, either shallow (e.g. Read et al. (2004); Espa et al. (2010)) or with deep structures (e.g. Manneville and Olson (1996); Yarom and Sharon (2014)). A distinction can also be made based on which forcing is used to inject energy in the system, either thermal (e.g. Smith et al. (2014); Read et al. (2015)) or mechanical (e.g. Espa et al. (2010); Noir and Cébron (2013)). In Figure 1.3 we reproduced two experimental results, left a spherical thermally forced convection, and right a cylinder with mechanical forcing, both experiments work with water.

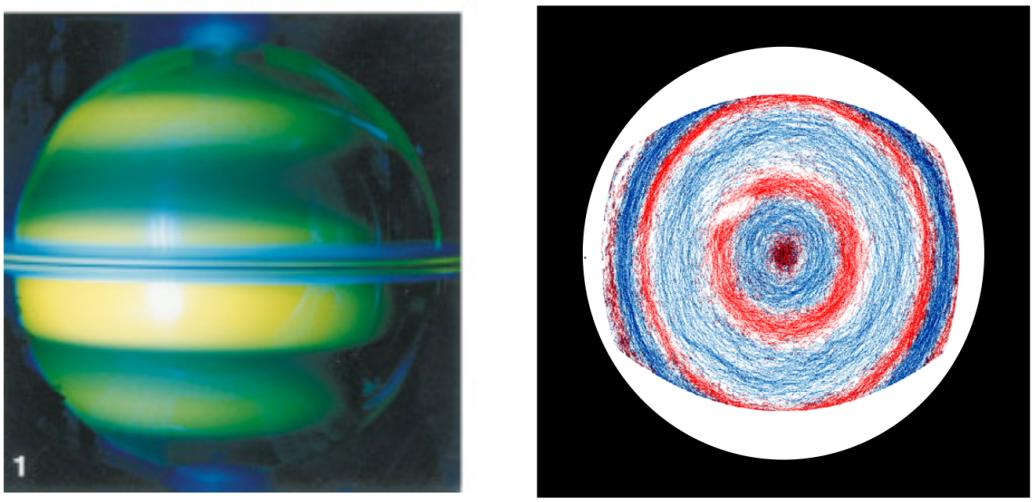

Figure 1.3: Left: Time lapse photos in UV light showing band structure of thermal convection in rotating spherical shells. The inner/outer radius ratio is 0.76, similar to the convecting regions of Jupiter. Values of the experimental parameters are $Ek = 2.10^{-6}$ and $Ra = 2.10^{9}$ (approx. 100 times the critical value). Adapted from Manneville and Olson (1996). Right: Experimental polar view of 4,900 Lagrangian particle tracks, collected between 4,900 and 5,350 rotations. Tracks are coloured on the basis of their instantaneous zonal azimuthal velocity direction, with red (blue) being prograde (retrograde) (Cabanes et al., 2017).

Among the deep fluid systems, we can distinguish the full three dimensional apparatus, such as spheres (Manneville and Olson, 1996) or quasi-spheres (Noir et al., 2009, 2012; Noir and Cébron, 2013), and the set-ups that take the beta-effect (Vallis, 2017) into account but stay mainly two-dimensional (e.g. Yarom et al. (2013); Zhang and Afanasyev (2014); Cabanes et al. (2017)). While the former are less constraining for the fluid, they are mainly oriented towards mechanical forcings such as libration or precession (Noir and Cébron, 2013; Le Dizès, 2015; Le Dizès and Le Bars, 2017).

Thermal convection is expected to drive the zonal flows, so the relevant dimensionless number to attain the correct balance of forces is the Prandtl number. In planetary fluids, the Prandtl number is small ($\sim 10^{-2}$), meaning that the thermal diffusivity dominates. Such regime is easily reached by liquid metals, but hardly by water ($Pr = 7$). This leads many experiments to prefer mechanical forcings, either by adding shear stress (Jougla, 2019) or by injecting energy at small scales and letting it (inverse) cascade (e.g. Yarom et al. (2013); Cabanes et al. (2017)).

We are interested in low Prandtl number fluids in a three-dimensional container with thermal forcings, that are the closest to the natural systems.

The new ZoRo experiment

We aim to build an experiment closer to the forcing balance found in geophysical bodies than previously done. We are also dedicated to build an experiment that is as less constrained as possible in order to keep a highly complex problem, since we believe this complexity is needed in order to see the emergence of global structures such as zonal flows.

We build a new experiment called Zonal flows in Rotating fluids (ZoRo), part of the Turbulence and Dynamo in planetary cores (TuDy) ANR-funded project. The ZoRo

experiment is a full (no inner core) quasi-sphere (oblate spheroid, flattened along the rotation axis) filled with gas that can rotate rapidly around its symmetry axis. It is one of the first laboratory experiment using gas in a rotating enclosure to study zonal flows, and very few laboratory experiments use rotating gas at all (Menaut et al., 2019).

The (quasi) spherical geometry allows us to explore the deeper structures, while cylindrical tanks mostly are in the shallow-water approximation, e.g. Afanasyev and Wells (2005). This fully three dimensional system also imposes less constraints on the fluid and better reproduce the natural geometry. In the pursue of building a relatively unconstrained experiment, thermal gradient is used to inject energy in the system, and we aim to observe the coupled effect of thermal convection and rapid rotation. Gases have a Prandtl number less than one (0.7 for air), and are easier to handle than liquid metal, especially since we focus on hydrodynamics (no magnetic field). Gases are also much lighter, allowing faster rotation rates, hence an equilibrium dominated by rotation as observed in planetary systems.

However flow velocity measurements in gas are challenging compared to transparent (in the visible wavelength) liquids, such as water. We will present a brief overview of the most commonly used velocimetry techniques, and show that modal acoustic velocimetry (MAV) is the best suited one for ZoRo.

1.2 Experimental velocimetry techniques

Since the aim of the experiment is to study zonal flows, the main quantity to retrieve is the azimuthal flow velocity. Depending on the specific conditions and fluid considered, some velocimetry techniques may be more suitable than others. We present a brief overview of the widely used velocimetry techniques, their advantages and drawbacks that led us to choose the modal acoustic velocimetry (MAV), recently proposed by Triana et al. (2014).

In order to constrain the fluid as little as possible, we want a non-intrusive measurement technique. This rules out the historical anemometers (e.g. hot film anemometer), that also present the disadvantage of being local, and thus giving sparse information on the flow.

Among the non-intrusive techniques, one major family of velocimetry techniques is based on optical means, with the obvious advantage to allow a direct visualisation of the flow. The idea is to acquire with an optical camera the fluid flow that is made visible, for example with particle seeding. The successive images are then compared to reconstruct the flow in time, for example with interferometry or with particle tracking, such as Particle Imaging Velocimetry (PIV) (Wereley and Meinhart, 2010). In order to improve the tracking, additional means can be used to make the seeds more visible, for example by choosing fluorescent particles, giving the Laser Induced Fluorescence (LIF) technique (Kinsey, 1977; Hishida and Sakakibara, 2000), or by heating them, with Laser Induced Incandescence (LII) (Vander Wal and Weiland, 1994; Michelsen et al., 2007). These techniques are widely used today, including in recent zonal jets experiments (Cabanes et al., 2017).

One major drawback of these methods is that, since the measurement is based on optics, it can only be applied to transparent fluids. Experiments using liquid metal prefer to use Doppler based velocimetry techniques. They present the advantage that they can be performed with visible light (laser Doppler (Albrecht et al., 2013)) but also with ultrasounds, which can propagate even in opaque fluids (Brito et al., 2001). Second drawback

is that they are mainly bi-dimensional, so the visualisation takes place in the lightened plane (e.g. laser sheet), which is limiting for zonal flows observations.

The techniques mentioned so far rely on the hypothesis that the seeds are neutrally buoyant particles, hence measuring the particle's velocity is equivalent to measuring the fluid's velocity. However the ZoRo experiment is filled with air for which it is very difficult to find such tracers (Melling, 1997), especially for the fast rotation rates attainable by ZoRo, up to 50 Hz or 3000 revolutions per minute (rpm). Fast rotation creates a strong centrifugal force that would rapidly gather the denser particles near the outer boundary (in less than 1 second for standard smoke particles in air rotating at 3000 rpm). So seeding the fluid is not practically feasible for ZoRo.

Other visualisation techniques such as ombroscopy or holography, rely on the variations of the medium's refractive index, due to temperature for example (Pentland, 1987). They present the advantage of not needing seeds in the fluid, but are effective only for shallow transparent fluids. In addition to this, we are also interested in reproducing in ZoRo some mechanically induced zonal flows (Le Bars et al., 2015), for which there would be no temperature nor density changes, hence disabling these techniques.

Following the pioneering work of Triana et al. (2014), we further develop modal acoustic velocimetry to measure the flows in a rapidly rotating gas cavity. This method relies on acoustic normal modes, present in any fluid filled cavity, and more generally in any enclosed system. Each normal mode is associated with an eigen-frequency, that depends on the system's shape and the propagating medium's properties. It is then possible to retrieve the medium's velocity by measuring the frequency variations, e.g. compared to the medium at rest. This method gives a full three-dimensional global measure of the fluid velocity by having non-intrusive sensors at the system's surface.

1.3 Acoustic normal modes

Measurements of acoustic normal mode frequencies have been used in various domains to infer very diverse properties of the resonating medium. We present three complementary domains that inspired us in various stages of this study.

1.3.1 Global seismology

Elastic waves propagation in the Earth, e.g. generated from earthquakes, is a major source of indirect information on the planet's interior (Dziewonski and Anderson, 1981). When an earthquake is large enough it can excite the planet's normal modes, or free oscillations (Backus and Gilbert, 1961; Park, 2005), giving insights on global properties, such as elasticity, density or anisotropy (Dahlen and Tromp, 1998). Seismologists distinguish pressure (or spheroidal) modes ${}_n\mathcal{S}_l$ and torsional (or toroidal) modes ${}_n\mathcal{T}_l$, where n and l gives the number of radial and surface nodes. Those modes can be identified in a long period spectrum of oscillations, as seen in Figure 1.4, from Park (2005).

It appeared that the measured normal frequencies are different from the expected values predicted by theoretical calculations developed for a radially-symmetric elastic sphere (Lamb, 1881). In particular, some peaks are splitted compared to the theory, with $2l+1$ peaks in place of one. This observation is succesfully explained by the rotation of the Earth which was not previously taken into account in the predictions (Backus and Gilbert, 1961;

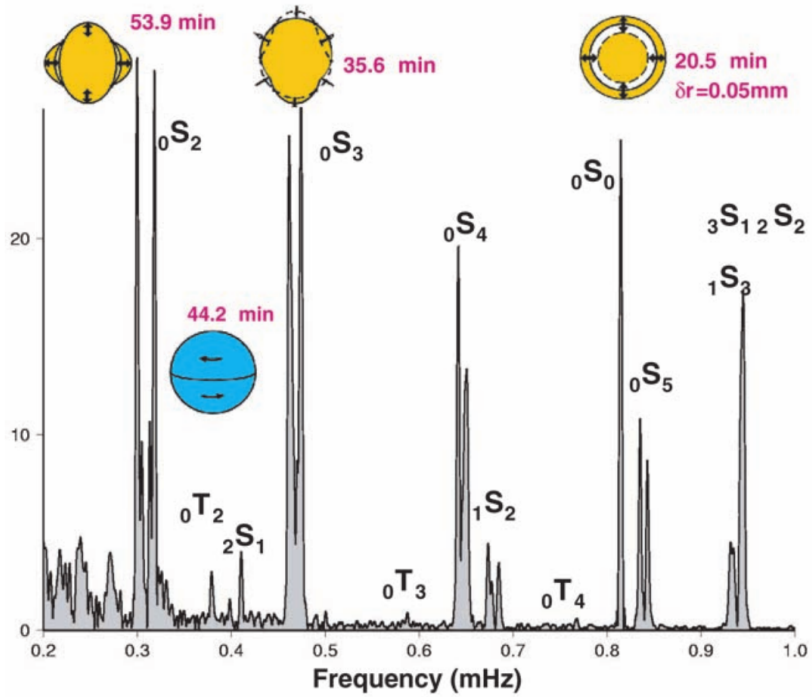

Figure 1.4: Schematic of the motion of free oscillations ${}_0\mathcal{S}_2$, ${}_0\mathcal{T}_2$, ${}_0\mathcal{S}_3$, and ${}_0\mathcal{S}_0$ superimposed on a spectrum computed from 240 hours of vertical seismic motions recorded at the CAN (Canberra, Australia) station of the Geoscope Network. From Park (2005).

Pekeris et al., 1961). Earth has many other parameters that differs from the simple model of an elastic sphere. One that is of great interest for us is the departures from sphericity. Just like rotation, it causes splitting in the normal mode frequencies that have been observed quite early as well (Woodhouse and Dahlen, 1978). Other effects include heterogeneity in the medium, in the elasticity parameter or density (Dahlen and Tromp, 1998). This perturbation method and effects influencing the Earth's normal modes (including at higher order in perturbation) are detailed in Dahlen and Tromp (1998).

1.3.2 Helio- and astero-seismology

Seismology applied to the Sun and then other stars, becoming helio- and astero-seismology, has also focused on normal modes to infer the bodies' interior structures and flow velocity (Aerts et al., 2010; Goupil, 2011). The rotation signature on the acoustic spectrum has been observed and interpreted (before its observation on the Earth) by Cowling (1941); Cowling and Newing (1949); Ledoux (1951).

For the Sun, the visible free surface allows to retrieve high-resolution pressure field from the free surface oscillations through its radial oscillations (Schou et al., 1998). It can then be converted into a spectrum with visible normal modes, an example is reproduced in Figure 1.5 (Schou et al., 1998; Chaplin and Basu, 2008).

Normal mode frequencies are linked to the interior properties, which can then be retrieved if the physical relationships between the two are well understood (Christensen-Dalsgaard et al., 1974; Christensen-Dalsgaard and Gough, 1976). This method is used

to infer internal flow velocity in the Sun (Christensen-Dalsgaard, 2002). A typical flow velocity map of the Sun obtained from such observations is reproduced in Figure 1.6. This motivated its transposition into laboratory experiment and the development of the MAV technique. It is useful to note that astero-seismologists developed local theoretical framework to accommodate the very large pressure and temperature gradients present in the stars' interior (Aerts et al., 2010). The helio-seismology methods are detailed in Christensen-Dalsgaard (2002); Aerts et al. (2010).

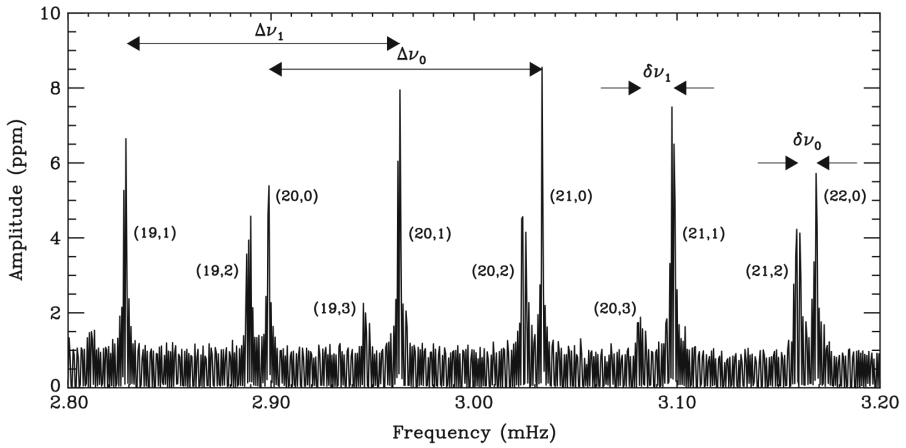

Figure 1.5: This amplitude spectrum of radial velocity variations observed with the GOLF (Global Oscillation at Low Frequencies) instrument on SOHO (SOlar and Heliospheric Observatory) shows the splittings ($\Delta\nu$ and $\delta\nu$) in the pressure modes of the Sun, from Aerts et al. (2010).

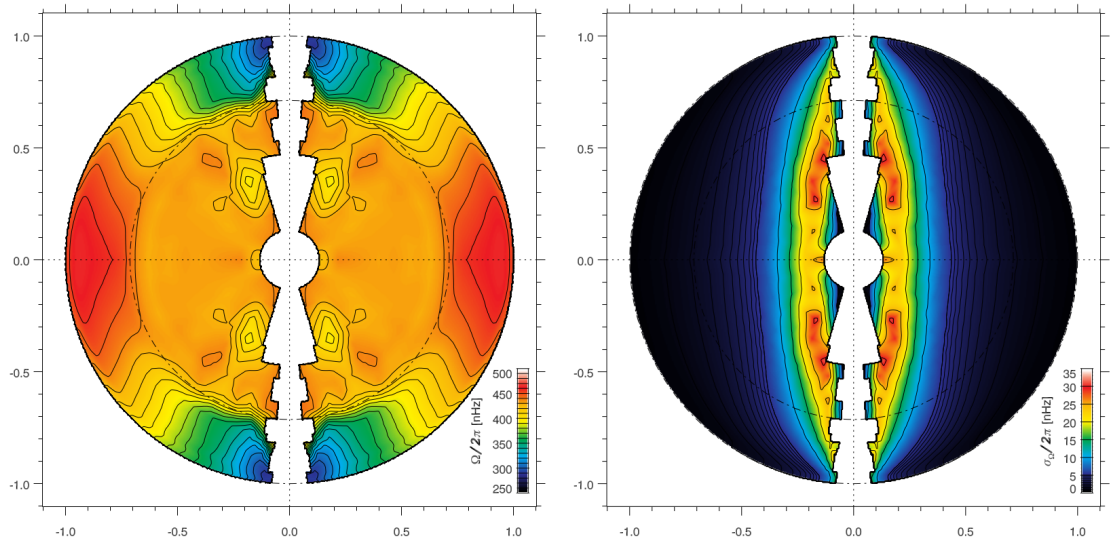

Figure 1.6: Rotation rate, as a function of depth and latitude, inferred from 12.6 yr of Michelson Doppler Imager (MDI) observations (left) and its associated uncertainty (right). (Korzennik and Eff-Darwich, 2011)

One main difference between ZoRo and both Earth and stars is the outer boundary conditions. The laboratory experiment has a rigid container while geophysical bodies have a free surface. This difference prevents the direct transposition of some of the mathematical tools developed for helioseismology onto experimental conditions, e.g. Rieutord et al. (2016), leading us to develop a new spectral decomposition suitable for laboratory experiments' boundary conditions (Vidal et al., 2020).

1.3.3 Gases metrology

The acoustic resonances of a gas-filled cavity are very sensitive to the gas properties, through the sound speed. This feature is of great interest for metrologists when trying to determine empirical laws such as state equations (Mehl et al., 2004; Moldover et al., 2014), gas properties (Hurly et al., 2003) and universal constants (Moldover et al., 1988; Trusler, 1991). It appears that this method is so precise that measuring the eigen-frequencies of quasi-spherical resonators is still today the most accurate technique used to determine the Boltzmann constant (Pitre et al., 2009). Metrologists first used spherical resonators (Mehl and Moldover, 1989) whose analytical solutions are easy to obtain. Then they switched to quasi-spherical spheroidal (Mehl, 1982, 1986, 2007) and ellipsoidal (Guianvarc'h et al., 2009; Mehl, 2010, 2015) shapes, whose frequencies are split due to the deviations from sphericity (as on the Earth and stars), allowing more precise frequency determination.

In pursue of high precision measurements, metrologists developed many theoretical tools to accurately predict all possible effects that may influence the mode frequencies, including the container elasticity (Rand and DiMaggio, 1967; Mehl, 1985), shape defaults due to manufacture, etc., summarized in Moldover et al. (1986). In particular they developed a perturbation theory for quasi-spherical cavity up to second-order (while Dahlen and Tromp (1998) and Aerts et al. (2010) only use first-order) that is of great interest for ZoRo since its ellipticity is large.

Metrologists also investigated the modes' attenuation (due to diffusion, sound radiation etc.) (Mehl, 1978; Moldover et al., 1986; Trusler, 1991), helping us to better understand the experimental spectra.

Note that acousticians used the pressure normal modes perturbation due to rotation to build a gyrometer (Bruneau et al., 1986; Herzog and Bruneau, 1989; Dupire and Bruneau, 1998; Ecotiere et al., 2004). They aim to measure a scalar rotation rate, so they focus on a few (1 or 2) modes that are easiest to measure in their experimental apparatus. They also work with a cylindrical cavity in order to make their device more practical to use and worked towards miniaturization (Bourouina et al., 1997). Acoustic gyrometer is a claimed patent (LeBlond et al., 1990).

The main difference between MAV and acoustic gyrometers is that acoustic gyrometers focus on retrieving one scalar rotation rate, while MAV aims to retrieve the whole velocity field.

1.4 Outline of the thesis

This thesis is organised as follow. This section concludes the brief general introduction of Chapter 1. In Chapter 2, we present the more specific theoretical framework we choose to use, including the whole physical description of the problem using perturbation theory. We will summarise the effects of rotation, ellipticity and diffusion on the acoustic spectral response. Then we combine those effects to produce theoretical synthetic acoustic spectra to be compared with the experimental data. Chapter 3 is dedicated to the experimental set-up. We present the ZoRo apparatus and describe the complete measurement chain. We start from data acquisition protocol and follow all steps in the analysis of the measured sound signal, including the crucial step of mode identification, up to the extraction of acoustic splitting. Then in Chapter 4 we present the Bayesian inversion problem formalism and apply it to synthetic acoustic data. This leads us to propose quantitative measures of an inversion accuracy. We also investigate the influence of the available mode collection on the inversion results. Finally, in Chapter 5 we apply all the methods developed in the previous chapter to an experimental unknown flow and try to invert it. We study a centrifugally driven flow through open holes. A brief discussion in Chapter 6 concludes this thesis.

2

Theoretical acoustic spectra

Consider that with many calculations one can win the victory, so fear their insufficiency. How unlikely is it that anyone who does not do so will win!

- Sun Tzu, *The Art of War*

In this chapter, we aim to give a common theoretical framework to describe sound waves and rotating fluids. We describe more specifically normal modes of an enclosed quasi spherical fluid cavity and how their frequency can be a signature of the flow field. To do that, we use a perturbation theory, assuming that the effects we take into account are small thus the system stays close to a the simpler reference problem of a cavity at rest, where solutions are known.

We consider a fluid, governed by the usual conservation equations (mass, momentum and heat). We linearise them under the assumption that the acoustic waves cause a small disturbance, and complete them with constitutive equations. We are interested in the resonances of the fluid cavity, hence its modal response. This leads to expressing this closed system into an eigenvalue problem. This problem corresponds to the Helmholtz wave equation if we assume a diffusionless fluid at rest, for which exact analytical solutions are available for the the specific spherical geometry. We take this as our reference model, that we will then perturb.

We successively add as independent perturbations the effects that are present in the experimental apparatus and not yet taken into account in the reference model. First we consider background rotating flows including Coriolis forces, then we perturb the resonator geometry into a spheroid (matching our experimental apparatus' shape), and add both thermal and viscous diffusions. We show that second-order perturbation is needed for geometrical correction at our apparatus' flattening, while first-order is a priori enough for both diffusion and rotational corrections.

By taking all those effects into account, we are able to obtain analytical prediction of the eigenfrequencies for our resonator. We confront the theoretical values obtained with perturbation theory with finite-element calculations, and show that they are in very good agreement. This gives us robust theoretical predictions needed to interpret experimental data.

2.1 Formulation of the problem

We present the general framework used to describe acoustic eigen-frequencies of a cavity. We describe the classic problem formulation, following Blackstock (2000), where we remind the useful equations for our problem, the set of approximations we take, as well as the boundary conditions. We also present the resolution method we use (perturbation theory) as well as the full resolution of the problem for the reference model we choose.

2.1.1 Governing equations

General formulation

The description of a fluid behaviour breaks down to the conservation and constitutive equations. The conservation equations for mass, momentum and energy write (Blackstock, 2000)

$$\frac{\partial \rho}{\partial t} + \nabla \cdot (\rho \boldsymbol{v}) = M, \tag{2.1}$$

$$\rho \frac{\mathrm{D}\boldsymbol{v}}{\mathrm{D}t} = \nabla \cdot \boldsymbol{\sigma} + \boldsymbol{F}, \tag{2.2}$$

$$\rho T \frac{\mathrm{D}s}{\mathrm{D}t} = -\nabla \cdot \boldsymbol{q} + \varphi + Q, \tag{2.3}$$

where $\boldsymbol{v}$ is the velocity field, ρ is the density, T is the temperature, s is the specific entropy, $\boldsymbol{\sigma}$ is the stress tensor, $\boldsymbol{q}$ is the local heat flux, φ is the viscous dissipation function, and M, $\boldsymbol{F}$ and Q are possible source terms. And where the operator $\mathrm{D}/\mathrm{D}t$ is the material derivative (or advection operator) defined as

$$\frac{\mathrm{D}(\,\cdot\,)}{\mathrm{D}t} = \frac{\partial(\,\cdot\,)}{\partial t} + (\boldsymbol{v} \cdot \nabla)(\,\cdot\,). \tag{2.4}$$

We want to reformulate the energy conservation equation with thermodynamic variables that are more easily measurable (than entropy). Usual sets of variables involve the pressure p, such as (p, T) or (ρ, p). To do so, thermodynamics relations are necessary, for instance, by definition,

$$\rho T \mathrm{d}s = \rho C_p \mathrm{d}T - \alpha T \mathrm{d}p, \tag{2.5}$$

where α is the coefficient of isobaric thermal expansion and C_p is the specific heat at constant pressure. For an ideal gas, it can be simplified into

$$\mathrm{d}s = C_v \frac{\mathrm{d}p}{\rho} - C_p \frac{\mathrm{d}\rho}{p}, \tag{2.6}$$

with C_v the specific heat at constant volume.

In this general formulation, we introduced 6 variables ρ, $\boldsymbol{v}$, p, T, $\boldsymbol{\sigma}$, $\boldsymbol{q}$ and only 3 equations. We need to add constitutive equations into the system. Since these equations are inherent to the fluid properties, this causes a slight loss in generality.

From now on, we will assume that:

(i) the working fluid is Newtonian, meaning that the stress tensor $\boldsymbol{\sigma}$ follows

$$\boldsymbol{\sigma} = -p\mathbf{I} + \boldsymbol{\tau} = -p\mathbf{I} + \mu[\nabla \boldsymbol{v} + (\nabla \boldsymbol{v})^\top] + \lambda(\nabla \cdot \boldsymbol{v})\mathbf{I}, \tag{2.7}$$

where $\mathbf{I}$ is the identity matrix and $\boldsymbol{\tau}$ is the dissipative part of the stress tensor.

In the particular case of uniform viscosities, it becomes

$$\nabla \cdot \boldsymbol{\sigma} = -\nabla p + \mu \nabla^2 \boldsymbol{v} + (\lambda + \mu) \nabla (\nabla \cdot \boldsymbol{v}), \tag{2.8}$$

where μ is the dynamic (shear) viscosity, λ is the second coefficient of viscosity which is related to the bulk viscosity μ_B through $\lambda = \mu_B - 2\mu/3$;

(ii) the heat transfer obeys Fourier's law

$$\boldsymbol{q} = -\rho_0 C_p \kappa \nabla T, \tag{2.9}$$

where κ is the thermal diffusivity.

This is used to define the viscous dissipation function

$$\varphi = (\nabla \boldsymbol{v}) : \boldsymbol{\tau}, \tag{2.10}$$

where $\boldsymbol{\tau}$ is the dissipative part of the stress tensor. We recall that the double dot product of 2 matrices $\boldsymbol{A}$ and $\boldsymbol{B}$ is defined as $\boldsymbol{A} : \boldsymbol{B} = A_{ij} B_{ij}$ using Einstein summation notation.

One last relation is needed to close the problem, that is the equation of state, which gives an additional relation between thermodynamic variables, usually $p(\rho, T)$ or $\rho(p, T)$. A general isentropic state equation can be expressed as small variations around a background state (ρ_0, T_0, p_0), which writes at leading order

$$\rho - \rho_0 = (p - p_0) \left.\frac{\partial \rho_0}{\partial p}\right|_T + (T - T_0) \left.\frac{\partial \rho_0}{\partial T}\right|_p. \tag{2.11}$$

Assuming that the partial derivatives are constant within the small variations range, it becomes

$$\rho = \rho_0 \left[1 + \beta_T (p - p_0) - \alpha (T - T_0)\right], \tag{2.12}$$

where $\beta_T = \gamma \beta_s$ is the isothermal compressibility with γ the specific-heat ratio and β_s the isentropic compressibility.

We can here introduce the isentropic sound speed c as

$$c^2 = \left.\frac{\mathrm{d}p}{\mathrm{d}\rho}\right|_{s=cste}, \tag{2.13}$$

or more usually, assuming small departures from background state ($\rho \to \rho_0$), the speed of sound c is given by

$$c = (\rho_0 \beta_s)^{-1/2} = [\gamma / (\rho_0 \beta_T)]^{1/2}, \tag{2.14}$$

and the heat capacity at constant volume C_v is $C_v = C_p / \gamma$.

We now have a closed system. Injecting the constitutive equations into the momentum and energy conservation equations, the system eq. (2.2)–eq. (2.3) leads to

$$\rho \left[\partial_t \boldsymbol{v} + \boldsymbol{v} \cdot \nabla \boldsymbol{v}\right] = \nabla \cdot \left(-p\mathbf{I} + \mu[\nabla \boldsymbol{v} + (\nabla \boldsymbol{v})^\top] + \lambda (\nabla \cdot \boldsymbol{v}) \mathbf{I}\right) + \boldsymbol{F}, \tag{2.15}$$

$$\rho C_p \left(\partial_t T + \boldsymbol{v} \cdot \nabla T\right) - \alpha T \left(\partial_t p + \boldsymbol{v} \cdot \nabla p\right) = \nabla \cdot (\rho C_p \kappa \nabla T) + \varphi + Q. \tag{2.16}$$

We further assume that viscous and thermal diffusivities are uniform (λ, μ, κ are constants), there is no source terms ($M = Q = 0$), and the only additional force is due to gravity $\boldsymbol{F} = \rho\boldsymbol{g}$.

The complete set of conservation equations eq. (2.1), eq. (2.15)–eq. (2.16) finally becomes

$$\partial_t\rho + \nabla\cdot(\rho\boldsymbol{v}) \;=\; 0, \tag{2.17}$$

$$\rho\left[\partial_t\boldsymbol{v} + \boldsymbol{v}\cdot\nabla\boldsymbol{v}\right] \;=\; -\nabla p + \mu\nabla^2\boldsymbol{v} + (\lambda+\mu)\nabla(\nabla\cdot\boldsymbol{v}) + \rho\boldsymbol{g}, \tag{2.18}$$

$$\rho C_p\left(\partial_t T + \boldsymbol{v}\cdot\nabla T\right) - \alpha T\left(\partial_t p + \boldsymbol{v}\cdot\nabla p\right) \;=\; \rho C_p\kappa\nabla^2 T + \varphi. \tag{2.19}$$

We can now recognize the usual Navier-Stokes equation in eq. (2.18) and the usual heat equation in eq. (2.19). For rotating fluids, it is useful to express the momentum conservation, or Navier-Stokes equations, eq. (2.18) in the referential rotating with the fluid. The change of referential from the inertial referential to a rotating (non-Galilean) referential implies that additional terms appear due to the velocity composition law (Varignon's theorem). It then becomes in the referential rotating along $\boldsymbol{\Omega}$

$$\begin{aligned}\rho\left[\partial_t\boldsymbol{v} + \boldsymbol{v}\cdot\nabla\boldsymbol{v} + 2\boldsymbol{\Omega}\times\boldsymbol{v} + \boldsymbol{\Omega}\times(\boldsymbol{\Omega}\times\boldsymbol{r}) + \mathrm{d}_t\boldsymbol{\Omega}\times\boldsymbol{r}\right]&\\ = -\nabla p + \mu\nabla^2\boldsymbol{v} + (\lambda+\mu)\nabla(\nabla\cdot\boldsymbol{v}) + \rho\boldsymbol{g},&\end{aligned} \tag{2.20}$$

with $\boldsymbol{\Omega}$ the angular velocity vector of the referential and $\boldsymbol{r}$ the position vector.

We can recognize the rotating Navier-Stokes equations, with the additionnal terms being, from left to right, the Coriolis $2\boldsymbol{\Omega}\times\boldsymbol{v}$, the centrifugal $\boldsymbol{\Omega}\times(\boldsymbol{\Omega}\times\boldsymbol{r})$ and the Poincaré effects $\mathrm{d}_t\boldsymbol{\Omega}\times\boldsymbol{r}$.

The final set of equations eq. (2.1), (2.19)–(2.20) completely describes the problem by taking all potential effects into account. This implies a high complexity, seen both in the number of the variables and the non-linearity of the equations. In order to solve this system, we will further simplify it by linearizing it around a background state.

Linearized equations

The above equations are non-linear. We can consider a linearized version of those by assuming that all quantities stay close enough to the background state so that their variations can be considered as small. We separate the total particle velocity into $\boldsymbol{v}_t = \boldsymbol{v_0} + \boldsymbol{v}$ with $\boldsymbol{v}$ the variations around the background state (in the rotating frame) $\boldsymbol{v_0}$, and do the same for pressure $p_t = p_0 + p$, temperature $T_t = T_0 + T$ and density $\rho_t = \rho_0 + \rho$.

In the acoustic framework, the sound waves cause disturbances in the medium (here defined as the fluid with its background state, possibly in motion) that can be considered small if $|\boldsymbol{v}| \ll c_0$ or $M_S = |\boldsymbol{v}|/c_0 \ll 1$ with M_S the (sonic) Mach number. In this small-signal limit, the conservation equations can be linearized into (Blackstock, 2000)

$$\partial_t\rho + \nabla\cdot(\rho_0\boldsymbol{v} + \rho\boldsymbol{v_0}) = 0, \tag{2.21}$$

$$\begin{aligned}\rho_0\left[\partial_t\boldsymbol{v} + \boldsymbol{v_0}\cdot\nabla\boldsymbol{v} + \boldsymbol{v}\cdot\nabla\boldsymbol{v_0} + 2\boldsymbol{\Omega}\times\boldsymbol{v}\right]&\\ + \rho\left[\partial_t\boldsymbol{v_0} + (\boldsymbol{v_0}\cdot\nabla\boldsymbol{v_0}) + 2\boldsymbol{\Omega}\times\boldsymbol{v_0} + \boldsymbol{\Omega}\times(\boldsymbol{\Omega}\times\boldsymbol{r}) + \mathrm{d}_t\boldsymbol{\Omega}\times\boldsymbol{r}\right]&\\ = -\nabla p + \mu\nabla^2\boldsymbol{v} + (\lambda+\mu)\nabla(\nabla\cdot\boldsymbol{v}) + \rho\boldsymbol{g},&\end{aligned} \tag{2.22}$$

$$\begin{aligned}\rho_0 C_p \left[\partial_t T + \boldsymbol{v_0}\cdot\nabla T + \boldsymbol{v}\cdot\nabla T_0\right] + \rho C_p \left[\partial_t T_0 + (\boldsymbol{v_0}\cdot\nabla T_0)\right] \\ - \alpha T_0 \left[\partial_t p + \boldsymbol{v_0}\cdot\nabla p + \boldsymbol{v}\cdot\nabla p_0\right] - \alpha T \left[\partial_t p_0 + \boldsymbol{v_0}\cdot\nabla p_0\right] \\ = \rho C_p \kappa \nabla^2 T + \varphi.\end{aligned} \tag{2.23}$$

This system is to be considered along with the constitutive equations

$$\rho = \rho_0 \left[1 + \beta_T (p = p_0) - \alpha (T - T_0)\right], \tag{2.24}$$

$$\varphi = (\nabla \boldsymbol{v}) : \boldsymbol{\tau}(\boldsymbol{v_0}) + (\nabla \boldsymbol{v_0}) : \boldsymbol{\tau}(\boldsymbol{v}). \tag{2.25}$$

Finally this linearized system can be solved in the frequency domain, by assuming time periodic solutions. We seek the normal modes with a harmonic time dependence $\exp(-\mathrm{i}\omega t)$, where ω is the pulsation (possibly complex). The system of governing equations (2.21)–(2.23) can be cast into a symbolic eigenvalue equation as

$$-\omega^2 \boldsymbol{u} = \mathcal{H}\boldsymbol{u}, \tag{2.26}$$

where $\mathcal{H}$ is a complex vectorial operator linear in $\boldsymbol{u}$, which can be the velocity $\boldsymbol{v}$ or the Lagrangian displacement for isentropic fluids (e.g. Ledoux, 1951). Usually in acoustics, this is then used to obtain a single (generalized) pressure equation (Hunt, 1955; Morse and Ingard, 1986; Pierce, 1990; Blackstock, 2000; Bergliaffa et al., 2004). We keep this more general formulation, which is later needed to take flows into account (see §2.2.1).

In order to solve this equation, it needs to be supplemented with boundary conditions.

Boundary conditions

To match the experimental conditions, we consider a gaseous cavity enclosed within a metallic rigid container. As such, it is a good approximation to consider an infinitely rigid container since the sound speed in the container is much larger than in the air (Moldover et al., 1986). Then we impose at the rigid wall of the container a no-slip condition ($\boldsymbol{v} = \boldsymbol{0}$) and continuity of temperature and heat flux. In our case, where the thermal conductivity is much larger in the container, it is equivalent to assume isothermal boundary condition (Herzfeld, 1938). Note that the rigid container boundary condition has proven to be a constraint for existing eigensolvers leading us to develop our own (Vidal et al., 2020).

Using these boundary conditions leads to an apparition of thermal and viscous acoustic thicknesses d_{th} and d_{visc} (when diffusions are not neglected), defined as (Blackstock, 2000)

$$d_{th} = \sqrt{\frac{2\kappa}{\omega}} \qquad \text{and} \qquad d_{visc} = \sqrt{\frac{2\nu}{\omega}}, \tag{2.27}$$

with ω the angular frequency of the sound wave. Note that these acoustic layer thicknesses depend on the frequency of the periodic solutions.

2.1.2 Resolution method for the ZoRo case

This exact description of our problem as written in the system eq. (2.21)–(2.23) involves non-trivial solutions. The corresponding wave equation has analytical solution only for specific cases. In general, they can be approached with numerical schemes or spectral decomposition (e.g. Vidal et al., 2020) but both might involve heavy calculations. Instead we choose to use a perturbation approach.

Overview of perturbation theory

The idea of perturbation theory is to define a reference model for which simple analytical solutions are available, and to add missing terms as a series of small perturbations (Bender and Orszag, 1978). This method is a classic and powerful approach that has been useful for many problems (e.g. Landau et al., 1977; Cohen-Tannoudji et al., 2018). Its drawbacks include that we need to know a simple solution “close" to the considered case. And second that the problem at hand and the model for which solutions are known are “close", i.e amplitude of deviations from the chosen reference model are small, so that it stays relevant. A perturbation series is typically

$$X = X_0 + \epsilon X_1 + \epsilon^2 X_2 + \epsilon^3 X_3 + \dots, \tag{2.28}$$

where X is the solution of the complete problem as described by $\mathcal{H}$, X_0 is the solution of the reference model, ϵ is the small parameter characterizing the deviations, and X_i are the successive higher orders correction from the reference model.

Our primary goal is to accurately describe the flows and acoustic response within the ZoRo experiment. ZoRo is an oblate spheroid of ellipticity $e = (r_{eq} - r_{pol})/r_{eq} = 0.05$, filled with gas (air) and rotating around its revolution axis up to 30 Hz. The ZoRo experimental set-up is detailed in Chapter 3.

ZoRo is a rotating aspherical cavity, relatively close to a diffusionless sphere at rest, that we will choose as our reference model. The main deviations from this idealised reference model are: the spheroidal shape, the rotation and the diffusion effects. We can define for each of these effects a dimensionless number that characterizes their deviation from the reference model, and we will consider the perturbation theory valid if this number is small. The shape deviation is defined by the ellipticity $e = 0.05 \ll 1$. The rotational effects relative strength is given by the sonic Mach number M_S, that compares the rotation rate (maximum 30 Hz in ZoRo) to the typical resonance frequency (the fundamental mode is around 600 Hz) so $M_S < 30/600 = 0.05 \ll 1$. The viscous and thermal adimensionned diffusions are given by $\nu/(ca) \simeq 2 \cdot 10^{-7}$ and $\kappa/(ca) \simeq 3 \cdot 10^{-7}$ respectively, with a the cavity typical lengthscale and c the sound speed.

In conclusion ZoRo rotates slowly (compared to the sound speed), it is relatively non-dissipative (Moldover et al., 1986) and its ellipticity is moderate enough to stay close to a sphere, justifying the perturbation method with the diffusionless sphere at rest as reference model. For the chosen reference model, the above equations are equivalent to the Helmholtz equation for which exact analytical solutions are known for the sphere. The rotational, geometry and diffusion effects will then be successively treated as perturbations, following Lynden-Bell and Ostriker (1967).

Note that for spheroids, complete solutions for diffusionless medium at rest exist but involve spheroidal coordinates, which considerably increase the resolution complexity (Chang, 1971, 1972).

Reference model: the diffusionless sphere at rest

We take as reference model a diffusionless fluid at rest enclosed in a perfect sphere of radius a, so that $\lambda = \mu = 0$ and $\boldsymbol{\Omega} = \mathbf{0}$, and neglect the gravity. Under these restrictive assumptions, and assuming the time-dependence $\propto \exp(-\mathrm{i}\omega t)$, the eigenvalue equation eq. (2.26) becomes

$$\omega^2 \boldsymbol{v} = -c^2 \nabla (\nabla \cdot \boldsymbol{v}) = \mathcal{H}_0 \boldsymbol{v}. \tag{2.29}$$

Assuming that the sound waves are irrotational, we can then introduce the velocity potential Ψ as $\boldsymbol{v} = \nabla\Psi$, which is linked to acoustic pressure by $p = -\partial\Psi/\partial t$ (Blackstock, 2000). Coupled with the further assumption of time-periodicity, this allows us to retrieve the well-known Helmholtz equation, or the usual wave equation

$$\left(\nabla^2 + k^2\right) p(\boldsymbol{r}) = 0, \tag{2.30}$$

with $k = \omega/c$ the wavenumber.

The Helmholtz equation eq. (2.30) is projected onto spherical coordinates (r, θ, ϕ), so that $p(\boldsymbol{r}) = p(r, \theta, \phi) = R(r)\Theta(\theta)\Phi(\phi)$. Its solutions are (Russell, 2010)

$$p(r, \theta, \phi) = \left[j_l(kr) + B y_l(kr)\right] \; \mathcal{P}_l^m(\cos\theta) \; A\cos(m\phi + C), \tag{2.31}$$

where A, B, C are integration constants to be determined with boundary conditions.

We also introduced $\mathcal{P}_l^m$ the associated Legendre polynomial of order l and degree m, that carries the angular dependence, defined as

$$\mathcal{P}_l^m(x) = (-1)^m (1-x)^{m/2} \frac{\mathrm{d}^m \mathcal{P}_l(x)}{\mathrm{d}x^m}, \tag{2.32}$$

where $\mathcal{P}_l(x)$ is the Legendre polynomial of order l, given by

$$\mathcal{P}_l(x) = \frac{1}{2^l l!} \frac{\mathrm{d}^l}{\mathrm{d}x^l} \left[(x^2 - 1)^l\right]. \tag{2.33}$$

The radial dependence is taken into account with j_l and y_l the spherical Bessel functions of the first and second kind respectively, defined as

$$j_l(kr) = \sqrt{\frac{\pi}{2r}} J_{l+1/2}(kr), \tag{2.34}$$

$$y_l(kr) = (-1)^{l+1} \sqrt{\frac{\pi}{2r}} J_{-l-1/2}(kr), \tag{2.35}$$

where $J_l(kr) = \displaystyle\sum_{n=0}^{\infty} \frac{(-1)^n}{n!\,\Gamma(n+l+1)} \left(\frac{kr}{2}\right)^{2n+l}$ is the Bessel function and Γ is the Gamma function.

Another usual expression for the general pressure solution eq. (2.31) consists in separating the angular and radial dependences into

$$p(r,\theta,\phi) = [j_l(kr) + By_l(kr)]\,\mathcal{Y}_l^m(\theta,\phi), \tag{2.36}$$

where $\mathcal{Y}_l^m(\theta,\phi)$ is the spherical harmonic of order l and degree m and fully describes the surface pressure field.

We consider a full sphere (with no inner core), so the boundary condition at the center ($r = 0$) imposes $B = 0$. For each l there is an infinity of k that are solutions of eq. (2.36), forming a continuous spectrum of modes. We index them with n going from 0 to ∞.

Finally the pressure field associated to the cavity's free oscillations is given by

$$p_{nlm}(r,\theta,\phi) = j_l(k_{nl}r)\mathcal{Y}_l^m(\theta,\phi). \tag{2.37}$$

The triplet (n,l,m) fully characterizes one acoustic mode, we will denote it ${}_n\mathcal{S}_l^m$, following the nomenclature used for the eigenmodes in the Earth (Dahlen and Tromp, 1998). Some modes hold special properties, that we will use further in the manuscript.

In particular we distinguish:

- zonal modes, $m = 0$, which are independent of ϕ i.e. symmetric around the z axis,

- radial modes, $l = 0$, which are homogeneous at the sphere surface,

- overtones, $n > 0$, which have at least one radial node.

The addition of the outer boundary condition: a rigid, no-slip boundary at the container enclosure, writes out as

$$\left.\frac{\partial j_l(k_{nl}r)}{\partial r}\right|_{r=a} = 0. \tag{2.38}$$

This completes the quantification of modes, and leaves only the discrete modes where n is an integer. The quantified wavenumber k_{nl} can thus be written as $k_{nl} = z_{nl}/a$, with z_{nl} the n^{th} zero of the derivative of the spherical Bessel function of order l. Its corresponding resonance frequency f_{nl} is given by

$$f_{nl} = \frac{ck_{nl}}{2\pi} = \frac{cz_{nl}}{2\pi a}. \tag{2.39}$$

We remark here that the frequency is independent of m so all modes with the same n and l share the same frequency in the sphere: the modes are *degenerated* in frequency. This property is directly linked to the spherical symmetry, where the longitudinal direction ϕ cannot be distinguished without more constraints.

The eigenfrequencies with the relevant values for ZoRo are computed for the sphere of same volume, which corresponds to a radius $a = 0.1966$ m, and $c = 343.2638$ m.s^{-1}. The lowest frequencies are given in Table 2.1 and represented in figure Figure 2.1.

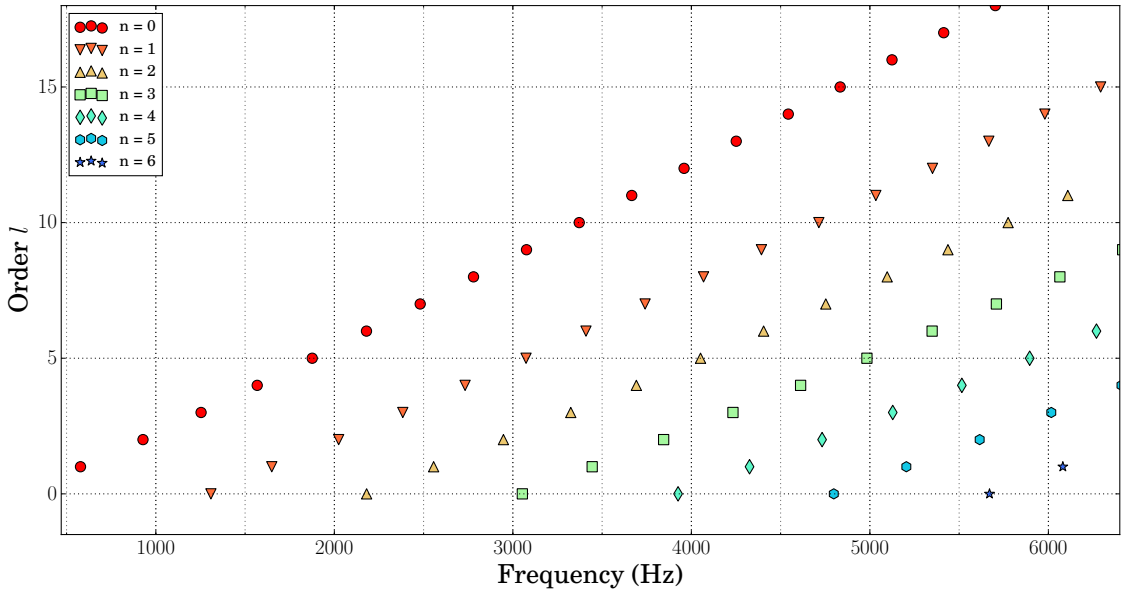

Figure 2.1: Acoustic eigenmode frequencies for a sphere of radius $a = 0.1966$ m and sound speed $c = 343.2638$ m/s for increasing order l, up to $n = 6$.

	$n=0$	$n=1$	$n=2$	$n=3$	$n=4$	$n=5$
$l=0$	0	1309	2183	3056	3929	4802
$l=1$	578	1651	2558	3447	4329	5208
$l=2$	928	2026	2949	3848	4736	...
$l=3$	1254	2385	3327	4236	5132	
$l=4$	1569	2735	3695	4615	...	
$l=5$	1877	3076	4054	4987		
$l=6$	2181	3412	4408	5353		
$l=7$	2483	3744	4757	...		
$l=8$	2782	4071	5101			
$l=9$	3078	4396	...			
$l=10$	3374	...				
$l=11$	3669					
$l=12$	3962					
$l=13$	4255					
...						

Table 2.1: Frequency (Hz) of the first (n, l) eigenmodes for a sphere of radius $a = 0.1966$ m and sound speed $c = 343.2638$ m/s.

2.2 Perturbation theory for our study cases

In order to accurately predict the acoustic resonances of the experimental apparatus, we need to perturb the reference model into a system closer to the experiment. Starting from the reference model described above, we will now successively add fluid flow and rotation as a perturbation from the chosen reference model. Then we will perturb the shape of the container, and finally consider diffusion effects.

2.2.1 Background rotating flows

We focus on a sphere rotating around one of its diameter. This configuration breaks the spherical symmetry by imposing a rotation axis and more importantly by creating azimuthal flows (from solid body rotation to more complicated ones). The existence of these flows breaks the azimuthal symmetry and lifts the m-degeneracy, leading to a *splitting* of the eigenfrequency of the sphere at rest (in the inertial frame).

We aim to characterize and calculate the modes' rotational splittings. To do so, we follow the method detailed in Aerts et al. (2010), from where we extracted the steps relevant for our study and simplified their general formalism for our specific case. This method gives the acoustic rotational splitting compared to the reference model which is a motionless sphere. All the calculations (from eq. (2.42) onward) are valid in the non-rotating inertial referential, which is the referential of interest for stars measurements, as the observer is supposed immobile with respect to the body's rotation.

First-order perturbation theory in flow velocity

We start from the reference model described in §2.1.2. We assume that the rotation rate Ω is slow compared to the acoustic frequencies, allowing us to consider first-order perturbation only. In practice, this leads us to neglect the centrifugal effects that are second-order in Ω, and keep only the (first-order) Coriolis effects. Within the attainable experimental conditions, the rotation rate has slow temporal variations, so we expect the Poincaré effects to be negligible as well. We will also assume that axisymmetric rotation is the only source of motion so $\boldsymbol{v_0} = \boldsymbol{\Omega} \times \boldsymbol{r} = \Omega r \sin\theta \boldsymbol{e_\phi}$. We now take the Coriolis effect into account. Since it is directly related to the fluid background velocity, the simple acoustic way of expressing the eigenvalue problem with the (scalar) pressure variable only is not valid anymore, and we go back to the vectorial momentum conservation equation eq. (2.22). With the approximations for the reference model (no diffusions, gravity neglected), eq. (2.22) valid in the non-rotating inertial frame thus reduces to

$$\rho \left(\frac{\partial \boldsymbol{v}}{\partial t} + (\boldsymbol{v} \cdot \boldsymbol{\nabla}) \boldsymbol{v} \right) = -\boldsymbol{\nabla} p. \tag{2.40}$$

We separate the variables into a background and perturbation part, following Lynden-Bell and Ostriker (1967). We write $\boldsymbol{v} = \boldsymbol{v_0} + \boldsymbol{v'}$ with $'$ denoting the Eulerian perturbation, and use the same notation for ρ, p and $\boldsymbol{g}$. The perturbed continuity equation writes as

$$0 = \frac{\partial \rho}{\partial t} + \boldsymbol{\nabla} \cdot (\rho \boldsymbol{v}) = \frac{\partial (\rho_0 + \rho')}{\partial t} + \boldsymbol{\nabla} \cdot ((\rho_0 + \rho')(\boldsymbol{v_0} + \boldsymbol{v'})), \tag{2.41}$$

keeping only the first-order of perturbation, it becomes

$$0 = \frac{\partial \rho'}{\partial t} + \rho_0 \boldsymbol{\nabla} \cdot \boldsymbol{v'} + \rho' \boldsymbol{\nabla} \cdot \boldsymbol{v_0}. \tag{2.42}$$

The Lagrangian description is necessary when the system is self-graviting (Chandrasekhar, 1964). It is also of particular interest when the medium properties are not homogeneous and display large variations across the system, as encountered in stars due to the strong pressure and temperature gradients (Aerts et al., 2010). Following the asteroseismology framework from Aerts et al. (2010), we will use the Lagrangian description as well.

Let $\boldsymbol{\delta r}$ be the local fluid displacement due to acoustic perturbation, $\boldsymbol{\delta v}$ the local perturbed velocity. The correspondence between Eulerian and Lagrangian descriptions is given by

$$\boldsymbol{\delta v} = \frac{D\boldsymbol{\delta r}}{Dt} = \frac{\partial \boldsymbol{\delta r}}{\partial t} + (\boldsymbol{v_0} \cdot \boldsymbol{\nabla})\boldsymbol{\delta r} = \boldsymbol{v'} + (\boldsymbol{\delta r} \cdot \boldsymbol{\nabla})\boldsymbol{v_0}, \tag{2.43}$$

where $D/(Dt)$ stands for the material derivative defined in eq. (2.4).

The first-order Lagrangian momentum equation is then,

$$\rho_0 \frac{\partial^2 \boldsymbol{\delta r}}{\partial t^2} + 2\rho_0 \left(\boldsymbol{v_0} \cdot \boldsymbol{\nabla}\right) \frac{\partial \boldsymbol{\delta r}}{\partial t} = -\boldsymbol{\nabla} p', \tag{2.44}$$

where we neglected the quadratic term in velocity $\left(\boldsymbol{v_0} \cdot \boldsymbol{\nabla}\right)^2 \boldsymbol{\delta r}$.

To proceed further we assume that time dependencies are all $\propto \exp(-\mathrm{i}\omega t)$ only, allowing the momentum equation to be rewritten

$$-\rho_0 \omega^2 \boldsymbol{\delta r} - 2i\omega\rho_0 \left(\boldsymbol{v_0} \cdot \boldsymbol{\nabla}\right) \boldsymbol{\delta r} = -\boldsymbol{\nabla} p'. \tag{2.45}$$

This equation corresponds to the general form of perturbed eigenvalue equation, eq. (3.330) from Aerts et al. (2010)

$$\omega^2 \boldsymbol{\delta r} = \mathcal{H}\, \boldsymbol{\delta r} = \left(\bar{\mathcal{H}_0} + \delta\mathcal{H}\right) \boldsymbol{\delta r}, \tag{2.46}$$

with $\bar{\mathcal{H}_0} = 1/\rho_0 \boldsymbol{\nabla} p'$ the equivalent of the $\mathcal{H}_0$ operator valid for the reference model for local displacement and $\delta\mathcal{H} = -2\mathrm{i}\omega \left(\boldsymbol{v_0} \cdot \boldsymbol{\nabla}\right)$ the perturbation operator. Both $\bar{\mathcal{H}_0}$ and $\delta\mathcal{H}$ are linear functionals of $\boldsymbol{\delta r}$.

We project the displacement $\boldsymbol{\delta r}$ onto the natural spherical coordinates, separating the radial and horizontal components as $\boldsymbol{\delta r} = \xi_r \boldsymbol{e_r} + \boldsymbol{\xi_h} = \xi_r \boldsymbol{e_r} + \xi_\theta \boldsymbol{e_\theta} + \xi_\phi \boldsymbol{e_\phi}$. Combining ξ_r and ξ_h gives the complete local displacement $\boldsymbol{\delta r}$, Aerts et al. (2010), eq. (3.132),

$$\boldsymbol{\delta r} = \sqrt{4\pi}\mathfrak{Re}\left\{\left[\tilde{\xi_r}(r)\mathcal{Y}_l^m(\theta,\phi)\boldsymbol{e_r} + \tilde{\xi_h}(r)\left(\frac{\partial \mathcal{Y}_l^m}{\partial \theta}\boldsymbol{e_\theta} + \frac{1}{\sin\theta}\frac{\partial \mathcal{Y}_l^m}{\partial \phi}\boldsymbol{e_\phi}\right)\right] \mathrm{e}^{-\mathrm{i}\omega t}\right\}. \tag{2.47}$$

Splitting calculation

The perturbation of the squared eigenfrequency is given, from Schiff (1969), by

$$\delta f^2 = \frac{\langle \boldsymbol{\delta r} | \delta \mathcal{H}\, \boldsymbol{\delta r} \rangle}{\langle \boldsymbol{\delta r} | \boldsymbol{\delta r} \rangle}, \tag{2.48}$$

with $\langle \cdot | \cdot \rangle$ the inner product defined as

$$\langle \boldsymbol{x} \mid \boldsymbol{y} \rangle = \int_V \rho_0\, \boldsymbol{x}^* \cdot \boldsymbol{y}\, \mathrm{d}V, \tag{2.49}$$

where * stands for the complex conjugate and $\int_V \mathrm{d}V$ is the integral over the system's volume.

Injecting the $\delta\mathcal{H}$ deduced from the momentum equation, the squared frequency perturbation becomes,

$$\delta f^2 = \frac{\langle \boldsymbol{\delta r} | - 2\mathrm{i}\omega\, (\boldsymbol{v_0} \cdot \boldsymbol{\nabla})\, \boldsymbol{\delta r} \rangle}{\langle \boldsymbol{\delta r} | \boldsymbol{\delta r} \rangle}. \tag{2.50}$$

For small perturbations the frequency perturbation can be approximated by $\delta f = \delta f^2/(f + f_0) \simeq \delta f^2/(2f_0) \simeq \delta f^2/(2f)$, so the first-order acoustic splitting is given by (eq. (3.332) in Aerts et al. (2010))

$$\delta f \simeq -\mathrm{i}\, \frac{\displaystyle\int_V \rho_0 \boldsymbol{\delta r}^*\, (\boldsymbol{v_0} \cdot \boldsymbol{\nabla})\, \boldsymbol{\delta r}\, \mathrm{d}V}{\displaystyle\int_V \rho_0 |\boldsymbol{\delta r}|^2 \mathrm{d}V} = -\mathrm{i}\, \frac{\mathrm{R}}{\mathrm{I}}. \tag{2.51}$$

For the simple case where the velocity is due to axisymmetric rotation only, in the inertial frame we have $\boldsymbol{v_0} = \boldsymbol{\Omega} \times \boldsymbol{r} = \Omega r \sin\theta \boldsymbol{e_\phi}$, so

$$\begin{aligned}(\boldsymbol{v_0} \cdot \boldsymbol{\nabla})\boldsymbol{\delta r} &= \mathrm{i}m\Omega \boldsymbol{\delta r} \\ &\quad + \Omega\left[-\sin\theta \boldsymbol{\delta r} \cdot \boldsymbol{e_\phi} \boldsymbol{e_r} - \cos\theta \boldsymbol{\delta r} \cdot \boldsymbol{e_\theta} \boldsymbol{e_\theta} + (\sin\theta \boldsymbol{\delta r} \cdot \boldsymbol{e_r} + \cos\theta \boldsymbol{\delta r} \cdot \boldsymbol{e_\theta}) \boldsymbol{e_\phi}\right] \\ &= \mathrm{i}m\Omega \boldsymbol{\delta r} \\ &\quad + \sqrt{4\pi}\Omega \left[\tilde{\xi}_h \frac{\partial \mathcal{Y}_l^m}{\partial \phi} \boldsymbol{e_r} - \cot\theta \tilde{\xi}_h \frac{\partial \mathcal{Y}_l^m}{\partial \phi} \boldsymbol{e_\theta} + \left(\sin\theta \tilde{\xi}_r \mathcal{Y}_l^m + \cos\theta \tilde{\xi}_h \frac{\partial \mathcal{Y}_l^m}{\partial \theta}\right) \boldsymbol{e_\phi}\right].\end{aligned} \tag{2.52}$$

By injecting the local displacement $\boldsymbol{\delta r}$ from eq. (2.47) in eq. (2.51), we have the numerator

$$\begin{aligned}\mathrm{R} &= \int_V \rho_0 \boldsymbol{\delta r}^* \cdot \left\{ \mathrm{i}m\Omega \boldsymbol{\delta r} + \sqrt{4\pi}\Omega \left[\tilde{\xi}_h \frac{\partial \mathcal{Y}_l^m}{\partial \phi} \boldsymbol{e_r} - \cot\theta \tilde{\xi}_h \frac{\partial \mathcal{Y}_l^m}{\partial \phi} \boldsymbol{e_\theta} \right.\right. \\ &\qquad \left.\left. + \left(\sin\theta \tilde{\xi}_r \mathcal{Y}_l^m + \cos\theta \tilde{\xi}_h \frac{\partial \mathcal{Y}_l^m}{\partial \theta}\right) \boldsymbol{e_\phi}\right]\right\} \mathrm{d}V \\ &= \mathrm{i}m \int_V \rho_0 \Omega |\delta r|^2 \mathrm{d}V \\ &\quad + 4\pi \int_V \rho_0 \Omega \left[-\tilde{\xi}_r{}^* \mathcal{Y}_l^{m*} \xi_h \frac{\partial \mathcal{Y}_l^m}{\partial \phi} - \cot\theta |\xi_h|^2 \left(\frac{\partial \mathcal{Y}_l^m}{\partial \theta}\right)^* \frac{\partial \mathcal{Y}_l^m}{\partial \phi} \right. \\ &\qquad \left. + \tilde{\xi}_h{}^* \tilde{\xi}_r \left(\frac{\partial \mathcal{Y}_l^m}{\partial \phi}\right)^* \mathcal{Y}_l^m + \cot\theta |\xi_h|^2 \left(\frac{\partial \mathcal{Y}_l^m}{\partial \phi}\right)^* \frac{\partial \mathcal{Y}_l^m}{\partial \theta}\right] \mathrm{d}V.\end{aligned} \tag{2.53}$$

We remark that in this expression, the spherical harmonic $\mathcal{Y}_l^m$, or its derivative, is always multiplied by its complex conjugate. Here we use the convention $\mathcal{Y}_l^m(\cos\theta) = (-1)^m c_{lm}\mathcal{P}_l^m(\cos\theta)\exp(\mathrm{i}m\phi)$, so all the $\exp(\pm\mathrm{i}m\phi)$ vanish, and the integration over ϕ is trivial. Using these simplifications, and dropping the $\tilde{\cdot}$, we have at the end

$$\begin{aligned}\mathrm{R} = \mathrm{i}m8\pi^2 c_{lm}^2 \int_0^\pi \int_0^a \rho_0\Omega \Bigg[& |\xi_r|^2 \mathcal{P}_l^m(\cos\theta)^2 + |\xi_h|^2 \left(\left(\frac{\partial \mathcal{P}_l^m(\cos\theta)}{\partial\theta} \right)^2 \right. \\ & \left. + \frac{m^2}{\sin^2\theta}\mathcal{P}_l^m(\cos\theta)^2 - 2\cot\theta \mathcal{P}_l^m(\cos\theta)\frac{\partial \mathcal{P}_l^m(\cos\theta)}{\partial\theta} \right) \\ & - \xi_r^*\xi_h \mathcal{P}_l^m(\cos\theta)^2 - \xi_h^*\xi_r \mathcal{P}_l^m(\cos\theta)^2 \Bigg] r^2 \sin\theta \mathrm{d}r\mathrm{d}\theta \\ = \mathrm{i}m8\pi^2 c_{lm}^2 R_{nlm}.\end{aligned} \tag{2.54}$$

The same arguments can be applied to the denominator I of $\delta\omega$ in eq. (2.48), leading to

$$\begin{aligned}\mathrm{I} = 8\pi^2 c_{nlm}^2 \int_0^\pi \int_0^a \rho_0 \Bigg[& |\xi_r|^2 \mathcal{P}_l^m(\cos\theta)^2 + |\xi_h|^2 \left(\frac{\partial \mathcal{P}_l^m(\cos\theta)}{\partial\theta} \right)^2 \\ & + |\xi_h|^2 \frac{m^2}{\sin^2\theta}\mathcal{P}_l^m(\cos\theta)^2 \Bigg] r^2 \sin\theta \mathrm{d}r\mathrm{d}\theta \\ = 8\pi^2 c_{nlm}^2 I_{nlm}.\end{aligned} \tag{2.55}$$

We can associate to each eigen mode ${}_n\mathcal{S}_l^m$ a quantified rotational splitting δf_{nlm} given by

$$\delta f_{nlm} = m\frac{R_{nlm}}{I_{nlm}} = f_{nlm} - f_{nl}, \tag{2.56}$$

with f_{nl} the degenerated frequency at rest of all modes from the ${}_n\mathcal{S}_l$ multiplet and f_{nlm} the non-degenerate frequencies perturbed by rotation of each ${}_n\mathcal{S}_l^m$ mode. In practice in the experiment, we are able to measure $|f_{nlm} - f_{nl(-m)}| = 2\,\delta f_{nlm}$.

From now on we will use the fully normalized Legendre polynomials $\widetilde{\mathcal{P}}_l^m$ defined as

$$\widetilde{\mathcal{P}}_l^m = (-1)^m \sqrt{\frac{2l+1}{2}\frac{(l-m)!}{(l+m)!}}\mathcal{P}_l^m, \tag{2.57}$$

so that it verifies

$$\int_0^\pi \widetilde{\mathcal{P}}_l^m(\cos\theta)^2 \sin\theta \mathrm{d}\theta = 1. \tag{2.58}$$

Using this normalisation, we can rewrite I_{nlm} into I_{nl} (now independent from m), as

$$I_{nl} = \int_0^a \rho_0 \left(|\xi_r|^2 + l(l+1)|\xi_h|^2 \right) r^2 \mathrm{d}r. \tag{2.59}$$

Finally the rotational mode splitting is given by

$$\delta f_{nlm} = m \frac{\int_S \Omega \left[\left(|\xi_r|^2 - 2\xi_r \xi_h \right) \widetilde{\mathcal{P}}_l^{m\,2} + |\xi_h|^2 \left(\left(\frac{\partial \widetilde{\mathcal{P}}_l^m}{\partial \theta} \right)^2 + \frac{m^2}{\sin^2\theta} \widetilde{\mathcal{P}}_l^{m\,2} - 2\cot\theta \widetilde{\mathcal{P}}_l^m \frac{\partial \widetilde{\mathcal{P}}_l^m}{\partial \theta} \right) \right] \mathrm{d}S}{\int_0^a \left(|\xi_r|^2 + l(l+1)|\xi_h|^2 \right) r^2 \mathrm{d}r}, \tag{2.60}$$

with $\int_S \cdot \, \mathrm{d}S = \int_0^\pi \int_0^a \cdot \, r^2 \sin\theta \mathrm{d}r\mathrm{d}\theta$ integral over the surface, and $\widetilde{\mathcal{P}}_l^m$ is implicitly applied on $\cos\theta$.

Note that in our case, the displacement functions are real, hence $\xi_r^* \xi_h = \xi_r \xi_h^* = 2\xi_r \xi_h$. It is also useful to note that if to obtain this simplified we assumed axisymmetry, leading Ω to be independent of ϕ, in the general case $\Omega(r, \theta)$.

With this expression a few properties are useful to remark:

- R_{nlm} is an even function of m (and I_{nl} is independent of m) thus δf is an odd function of m, implying that $\delta f_{nl-m} = -\delta f_{nlm}$,
- $\widetilde{\mathcal{P}}_l^m(x)$ is either symmetric or antisymmetric with respect to $x = 0$, so for $x = \cos\theta$ this is verified around $\theta = \pi/2$, thus the rotational splitting is only influenced by the symmetric component of Ω with respect to the equator.

Useful formalism

It is useful to rewrite the acoustic splitting as (eq. (3.349), Aerts et al. (2010))

$$\delta f_{nlm} = m \int_0^\pi \int_0^a K_{nlm}(r, \theta) \Omega(r, \theta) \mathrm{d}r\mathrm{d}\theta, \tag{2.61}$$

with K_{nlm} the rotational sensitivity kernel defined as

$$\begin{aligned} K_{nlm} = \frac{1}{I_{nl}} \int_0^\pi \int_0^a \rho_0 \Bigg[& |\xi_r|^2 \mathcal{P}_l^m(\cos\theta)^2 + |\xi_h|^2 \left(\left(\frac{\partial \mathcal{P}_l^m(\cos\theta)}{\partial \theta} \right)^2 \right. \\ & \left. + \frac{m^2}{\sin^2\theta} \mathcal{P}_l^m(\cos\theta)^2 - 2\cot\theta \mathcal{P}_l^m(\cos\theta) \frac{\partial \mathcal{P}_l^m(\cos\theta)}{\partial \theta} \right) \\ & - 2\xi_r \xi_h \mathcal{P}_l^m(\cos\theta)^2 \Bigg] r^2 \sin\theta \mathrm{d}r\mathrm{d}\theta, \end{aligned} \tag{2.62}$$

where we dropped the $\widetilde{}$ over the fully normalized Legendre polynomials.

Sensitivity kernel vary vastly between modes, as shown in Figure 2.2, allowing us to deduce the spatial distribution of $\Omega(r, \theta)$ depending on which modes are affected (see Appendix A for a more exhaustive list of kernels).

These expressions give the acoustic rotational splitting compared to the reference model which is a motionless sphere, hence valid in the non-rotating inertial frame. However, in the experiment the acoustic sensors are embarked in the rotating container for practical reasons. The acoustic response we measure is thus in the referential rotating with the container (which can be different from the fluid mean rotating referential, especially for non-uniform rotating flows).

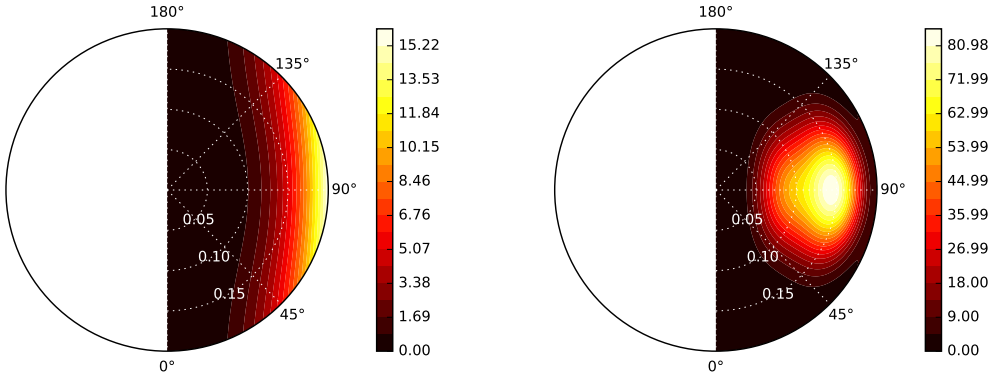

Figure 2.2: Sensitivity kernels K_{nlm} in the (r, θ) meridional plane, left K_{011} for mode ${}_0\mathcal{S}_1^1$, right K_{133} for mode ${}_1\mathcal{S}_3^3$.

The measured splitting (in the rotating frame) is then $\delta f_{nlm}^{\text{rot}}$ and its expression is given by

$$\delta f_{nlm}^{\text{rot}} = m\Omega^{\text{ref}} - m \int_0^a \int_0^\pi K_{nlm}(r,\theta)\Omega(r,\theta) r \mathrm{d}r\mathrm{d}\theta, \tag{2.63}$$

with Ω^{ref} the angular velocity in the rotating referential. In practice, we will choose the referential as the frame rotating with the experimental container, which is the frame attached to the acoustic sensors. Note that the fluid angular velocity $\Omega(r, \theta)$ should still be expressed in the inertial frame.

Ledoux coefficients

In general, the fluid angular frequency depends on r and θ. In the specific case where Ω depends on r only (shellular rotation), we can rewrite R_{nlm} using the properties of the fully normalised Legendre polynomials as done with I_{nlm}. $\Omega(r)$ lets the integrals in r and θ to be independent with only Legendre polynomials in the integrals over θ.

Then R_{nlm} becomes

$$R_{nlm} = \int_0^a r^2 \rho_0(r)\Omega(r) \left[|\xi_r(r)|^2 + |\xi_h(r)|^2 \left(l(l+1) - 1\right) - \xi_r^* \xi_h - \xi_r \xi_h^* \right] \mathrm{d}r, \tag{2.64}$$

and we can rewrite eq. (2.61) as (eq. (3.355)–(3.357), Aerts et al. (2010))

$$\delta f_{nlm} = m\beta_{nl} \int_0^a K_{nl}(r)\Omega(r)\mathrm{d}r, \tag{2.65}$$

where the rotational sensitivity kernel from eq. (2.62) takes the simpler (independent from m) form

$$K_{nl} = \frac{r^2 \rho_0(r) \left(|\xi_r(r)|^2 + l(l+1)|\xi_h(r)|^2 \right)}{\displaystyle\int_0^a r^2 \rho_0(r) \left(|\xi_r(r)|^2 + l(l+1)|\xi_h(r)|^2 \right) \mathrm{d}r}, \tag{2.66}$$

and the constant coefficient β_{nl} is

$$\beta_{nl} = \frac{\int_0^a r^2 \rho_0(r) \left[|\xi_r(r)|^2 + |\xi_h(r)|^2 \left(l(l+1) - 1\right) - \xi_r^* \xi_h - \xi_r \xi_h^* \right] \mathrm{d}r}{\int_0^a r^2 \rho_0(r) \left(|\xi_r(r)|^2 + l(l+1) |\xi_h(r)|^2 \right) \mathrm{d}r}. \tag{2.67}$$

Note that the sensitivity kernels are normalised so that $\int_0^a K_{nl}(r)\mathrm{d}r = 1$. When Ω is uniform (solid-body rotation), the rotational splitting simply becomes

$$\delta f_{nlm} = m \beta_{nl} \Omega. \tag{2.68}$$

Equivalently, in the frame rotating with the fluid ($\Omega^{\text{shell}} = \Omega$), it writes

$$\delta f_{nlm}^{\text{rot}} = -m C_{nl} \Omega, \tag{2.69}$$

where we introduced C_{nl} the spherical Ledoux coefficient for rotational splitting, named after Ledoux (1951),

$$C_{nl} = 1 - \beta_{nl} = \frac{\int_0^a r^2 \rho_0(r) \left(\xi_h(r)^2 + 2\xi_r \xi_h \right) \mathrm{d}r}{\int_0^a r^2 \rho_0(r) \left(\xi_r(r)^2 + l(l+1) \xi_h(r)^2 \right) \mathrm{d}r}. \tag{2.70}$$

To have a better idea of the extent of splitting for each mode, we consider the special case of solid-body rotation through the Ledoux coefficient. As seen in its definition eq. (2.70), the coefficient depends only on the local displacements ξ_r and ξ_h due to the acoustic pressure waves. By using eq. (2.47) they can be written as:

$$\xi_r = \frac{\mathrm{d}j_l}{\mathrm{d}r}(k_{nl} r) = R'(r) \quad \text{and} \quad \xi_h = \frac{j_l(k_{nl} r)}{r} = R(r)/r,$$

making the n dependence obvious. Note that $R(r)$ is the radial component of the solution from the wave equation resolution (as given in eq. (2.36)) and that the Ledoux coefficients are independent from the system's dimensions, frequencies, and density (if we suppose the fluid homogeneous). We give their evolution for the first modes in Figure 2.3 and their values for a chosen collection of modes in Table 2.2. For high-degree (large l) modes, the Ledoux coefficient is $\propto l^{-2}$ so approaches 0 asymptotically, as seen in eq. (2.70).

Note that this rotational splitting exists in the case of a solid-body rotation observed in the frame rotating with the fluid. This is non-trivial since in that referential the fluid is effectively immobile. But due to the existence of the Coriolis effects that interact with the acoustic waves, a clear splitting signature is visible on the acoustic eigenfrequencies.

This is actually an exact mechanical analogue of the Zeeman effect (Zeeman, 1897; Pekeris et al., 1961), where the presence of an external magnetic field (ana. rotational field) causes to lift the degeneracy in the energy levels of an atom (ana. frequency of an acoustic mode) leading to splitting of its spectral lines (Cohen-Tannoudji et al., 2018).

Acoustic splitting in rotating frame

The simple solid-body rotation case, can be used as verification of the change of referentials between inertial and rotating. Let us remind eq. (2.63)

$$\delta f_{nlm}^{\text{rot}} = m \Omega^{\text{ref}} - m \int_0^a \int_0^\pi K_{nlm}(r, \theta) \Omega(r, \theta) r \mathrm{d}r \mathrm{d}\theta.$$

For solid-body rotation measured in the frame rotating with the fluid, $\Omega^{\rm ref} = \Omega$, so eq. (2.63) becomes

$$\delta f^{\rm rot}_{nlm} = m\Omega \left(1 - \int_0^a \int_0^\pi K_{nlm}(r,\theta) r {\rm d}r{\rm d}\theta\right) = m\Omega\left(1 - \beta_{nl}\right), \tag{2.71}$$

and we retrieve the Ledoux coefficient $C_{nl} = 1 - \beta_{nl}$.

Another interesting extreme case is the measure of a still fluid from a rotating frame. Then $\Omega(r,\theta) = 0$, but an acoustic splitting still appear, purely due to Doppler effect, and takes the form

$$\delta f^{\rm rot}_{nlm} = m\Omega^{\rm ref}. \tag{2.72}$$

For more general velocity profile, it is useful to decompose $\Omega(r,\theta)$ into $\Omega^{\rm ref} + \Omega^{\rm rot}(r,\theta)$, where we singled out the flow velocity present in the rotating frame. Then eq. (2.63) becomes

$$\delta f^{\rm rot}_{nlm} = m\Omega^{\rm ref} - m\int_0^a \int_0^\pi K_{nlm}(r,\theta)\left[\Omega^{\rm ref} + \Omega^{\rm rot}(r,\theta)\right] r{\rm d}r{\rm d}\theta \tag{2.73}$$

$$= m\Omega^{\rm ref} C_{nl} - m\int_0^a \int_0^\pi K_{nlm}(r,\theta)\Omega^{\rm rot}(r,\theta) r{\rm d}r{\rm d}\theta. \tag{2.74}$$

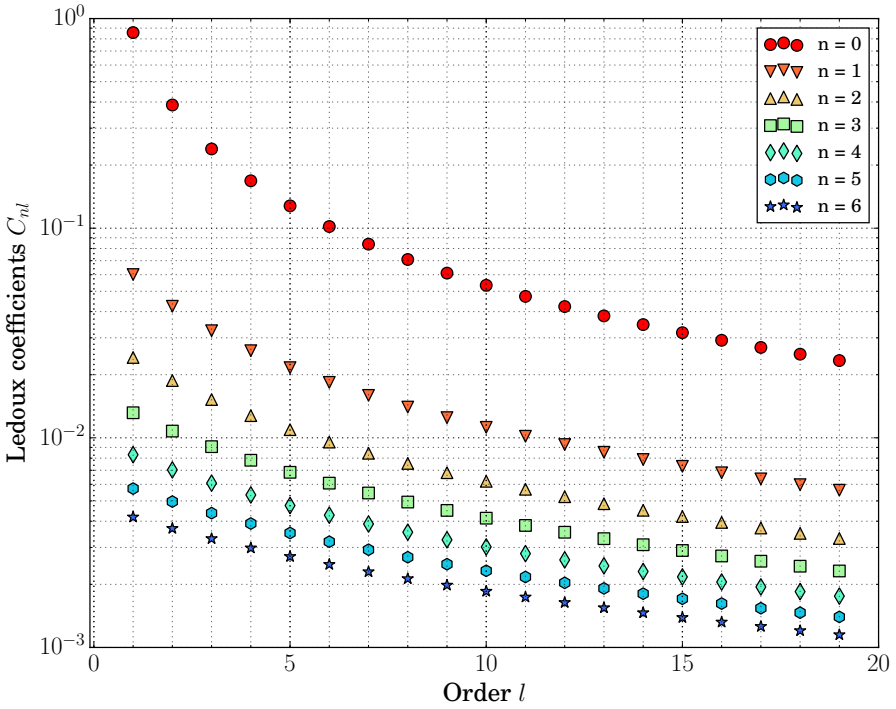

Figure 2.3: Ledoux coefficients for the first modes.

2.2.2 Geometry of the resonator

Azimuthal fluid flows provoke a frequency splitting that lifts the frequency degeneracy within a ${}_n\mathcal{S}_l^m$ multiplet. In the experiment we measure the frequency difference between the $\pm m$ modes. In a spherical geometry, all the ${}_n\mathcal{S}_l^m$ modes share the same frequency at rest, so when rotational flows are added, the spectrum can become crowded, leading to delicate identification of the different modes. Since each multiplet is $2l+1$ degenerated, this difficulty is even more pronounced for high l modes. Yet those modes carry important information for the velocity field retrieval due to their finer spatial sensitivity kernels K_{nlm}, as seen in eq. (2.62) (more nodes as n and l increase). These modes with higher l (and n) are necessary to improve the spatial resolution of the flow inversion, so the mode identification problem is very limiting.

In order to overcome this issue, it is helpful to spread the spectrum by lifting some of the degeneracy at rest. This can be achieved by breaking the spherical symmetry of the cavity. Since we are interested in studying zonal flows, it is worthwhile to only partially break the spherical symmetry and keep the resonator axisymmetric. By doing so, the frequency degeneracy is partially lifted by the geometry at rest and then further lifted by rotational flows. Perturbation theory for quasi-spherical geometries have been developed up to second-order by metrologists (Mehl, 1982, 1986, 2007), as such resonators have been of major interest for the determination of the universal gas constant R (Moldover et al., 1988) or the Boltzmann constant (Pitre et al., 2009).

An interesting shape for us is thus the oblate spheroid and we choose its revolution axis identical to the rotation axis. For this particular geometry, a first-order perturbation development has also been proposed by seismologists to account for the Earth's shape (Dahlen, 1968), and up to second-order by metrologists (Mehl, 2007).

Formalism

We will follow the method presented by Mehl (2007) who used Morse and Feshbach (1953b)'s formalism to develop a perturbation theory up to second-order on the resonator's geometry. Their method is general and applicable to any quasi-spherical shape. Matching the experiment's shape, we will consider the oblate spheroid only. ZoRo is an oblate spheroid with equatorial radius $r_{eq} = 20$ cm and polar radius $r_{pol} = 19$ cm. We define its flattening as

$$e = (r_{eq} - r_{pol})/r_{eq} = 0.05. \tag{2.75}$$

Note that the deformation expression is different from Mehl's formulation, and that he takes as reference model, the sphere of same volume as the spheroid. Instead of the usual ellipse equation

$$\left(\frac{x}{r_{eq}}\right)^2 + \left(\frac{y}{r_{pol}}\right)^2 = 1, \tag{2.76}$$

Mehl defines the shape of the aspherical cavity by the evolution of its boundary radius r_s with θ and ϕ as (Mehl, 1986)

$$r_s = r_{eq}[1 - \epsilon\mathcal{F}(\theta, \phi)], \tag{2.77}$$

where $\mathcal{F}$ is a smooth positive function of order 1 and ϵ is another measure of the flattening, which will serve as the expansion parameter. Note that when $\mathcal{F}$ describes the

ellipse of eq. (2.76), the correspondence between the two flattening parameters e and ϵ is straightforward and given by

$$\epsilon = (r_{eq} - r_{pol})/r_{pol} = e\, r_{eq}/r_{pol}. \tag{2.78}$$

The shape function $\mathcal{F}$ itself can be expanded in ϵ as

$$\mathcal{F} = \mathcal{F}_0 + \epsilon\mathcal{F}_1 + O(\epsilon^2). \tag{2.79}$$

The perturbation method used by Mehl (2007) expands the shape functions into spherical harmonics. For our oblate spheroid, they correspond to (truncated at second-order),

$$\begin{aligned} \mathcal{F}_0 &= \frac{2}{3}\sqrt{\pi}\,\mathcal{Y}_0^0 + \frac{4}{3}\sqrt{\frac{\pi}{5}}\,\mathcal{Y}_2^0, \\ \mathcal{F}_1 &= -\frac{4}{15}\sqrt{\pi}\,\mathcal{Y}_0^0 - \frac{22}{21}\sqrt{\frac{\pi}{5}}\,\mathcal{Y}_2^0 - \frac{8}{35}\sqrt{\pi}\,\mathcal{Y}_4^0. \end{aligned} \tag{2.80}$$

Then the shape description given in eq. (2.81) becomes, from the corrected eq. (53) of Mehl (2007),

$$r_s = \frac{r_{pol}}{\sqrt{1 + (2\epsilon + \epsilon^2)\cos^2\theta}}. \tag{2.81}$$

Combining eq. (2.79) with eq. (2.81), we get eq. (54) of Mehl (2007),

$$\mathcal{F} = \cos^2\theta + \epsilon\left(\frac{1}{2}\cos^2\theta - \frac{3}{2}\cos^4\theta\right) + O(\epsilon^2). \tag{2.82}$$

Following Morse and Feshbach (1953b)'s formalism, we express the geometry perturbation as the difference of squared wavenumbers. The perturbation valid at second-order is then defined as

$$\frac{[k_{nlm}^{(2)}]^2 - k_{nl}^2}{k_{nl}^2} = {dk^2_{nlm}}^{(1)}\epsilon + {dk^2_{nlm}}^{(2)}\epsilon^2, \tag{2.83}$$

with ${dk^2_{nlm}}^{(i)}$ the i^{th}-order correction for the squared wavenumber, following Mehl (2007).

We will successively consider first- and second-order (in ϵ) shape perturbation terms for an oblate spheroid (compared to the sphere of same volume).

First-order ellipticity correction

At first-order (in ϵ), the radial eigenvalue $k_{nlm}^{(1)}$ of a ${}_n\mathcal{S}_l^m$ mode in an aspherical cavity defined by (2.81) and (2.79) is given by

$$\frac{[k_{nlm}^{(1)}]^2 - k_{nl}^2}{k_{nl}^2} = \epsilon\, {dk^2_{nlm}}^{(1)}. \tag{2.84}$$

At first-order, the geometry correction corresponds to a (first-order) self-coupling term given by

$${dk^2_{nlm}}^{(1)} = SC_{nlm}^{(1)} = 2\frac{\int \left[z_{nl}^2\,|\mathcal{Y}_l^m|^2\,\mathcal{F}_0 - |r\nabla\mathcal{Y}_l^m|^2\,\mathcal{F}_0\right]\mathrm{d}\Omega}{z_{nl}^2 - l(l+1)}, \tag{2.85}$$

where $\int \mathrm{d}\Omega$ represents the integral over solid angle, and $z_{nl} = k_{nl}a$ is the n^{th} root of j_l' and a the radius of the reference sphere. A term equal to $-2\langle\mathcal{F}_0\rangle$ must be added to the

right hand-side of eq. (2.85) if one uses a reference sphere with the same volume as the aspherical cavity, as done in Mehl (2007).

The shape function $\mathcal{F}_0(\theta, \varphi)$ can be expanded in spherical harmonics as

$$\mathcal{F}_0 = \sum_{l_0,\, m_0} F_{l_0}^{m_0} \mathcal{Y}_{l_0}^{m_0}, \tag{2.86}$$

It is then convenient to introduce the following functions:

$$A_{ll'}^{mm'}(\mathcal{F}_0) = 2 \sum_{l_0,\, m_0} F_{l_0}^{m_0} \int \mathcal{Y}_{l_0}^{m_0} \left[\mathcal{Y}_{l'}^{m'}\right]^* \mathcal{Y}_l^m \, \mathrm{d}\Omega, \tag{2.87}$$

$$B_{ll'}^{mm'}(\mathcal{F}_0) = -2 \sum_{l_0,\, m_0} F_{l_0}^{m_0} \int \mathcal{Y}_{l_0}^{m_0} \left[r\nabla \mathcal{Y}_{l'}^{m'}\right]^* \cdot r\nabla \mathcal{Y}_l^m \, \mathrm{d}\Omega. \tag{2.88}$$

where * stands for the complex conjugate.

Then, we rewrite equation (2.85) as

$$SC_{nlm}^{(1)} = \frac{z_{nl}^2 A_{ll}^{mm}(\mathcal{F}_0) + B_{ll}^{mm}(\mathcal{F}_0)}{z_{nl}^2 - l(l+1)}. \tag{2.89}$$

These quantities have been individually determined by Mehl (2007), §3.2. In order to have a systematic determination, we express the solid angle integrals of equations (2.87) and (2.88) as Gaunt-type integrals, which are related to Wigner 3j symbols through

$$\begin{aligned} &\int \mathcal{Y}_{l_1}^{m_1} \left(\mathcal{Y}_{l_2}^{m_2}\right)^* \mathcal{Y}_{l_3}^{m_3} \, \mathrm{d}\Omega \\ &\qquad = (-1)^{m_1} \sqrt{\frac{(2l_1+1)(2l_2+1)(2l_3+1)}{4\pi}} \begin{pmatrix} l_1 & l_2 & l_3 \\ 0 & 0 & 0 \end{pmatrix} \begin{pmatrix} l_1 & l_2 & l_3 \\ m_1 & -m_2 & m_3 \end{pmatrix}, \end{aligned} \tag{2.90}$$

and

$$\begin{aligned} &\int \left(r\nabla \mathcal{Y}_{l_1}^{m_1}\right) \cdot \left(r\nabla \mathcal{Y}_{l_2}^{m_2}\right)^* \mathcal{Y}_{l_3}^{m_3} \, \mathrm{d}\Omega \\ &\qquad = -\frac{-l_1(l_1+1) - l_2(l_2+1) + l_3(l_3+1)}{2} \int \mathcal{Y}_{l_1}^{m_1} \left(\mathcal{Y}_{l_2}^{m_2}\right)^* \mathcal{Y}_{l_3}^{m_3} \mathrm{d}\Omega, \end{aligned} \tag{2.91}$$

with the fully normalised spherical harmonics defined in Dahlen and Tromp (1998), p. 917.

For an oblate spheroid, eq. (2.80) shows that the first-order shape function $\mathcal{F}_0$ only contains $\mathcal{Y}_0^0$ and $\mathcal{Y}_2^0$ contributions, allowing us to compare with Dahlen (1968)'s result. At first-order the frequency splitting induced by geometry $\delta f_{geom} = f_{nlm} - f_{nl}$ is quadratic in m, which can be seen by rewritting it as (Dahlen, 1968, 1976)

$$\delta f_{geom} = f_{nl} \left(m^2 - \frac{l(l+1)}{3}\right) \gamma_{nl} \, e, \tag{2.92}$$

where γ_{nl} is the (first-order) ellipticity coefficient, defined as (Dahlen, 1976)

$$\gamma_{nl} = \frac{-3}{2l(l+1)} dk_{nl0}{}^{(1)}, \tag{2.93}$$

where we introduced the first-order geometry correction ${dk_{nlm}}^{(1)} = \frac{1}{2}{dk^2_{nlm}}^{(1)}$ at first-order. Note that with this formulation, the m^2 dependency is explicit and γ_{nl} is independent of m. This implies that ${dk_{nlm}}^{(1)}$ only needs to be evaluated for one $m = 0$, for example, considerably reducing the calculations.

Dahlen used a third definition of the spheroidal shape, that is slightly different from that of Mehl eq. (2.94), given by (Dahlen, 1976)

$$r_s(\theta)\left[1 - \frac{2}{3}\epsilon P_2^0(\cos\theta)\right] = a, \tag{2.94}$$

and plotted in Figure 2.4 for comparison, but both definitions are equivalent at first-order.

We verified that the first-order geometrical corrections given by Mehl (2007) and Dahlen (1976) give identical values (provided we take into account their different definitions of reference model and ellipticity). Dahlen (1968) also provides integral expressions to calculate γ_{nl} in the more general situation of Earth's normal modes.

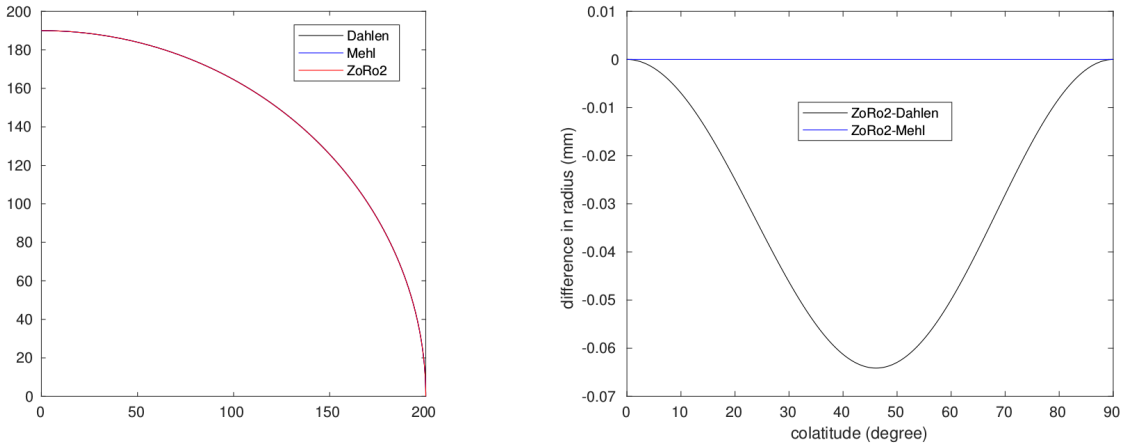

Figure 2.4: Shape difference between Dahlen (1968) and Mehl (2007) definition. Left overall quadrant, right difference between the two definitions.

Second-order ellipticity correction

Mehl (2007) obtained the expressions of the second-order geometry corrections, using the formalism of Morse and Feshbach (1953b).

In contrast to first-order, second-order corrections for a given ${}_n\mathcal{S}_l^m$ mode involve coupling with several ${}_{n'}\mathcal{S}_{l'}^{m'}$ modes. Thus, second-order corrections stem from both the second-order self-coupling term $SC^{(2)}_{nlm}$ and the $CC^{(2)}_{nlm}$ cross-coupling term,

$${dk^2_{nlm}}^{(2)} = SC^{(2)}_{nlm} + CC^{(2)}_{nlm}. \tag{2.95}$$

Expanding $\mathcal{F}_1$ and $\mathcal{F}_0^2$ in spherical harmonics as in eq. (2.86), the self-coupling second-order contribution can be written, using functions defined in eqs. (2.87)–(2.88), as

$$SC^{(2)}_{nlm} = \frac{z^2_{nl}A^{mm}_{ll}(\mathcal{F}_1 - \mathcal{F}_0^2) + B^{mm}_{ll}(\mathcal{F}_1)}{z^2_{nl} - l(l+1)} + \frac{z^2_{nl}A^{mm}_{ll}(\mathcal{F}_0) + B^{mm}_{ll}(\mathcal{F}_0)}{z^2_{nl} - l(l+1)} \cdot \frac{z^2_{nl}A^{mm}_{ll}(\mathcal{F}_0)}{z^2_{nl} - l(l+1)}. \tag{2.96}$$

A term equal to $-\langle\mathcal{F}_0\rangle^2 + 2\langle\mathcal{F}_0^2\rangle - 2\langle\mathcal{F}_1\rangle - 2\langle\mathcal{F}_0\rangle SC_{nlm}^{(1)}$ must be added to $SC_{nlm}^{(2)}$ if one uses a reference sphere with the same volume as the aspherical cavity. The cross-coupling contribution is

$$CC_{nlm}^{(2)} = \frac{\sum_{l'm'} |z_{nl}^2 A_{ll'}^{mm'}(\mathcal{F}_0) + B_{ll'}^{mm'}(\mathcal{F}_0)|^2 S_{nll'}}{z_{nl}^2 - l(l+1)} + \frac{|z_{nl}^2 A_{l0}^{m0}(\mathcal{F}_0) + B_{l0}^{m0}(\mathcal{F}_0)|^2}{2z_{nl}^2\left[z_{nl}^2 - l(l+1)\right]}, \quad (2.97)$$

where the $S_{nll'}$ sums up the contribution of all l'-modes with radial mode number $n' \neq n$. The $S_{lnl'}$ sums are the only elements that are linked to the radial functions, and they are evaluated explicitly by Mehl (2007), eqs. (26)–(27), after correcting the sign of the second term of S_{ln0}, as pointed out by Mehl (2010).

At this order, the equivalence between ${dk^2_{nlm}}^{(2)}$ and ${dk_{nlm}}^{(2)}$ is not trivial anymore, so we instead express the geometrical frequency correction as

$$\frac{f_{nlm}^{(2)}}{f_{nl}} = \frac{k_{nlm}^{(2)}}{k_{nl}} = \left(1 + {dk^2_{nlm}}^{(1)}\epsilon + {dk^2_{nlm}}^{(2)}\epsilon^2\right)^{1/2}. \quad (2.98)$$

Application to ZoRo's geometry

We used the first-order formulation to determine ZoRo's flattening before construction. We wanted a deformation big enough to clearly distinguish the different $|m|$ modes' frequency at rest and allow precise mode identification. But keeping in mind that we want to measure the flow velocity, the ellipticity must be moderate enough so the combined splitting from both geometry and rotation is small enough so that the resulting frequency is far enough from the neighbour modes, again to allow accurate mode identification. This preliminary study allowed us to choose the flattening $e = 0.05$.

Using the formulas given above, we can now have a more precise prediction of the influence of the geometry on ZoRo's acoustic spectrum. We computed both orders geometry corrections for ZoRo's configuration. We also compared these values with finite-element calculations done with the commercial software COMSOL. Details on the numerical implementation are given in Appendix B. The finite-element scheme cannot be separated into first and second-order. In order to compare the coefficients, we fitted the frequencies for ZoRo with a third-order polynomial for increasing ellipticity ϵ as

$$f_{nlm}(\epsilon) = f_{nl} + \gamma_{nlm}^{(1)}\epsilon + \gamma_{nlm}^{(2)}\epsilon^2 + \gamma_{nlm}^{(3)}\epsilon^3, \quad (2.99)$$

with $\epsilon = e\, r_{eq}/r_{pol}$. We have checked that the results are unchanged when higher orders are taken into account in this fit.

We then are able to compare $\gamma_{nlm}^{(1)}$ with $f_{nl}\,{dk^2_{nlm}}^{(1)}/2$ and $\gamma_{nlm}^{(2)}$ with

$$f_{nl}\left[\frac{1}{2}\left({dk^2_{nlm}}^{(2)} + 2\langle\mathcal{F}_0\rangle{dk^2_{nlm}}^{(1)}\right) - \frac{1}{8}\left({dk^2_{nlm}}^{(1)} + \langle\mathcal{F}_0\rangle\right)^2\right].$$

First-order ellipticity coefficients $\gamma_{nlm}^{(1)}$ from eq. (2.93) agree with the finite-element simulation with COMSOL. We give the values of γ_{nl} for a selection of modes in Table 2.2. For second-order, we again compare the theoretical correction with the coefficients obtained with finite-element calculations, and add the values given by Mehl (2007). We compile all results in Figure 2.5.

When the mode order increases (larger l), we remark a few important points:

(i) the second-order correction can be very large (even larger than the first-order), especially for $m = 0$, as seen in the higher frequency modes in Figure 2.5,

(ii) the second-order correction can take (large) negative values for $l = 2$, $m = 0$, which may take precedence over the first-order and thus reduce or even invert the sign of the geometrical splitting, causing modes to switch in frequency.

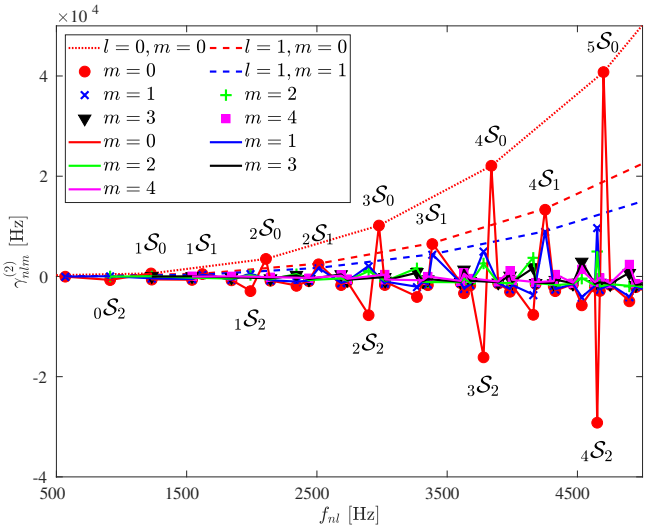

Figure 2.5: Ellipticity second order $\gamma^{(2)}_{nlm}$ corrections for diffusionless acoustic eigenmodes in our experiment. We reproduced Mehl (2007)'s original results for modes $l = 0$ (connected by dotted line) and $l = 1$ (connected by dashed lines) and compare them with our implementation of the theory of Mehl (2007) (symbols) and with finite element calculations in oblate spheroids (dots connected by solid lines for a given m). All results from the three different methods are consistent.

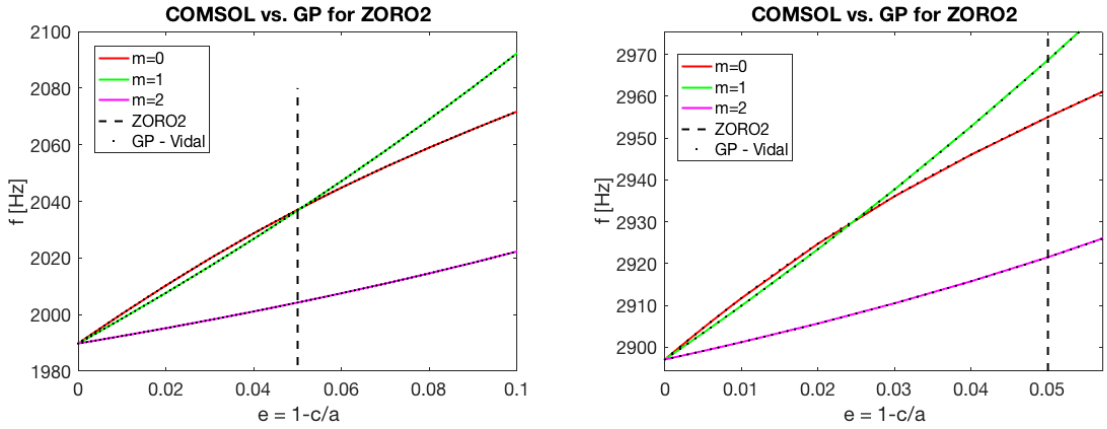

Figure 2.6: Frequency evolution with ellipticity, for the $_1\mathcal{S}_2$ multiplet left, and $_2\mathcal{S}_2$ right. Solid colour lines are from COMSOL simulations, dotted lines from Vidal et al. (2020). Dashed line indicates the chosen ellipticity for the experimental set-up.

Indeed, combining geometrical corrections from both orders, we observe that modes ${}_1\mathcal{S}_2^0$ and ${}_1\mathcal{S}_2^1$ have the same frequency and that ${}_2\mathcal{S}_2^0$ and ${}_2\mathcal{S}_2^1$ have switched place, which is consistent with experimental observations.

These two multiplets are the first in frequency to display such behaviour. We focus on them and look at their frequency evolution with increasing flattening. We compare the perturbation theory with the finite-element calculations described above and with a Galerkin spectral decomposition (Vidal et al., 2020) in Figure 2.6. For those modes, we can see that ZoRo's flattening is out of the range of validity for first-order perturbation, corresponding to the tangents at $e = 0$, and that second-order is sufficient to accurately predict the frequency. In the following, we will take both orders in perturbation as geometrical correction.

2.2.3 Dissipation in the fluid

In a laboratory experiment, viscous and thermal diffusion takes place in the medium. To include them in the theoretical predictions, we proceed by perturbation theory from a diffusionless sphere at rest (Rayleigh, 1894).

In the reference model, we also neglected all dissipation terms. Although they are expected to be relatively small, it can be useful to take their effects into account. We inject their effects as perturbations in our problem (Kirchhoff, 1868; Jordan and Keiffer, 2016). We follow the approach of Moldover et al. (1986) to calculate diffusion contribution on eigenmodes.

Since the diffusionless medium only give the resonance diffusionless (real) frequency, diffusion is needed to predict their width, relative amplitude and exact location (Trusler, 1991). In air, dissipation of acoustic modes is mostly dominated by viscous friction and heat diffusion at the boundaries in contact with the enclosing shell. Some minor contributions might come from the bulk viscosity (Moldover et al., 1986).

In the spherical geometry, exact solutions for standing waves are well-known and conveniently represented by a complex frequency $\Delta f_{nlm} = \delta_{nlm} + \mathrm{i} g_{nlm}$ where the imaginary part g_{nlm} describe the resonance's half-width. In presence of a rigid shell, effects influencing the complex frequencies can be linearly superposed (Moldover et al., 1986). Among the significant effects, we take into account thermal and viscous boundary $\Delta f_{bound} = \delta_{bound} + \mathrm{i} g_{bound}$ and thermal and viscous bulk effects $\Delta f_{bulk} = \mathrm{i} g_{bulk}$ (very small compared to the boundary contribution for air). Note that the bulk's contribution only affect the imaginary part of the frequency, i.e. does not affect the mode's frequency. Thus, frequencies are the sum of those correction terms added onto the diffusionless solutions, i.e.

$$f_{nlm} = f_{nl} + \delta_{bound}, \tag{2.100a}$$

$$g_{nl} = g_{bound} + g_{bulk}, \tag{2.100b}$$

with f_{nl} the eigen frequencies for the reference model. The equivalent imaginary part equals 0 as the reference model is diffusionless. Expression for each term is detailed in Moldover et al. (1986), Part I.

The bulk contribution is Moldover et al. (1986), eq. (39),

$$g_{bulk} = \frac{k_{nl}^2}{4\pi a^2} \left[(\gamma - 1)\kappa + \frac{4}{3}\nu + \nu_{bulk} \right], \tag{2.101}$$

where $d_{th} = \sqrt{\kappa/(\pi f_{nl})}$ and $d_{visc} = \sqrt{\nu/(\pi f_{nl})}$ are the thicknesses of the thermal and viscous boundary layers respectively, as defined in eq. (2.27).

The boundary contribution is given in Moldover et al. (1986), eq. (42), by

$$\delta_{bound} + \mathrm{i} g_{bound} = f_{nl} \frac{(1-\mathrm{i})}{2a} \frac{(\gamma-1)\, d_{th} + l(l+1)\, d_{visc}/z_{nl}^2}{1 - l(l+1)/z_{nl}^2}, \tag{2.102}$$

Note that boundary effects, both due to thermal and viscous layers, have a non-zero real part that shift the real part of the frequency, f_{nl} is reduced by δ_{bound}.
We give the values of the total contribution g_{nl} for a selection of modes in Table 2.2. Note that contrary to the real part, g_{nl} is independent of m hence all modes within a multiplet display a similar peak shape.

2.3 Building of a theoretical synthetic spectra

2.3.1 Superposition of perturbations

In presence of a rigid shell, effects influencing the complex frequencies can be linearly superposed (Moldover et al., 1986; Trusler, 1991). Thus, frequencies are the sum of those correction terms added onto the diffusionless solutions, i.e.

$$f_{nlm} = f_{nl} + \delta_{\Omega} + \delta_{geom} + \delta_{bound}, \tag{2.103a}$$

$$g_{nl} = g_{bound} + g_{bulk}, \tag{2.103b}$$

with $f_{nl} = c z_{nl}/(2\pi a)$, where we take δ_{Ω} as first-order rotational correction, δ_{geom} second-order geometry correction and δ_{bound} first-order dissipation correction. The predicted frequencies taking into account all those effects is plotted in Figure 2.7.

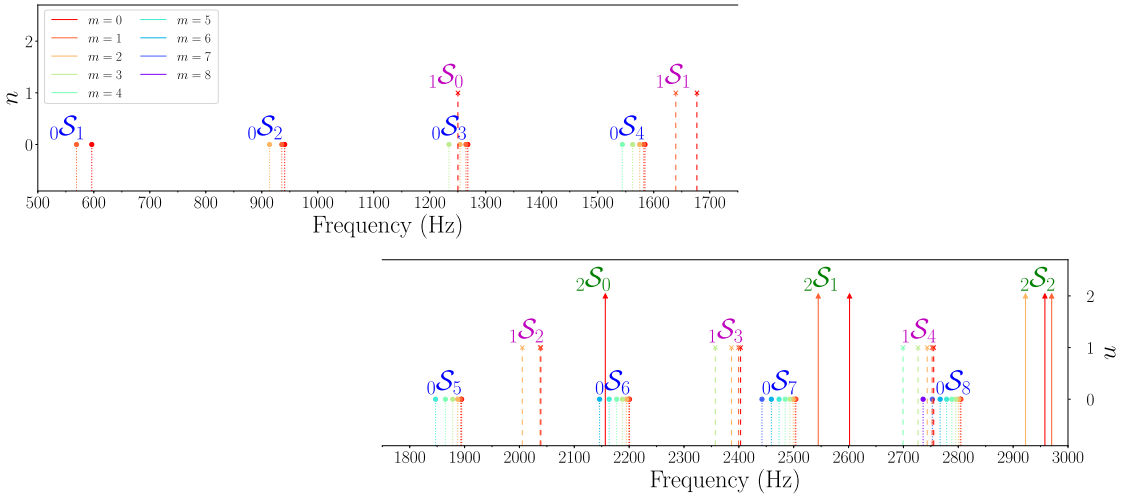

Figure 2.7: Theoretical eigenfrequencies for spheroid of $e = 0.05$ at rest, with both first and second-order geometrical corrections obtained with perturbation theory taken into account.

n	l	f_{nl} (Hz)	C_{nl}	γ_{nl}	g_{nl} (Hz)
0	1	578.41	0.8573	−0.9144	0.2340
0	2	928.67	0.3869	−0.1505	0.3731
0	3	1254.34	0.2387	−0.0604	0.5135
0	4	1569.06	0.1683	−0.0325	0.6568
0	5	1877.42	0.1278	−0.0204	0.8030
0	6	2181.59	0.1018	−0.0140	0.9519
0	7	2482.73	0.0839	−0.0102	1.1035
0	8	2781.59	0.0709	−0.0078	1.2574
0	9	3078.65	0.0611	−0.0061	1.4136
0	10	3374.25	0.0534	−0.0049	1.5720
0	11	3668.63	0.0473	−0.0041	1.7323
0	12	3961.98	0.0423	−0.0034	1.8946
1	0	1248.59	0.0991	0.0000	0.0956
1	1	1650.66	0.0601	−0.4360	0.1311
1	2	2025.66	0.0424	−0.1013	0.1714
1	3	2385.18	0.0324	−0.0466	0.2145
1	4	2734.38	0.0260	−0.0270	0.2596
1	5	3076.09	0.0216	−0.0176	0.3063
1	6	3412.07	0.0184	−0.0125	0.3543
1	7	3743.49	0.0159	−0.0093	0.4035
1	8	4071.16	0.0140	−0.0072	0.4538
2	0	2146.63	0.0335	0.0000	0.1283
2	1	2558.04	0.0242	−0.4145	0.1519
2	2	2949.29	0.0188	−0.0979	0.1795
2	3	3326.88	0.0152	−0.0455	0.2094
2	4	3694.45	0.0128	−0.0265	0.2411
2	5	4054.30	0.0109	−0.0174	0.2742
3	0	3029.94	0.0168	0.0000	0.1568
3	1	3446.84	0.0132	−0.4079	0.1761
3	2	3847.44	0.0108	−0.0968	0.1984
3	3	4236.01	0.0091	−0.0450	0.2229

Table 2.2: For an air-filled sphere reference model with $c = 343.2638$ m/s and $a = 0.1966$ m. We give for a selection of modes labelled by n the radial mode number and l the angular mode number: f_{nl} the mode frequency, and coefficients computed by first-order perturbation theory C_{nl} the Ledoux coefficient, γ_{nl} the ellipticity coefficient, g_{nl} the imaginary part of mode frequency due to dissipation.

Under our set of approximations, acoustic resonances are equivalent to damped harmonic oscillators. Close to their resonant frequencies, such oscillators have a (complex) frequency response following (at first-order) a Lorentzian function (Trusler, 1991; Morse and Ingard, 1986)

$$\mathcal{A}_{nlm}(f) = \left| \frac{A_{nlm}}{(f - f_{nlm}) - \mathrm{i}g_{nl}} \right|, \tag{2.104}$$

with

$$A_{nlm} = A \left| \mathcal{P}_l^m(\cos\theta_{sp})\, \mathcal{P}_l^m(\cos\theta_{el})\, j_l(k_{nl}a) \cos\left[m(\phi_{el} - \phi_{sp})\right] \right|, \tag{2.105}$$

where A is a constant, $\mathcal{P}_l^m$ is the associated Legendre polynomial of degree l and order m, θ_{sp}, ϕ_{sp} and θ_{el}, ϕ_{el} the co-latitude and longitude of the source (in the experimental setup, a speaker), resp. receiver (electret).

Taking into account all the previously described perturbations, we can have a theoretical expression of the frequency response for each acoustic eigenmode, by taking the damping factor as g_{nl} and the peak maximum frequency as f_{nlm}. Then, by adding all mode contributions, we are able to create a theoretical synthetic acoustic spectrum matching our experimental configuration. In Figure 2.8 we compare our theoretical synthetic spectrum (in green) with finite-element calculations (in blue), and find very good agreement again. All major features: (real) frequency, relative amplitude and width are successfully reproduced. Comparison between theoretical and experimental acoustic spectra is discussed in Chapter 3.

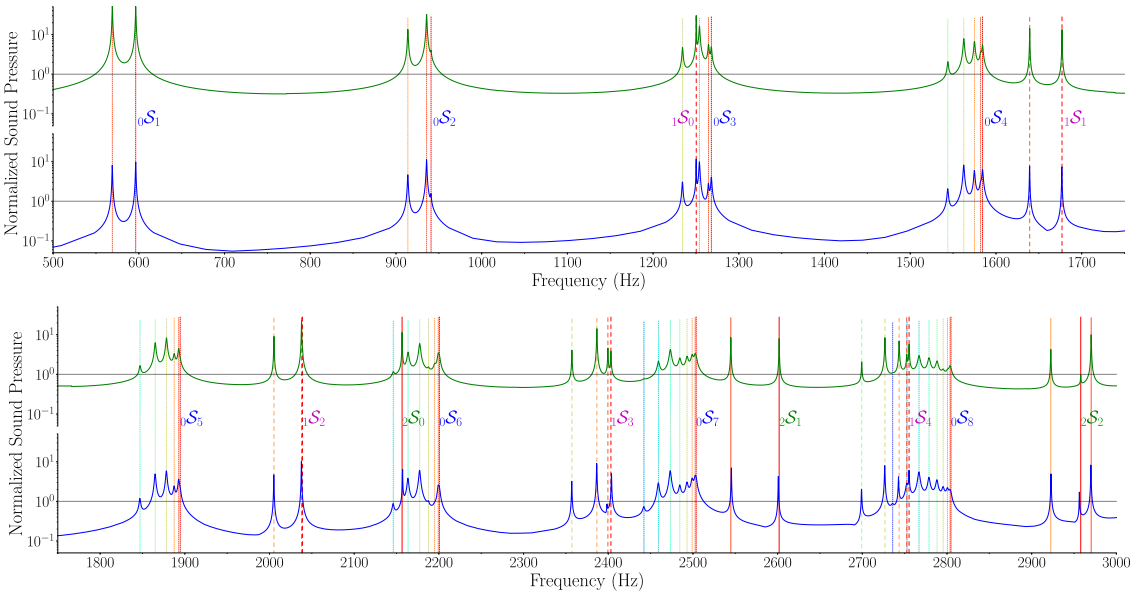

Figure 2.8: Synthetic acoustic spectrum for ZoRo configuration, calculated with perturbation theory second-order in geometry and first-order in diffusion (in green), and finite-element (in blue). Spectra are continued from top to bottom panel. Both spectra are normalised to have the average amplitude over the given frequency window (grey line) equals to 1. The real frequencies from perturbation theory (with diffusion) are given for comparison across the spectra.

We can do the same exercise in presence of a background flow. In Figure 2.9 we choose to add a solid-body rotation of the fluid at 10 Hz, and compute the theoretical spectra we obtain with perturbation theory (first-order rotation, second-order geometry and first-order diffusion). As detailed above, at first order, rotational flows only influence the real part of the eigenfrequency, and the $|m|$ degeneracy is lifted.

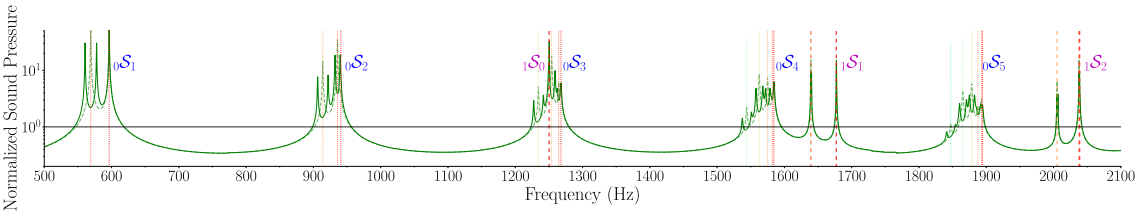

Figure 2.9: Synthetic acoustic spectrum for ZoRo configuration with solid-body rotation flow at 10 Hz, calculated with perturbation theory first-order in rotation, second-order in geometry and first-order in diffusion. Spectrum at rest is given in comparison in dashed lines. The real frequencies from perturbation theory (with diffusion) are given for comparison across the spectra.

2.3.2 Discussion

Other effects might influence the spheroid's acoustic spectrum. We list and explore a few of them that are mentioned in the literature as potentially relevant. They include uneven shell surface finishing, presence of holes in the shell or a seam between the two hemispheres. All of those are expected to be negligible for our apparatus (Moldover et al., 1986).

The finite elasticity of the container may modify significantly the acoustic resonances when acoustic and elastic eigenfrequencies are close (Moldover et al., 1986). The finite elasticity of the ZoRo container allows a coupling between acoustic and elastic modes, modifying their eigenfrequencies (Moldover et al., 1986). Elastic eigenfrequencies of the ZoRo spheroidal shell container have been estimated with finite-element (COMSOL Multiphysics) and analytical calculations. In the latter case, the elastic influence on acoustic eigenfrequencies can be calculated with the thin-shell approximation (Rand and DiMaggio, 1967). This allows us to consider spherical and spheroidal containers. In the spherical geometry, this calculation can also be done without the thin-shell approximation by following Mehl (1985) or Lonzaga et al. (2011), who corrected some typos and gave also the modification of elastic modes due to the fluid coupling. The two approaches give very similar results and predict frequency shifts from 0.1 to 1 Hz far from the eigenfrequencies, but they can reach 10 Hz near acoustic resonances of the container. We have successfully compared those predictions with finite element calculations.

Further comparison with the experiment is difficult, due to the complex shell geometry (sensors holes, shafts, equatorial bulge, etc.) and the influence of the frame supporting the spheroid. Nevertheless, finite-element calculations confirm that these complexities do not modify the order of magnitude of elastic effects. Near acoustic resonances, elastic resonances can thus be one of the cause to the shifts left in the experimental spectrum that are unexplained by the finite-element computations. It can be noted that the sign of acoustic frequency shifts due to the shell elasticity is not uniform (it can either lower or raise acoustic frequencies). Yet, since the shifts are very small compared to the flattening effect, no mode switching should occur, so it should not impede mode identification.

Coupling between the elastic shell and the outer surrounding fluid is expected to also possibly have an influence on the complex eigenfrequency, i.e. both on the frequency and on the damping rate of modes. Theoretical calculations on the modes $l = 0$ can be performed (Moldover et al., 1986), confirming finite-element predictions. This suggests that this effect is very small in ZoRo. Sound radiation in the surrounding air can thus be discarded in the interpretation of the ZoRo experimental results.

Key points

We aim to use acoustic resonances to measure flow velocity within our experimental apparatus. In order to interpret the acoustic signatures, we rely on theoretical developments to understand the influence of various physical effects on the acoustic spectra without flows (at rest).

To do that we choose as reference model the diffusionless sphere at rest, where analytical solutions are simple, and we use perturbation theory to accommodate for the remaining effects that are expected to be at play in the experiment.

We add the spheroidal geometry and diffusion (viscous and thermal) corrections and are able to predict the complex eigenfrequencies of our experimental resonator.

Using the same method, we are able to predict the acoustic signature of axisymmetric rotational flows within the cavity. This provides the tools to tackle the inverse problem, which consists, in our case, in retrieving the flow field with acoustic measurements.

Rotational splitting

$$\delta\omega_{nlm} = m \int_0^{\pi} \int_0^{a} K_{nlm}(r,\theta)\Omega(r,\theta) r \mathrm{d}r\mathrm{d}\theta$$

or in the rotating frame

$$\begin{aligned}\delta f^{\mathrm{rot}}_{nlm} &= m\Omega^{\mathrm{ref}} - m \int_0^{a} \int_0^{\pi} K_{nlm}(r,\theta) \left[\Omega^{\mathrm{ref}} + \Omega^{\mathrm{rot}}(r,\theta)\right] r\mathrm{d}r\mathrm{d}\theta \\ &= m\Omega^{\mathrm{ref}} C_{nl} - m \int_0^{a} \int_0^{\pi} K_{nlm}(r,\theta)\Omega^{\mathrm{rot}}(r,\theta) r\mathrm{d}r\mathrm{d}\theta.\end{aligned}$$

3

Acoustic splitting measurements in the ZoRo experiment

Ce n'est qu'en essayant continuellement que l'on finit par réussir. Autrement dit : plus ça rate, plus on a de chances que ça marche.

- Jacques Rouxel, *Les Shadocks*

Physical properties of resonators control their resonances, hence their acoustic spectra. For a given resonator, a thorough understanding of those spectra allows to retrieve the physical quantity of interest, such as internal flow velocity. We aim to measure experimental acoustic signatures of rotational flows. In order to retrieve zonal flows, we built a spheroidal resonator called Zonal flows in Rotating fluids (ZoRo).

This chapter contains in §3.1 a full description of the experimental set-up, as well as a typical protocol used to measure the acoustic response of the apparatus. Then in §3.2, we present the data processing used to obtain useful acoustic spectra, including the crucial step of mode identification. Starting from the theoretical predictions, we are able increase the accuracy of this identification by taking advantage of the symmetry properties of the pressure field. From fully identified spectra, we then extract the frequency splittings due to presence of flows for a number of modes. To do this we developed two complementary fit procedures.

We are then able to extract a number of frequency splittings out of an experimental spectrum at rest. Finally in §3.3, we apply our procedure to solid-body rotation (without internal flows) and show that the experiment is in very good agreement with both analytical and numerical predictions from Chapter 2.

Prior to this experiment, we built a spherical prototype called ZoRo1 that helped us in the design and development of the data analysis. We briefly present some of the results we obtained in the ZoRo1 prototype in Appendix D.

3.1 Experimental setup

3.1.1 Presentation of ZoRo

Spheroidal container

The experimental set-up consist of a 1 cm thick container made with aluminium based alloy (Thyssenkrupp by Constellium cast, MecAlu+ 7000 series) enclosing an axisymmetric oblate spheroidal cavity filled with gas of equatorial radius $r_{eq} = 20$ cm, and polar radius $r_{pol} = 19$ cm (Figure 3.1). The ellipticity is defined as $e = (r_{eq} - r_{pol})/r_{eq} = 0.05$. Dimensions of the shell are ensured up to 0.1 mm. In order to attain such precision, special care has been given during the fabrication process, especially to the junction plane between the two hemispheres and the coaxiality (both between the hemispheres and the shafts) which have been identified in the literature as potential defaults (Mehl, 1986). Static and dynamic balancing with the shell rotating up to $f_\Omega = \Omega/(2\pi) = 70$ Hz in the experimental conditions, revealed less than 0.2 g of unbalanced mass for a total rotating spheroid mass of 32.5 kg (balancings were done by a mandated expert using accelerometers).

Air-tightness is ensured by custom made plastic gaskets on each sensor hole and at the equatorial seam of the shell. Additional holes provided for future temperature and pressure sensors, are plugged closed for acoustic campaigns. The spheroidal shell can accommodate overpressure up to 4 times the atmospheric pressure P_0 and under-pressure down to $P_0/2$. In the following, the cavity is filled with air at atmospheric pressure P_0.

Rotation and motor

The spheroid's revolution axis is mounted on the shaft of an electric motor (ref. Kollmorgen AKM73Q). In order to minimize the motor vibrations, it is mounted on a frame distinct from the frame supporting the acoustic cavity. The spheroid's shaft is coupled with the motor through a vibration-reducing jaw-type coupler (ref. ROTEX SH38 from KTR). In this configuration, the motor can rotate up to 50 Hz, or 3000 revolutions per minute (rpm). We successfully rotated the apparatus up to 70 Hz (without instrumentation).

The motor is controlled through a compact Remote Input Output controller (ref. cRIO-9064 from National Instruments), allowing up to one operation every 62 μs. The rotation rate is independently measured with a magnetic revolution counter, 3 magnets are embedded in the shell's equatorial bulge, and are detected in the non-rotating frame. Thanks to this, we verified that the rotation rate displays less than 1% of variation from the instructed value (mainly oscillations around the instructed value).

Acoustic instrumentation

At $T = 20°$C and atmospheric pressure, the cavity's fundamental mode is around 578 Hz, which is in the audible range. This allows us to use standard audio material. Acoustic pressure is measured by electrets (ref. Projects Unlimited TOM-1545P-R) connected to a mixing table (ref. TASCAM US-16x08). Acoustic waves are produced by 36 mm-diameter audio speakers with working range 400-6000 Hz (ref. Multicomp MCKP3648SP1-4758) connected to a sound card (ref. Asus TeK, Xonar DGX), through 20 W amplifiers (ref. LEPY LP-808), see Figure 3.2, right panel, for a schematic of the acquisition chain.

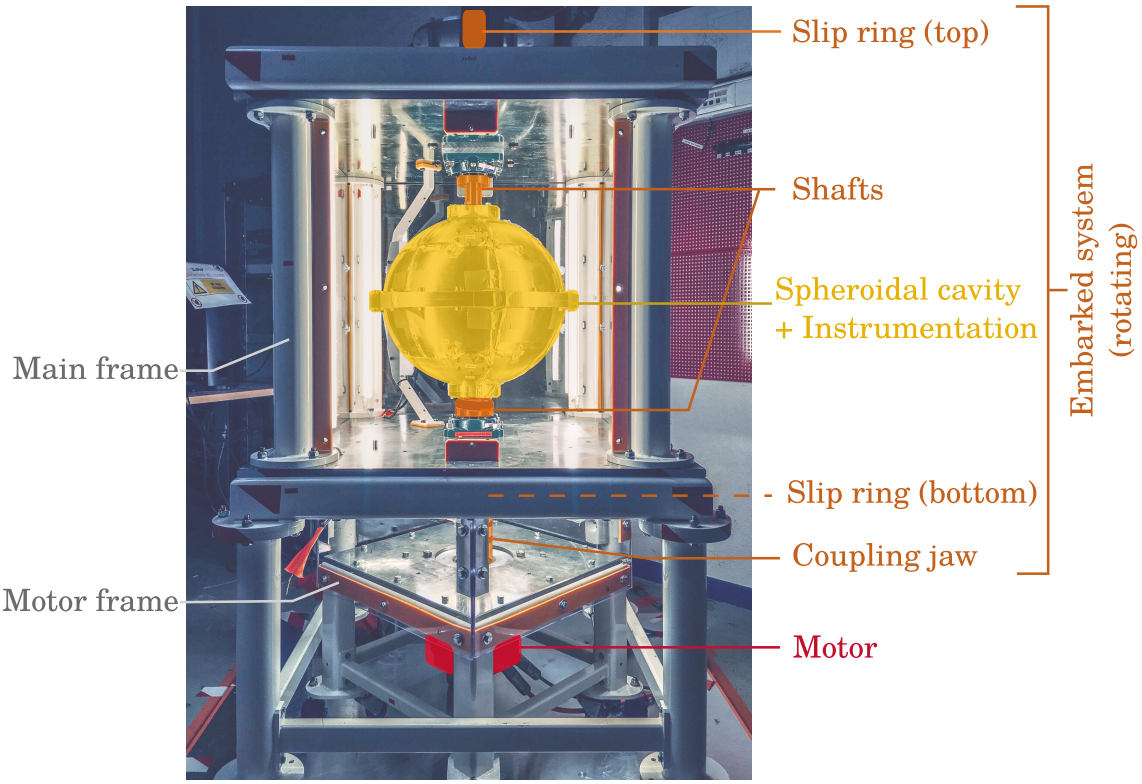

Figure 3.1: Schematic photo of the experimental apparatus mounted on its working frame (photo by Max Solazzo).

For cleaner signals, acoustic resonances are excited by chirps sweeping over the frequencies of interest. Both source and data files are sampled at 44.1 kHz and written in 16-bits in the uncompressed audio Waveform Audio File Format (WAVE), corresponding to standard CD audio quality.

The instrumentation is mounted in through holes in the aluminium shell to be in direct contact with the gas, and have been fixed to be as less protruding as possible (less than 1 mm). Ideally their protrusion should be kept within the viscous Ekman layer in order to have as little influence on the internal flow as possible.

The apparatus can accommodate up to four speakers and fourteen electrets, half on each hemisphere, at respectively $\pm 45°$ and $\pm 30°$ latitude (Figure 3.2). All speakers are on the same meridional plane (at $0°$ and $180°$), electrets are evenly spaced on their latitude (every $51.4°$); lower and upper hemispheres are strictly symmetric (with respect to the equator). The exact sensor positions are detailed in the technical drawings used to manufacture ZoRo, chosen excerpts are reproduced in Appendix C.

The instrumentation is embarked and rotates with the shell (see embarked system in Figure 3.1). Electric signals (power and data) are transmitted from the rotating to the laboratory referential through two slip rings with gold-gold contacts (ref. PSR-HSC-36 and ref. PSRT-38H-24 from Panlink), located above and under the main frame. To avoid contamination, acoustics acquisition (electrets' signals) pass through the top slip-ring and excitation (speakers' signals) pass through the bottom one.

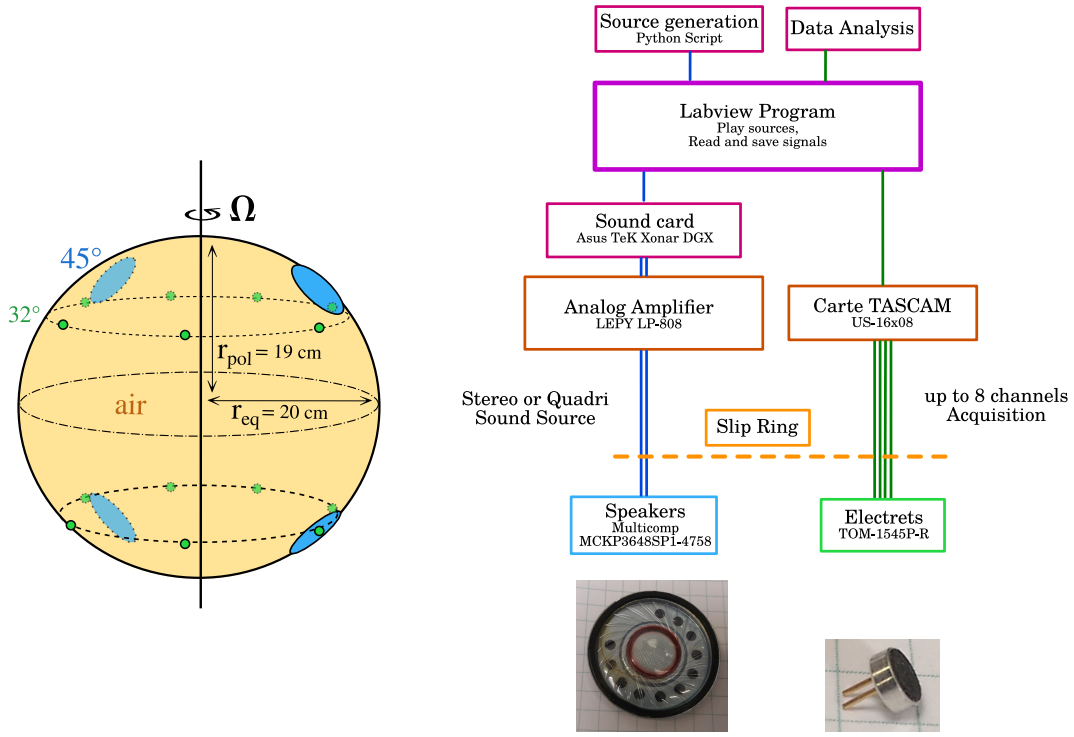

Figure 3.2: Left: Schematic of the experimental set-up ZoRo, with acoustic instrumentation: electrets (green) and speakers (blue). Right: Function diagram of acoustic data acquisition chain with photo of speaker and electret.

3.1.2 Experimental protocol

Acoustic source generation

In order to increase the signal over noise ratio, we excite the resonances of interest with the speakers. We can play up to four different soundtracks, one on each speaker, which allows us to excite up to four resonances at the same time, assuming that the signals are linearly superposed.

In practice we play linear chirps centered on the predicted frequency of the mode we want to measure (obtained with analytical computations from Chapter 2). Chirps are signals whose frequency changes, either increasing or decreasing, with time. In this sense it is a special case of frequency modulation (where frequencies can go up and down successively). The signal $x(t)$ is defined on a time-dependent phase ψ as $x(t) = \sin(\psi(t))$. Thus the instantaneous frequency $f(t)$ is defined as the phase rate

$$f(t) = \frac{1}{2\pi}\frac{\mathrm{d}\psi(t)}{\mathrm{d}t}. \tag{3.1}$$

We use the simple linear chirp, where frequency changes linearly with time, going from f_1 to f_2 during a time T as

$$f(t) = f_1 + \frac{f_2 - f_1}{T}t. \tag{3.2}$$

In this case, the signal takes the form

$$x(t) = \sin\left(\psi_0 + 2\pi\left(f_0 t + \frac{f_2 - f_1}{2T}t^2\right)\right), \tag{3.3}$$

with $\psi_0 = \psi(t = 0)$, the initial phase.

For time-dependent flows, we need to find a compromise between the time of the chirp T, to maximize the sweep time on the resonance frequency, and the typical time-scale of the flow. A typical source sweeps over a 40 Hz window centred on the estimated frequencies at rest $f_0 = (f_2 - f_1)/2$ with a sweep time of 1 s (see skematic of the source frequency played by the speaker in Figure 3.3).

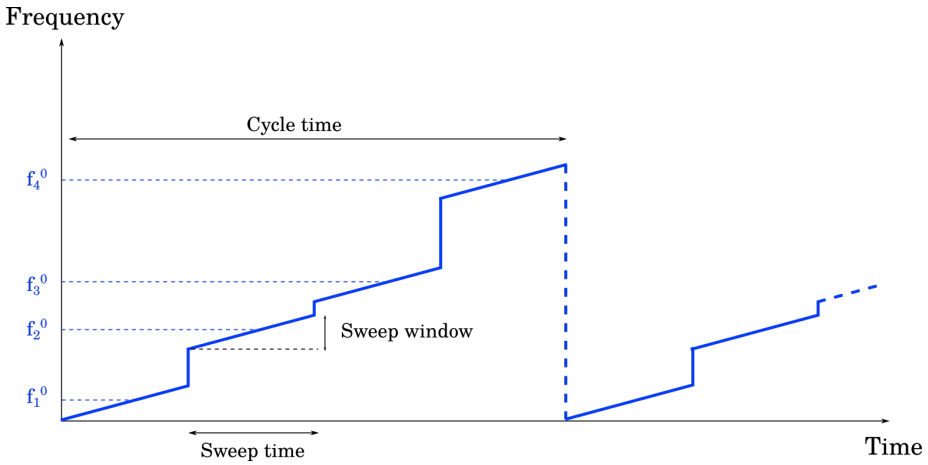

Figure 3.3: Schematic of frequency over time of a typical sound source played by the speakers. Succession of several chirps centred on the predicted frequency of interest.

Sound speed variations

Resonance eigenfrequencies are directly related to the sound speed (as seen in eq. (2.39)) which in turn is sensitive to the gas thermodynamic properties. Eigenfrequencies are mainly dependent on the fluid temperature and humidity (Zuckerwar, 1996) that can drastically change from one experimental run to another. Long term variations are typically due to season change and weather. Short term variations (within an hour) can be attributed to the viscous or vibratory heating and cooling caused by the rotation.

Dependence of the sound speed with temperature can be expressed for dry air, combining eq. (2.14) and Diu et al. (1989), through the empirical relation

$$c = 331.3 \times \sqrt{\frac{T(K)}{273.15}}\ \mathrm{m/s}. \tag{3.4}$$

The system is highly sensitive to temperature, as a difference of 1 K causes a shift of frequency about 1 Hz of the fundamental mode. The same temperature difference causes increasingly large frequency shifts for higher frequency modes.

Due to this sensitivity, the source we play may easily miss the resonances if the frequency shift causes the eigenfrequency to be outside our excitation window. It is challenging to obtain high precision measurements in both temperature and humidity, hence

accurate prediction of the resonance frequencies are out of reach in our experiment. In order to address this issue, we take advantage of the linear relation between eigenfrequency and the sound speed. A single eigenfrequency is enough to determine all mode frequencies by determining the apparent sound speed of the run (Koulakis et al., 2018).

In order to accurately tune the experiment, we choose a non-degenerate mode as reference (for example ${}_2\mathcal{S}_0$, around 2170 Hz) and we play a larger range frequency chirp to make sure the mode will be excited. Thanks to this mode frequency reference, we are able to deduce any eigenmode frequency by applying a homothetic transformation and generate the ad hoc sources. The ad hoc frequencies are simply related to a reference by $f_{ad\,hoc} = f_{ref} \times f_{200}^{ref}/f_{200}^{mes}$, where the reference frequency is arbitrary, typically taken as f_{nlm} obtained from theoretical calculations. In practice, a tuning (verification of the shift in frequency) is needed every hour or more often depending on the mechanical forcings applied to the spheroid.

Data acquisition

We can acquire up to 8 acoustic signals simultaneously. We make use of this multiple measurements to probe the pressure field at several locations. This feature is of great interest to separate modes that are close in frequency, as detailed later in 3.2.2.

Since we do not amplify or pre-amplify our acquisition signal, the calibration of the sound volume is done with the source output. The resonances can reach amplitudes several order of magnitude above the source level. Thus the calibration is done manually, aiming to use the dynamic range as much as possible without saturating the electrets.

In addition to the acoustic response of ZoRo, the data files also contain information on synchronisation with the source and with the rotation. We take advantage of the internal synchronisation system of the mixing table, and directly wire both the source and the revolution counter on separated acoustic inputs.

At the end, the acquired data file presents 10 channels in WAVE format, channels 1–8 are the acoustic data signals from the spheroid, channel 9 gives the start of each chirp played by the source and channel 10 gives the rotation frequency (divided by 3, the number of magnets we embedded on ZoRo as counters).

3.2 Data analysis

3.2.1 Spectral domain Fourier transform

We are interested in the acoustic spectra of the resonating cavity. Starting from the temporal signal, we use a Fourier transform to represent our acoustic signal in the frequency domain. For a measured data, the signal is discretely sampled (at 44.1 kHz in our case). The discrete Fourier transform is defined as

$$\hat{x}_{\mathtt{k}} = \sum_{\mathtt{j}=0}^{N-1} \exp^{-2\mathrm{i}\pi \mathtt{k}\mathtt{j}/N} x_{\mathtt{j}}, \tag{3.5}$$

where $x_{\mathtt{j}}$ are discrete values taken by the temporal signal, N the number of sampled points and $\hat{x}_{\mathtt{k}}$ the discrete spectral response in the Fourier domain.

Here some subtleties are at play to avoid aliasing when doing so. It is useful to recall that the source we play, hence the signal we retrieve, is mostly a linear chirp. It is quite

intuitive to see that in the frequency domain, frequencies between f_0 and f_1 will contribute whereas all the others do not, which leads to a hat-like spectrum plus Gibbs oscillations. Analytic formulation is not simple and involves the so-called Fresnel integrals

$$C(X) = \int_0^X \cos\left(\frac{\pi y^2}{2}\right) \mathrm{d}y \qquad \text{and} \qquad S(X) = \int_0^X \sin\left(\frac{\pi y^2}{2}\right) \mathrm{d}y, \tag{3.6}$$

where the Gibbs oscillation rate is proportional to $T(f_2 - f_1)$.

Analytic expression of the Fourier transform of a linear chirp is given by

$$\hat{x}_{\mathtt{k}} = \sqrt{\frac{T}{2(f_2 - f_1)}} \exp\left(-\mathrm{i}(\mathtt{k} - f_0)^2 \frac{T}{4\pi(f_2 - f_1)}\right) \left[C(X_+) + \mathrm{i}S(X_+) + C(X_-) + \mathrm{i}S(X_-)\right], \tag{3.7}$$

with

$$X_\pm = \sqrt{\pi T(f_2 - f_1)} \left(1 \pm \frac{\mathtt{k} - 2\pi f_0}{\pi(f_2 - f_1)}\right).$$

For a time-dependent flow, we are interested in exciting a frequency over and over in order to follow its time dependency. The signal we use in our source is then a succession of M times the same chirp. The Fourier transform of such a signal is tricky since the same frequency is met M times but with possibly different phases which leads to aliasing the signal at the chirp duration rate. To avoid this effect, we need all frequencies to have the same phase function $\psi(t)$ throughout all iterations of chirps, in other words, each frequency should be able to be continuously completed between two chirps.

The frequency met at a given time $0 < t_i < T$ during the linear chirp eq. (3.8) is associated with a phase $\psi_i(t)$ written in eq. (3.9), which is obtained by integrating eq. (3.1).

$$f_i = f_1 + \frac{f_2 - f_1}{T} t_i, \tag{3.8}$$

$$\psi_i(t) = \psi_0 - 2\pi \frac{f_2 - f_1}{2T} t_i^2 + 2\pi t \left(f_1 + \frac{f_2 - f_1}{T} t_i\right). \tag{3.9}$$

The non-aliasing condition can be written as a phase equality between the chirp at time $t_i + \mathtt{m}T$ and the sinusoidal signal at constant frequency f_i, leading to eq. (3.10). Since at each chirp iteration, the frequency f_i of interest will be met at the same phase $\psi_i(t_i)$, it is equivalent to say that an entire number of period $\mathtt{M}$ of the constant signal should be able to fit in any of chirp duration period T, which gives eq. (3.11)

$$\psi_i(t = t_i + \mathtt{m}T) = \psi_i(t_i) + 2\pi\mathtt{n}, \tag{3.10}$$

$$\mathtt{m} = (f_0 T + (f_1 - f_0)t_i)\,\mathtt{n}. \tag{3.11}$$

In particular $\mathtt{m}$ must be an integer. Let us verify if it can be satisfied through an entire chirp. In practice we sample the data discretely at $f_{\text{sample}} = 44.1$ kHz. Since the frequency is linearly changing due to the chirp, each data point can be associated with its own specific frequency, and we want eq. (3.11) to be verified for each of them, i.e. for each $t_i = T/\mathtt{i}$ with $\mathtt{i}$ from 1 to f_{sample}. It is clear that eq. (3.11) is only satisfied for specific values of t_i, and in general not for all of them.

That implies that any succession of chirps will be aliased. To avoid this problem, we analyse each chirp separately. It is therefore needed to have precise time of chirp's starts

to be able to separate them without mixing two iterations, and thus mixing the phases from different chirps.

We show in Figure 3.4 an acoustic spectrum obtained for ZoRo at rest for one electret, with a continuous linear chirp going from 400 to 5000 Hz in 90 s. The resonances are clearly visible, with their amplitude well above the noise and source level.

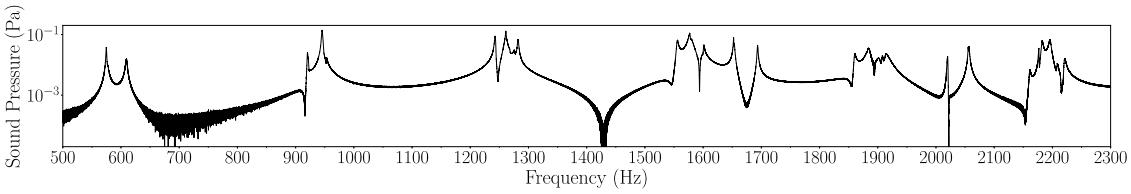

Figure 3.4: Experimental acoustic spectrum of ZoRo for the lowest resonances.

We remark that some "anti-peaks" appear clearly (in log-scale), with a sound pressure level much lower than even the mean noise, around 1400 Hz for example. These can be interpreted as frequencies that have their nodes close to the sensor position. Indeed, when we take the average over longitude, taking all spectra from the 7 electrets of one hemisphere, the anti-peaks disappear and leave a much smoother spectrum. In the following, the spectra we show are averaged over the longitudes unless mentioned otherwise.

Note that when the apparatus rotates, the data can become noisier. A solution to still exploit the noisier data is to stack several spectra, using the fact that the signal is coherent from a run to another while noise is random. We sometimes apply a low-pass filter, in which case the spectrum is used for visualisation purposes only.

3.2.2 Mode identification at rest

We are interested in the relation between the eigenfrequencies and spatial structure, as detailed in Chapter 2. In order to link the two, it is essential to identify the acoustic peaks, meaning to uniquely attribute a (n, l, m) triplet to each peak. Mode identification is also crucial to accurately measure the splitting of a ${}_n\mathcal{S}_l^{\pm m}$ doublet. A wrong label might lead us to pair together different modes or even from different multiplets. This creates false information that would severely impair the inversion problem by either imposing contradictory splittings or that would lead to non-physical flows. We focus here on the spectra obtained from ZoRo at rest.

Continuity from sphere

At leading order, ZoRo is close to a sphere, so we expect its eigenfrequencies to be close to those of a sphere of similar dimensions, as detailed in Chapter 2. Following Mehl (2007), we choose to consider the sphere of same volume as our spheroid (radius $a = 0.1966$ m), and we reported the predicted eigenfrequencies f_{nl} of a sphere obtained with the Helmholtz equation eq. (2.30), along with their labels ${}_n\mathcal{S}_l$ in Figure 3.5 (dashed lines). As discussed above, the frequencies can shift due to the conditions in the lab at the time of the run. In this case, we calculated the spherical eigenfrequencies with the apparent sound speed deduced using the experimental frequency of the reference mode ${}_2\mathcal{S}_0^0$.

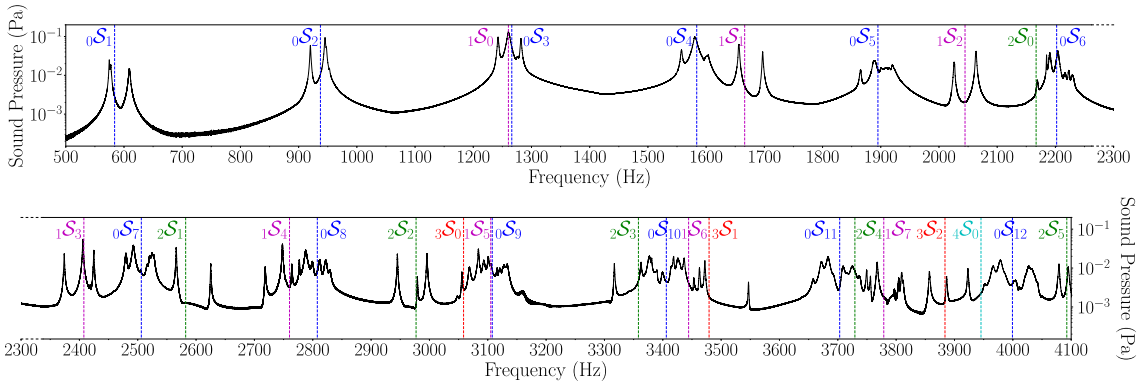

Figure 3.5: Spectrum of ZoRo, averaged over all electrets of the northern hemisphere (longitudinal average). Theoretical predictions for the sphere of same volume is plotted for comparison with their labels (vertical lines).

We first observe that all peaks are close to the resonances of the reference model, confirming the use of a perturbation method for geometry. Around the spherical predictions f_{nl}, there are groups of peaks that we label with the spherical ${}_n\mathcal{S}_l$ multiplet. They correspond to degeneracy lifting of the resonances. The lowest frequency modes are clearly separated. We note that those groups contain $l+1$ peaks confirming that the degeneracy is only partially lifted, as predicted by the geometrical perturbation theory.

Qualitatively, the frequency splitting can be compared to the difference between eigenfrequencies of spheres of radius r_{eq} and r_{pol}. For example, the fundamental mode ${}_0\mathcal{S}_1$ of a sphere of radius r_{eq} is predicted at 578 Hz and at 604 Hz for a radius r_{pol}, agreeing, at lowest order, with the splitting observed in our spheroid between the two peaks near ${}_0\mathcal{S}_1$.

We also use the synthetic spectra to further identify the $|m|$ peaks within a multiplet. In Figure 3.6, we show the experimental spectrum (in black) alongside with both the analytical (green) and finite-element predictions (blue), reproduced from Figure 2.8. To compare with the synthetic spectra, we apply the homothetic transformation described in §3.1.2 on the experimental spectrum to match the theoretical value of ${}_2\mathcal{S}_0^0$ frequency (i.e. 2146 Hz, see Table 2.2).

This comparison shows that all major features are reproduced by the perturbation theory: both frequencies (real part), relative amplitude of peaks and their shape (imaginary part) are very similar. This further confirms that the perturbation theory is a valid approach for ZoRo, both for geometry and dissipation. Deviations between synthetic and experimental spectra are visible in some narrow frequency range (e.g. around 1600 Hz) where some experimental peaks seem to be missing. The dissipation in the experiment is expected to be higher than from the values used in the theory, where we neglected air humidity and other effects such as the container elasticity. This might cause some peaks to be hidden in the experimental spectrum by the neighbouring peaks.

Another helpful observation is the difference in the frequency imaginary part, hence half-width of peaks. Modes with $n = 0$ are more diffusive than the overtones $n > 0$ (Mehl, 2007), and this is exacerbated if the mode is non-degenerate ($l = 0$). The difference is clearly visible in frequency range where two multiplets with different n overlap, around 2750 Hz the transition frequencies between ${}_1\mathcal{S}_4$ and ${}_0\mathcal{S}_8$, or around 2150 Hz, where ${}_2\mathcal{S}_0$ is surrounded by the high m modes of the ${}_0\mathcal{S}_6$ multiplet.

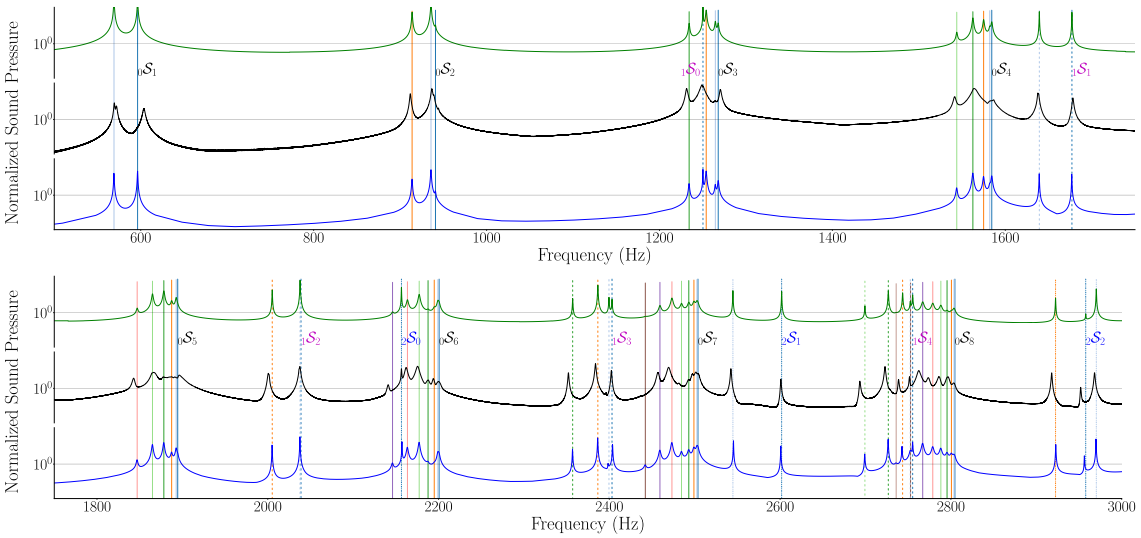

Figure 3.6: Acoustic spectra for ZoRo configuration at rest obtained with perturbation theory (top), experimental data (middle) and finite-element calculations (bottom). Mode frequencies and labels from the theory are given across the three spectra for comparison (vertical lines, different line types are used for n, different colours for m). Experimental spectrum is averaged over all electrets of one hemisphere. For each spectrum, amplitude is normalised by its mean on the given frequency window.

This allows to identify experimental peak when the spectrum is sparse. However this method reaches its limit for higher l multiplets and high frequency (in our configuration around 2800 Hz), where eigenmodes are close. In those cases, the modes interact with each other (mountain range instead of peaks) leading to uncertainties in the identification.

Usage of symmetry

To help identify the modes, we use symmetry properties of the pressure field, in particular with respect to the equator, thanks to the symmetrical disposition of both the acoustic sources and sensors.

Since the pressure field at the resonator's surface is mapped on the spherical harmonics $\mathcal{Y}_l^m$, as shown in eq. (2.36), it displays the same symmetries. Acoustic modes with even $l-m$ are symmetric with respect to the equator; those with odd $l-m$ are anti-symmetric (Morse and Feshbach, 1953a). Acoustic sources impose both wave phase and the positions of the anti-nodes, so playing several speakers at the same time strengthens modes with the same symmetries as the source pattern, whereas modes with incompatible symmetries are extinguished, or, in practice, strongly weakened. To amplify this effect, acoustic response of the resonator is systematically measured with at least a pair of equatorially symmetric electrets and we make use of the symmetry properties in the data analysis as well. Measured signals are summed, or subtracted, to match the source pattern and further attenuate the unwanted modes.

In Figure 3.7, we show an example of symmetry usage on mode ${}_2\mathcal{S}_2$ (around 2940 Hz). To obtain these spectra two speakers symmetric with respect to the equator simultaneously play first in-phase then in anti-phase (phase opposition). Acoustic response is measured with four pairs of equatorially symmetric electrets. Measured time series of the in-phase

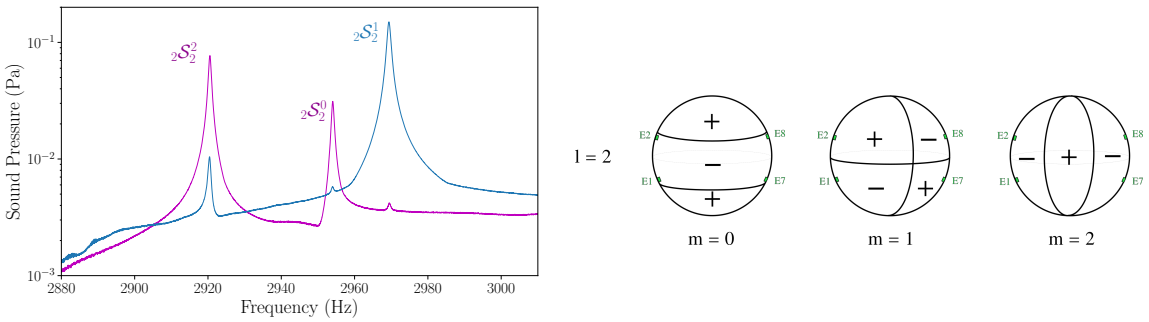

Figure 3.7: Left: Experimental acoustic spectra centered on the ${}_2\mathcal{S}_2$ multiplet. Two speakers symmetric with respect to the equator simultaneously play, first in-phase (purple) then in phase opposition (blue). Right: sketch of the surface pressure field for the corresponding modes modes. Symmetric positioning of the electrets allows to further extinguish modes with sum and subtraction of temporal signals. The sum strengthens the symmetric modes with even $|m| = 0, 2$ and subtraction strengthens the odd $|m| = 1$.

speakers are summed for each pair. We compute the frequency spectra which are then averaged, shown in figure 3.7 (purple). We do the equivalent for phase opposition sources signal with subtraction of each pair, shown in figure 3.7 (blue). The summed spectra of the in-phase source (purple) enhance the even $|m|$ (0 and 2), subtracted spectra of phase opposition source (blue) enhance the odd $|m| = 1$.

By successively extinguishing even and odd $l - m$ modes, we are able to identify, each peak of the experimental spectrum up to 3500 Hz. Symmetry provides a confirmation on the coarse identification from comparison with the synthetic spectra. And at higher frequency it provides complementary information by identifying the different $|m|$ within a multiplet.

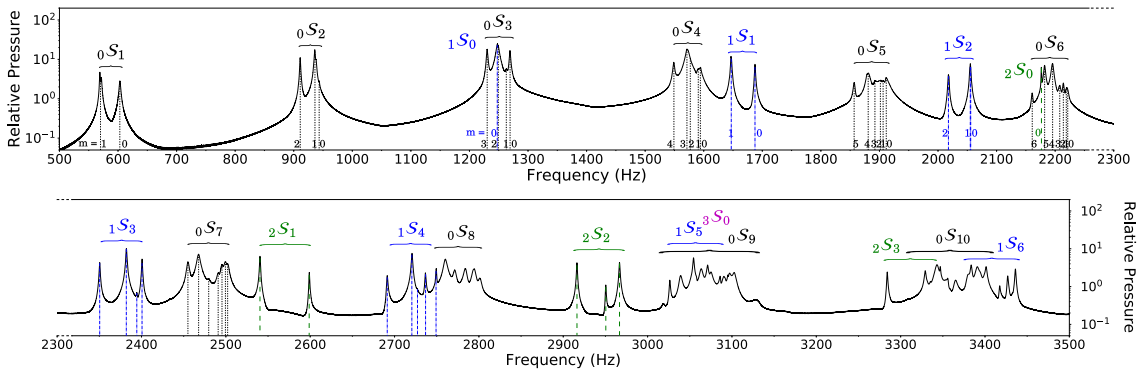

Figure 3.8: Experimental acoustic spectrum at rest for the lowest modes, averaged over all electrets of one latitude. The spectrum is continued from top to bottom frame. Acoustic resonances are excited by speakers with a continuous linear chirp from 500 to 3500 Hz. Groups of peaks can be labelled with ${}_n\mathcal{S}_l$ according to theoretical prediction of a sphere of same volume (labels on brackets). Using the symmetry technique developed in III B, peaks can be systematically identified by their m numbers (dashed lines) up to 2500 Hz. Above this threshold, we can only identify some modes among those that are not too close.

With this we can further compare measured with synthetic spectra on Figure 3.6. We observe that the synthetic spectra accurately reproduces the experimental acoustic behaviour, including the mode switching predicted between ${}_2\mathcal{S}_2^0$ and ${}_2\mathcal{S}_2^1$. This also comforts us in the understanding that second-order correction in geometry is indeed needed at ZoRo's ellipticity. Focusing on the ${}_2\mathcal{S}_2$ multiplet, we compare more precisely the predicted and measured frequency in Figure 3.9 and show that second-order is sufficient.

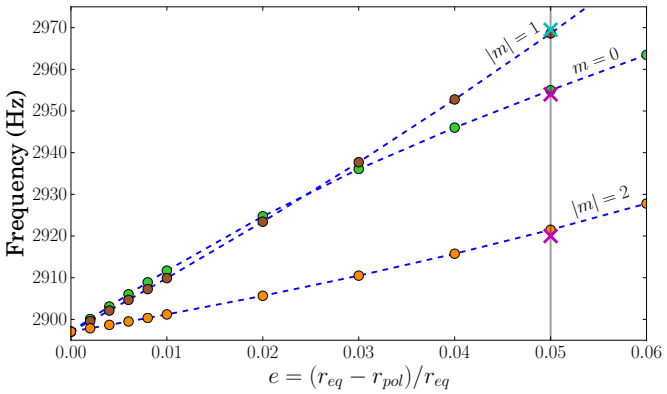

Figure 3.9: Frequency evolution of ${}_2\mathcal{S}_2^m$ modes with e, r_{eq} being kept constant, given by finite-element simulations (circles) and global polynomial computations (Vidal et al., 2020) (dashed lines). Both agree with experimental data (crosses) at ZoRo ellipticity $e = 0.05$ (black line).

3.2.3 Splitting extraction

Having identified the peaks in the experimental spectrum, we are now interested in extracting splitting between $\pm m$ modes of the same doublet, in order to retrieve the velocity field. We have developed two routines of splitting extraction, both are semi-manual fit of the measured acoustic spectrum to retrieve the local maxima.

They heavily rely on the identification described above, as the fits run in a given narrow window, determined for each mode based on their identification. Furthermore, the two fits both require initial guess of the peak frequency, that we choose close to the right modes, according to mode identification. In both case, we apply the fits to the separated spectra (either symmetric or anti-symmetric modes only), to minimize the fitting errors. Note that we measure the frequency gap between the two $\pm m$ modes, which corresponds to $|2\delta f_{nlm}|$, twice the splitting from eq. (2.69).

The first routine is a linear fit starting from the theoretical synthetic spectra, and the second routine is a non-linear fit starting from local maxima. We show examples on splitting extraction on both solid-body rotation and internal flows data.

Linear fit from theoretical spectra

We fit the observed $\pm m$ pairs of spectral peaks with theoretical synthetic spectra, carrying a grid search on the four following parameters: the frequency splitting between the two peaks, their mean frequency, their width, and their amplitude, see eq. (2.104)–(2.105).

For each combination of parameters, we evaluate the misfit as the root-mean square (rms) difference between the observed and theoretical synthetic spectra (in log scale) in the frequency window of the mode. The neighbouring modes contribution is taken into account as background. We obtain the best frequency splitting from the combination yielding the smallest misfit. The error is estimated from the minimum and maximum splittings for which some parameter combinations produce a misfit of typically 1.05 times the minimum misfit.

In Figure 3.10 we show examples of the fits of acoustic spectra performed for obtaining rotational splittings for a solid-body rotation of 10 Hz.

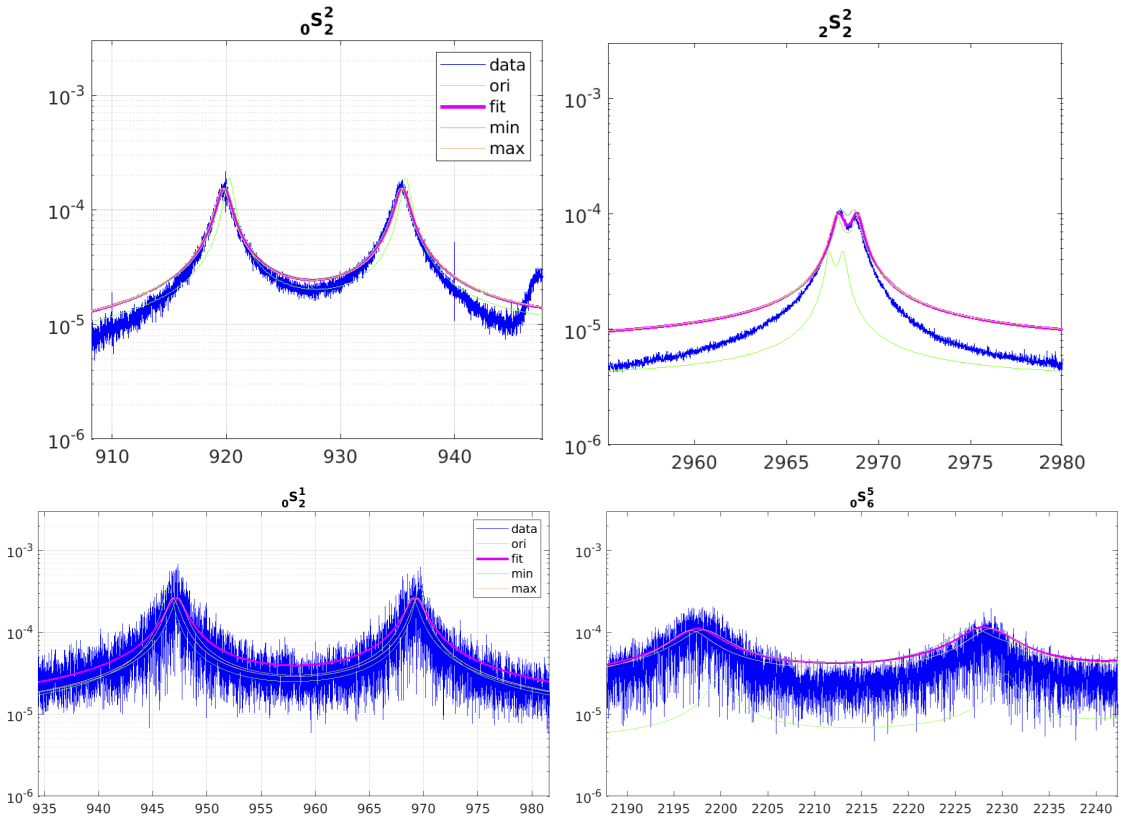

Figure 3.10: Experimental spectra (blue) for a selection of equatorially-symmetric acoustic modes for $f_\Omega = 10$ Hz, and synthetic spectra built with the method described in the main text. The thick magenta line is the best fit provided by the grid search, yielding the rotational splitting. The thin "min" and "max" lines are the spectra yielding the min and max acceptable splitting. The "ori" green spectra is built with the "nominal" parameters, used as a starting point of the grid search.

Note that this fit implicitly imposes that: the two $\pm m$ peaks are supposed symmetric/identical, no filtering is required (all signal is taken as part of the Lorentzian), and the Lorentzian function implies that the modes are independent and the window frequency is narrow. This method is useful for known flows allowing us to compute the theoretical synthetic spectra. If the measured splitting deviates greatly from the synthetic spectrum (eg unknown flow far from the assumption), the initial guess is manually created by hand-picking the peak maxima and creating a new ad hoc synthetic spectrum with two Lorentzian function (half-width is kept the same).

Non-linear fit using local maxima

We developed a second complementary mode extraction routine. This time the peak form is taken as the general solution of a damped harmonic oscillator, as done by Mehl (1978), (note that close to f_0, this expression is equivalent to the previously introduced Lorentzian function)

$$x(f) = \frac{(a_1 + \mathrm{i}a_2)f}{2g_{nl}f_0 + \mathrm{i}(f^2 + g_{nl}^2 - f_0^2)}. \tag{3.12}$$

Its real part, corresponding to signal amplitude, is then

$$A_0 = |x(f)| = \frac{\sqrt{a_1^2 + a_2^2}\, f}{\sqrt{(f^2 - f_0^2 + g_{nl}^2)^2 + 4g_{nl}^2 f_0^2}}, \tag{3.13}$$

with f_0 the frequency of the peak maximum, g_{nl} the attenuation, a_1, a_2 amplitude parameters.

We fit the data with a sum of two independent functions, and add a complex linear background as $b_1 + \mathrm{i}b_2 + (c_1 + \mathrm{i}c_2)f$, with b_1, b_2, c_1, c_2 parameters to account for the background noise. So instead of the 4 parameters from the previous fit, we now have to find 12 unknowns (we need to fit 2 Lorentzians, one for each mode, the background parameters are assumed the same for both). To find them, we use the Python scipy.optimize.curve_fit function. It consists of a non-linear least-square fit based on the MINPACK Fortran library (Cowell, 1984). We choose to use the Trust Region Reflective algorithm method (Byrd et al., 1988).

This time the initial guess is taken as the local maxima, found by a simple threshold condition (blue circles). Again, this method is semi-manual in the sense that when the data are noisy, initial guesses are given by hand. In Figure 3.11 we show examples of this fit for same modes and same data as Figure 3.10. We consider that the fit fails if the covariance is more than 1 Hz, which corresponds to a reasonable error in the peak detection, in which case we take the local maxima as initial guess.

Note that this time the spectrum is fitted in linear scale (log scale in the first fit procedure), the noise is accounted for with separated parameters allowing constant noise and linear noise evolution with frequency, the fit being non-linear it is very sensitive to the initial guess. We do not impose symmetry between the two $\pm m$ modes anymore.

Data analysis steps:

1. sum/difference of temporal signal to separate symmetric and anti-symmetric modes,
2. Fourier transform of each part of the signal to obtain acoustic spectra,
3. apply homothetic transformation to match a chosen reference mode frequency in all spectra (by default the reference is ${}_2\mathcal{S}_0^0$),
4. identify modes with symmetry and comparison with synthetics,
5. define frequency ranges for each doublet ${}_n\mathcal{S}_l^{\pm m}$ of interest,
6. apply either of the fits on the small frequency windows to extract the splitting.

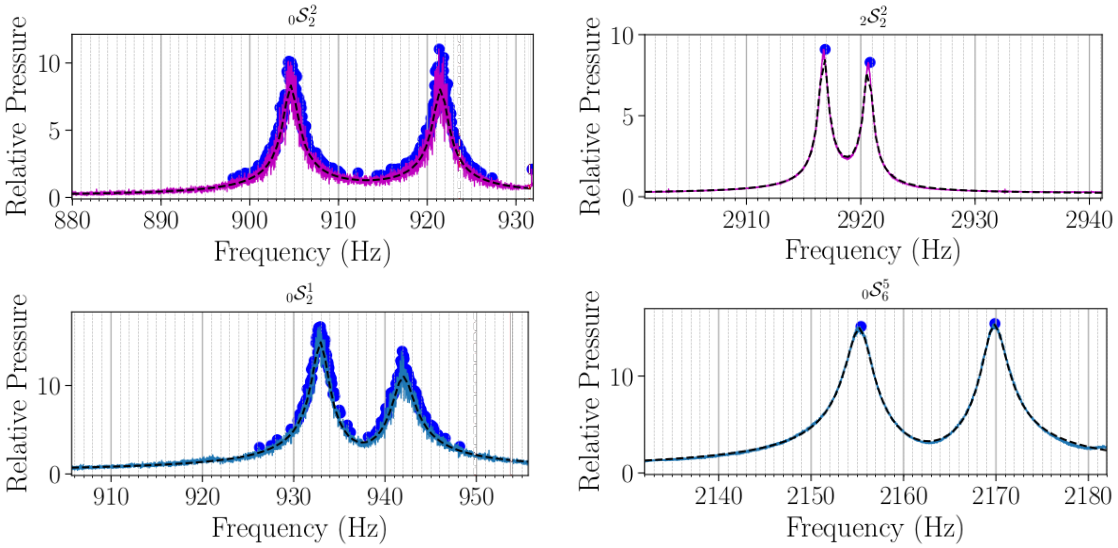

Figure 3.11: Example of non-linear fit procedure for a non-trivial internal flow (centrifugal flow driven by open holes at $f_\Omega = 10$ Hz, see Chapter 5 for more details on this flow). Experimental data in colour lines (purple for symmetric modes, blue for anti-symmetric modes), non-linear fit in dashed black lines, circles gives the local maximum detection. When the signal is noisy, local maximum detection is not helpful anymore.

3.3 Application to solid-body rotation

We consider the case of solid-body rotation (no flows) and apply the procedures we developed to treat the data, compute the spectra and extract splittings. To obtain these flows, we impose a constant rotation rate to the container and we wait for 2 minutes, a long time compared to the spin-up time (~ 5 s at 10 Hz), such that the fluid is uniformly rotating with the container (Greenspan, 1968). Then, the fluid is at rest in the frame rotating with the container. For more details on the spin-up flows see §4.3.1.

Using the protocol developed above to acquire and identify acoustic modes at rest, we measure the acoustic response in presence of rotation. The top panel of Figure 3.12 shows typical splittings due to solid-body rotations for the $_0\mathcal{S}_2$ multiplet. Focusing first on the original peak (i.e. with no rotation) around 910 Hz, we observe that it splits into two peaks about half-height on both sides of the original peak. We note that the splitting increases with the rotation rate.

For certain resonances, we remark that the spectrum can display less peaks than predicted by the perturbation theory, the degeneracy should be completely lifted, yielding $2l + 1$ peaks. When the frequencies of peaks are too close, this may lead to an apparent single peak (accidental degeneracy), as shown near 930 Hz at the rotation rate 20 Hz (Figure 3.12, top, blue curve). This is confirmed by the fact that when modes are degenerated in frequency (accidentally or from geometrical symmetry), their amplitudes are summed up. The blue peak around 930 Hz is indeed higher than expected (from continuity from previous and following rotation rates). This is also visible near 910 Hz where the modes

are degenerated at rest (Figure 3.12 top, red curve), and the peak's amplitude is halved when the modes are separated by rotation (Figure 3.12 top, orange curve). Symmetry separation is also useful to confirm each mode identification after rotation is added. We use the symmetry method detailed above to separate odd and even m modes. In the bottom panel of Figure 3.12 we separate the ${}_0\mathcal{S}_2$ multiplet by symmetry at $f_\Omega = 25$ Hz. The vertical lines show the frequencies given by the perturbative approach taking into account the first-order rotation effects. This allows to identify the mode ${}_0\mathcal{S}_2^{-2}$ at 930 Hz and the mode ${}_0\mathcal{S}_2^{+1}$ at 926 Hz, and shows that a large rotation rate can cause a frequency switch as seen for these two modes.This lifts the ambiguity that could have arisen from a naive reading of the bottom purple curve ($f_\Omega = 25$ Hz) in the top panel. This enforces the need to have robust mode identification technique in order to retrieve accurate splitting measurement. We can also identify the $m = 0$ mode around 940 Hz by the fact that it is the only mode not influenced by rotation at first-order, as shown by eq. (2.69).

For a given ${}_n\mathcal{S}_l^m$ mode, perturbation theory predicts a linear increase of the rotational splitting with the rotation rate. To verify this prediction and its validity domain, we extract splittings for a collection of non-axisymmetric eigenmodes over our range of working rotation rates (from rest to 30 Hz).

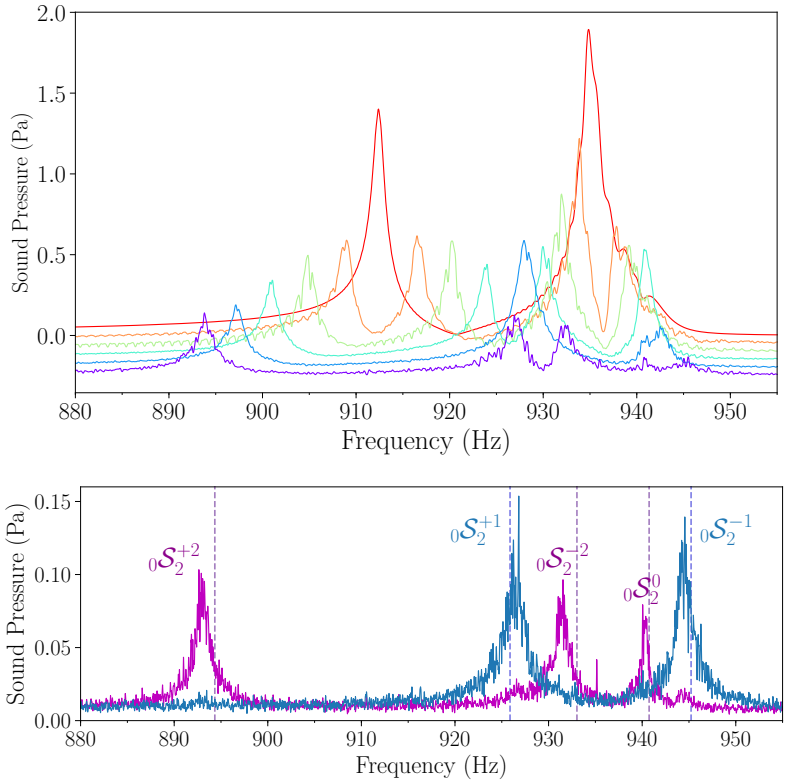

Figure 3.12: Experimental spectra centred on ${}_0\mathcal{S}_2$. Top: for solid body rotation at increasing rotation rates from rest (top, red) to $f_\Omega = 25$ Hz (bottom, violet) with 5 Hz increment. Spectra are filtered (low-pass) and vertically shifted for visualisation purposes. Bottom: for solid body rotation at $f_\Omega = 25$ Hz separated by symmetry, $m = \pm 1$ (blue, subtracted) and $m = 0, \pm 2$ (purple, summed). The dashed lines shows the perturbation theory predictions.

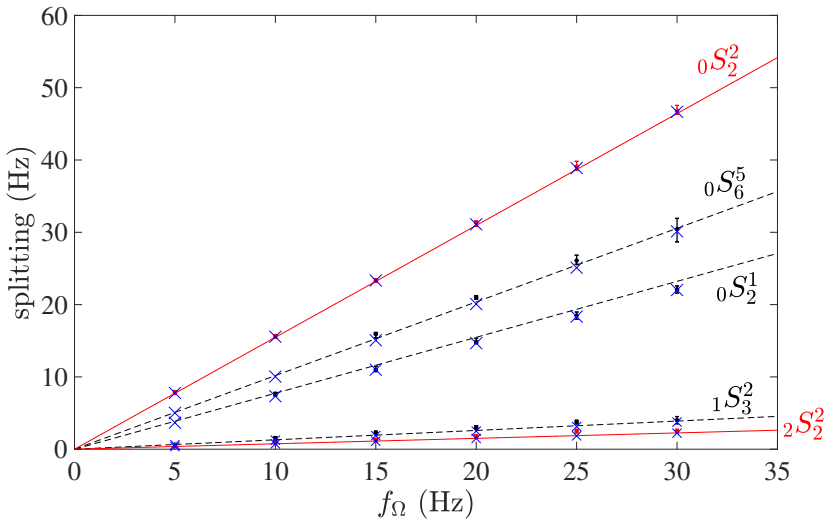

Figure 3.13: Rotational splittings of chosen modes for increasing rotation rates. Experimental (circles) and finite element (blue crosses) splittings are measured by the difference between the $\pm m$ peak frequencies. Theoretical linear splittings (lines) are given by $|2\delta_\Omega|$, see equation (2.69). For theoretical splittings, equatorially symmetric modes are shown in red solid lines and anti-symmetric modes in black dashed line; we use the same choice of colours for the experimental splittings.

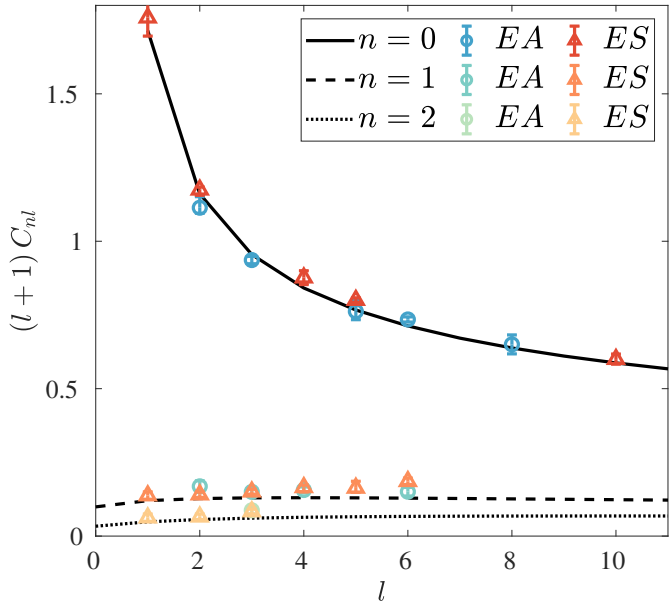

Figure 3.14: Comparison between the theoretical Ledoux coefficients multiplied by $l+1$ (connected by lines for $n = 0, 1, 2$) and their experimental counterparts deduced from the mode splitting measured in ZoRo (rotating at 20 Hz) for several l-modes of various m, being either symmetric (ES, hot-coloured triangles) or anti-symmetric (EA, cold-coloured circles) with respect to the equator (colour online). When possible, several $\pm m$ pairs are included for one ${}_n\mathcal{S}_l$ multiplet.

In Figure 3.13, we show a selection of experimental splittings as a function of rotation rate (the experimental splittings being measured by the difference between the $\pm m$ peak frequencies). At first glance, we observe that they agree well with the theoretical linear predictions $|2\delta_\Omega|$ given by equation (2.69) and shown by the lines. The blue crosses show our finite-element calculations predictions which are, in many cases, closer to the experimental data than the theory (see e.g. ${}_0\mathcal{S}_2^2$ or ${}_0\mathcal{S}_2^1$). In our range of rotation rates, the numerical splittings also follow a linear trend with a different slope due to the effect of ellipticity (Vidal et al., 2020). The different slope defines a spheroidal Ledoux coefficient, which now depends on m by contrast with the spherical one (which is independent of m, see eq. (2.70)).

In our range of rotation rates, rotational splittings in the sphere are predicted to be proportional to f_Ω, but also to m through the spherical Ledoux coefficients. By successively focusing on various non-axisymmetric multiplets, we retrieve the rotational splittings for a larger collection than before. We have extracted rotational splittings for 24 modes at $f_\Omega = 20$ Hz with the method detailed above and computed the associated spheroidal Ledoux coefficients (frequency splitting divided by $2mf_\Omega$). Figure 3.14 shows these Ledoux coefficients for different $\pm m$ pairs of peaks as a function of l. For each mode, the experimental Ledoux coefficients (symbols) agree roughly with the linear theory (lines) and the deviations can be explained by the ellipticity of the container (see $l = 2$, $n = 0$ in Figure 3.13 and 3.14). Conversely, the determination of the rotation rate can be obtained by measuring any splitting if the spheroidal Ledoux coefficient is known.

We also verify that the ${}_n\mathcal{S}_l^m$ modes are still separated even with high rotation rates, to validate a posteriori that the chosen flattening of our apparatus is suitable for rotational flows measurements.

Key points

Experimental set-up ZoRo:

- Axisymmetric spheroid of 0.05 ellipticity,
- Filled with air,
- Rotates on its revolution axis up to 30 Hz,
- Instrumented with embarked speakers and electrets.

Data analysis:

- Fourier transform for acoustic spectrum,
- Identify peaks with ${}_n\mathcal{S}_l^m$ doublet or modes,
- Extract splittings between ${}_n\mathcal{S}_l^{\pm m}$ modes in presence of rotation and flows.

4

Acoustic splitting inversion of known flows

Reannuals are plants that grow backwards in time. You sow the seed this year and they grow last year. [...] anyone who forgets to sow seeds of a crop that has already been harvested twelve months before risks disturbing the entire fabric of causality, not to mention acute embarrassment.

- Terry Pratchett, *Mort*

We described in Chapter 2 the analytical relationship between the flow field in a spheroidal cavity and its acoustic resonances. Thanks to this, we are able to predict the spectral acoustic response from any flow field. We aim to take advantage of this relation to do the reverse and use the acoustic spectrum to obtain information on the flow velocity. To do this we need to solve an inverse problem.

In our case the direct problem is to find the acoustic splittings knowing the flow field, and the inverse problem consists in finding the flow knowing the splittings. In this chapter we will present how to tackle our inverse problem, detail the procedure we use and apply it to various synthetic cases.

We use the linear Bayesian formalism to express the inverse problem and find the best matching flow field for a given dataset of acoustic splittings. Then we validate the inversion method using synthetic cases, where we try to retrieve known flows. We apply the inversion procedure on analytical velocity profiles for spins up. We then move onto more complicated azimuthal profiles from numerical simulations of realistic thermally driven zonal flows.

Finally we developed a working inversion implementation for our problem. Along the way we implemented objective criteria to determine if an inversion is accurate. Study of synthetic cases allowed us to confirm that the flows we aim to study are within the resolution of our modal acoustic velocimetry method. We also verified that the mode collections we are able to extract from experimental data are sufficient to accurately retrieve the flow field.

At the end of this chapter we have all the necessary tools to move on to the inversion of acoustic splittings obtained from real experimental data.

4.1 General inversion theory

The inverse problem allows to retrieve a physical quantity that we are not able to directly measure through other accessible data. In order to solve the inverse problem, it is essential to have the relationship between the two quantities at play, in our case flow velocity and acoustic splittings. We will focus on linear inversions as eq. (2.61) gives a linear relation between the measured data and the model. We recall their relationship from eq. (2.61) as

$$\underbrace{\delta\omega_{nlm}}_{\boldsymbol{\Delta}} = \underbrace{m \int_0^{\pi} \int_0^{a} K_{nlm}(r,\theta)\, \overbrace{\Omega(r,\theta)}^{\mathfrak{m}}\, r \mathrm{d}r \mathrm{d}\theta}_{G},$$

We used this formulation to predict the acoustic splitting for a given flow, which is called the forward (or direct) problem. In symbolic formulation we can write the forward linear problem as

$$\boldsymbol{\Delta} = \boldsymbol{G}\boldsymbol{\mathfrak{m}}, \tag{4.1}$$

with $\boldsymbol{\Delta}$ the data vector, $\boldsymbol{\mathfrak{m}}$ the model vector and $\boldsymbol{G}$ the matrix which gives the theoretical relationship between the two. In our case the data are the acoustic splittings, the model is the flow velocity and $\boldsymbol{G}$ contains the sensitivity kernel integration. Note that in our case $\boldsymbol{\mathfrak{m}}$ encompasses the flow velocity at each wanted spatial position.

In practice, for a collection of M modes and a spatial discretized grid for (r,θ) of size $p \times q$, $\boldsymbol{\Delta}$ is a vector of length M and contains the acoustic splitting for each mode, $\boldsymbol{\mathfrak{m}}$ is a vector of length pq and contains the flow velocity on each grid point and $\boldsymbol{G}$ is a (non-square) matrix of size $M \times pq$. In order to be able to retrieve small flow structure, we want a relatively fine spatial grid. This causes $M \ll pq$ and our problem is largely under-determined. Then eq. (4.1) can equivalently be written as:

$$\begin{bmatrix} \Delta_1 \\ \vdots \\ \Delta_M \end{bmatrix} = \begin{bmatrix} G_{11} & \cdots & G_{pq1} \\ \vdots & \ddots & \vdots \\ G_{1M} & \cdots & G_{pqM} \end{bmatrix} \cdot \begin{bmatrix} \mathfrak{m}_1 \\ \vdots \\ \vdots \\ \mathfrak{m}_{pq} \end{bmatrix}. \tag{4.2}$$

Since the accessible measure, the acoustic splittings, is not the physical quantity of interest, the measurement method is *indirect*. Retrieving the fluid velocity is equivalent to solving the inverse problem

$$\boldsymbol{\mathfrak{m}} = \boldsymbol{G}^{-1}\boldsymbol{\Delta}. \tag{4.3}$$

However $\boldsymbol{G}$ is generally not invertible (often not square). To circumvent this difficulty many inversion methods have been developed (e.g. Bertero, 1986; Golub et al., 1999; Menke and Eilon, 2015). Here we choose to use the Bayesian inversion.

4.1.1 Bayesian formalism for Gaussian linear model

The Bayesian inversion was first developed by Tarantola and Valette (1982a,b). It takes a probabilistic approach and aims to find the most likely solution along with its probability density. It considers that a priori the solutions follow a homogeneous probability density and by adding more information with additional data, some become more likely than others (Tarantola, 1987). Since the information added are measured data of actual realisations,

it comes down to a conditional probability which is given by the Bayesian inference (Bayes and Price, 1763), hence the inversion's name. The method is fully described in Tarantola (1987), we will only remind here the useful formulas for our specific case.

We assume that both the data and the model contain errors that obey a Gaussian distribution. The measurement errors on the data can be expressed with the covariance matrix of the data $\boldsymbol{C}_{dd}$, and the a priori information on the model with the covariance matrix of model parameter $\boldsymbol{C}_{pp}$.

In this case, the best fitting model in the least-square sense $\hat{\mathbf{m}}$, is given by (Tarantola, 1987, eq. (1.106))

$$\hat{\mathbf{m}} = \boldsymbol{C}_{pp}\boldsymbol{G}^T(\boldsymbol{C}_{dd} + \boldsymbol{G}\boldsymbol{C}_{pp}\boldsymbol{G}^T)^{-1}\boldsymbol{\Delta}, \tag{4.4}$$

where $\cdot^T$ indicates the transposed matrix. The accuracy of the inversion can be estimated by looking at the difference between the real and inverted model, rendered by the resolution matrix $\boldsymbol{R}$ defined to verify $\hat{\mathbf{m}} = \boldsymbol{R}\mathbf{m}$, leading to (Tarantola, 1987, eq. (3.62))

$$\boldsymbol{R} = \boldsymbol{C}_{pp}\boldsymbol{G}^T(\boldsymbol{C}_{dd} + \boldsymbol{G}\boldsymbol{C}_{pp}\boldsymbol{G}^T)^{-1}\boldsymbol{G}. \tag{4.5}$$

In the ideal case, the inverted model should verify the forward model exactly, corresponding to $\boldsymbol{R} = \boldsymbol{I_d}$ the identity matrix, but in general what is retrieved is a posteriori reconstructed data $\hat{\boldsymbol{\Delta}} = \boldsymbol{G}\boldsymbol{R}\mathbf{m}$.

We use the difference between the measured data $\boldsymbol{\Delta}$ and the reconstructed data $\hat{\boldsymbol{\Delta}}$ to define the inversion misfit $\hat{\phi}$

$$\hat{\phi} = \sqrt{\frac{1}{M}\sum_{i=1}^{M}\left(\frac{\hat{\boldsymbol{\Delta}}_{\boldsymbol{i}} - \boldsymbol{\Delta}_{\boldsymbol{i}}}{e_i}\right)^2}. \tag{4.6}$$

A necessary condition for an accurate inversion is to have a misfit less than 1, meaning that in average, the reconstructed data are within the error of the measured data. This condition is sometimes not sufficient, as it would allow some modes to be very far from the measured value provided other modes are close enough to compensate that deviation.

A complementary indicator of the inversion accuracy is to count the number of data mode that are within the error of the measurements, we define this normalised number as

$$\hat{N} = \frac{\mathrm{N}\left(|\boldsymbol{\Delta}_{\boldsymbol{i}} - \hat{\boldsymbol{\Delta}}_{\boldsymbol{i}}| < e_i\right)_{i=1\ldots M}}{M}, \tag{4.7}$$

where $\mathrm{N}(X)$ counts the number of occurrences where the condition X is verified. This condition allows us to define a threshold of the number of splittings that are correctly retrieved after the inversion under which we will not consider the inversion accurate anymore. Typically we want at least $\hat{N} > 0.5$, i. e. more than half of the data can be retrieved (within their error bar) after the inversion.

4.1.2 Computation formulation

The effects of global solid-body rotation is well understood and we verified in §3.3 that they can be predicted at first-order with the theoretical spherical Ledoux coefficients. This allows us to focus on the remaining flows by performing the inversion in the frame rotating with the container. Then eq. (2.61) becomes

$$\delta f_{nlm}^{\mathrm{rot}} = \underbrace{-\,m \int_0^{\pi}\int_0^{a} K_{nlm}(r,\theta)\overbrace{\Omega^{\mathrm{rot}}(r,\theta)}^{\mathbf{m}} r\mathrm{d}r\mathrm{d}\theta}_{G}. \tag{4.8}$$

This also implies that all inversions will be considered in the spherical geometry. Although the spheroidal shape is taken into account in order to predict the acoustic frequencies (needed to accurately extract the splittings), it has no influence on the $\pm m$ modes splittings (at first order in rotation and at our current attainable rotation rates ≤ 30 Hz).

Projection onto spherical harmonics

We have an under-determined problem. In order to reduce the unknowns we want to retrieve, following Triana et al. (2014), we remark that, in the spherical geometry, the spherical harmonics form a natural basis for the angular dependence of the velocity field. Provided the velocity field is axisymmetric and symmetric with respect to the equator, the azimuthal velocity can then be written as (Nataf, 2013)

$$u_\phi(r,\theta) = \sum_{odd\ l''=1}^{l_{max}} u_{l''}(r)\mathcal{P}^1_{l''}(\cos\theta). \tag{4.9}$$

The rotational sensitivity kernel K_{nlm} can similarly be decomposed, as seen in eq. (2.62), into

$$K_{nlm}(r,\theta) = \sum_{odd\ l'=1}^{2l+1} K_{l'}(r)\mathcal{P}^1_{l'}(\cos\theta), \tag{4.10}$$

where $K_{l'}$, the reduced sensitivity kernel, depends on r only.

Then injecting both expressions into eq. (2.61), it becomes

$$\delta f_{nlm} = m\int_0^{a}\int_0^{\pi} \sum_{odd\ l'=1}^{2l+1}\sum_{odd\ l''=1}^{l''_{max}} K_{l'}(r)U_{l''}(r)\mathcal{P}^1_{l'}(\cos\theta)\mathcal{P}^1_{l''}(\cos\theta)\frac{\mathrm{d}r\mathrm{d}\theta}{\sin\theta}. \tag{4.11}$$

Taking advantage of the orthogonality and normalisation of the spherical harmonics, it simplifies into

$$\delta f_{nlm} = m\sum_{odd\ l'=1}^{2l+1}\sum_{odd\ l''=1}^{l''_{max}} \tilde{l}(\tilde{l}+1)\int_0^{a} K_{l'}(r)u_{l''}(r)\mathrm{d}r, \tag{4.12}$$

where $\tilde{l} = \min(l', l'')$ and l_{max} is the truncation degree of the velocity projection.

This expression allows the inversion to focus on the radial dependence while the angular θ dependence is entirely accounted for by the Legendre polynomials. The new numbers of unknown is then pl_{max} (instead of pq), where l_{max} is typically smaller than 10.

Cylindrical projection of sensitivity kernels

In rotating fluids, the geostrophic (or quasi-geostrophic) balance can rule the global structure of the flow by imposing invariance along the rotation axis (vertical axis in our case) (Vallis, 2017). In such cases it is useful to rewrite the rotation sensitivity kernels in cylindrical coordinates and take advantage of this invariance to reduce the number of unknowns once again. We change our variables from (r, θ) to (s, z) with the relations

$$\begin{cases} s = r\sin\theta, \\ z = r\cos\theta, \end{cases} \quad \text{or} \quad \begin{cases} \theta = \arctan(s/z), \\ r = \sqrt{s^2 + z^2}. \end{cases} \tag{4.13}$$

Our relation then becomes for geostrophic flows

$$\delta f_{nlm} = m \int_{s=0}^{a} \int_{z=-h(s)}^{h(s)} K_{nlm}(s,z)\Omega(s,z)\mathrm{d}s\mathrm{d}z = m \int_{s=0}^{a} \Omega(s) \left(\int_{z=-h(s)}^{h(s)} K_{nlm}(s,z)\mathrm{d}z \right) \mathrm{d}s, \tag{4.14}$$

with $h(s) = \sqrt{a^2 - s^2}$ the half-column height. We can now define a new radial sensitivity kernel, projected onto the cylindrical radius

$$N_{nlm}(s) = 2 \int_{z=0}^{h(s)} K_{nlm}(s,z)\,\mathrm{d}z, \tag{4.15}$$

and eq. (2.61) now depends on one dimension only, once again reducing the number of unknowns in the inversion. Note that both the cavity and the sensitivity kernels are symmetric with respect to the equator, allowing N_{nlm} to be determined on the half-column only (more cost-efficient). In Figure 4.1 we show examples of these radial kernels along with the corresponding K_{nlm}.

In the following, the flows we consider are all supposed geostrophic, at least at first-order, allowing us to use the cylindrical projection.

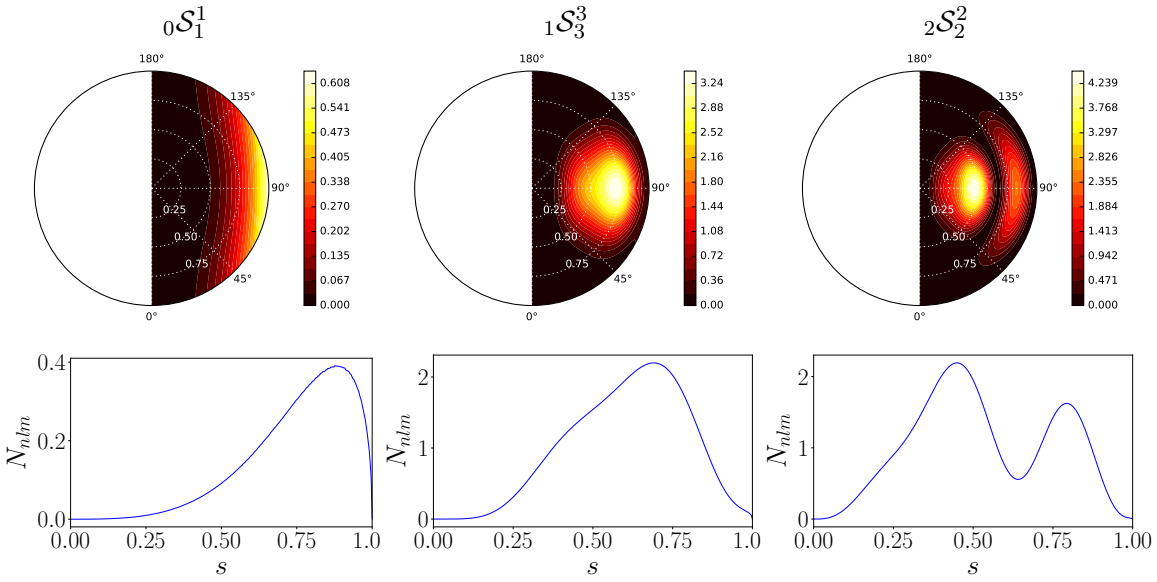

Figure 4.1: Sensitivity kernels in spherical coordinates as defined in eq. (2.62) (top) and $N_{nlm}(s)$ (bottom) for $_0\mathcal{S}_1^1$, $_1\mathcal{S}_3^3$ and $_2\mathcal{S}_2^2$. Note that they are both plotted against adimensional radius.

Covariance matrices

In the data covariance matrix, we include all the errors on the splitting determination e_i, possibly different for each mode. Those errors are assumed to be independent for each acoustic mode, thus uncorrelated and leading to a diagonal matrix

$$\boldsymbol{C}_{dd}(i,j) = e_i^2 \ \delta_{ij}, \tag{4.16}$$

where δ_{ij} stands for the Kroenecker symbol.

The model covariance matrix encompasses all a priori information on the model, which can also be interpreted as imposed constraints. We implemented a smoothing constraint which imposes a relaxation length on the spatial grid as (Triana et al., 2014)

$$C_{pp}(i,j) = \sigma_p^2 \ \exp\left(-\frac{|r_i - r_j|^2}{\delta^2}\right), \tag{4.17}$$

where δ is the radial correlation length and σ_p is a measure of the model allowed amplitude variations.

Our inversion then has two adjustable parameters: σ_p, which gives the amplitude freedom of the model; and δ, the radial correlation length. In order to determine the best fitting parameters for our specific inversion, we look at the difference between the data and reconstructed splittings. We consider that an inversion is accurate if the misfit $\hat{\phi}$ is smaller than 1. Among those, we want the inversions that fit a majority of the data, so $\hat{N}$ should be at least 0.5, preferably much larger. Then we want to have a reasonably well constrained inverse model, so we define as suitable inversion parameters the (σ_p, δ) pairs that verifies $\hat{\phi} < 1$ and $\hat{N} >> 0.5$, and whose inverted flow seems plausible (no oscillations at small length-scale). In practice we progressively decrease the acceptable threshold of $\hat{N}$ from 0.95 until we find a suitable pair of parameters or reach 0.5, value where the inversion is not considered accurate anymore.

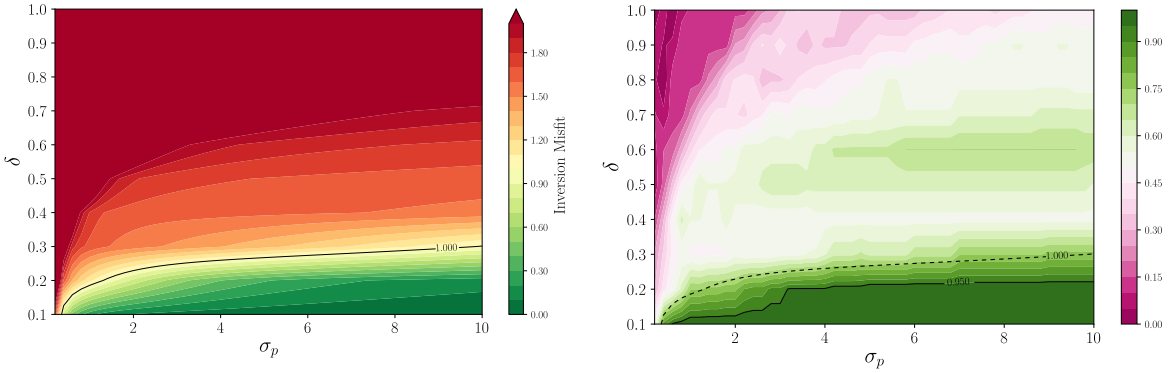

Figure 4.2: Illustrative case of quantitative parameters measuring the inversion accuracy (example given on the flow from Chapter 5). Left: Splitting misfit $\hat{\phi}$ between model and inverted splittings (in Hz) for different parameters σ_p and δ. Right: Normalised number of inverted splittings $\hat{N}$ within error bars of the data. The inversion is considered accurate for $\hat{\phi} < 1$ and normalised number of splittings $\hat{N} > 0.95$.

A typical misfit map for a scan of values for σ_p and δ is shown in Figure 4.2 (performed for a synthetic case of centrifugal open holes flow, described in Chapter 5, using a typical realistic mode collection presented in Figure 4.8). The misfit distribution corresponds to the intuitive understanding of the two inversion parameters, if the model is too constrained (with small σ_p or large δ), it cannot fit the data, hence the large misfit. Both parameters σ_p and δ can constrain the inversion either by imposing the solution to be close to the prior with small σ_p, or by imposing radial correlation with large δ.

In practice, δ can be quite small. This brings out the fact that our theory relation is smoothing the model, which is expected as we measure global modes. The sensitivity kernels are inherently correlating spatial regions with each other, as seen in Figure 4.1, so the addition of a correlation parameter is not essential.

For real data acquired in ZoRo, it is sometimes needed to engage in an iterative process between the inversion parameters and the splitting extraction. We remarked that the data that are not well fitted for any pair of parameters, are often the modes for which splitting extraction was difficult in the data analysis. This allows us to improve the splitting extraction (usually hand-picking the peaks) or remove the mode completely in order to avoid adding inaccurate information in the inversion. We then scan over the parameters again, etc.

4.2 Influence of mode collection

We first study some simple cases to have a better idea of the inversion biases. More particularly, we investigate the influence of the collection of modes used, since the number of modes available in the experiment is limited by whether we are able to correctly perform their identification. We choose to do this collection test on solid-body rotation flow, where the fluid rotates at a constant rotation rate Ω different from the observational referential frame rotation rate Ω^{ref}. The splittings are the flow splittings, corresponding to a solid-body rotation of 5 Hz (in the rotating referential). Starting from this solid-body rotation flow, we create the corresponding acoustic splittings using the forward model, described in eq. (2.61). We then try to retrieve the flow model with different mode collections. All inversions are done with the same spatial grid and an arbitrary error on the data $e_i = 0.1$, identical for all data. For each collection, we take the best inversion parameters σ_p and δ as described above.

4.2.1 All modes up to $n = 3$, $l = 10$

We first choose to perform the inversion using all modes up to $n = 3$ and $l = 10$, which corresponds to the ideal collection within the frequency range of our experiment (220 modes). This test serves to check which flow structures we will be able to resolve at best. We attributed the same arbitrary error to all the synthetic data of 0.1 Hz. For this collection, the best parameter pair is $\sigma_p = 3.2$ and $\delta = 0.1$.

In Figure 4.3 we plot the s-profile of the angular velocity found with this inversion (in solid blue line), along with the exact solution we used to produce the splittings (in dashed red). We remark first that for intermediate radii, between $s = 0.3$ and 0.9, the inverted velocity profile is very close to the model (in dimensionless cylindrical radius, with $s = 0$ the rotation axis and $s = 1$ the shell boundary). In the area close to the rotation axis (small s) the inverted solution overshoots the expected value then drops to zero, while the expected velocity is constant across the cavity, and same at lesser degree near the shell.

To understand this behaviour, it is useful to recall that in our case the prior model is taken as zero. When no information are available from the data the inversion will tend to this prior model. In our case the spatial extent of the data information is given by the radial sensitivity kernels N_{nlm} (as defined in eq. (4.15)). For this mode collection an averaged sensitivity kernel $\langle N_{nlm} \rangle$ is given for comparison in orange line in Figure 4.3. This is consistent with the intuitive understanding that no acoustic mode within our collection contains information on the central region below $s = 0.1$ where the sensitivity stays very low until $s = 0.3$, and same above $s = 0.95$.

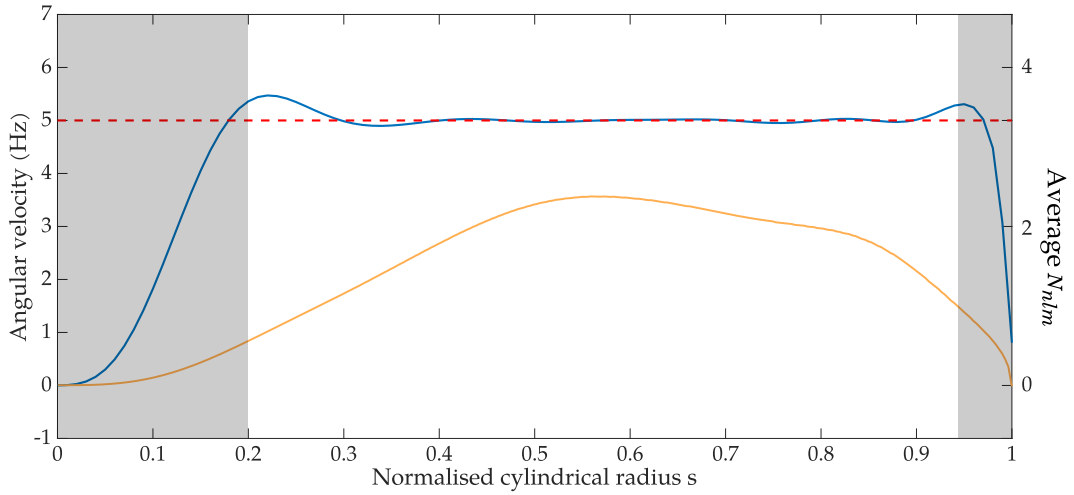

Figure 4.3: Rotation rate of the fluid for solid-body rotation (of the fluid) at $\Omega = 5$ Hz against adimensioned cylindrical radius. In solid blue, the results from inversion with all modes up to $n = 3$, $l = 10$. The model we want to retrieve is reminded in dashed red. For comparison the radial sensitivity kernel averaged over the mode collection $\langle N_{nlm} \rangle$ is added in solid orange.

Another approach to quantify the inversion trust regions is to consider the resolution kernel $\boldsymbol{R}$, defined in eq. (4.5). As described above, in the ideal case, $\boldsymbol{R}$ should be a Dirac centred on the target position. This can also be useful to infer the inversion spatial resolution. We show in Figure 4.4, the resolution kernel for different target radii. We can see that for radius $s \geq 0.2$, the kernel is centred at the target radius, although the peak is smoothed compared to the wanted Dirac function, with a half-width of about 0.15. For $s < 0.2$ the resolution kernel is not centered on the target anymore, which means that the inversion is not able to accurately retrieve the flow at those positions. This indicates that our inversion is inaccurate near the center (for s below $a/5$), so any flow inversion below this radius should not be taken as realistic.

It is interesting to note that this resolution quantification shows that the inversion is accurate down to $s = 0.2$, which is closer to the center than what the velocity profile suggests. This defines the regions where the inversion is not able to accurately predict the velocity, we indicate them in grey in Figure 4.3. The resolution kernel maximum also significantly drops when the targets are located near the center, showing that the inversion is also less sensitive in these regions, which is consistent with the observed behaviour of the mean sensitivity $\langle N_{nlm} \rangle$.

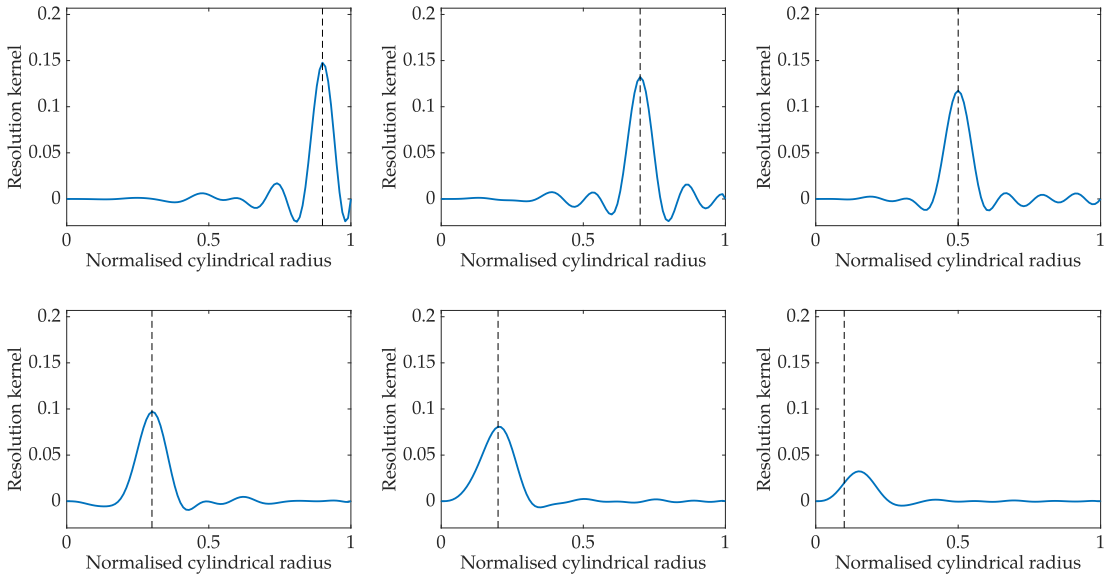

Figure 4.4: Resolution kernels $\boldsymbol{R}$ for target radius at $s = 0.9$, 0.7, 0.5, 0.3, 0.2 and 0.1 (dashed lines) in dimensionless cylindrical radius for solid-body rotation of the fluid of 5 Hz inverted using a all modes up to $n = 3$, $l = 10$. For $s < 0.2$ the inversion is not able to retrieve the target anymore.

From the resolution peaks half-width, we can deduce the apparent spatial resolution of the inversion. We are not able to describe structures smaller than this length, so for this given collection and set of parameters, we have a spatial resolution of $0.15\,a \approx 3$ cm with ZoRo's radius. The resolution kernels peak's half-width can be compared with the correlation length given by the δ parameter. As δ tends to smooth the model, the spatial resolution given by the mode collection is optimum if it is larger than δ. Here we have $0.15 > 0.1 = \delta$.

As a final verification, we apply the forward model on the inverted velocity profile, and compare the splittings we obtain to the ones we used to do the inversion. We show in Figure 4.5 the initial predictions in black and the splittings from the inverted model in red. All splittings obtained after the inversion match the initial ones within the error bar. This confirms that the inversion is free of errors, and the above mentioned features are inherent to our problem.

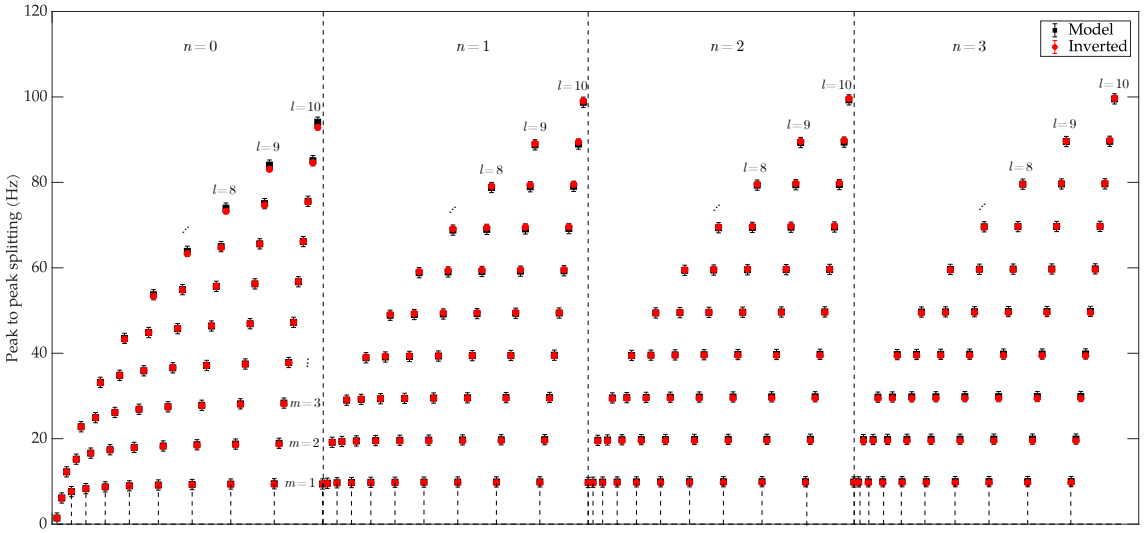

Figure 4.5: Acoustic splittings comparison between the initial splittings used to perform the inversion $\boldsymbol{\Delta_i}$ (in black) with the splittings obtained from the inverted flow $\hat{\boldsymbol{\Delta}}_{\boldsymbol{i}}$ (in red). The selection of modes (n, l, m) used for the inversion is shown on figure. All splittings obtained after the inversion match the initial ones within their error bar. Note that the splittings here are due to the flow only (solid-body rotation splittings predicted with the theoretical spherical Ledoux coefficients have been deducted), small splitting means that the mode is mainly sensitive to solid-body rotation.

4.2.2 Realistic mode collection

The above collection is very optimistic. We do the same exercise with a more realistic collection, comprising only of modes for which we have been able to extract the splittings from real experimental data. We choose here a typical collection of those modes. The collection is given in Figure 4.6, where we verify that we are able to retrieve the data splittings from the inversion result. For this collection, the best parameter pair is $\sigma_p = 7.4$ and $\delta = 0.01$.

The angular velocity resulting from the inversion is given in Figure 4.7. We see that we are still able to retrieve the correct angular velocity, but in a slightly smaller region between $s = 0.4$ and 0.95 (compared to $s = 0.3$ to 0.95). We also remark that this time the velocity profile is not as flat but displays small oscillations around the expected value. The overshoot near the center is also more pronounced and further away (around $s = 0.3$ compared to 0.2 previously).

The corresponding resolution kernels are shown in Figure 4.8, and we see that the spatial resolution is not changed much (from 0.15 to $\approx 0.2\,a$). The inversion with this collection is then considered accurate between 0.3 and 0.95.

This is very encouraging because it shows that the modes we are able to extract in the experimental data are a priori sufficient to image most of the cavity's extent and retrieve flow structures at the centimetre scale, down to ≈ 4 cm. We will now use this realistic mode collection and test it against different realistic flows, that display more complicated spatial structure than solid body rotation.

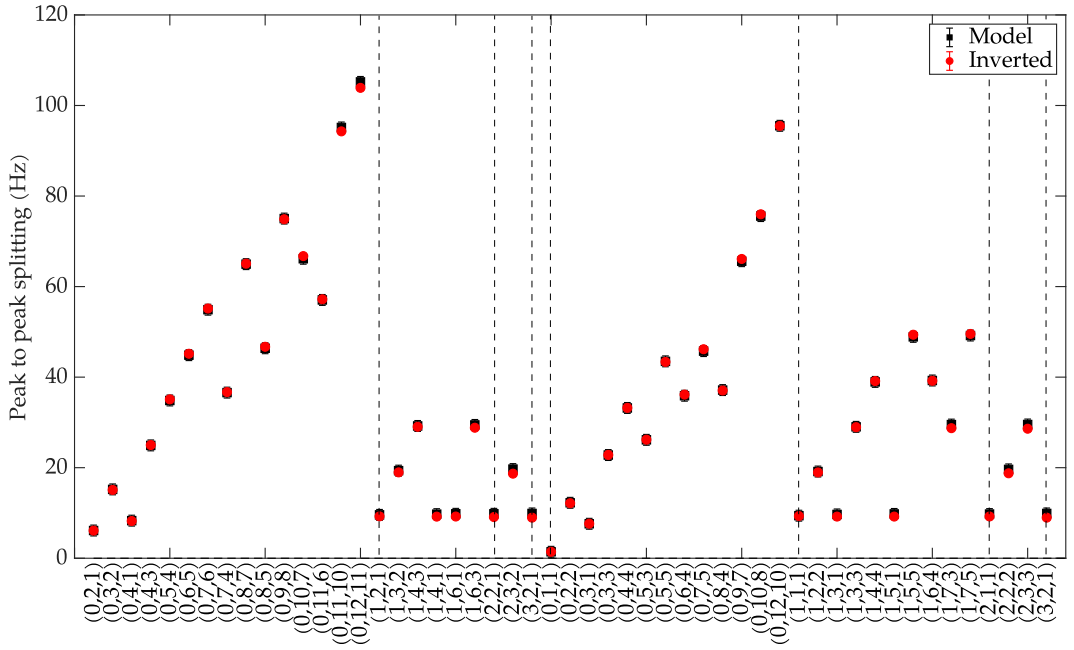

Figure 4.6: Acoustic splitting comparison for solid-body rotation of the fluid of 5 Hz between the (synthetic) data splittings used to perform the inversion (in black) with the splittings obtained from the inverted flow (in red). The realistic collection of modes (n, l, m) used for the inversion is shown in abscissa. All splittings obtained after the inversion match the initial ones within the error bar.

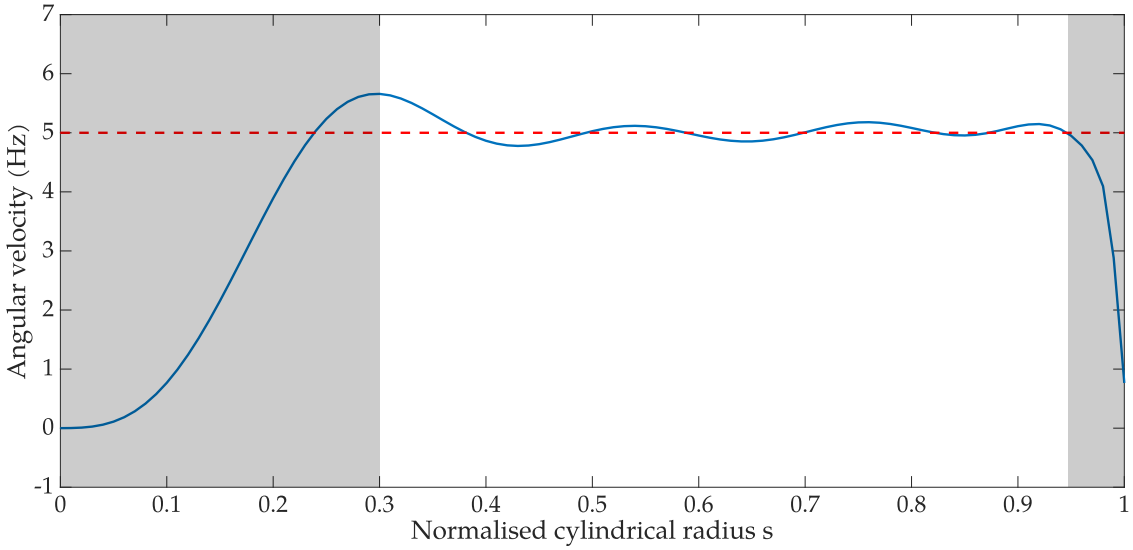

Figure 4.7: Angular velocity in the frame rotating with the container for solid body rotation of the fluid of $\Omega = 5$ Hz against adimensioned cylindrical radius. In solid blue, the results from inversion from a realistic mode collection, given in Figure 4.6. The model we want to retrieve is reminded in dashed red. The inversion seems to retrieve the correct angular velocity between $s = 0.4$ and 0.95 with small oscillations of typical lengthscale of around $0.1a$.

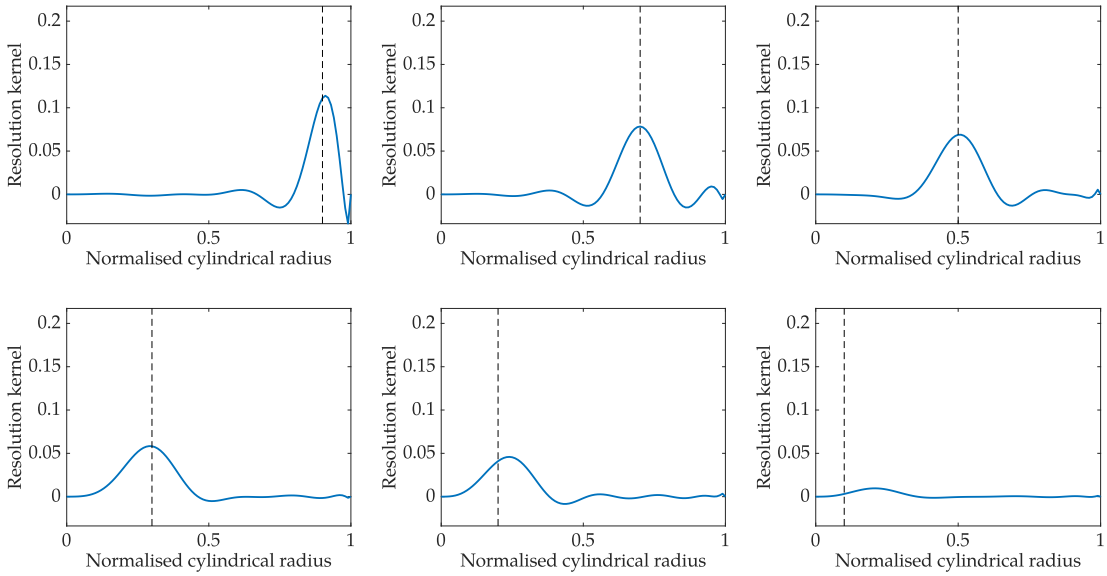

Figure 4.8: Resolution kernels for target radius at $s = 0.9$, 0.7, 0.5, 0.3, 0.2 and 0.1 (dimensionless cylindrical radius) for solid-body rotation of the fluid of 5 Hz inverted using a realistic mode collection. For radius $s < 0.3$ the inversion is not able to retrieve the target anymore.

4.3 Application to synthetic cases

We apply the above formalism to solve our inverse problem for synthetic cases. We use these studies as benchmarks before tackling real data inversion. To do this we choose realistic azimuthal flows relevant for our experiment. We deduce the acoustic splittings from the velocity field and then retrieve the velocity with the inverse problem.

We first focus on spin up, as it is close to solid-body rotation, being mechanically driven, while having a more complex structure. Spin up also has the advantage of having an analytical solution in the sphere which allows us to directly compare our results to known velocity fields. We then try to invert realistic zonal flows driven by thermal convection obtained with numerical simulations. We use the velocity profiles from Guervilly and Cardin (2017).

4.3.1 Spin up flows

We consider small changes in the rotation rate, and study the transient regimes between two rotation rates (Greenspan, 1968). In our case, we will consider a container rotating at a constant rate $\Omega - \Delta\Omega$ filled with fluid at equilibrium, i.e. rotating as solid-body rotation at the rate of the container. And we define the spin up as the instantaneous change of rotation rate of the container of $+\Delta\Omega$. The container then rotates at the new constant rate Ω. The response of the fluid and in particular its recovery up to equilibrium again was first studied by Greenspan and Howard (1963); Greenspan (1964, 1965) and then summarized in his monograph (Greenspan, 1968) and later by Benton and Clark (1974); Duck and Foster (2001).

Analytic solution and splitting prediction (forward model)

The spin up flow can be separated in different time scales, first creation of the Ekman layer in the dimensionless time scale Ω^{-1}, then Ekman pumping in the spin up time $\tau = \Omega^{-1}E^{-1/2}$, during which the all fluid particles passed through the Ekman layers, and finally all residual motions disappear after the diffusion time $\Omega^{-1}E^{-1}$, where the Ekman number $E = \nu/(\Omega a^2)$ is the ratio of viscous forces over Coriolis forces (Greenspan, 1968).

Under the linear approximation $Ro = \Delta\Omega/\Omega \ll 1$, or in practice $Ro < 0.2$ (Benton and Clark, 1974), analytical solutions are available for the spherical geometry. The solutions are developed in Greenspan (1968) section 2.12, and the velocity field (in the frame rotating with the container) is given in Deleplace (2005), eq. (2.35) and gives in their dimensional form

$$v_\phi^{\text{rot}}(r,\theta,t) = -\Delta\Omega \exp\left(\frac{-E^{1/2}t/\tau}{(a^2 - r^2\sin^2\theta)^{3/4}}\right) r\sin\theta, \tag{4.18}$$

or equivalently the fluid angular velocity $\Omega_{\text{flow}}^{\text{rot}}(r,\theta,t)$ is

$$\Omega_{\text{flow}}^{\text{rot}}(r,\theta,t) = -\Delta\Omega \exp\left(\frac{-E^{1/2}t/\tau}{(a^2 - r^2\sin^2\theta)^{3/4}}\right). \tag{4.19}$$

In a spin up, the velocity is maximum near the container immediately after the change of rotation rate. It then slowly decreases as the momentum is propagated from the container to the bulk. We show the evolution of velocity with cylindrical radius and time in Figure 4.9.

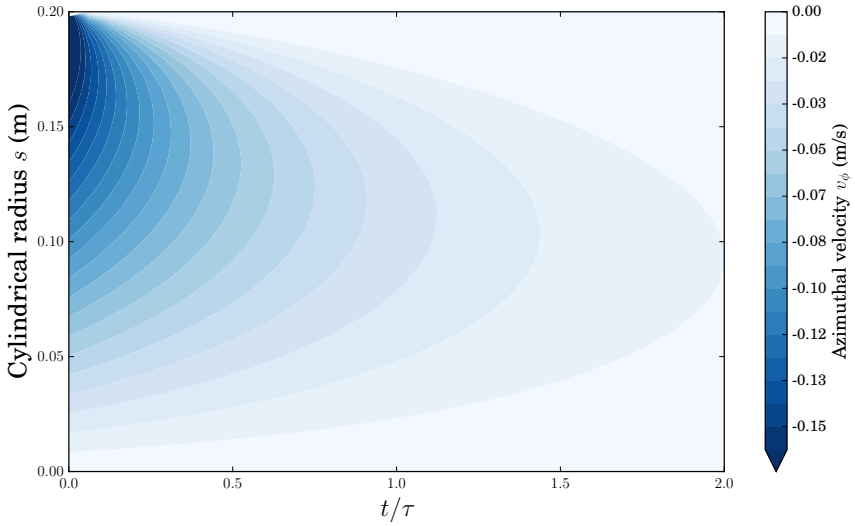

Figure 4.9: Azimuthal velocity in the frame rotating with the container at Ω for spin up from 9 to 10 Hz against cylindrical radius s and adimensionalised time t/τ. After one spin up time most of the volume rotates at the new rotation rate, and most of the differential velocity occur before half of the spin up time.

Using the routine we developed in Chapter 2, we can produce synthetic spectra corresponding to this flow. We show in Figure 4.10 the expected spectra for a collection of chosen modes. We can compare the splitting from spin up to solid-body rotation. Before the change of rotation rate, we have the spherical Ledoux splittings (red dashed lines). Then, immediately after the rotation change, the acoustic response varies greatly from mode to mode (solid lines), corresponding to spitting due to Doppler effect, as detailed in §2.2.1. For the $n = 0$ modes, almost no difference is visible while for $n = 1$ modes, the splitting is much larger than the one expected from solid-body rotation. After one spin up time ($\tau = 12$ s for $\Omega = 10$ Hz), we mostly recover the solid-body rotation splittings again at the new rotation rate. For comparison we show the splittings predicted by the spherical Ledoux coefficients again, at the new rotation rate Ω (purple dashed lines).

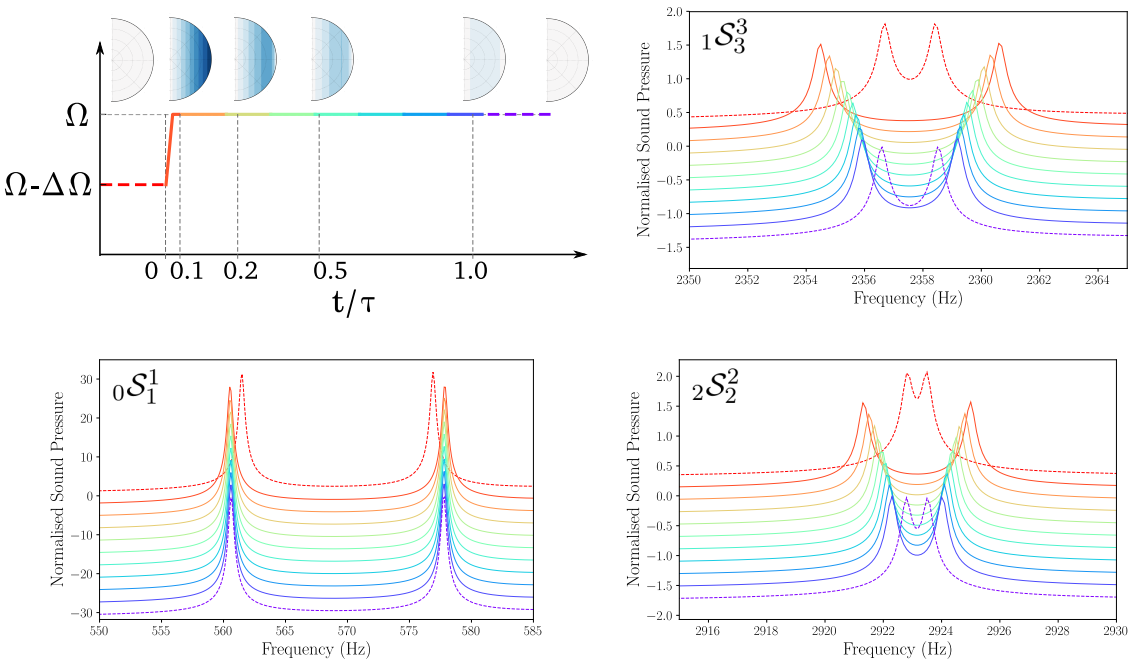

Figure 4.10: Top left: Spin up flow structure (hemispheres) for increasing time compared with the shell rotation rate (coloured line). The blue gradient gives the velocity in the fluid (same colour bar as Figure 4.9). Other panels: Synthetic spectra for corresponding increasing times (solid lines) for modes ${}_0\mathcal{S}_1^1$ (bottom left), ${}_1\mathcal{S}_3^3$ (top right), ${}_2\mathcal{S}_2^2$ (bottom right). Colours show successive dimensionless times, separated by 0.1τ, from 0.1τ to τ, and correspond to the timeline in top left panel. Solid-body rotation splittings for $\Omega - \Delta\Omega = 9$ Hz and $\Omega = 10$ Hz are given for comparison in dashed lines.

Inversion of acoustic splitting

Using this velocity profile, we can predict at any given time the residual splitting of any acoustic mode with eq. (2.61). We compute the splittings for the same typical realistic mode collection as above and show the results in Figure 4.11. Here the synthetic splitting data are associated to an arbitrary error $e_e = 0.2$. Then in this figure, if the residual splitting is close to 0, it means that the mode is not sensitive to differential flows (with spin up spatial structure). This is insightful to further understand the behaviour of acoustic modes and discriminate which modes to preferentially extract for a given flow structure.

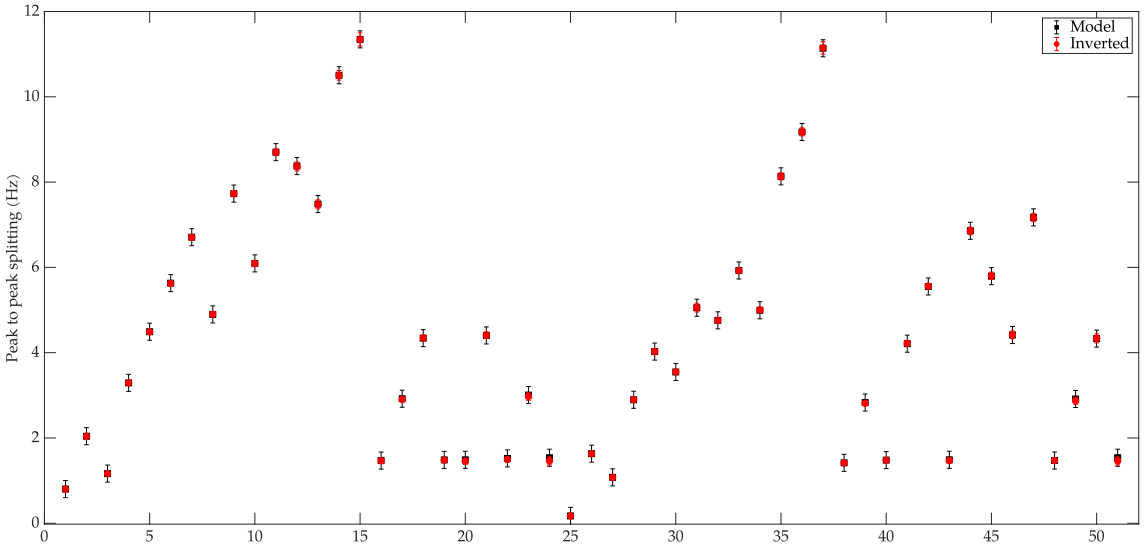

Figure 4.11: Acoustic splitting comparison for spin up from $\Omega - \Delta\Omega = 9$ Hz to $\Omega = 10$ Hz, at $t = 0.2\tau$ after change of rotation rate of the container, between the initial splittings used to perform the inversion (in black) with the splittings obtained from the inverted flow (in red). The selection of modes (n, l, m) used for the inversion is the same as in Figure 4.6. All splittings obtained after the inversion match the initial ones within the error bar.

To determine the best pair of parameters, we do a grid search on σ_p and δ, and consider the pairs that verify both $\hat{\phi}$ and $\hat{N}$ criteria. We find that $\delta = 0.1$ (in its dimensionless form) is always a good fit, while, depending on the spin up time, the best σ_p varies from 0.6 to 1.2. In order to compare the results for the different times, we take the same value for all inversions, and we choose the largest value $\sigma_p = 1.2$. The velocity profiles obtained as such are plotted on Figure 4.12 in blue solid lines, along with the expected models (dashed lines), for various times after change of rotation rate (from top to bottom 0.1, 0.2, 0.5 and 1 spin up time τ).

We seem to be able to retrieve the correct velocity profile for all radii above 0.35. However we recall that the mode collection we invert does not provide any information near the container boundary (close to $s = 1$), as shown by the sensitivity kernels. In Figure 4.12 we reproduced the irrelevant regions deduced from Figure 4.8 in grey. The good agreement between the inverted and initial velocity profiles near $s = 1$ is coincidental hence is not relevant to discriminate the inversions. Focusing on the region from $s = 0.3$ to 0.95, the inverted and model velocity match very well. The only notable difference is the presence of oscillations in the inverted profile, at lengthscale around the inversion resolution, as observed for the solid body rotation case.

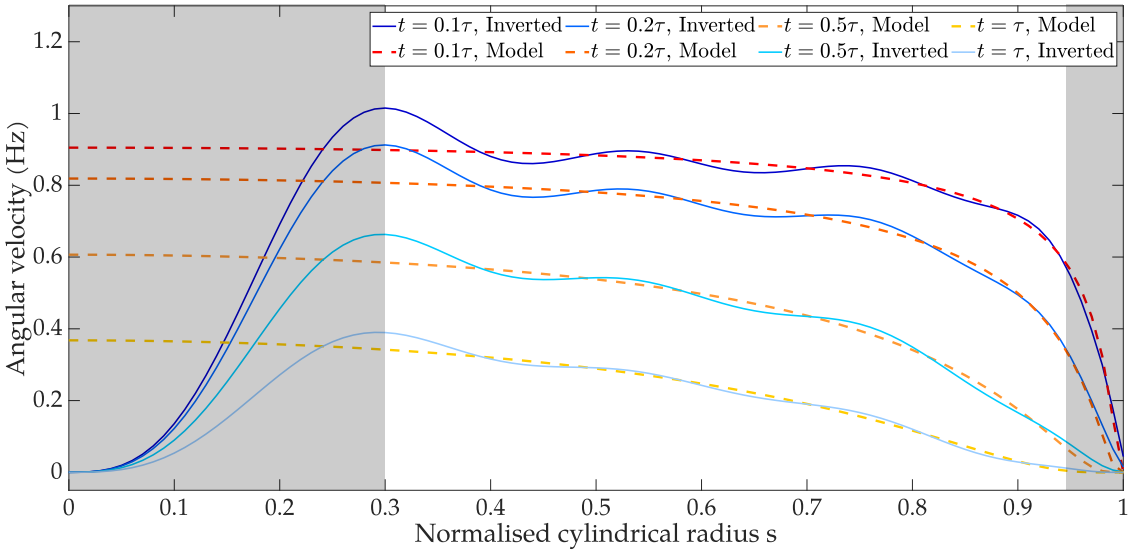

Figure 4.12: Angular velocity in the frame rotating with the container for spin up from $\Omega - \Delta\Omega = 9$ Hz to $\Omega = 10$ Hz, for increasing times after rotation change. In solid blue lines, the results from inversion from a realistic collection of modes. The model we want to retrieve is reminded in dashed lines. The inversion seems to retrieve the correct angular velocity for all radii above $s = 0.35$.

4.3.2 Zonal flows driven by thermal convection

We built ZoRo with the primary goal to study thermal convection in presence of fast rotation. Convective flows transport heat in the radial direction and it has been shown that due to the effects of rotation they form columnar quasi-geostrophic flows (Busse, 1994). In some regimes, in particular for low viscosity, strong alternating zonal jets appear that have been observed in gaseous giants or in the Earth's core (Porco et al., 2003; Livermore et al., 2017). Those jets are expected to form concentric cylindrical shells (Kaspi et al., 2018; Kong et al., 2018) that are expected to have significant influence on acoustic global modes (Aerts et al., 2010; Triana et al., 2014). These zonal flows have been successfully reproduced both in laboratory experiments (Manneville and Olson, 1996; Gillet et al., 2007; Read et al., 2015; Cabanes et al., 2017) and numerical simulations (Christensen, 2002; Gastine et al., 2014; Guervilly and Cardin, 2017).

Inversion of velocity profiles from realistic numerical simulations

In order to validate our experiment for convective zonal flows study, we apply the inversion procedure to try and retrieve typical zonal velocity profiles. We use the numerical results of Guervilly and Cardin (2017) who scanned different regimes with realistic values for geophysical bodies with a quasi-geostrophic assumption. Example of the velocity obtained with their numerical simulation is reproduced in Figure 4.13.

We selected three very different velocity profiles among the ones presented in Figure 2 of Guervilly and Cardin (2017). Note that the velocity profiles are given in the rotating frame, corresponding to the flow velocity we are able to invert.

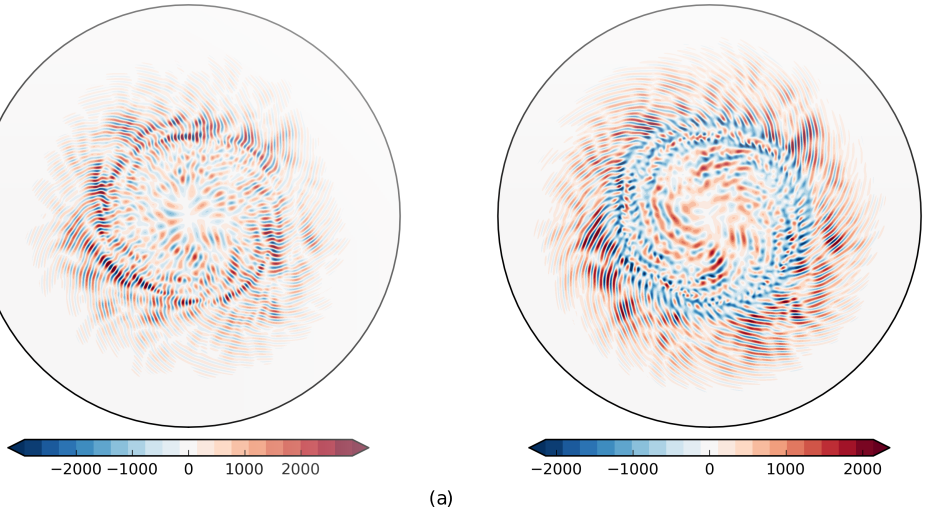

Figure 4.13: Snapshots of the radial velocity (left) and the azimuthal velocity (right) in the equatorial plane, for case (i), from Guervilly and Cardin (2017).

We choose to consider:

(i) $Ra = 7.45\,10^{10}$, $E = 10^{-8}$, $Pr = 0.1$, corresponding to $Ra/Ra_c = 0.96$ (profile 1 of Figure 2 from Guervilly and Cardin (2017), velocity map reproduced in Figure 4.13),

(ii) $Ra = 5\,10^{11}$, $E = 10^{-8}$, $Pr = 0.1$, corresponding to $Ra/Ra_c = 6.44$ (profile 5),

(iii) $Ra = 5\,10^{10}$, $E = 10^{-7}$, $Pr = 0.1$, corresponding to $Ra/Ra_c = 9.94$ (last frame).

Following the same procedure as above, we first produce the corresponding acoustic splittings predicted by the forward model. We attribute an arbitrary value to $e_i = 10$. We then invert those with the same realistic mode collection (as in Figure 4.6). The inversion parameters are $\delta = 0.01$ for all profiles, and $\sigma_p = 50$ for (i), $\sigma_p = 5000$ for (ii) and $\sigma_p = 1250$ for (iii). Note that this seemingly big discrepancy between the three parameter comes from the velocity profiles initial amplitudes. Indeed, with those values of σ_p, the relative constraint imposed on the model is constant for all three profiles, equal to 25%.

The inverted velocity profiles we obtain are shown in Figure 4.16 in solid blue lines, along with the initial profile from Guervilly and Cardin (2017), Figure 2, in dashed red. The splitting comparison and resolution kernels are shown for case (i) only in Figure 4.14 and Figure 4.15. Note that the angular velocity is non-dimensional (adimensionned by Ra, Guervilly and Cardin (2017)), leading to adimensionned splittings, hence the very large values shown in Figure 4.14.

We can see in Figure 4.16 that for both (i) and (iii) cases, the inverted velocity profile match the initial ones very well (in the relevant radial regions for our mode collection). But for (ii) in Figure 4.16, the inversion seems to be able to retrieve only an average of the expected profile. This case presents multiple jets that dominate the flow (Guervilly and Cardin, 2017) and display sign inversion at relatively small length-scale, around 0.1 (in dimensionless cylindrical radius). Unfortunately this length corresponds to our resolution limit, and we are indeed not able to retrieve the given profile, but only an estimation of the mean velocity amplitude. This is also visible on profile (iii) where the inversion smooths out the sharp negative jets.

In conclusion we are able with a realistic mode collection to retrieve complex velocity profiles even with several jets of opposite signs. We are however limited in resolution to around $a/5 \approx 4$ cm, so all flows that display features of this length-scale or smaller remain out of reach with our method.

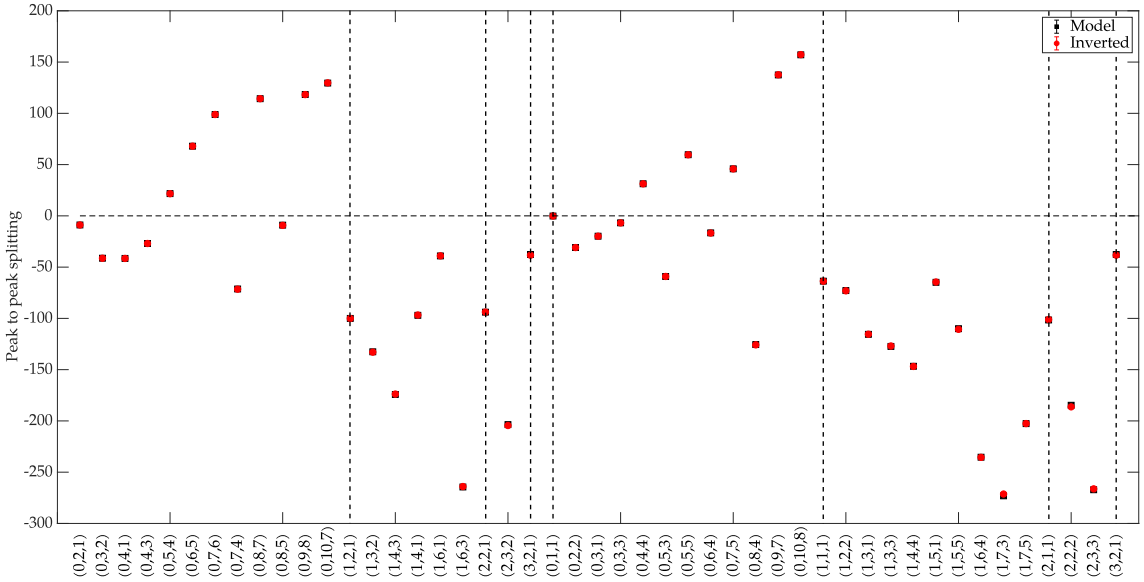

Figure 4.14: Acoustic splittings comparison between the initial splittings used to perform the inversion (in black) with the splittings obtained from the inverted flow (in red) for case (i). The selection of modes (n, l, m) used for the inversion is shown in abscissa. All splittings obtained after the inversion match the initial ones within the error bar.

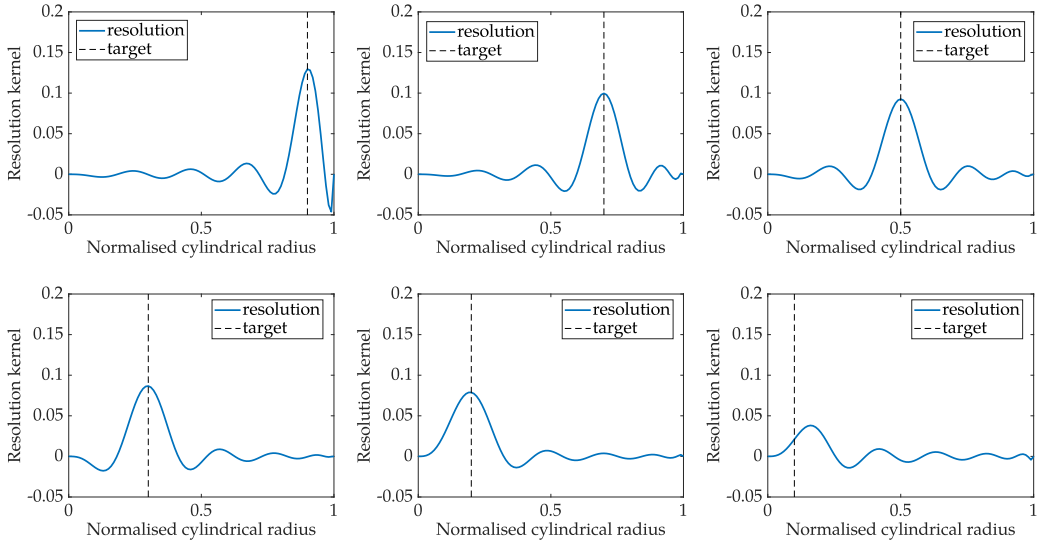

Figure 4.15: Resolution kernels for case (i) for target radius at $s = 0.9$, 0.7, 0.5, 0.3, 0.2 and 0.1 (dimensionless cylindrical radius). For radius $s < 0.2$ the inversion is not able to retrieve the target anymore.

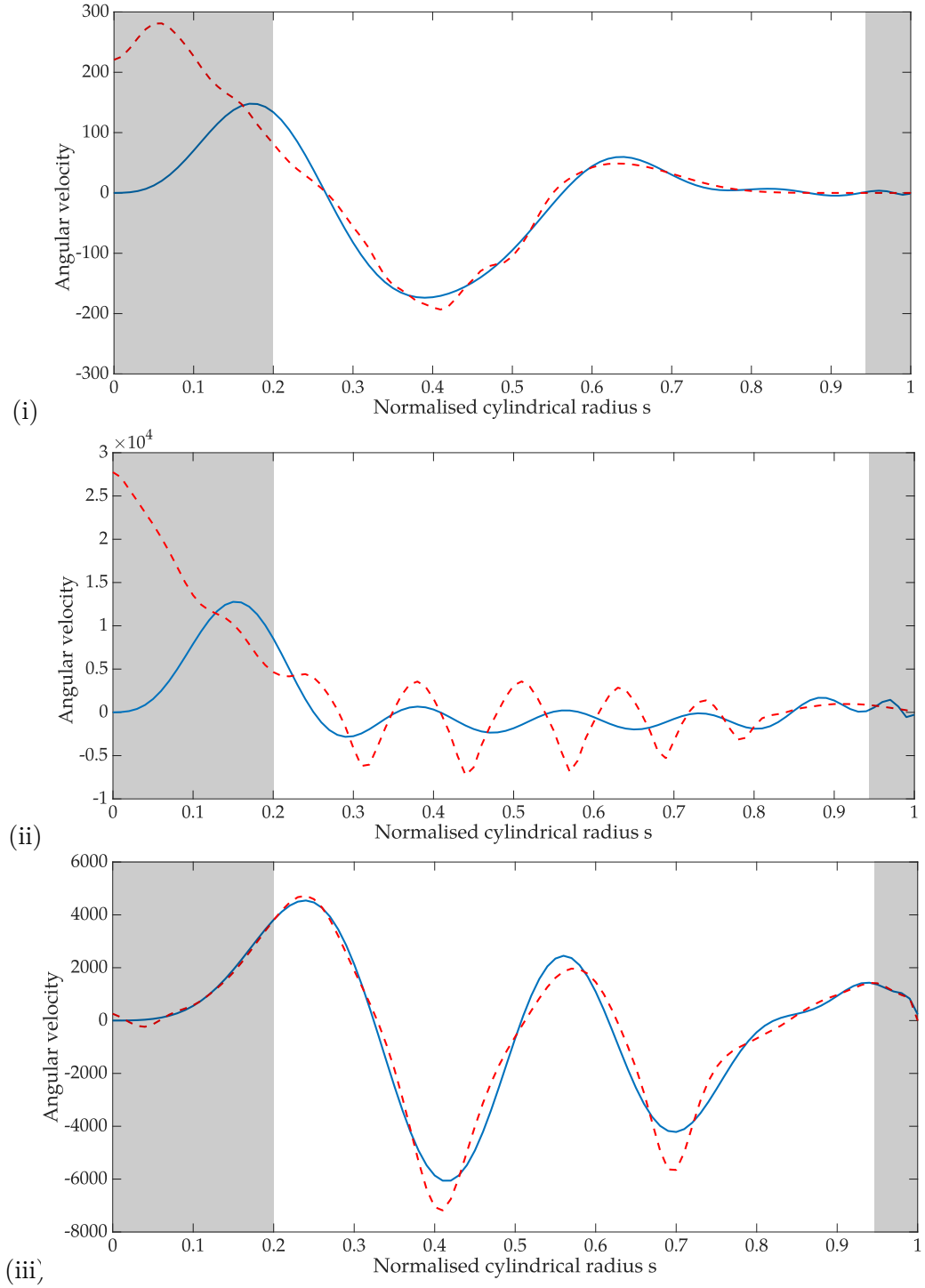

Figure 4.16: Angular velocity in the rotating frame for zonal flow from numerical simulations results from Guervilly and Cardin (2017), for chosen profiles described in main text (in dashed red). In solid blue lines, the results from inversion from our realistic collection of modes. The initial model we want to retrieve is reminded in dashed red. We are able to retrieve the correct velocity both structure and amplitude for (i) and (iii). In (ii) the oscillations length-scale is smaller than our inversion resolution. The inversion fails to retrieve a meaningful velocity profile, and only manages to retrieve an averaged velocity.

4.4 Discussion

Throughout the chapter we made several assumptions that we deemed reasonable. We will now more formally verify the validity of those assumptions and discuss how they affect the inversion accuracy and limits. We will also discuss the estimation of the errors due to the inversion and show that we currently have no good measure of these, and need to continue relying on the comparison with synthetic cases.

4.4.1 Validity of the z-invariance assumption

We will first investigate the z-invariance that we assumed throughout this chapter. We want to verify if the geostrophy can be retrieved without imposing it. To do that we recall that the numerical simulations from Guervilly and Cardin (2017) are performed on the equatorial plane only and then extrapolated in the whole spherical volume. They are thus invariant along the z direction by construction. We also use the same synthetic acoustic splittings as before, i.e. from the forward model where z-invariance is assumed. Thanks to both of these, the acoustic splittings fully carry the z-invariance, and any deviation from geostrophy will be due to the inversion procedure, through the sensitivity kernels structures of the mode collection or equivalently to insufficient inversion constraints (with an infinite number of modes, any structure should be perfectly retrieved).

Using the formalism detailed in §4.1.2, we perform the inversion in (r, θ) without further constraints. We show in Figure 4.17 the inverted angular velocity in (r, θ) for case (i) without assuming z-invariance. The synthetic splittings used for inversion are those we created for the radial inversion. The inversion was performed using the same parameters as for the radial one $\delta = 0.1$, $\sigma_p = 50$, and the truncation for angular projection $l_{max} = 6$. The splittings comparison are shown in Figure 4.18 and the resolutions kernels (one for each projection degree) in Figure 4.19.

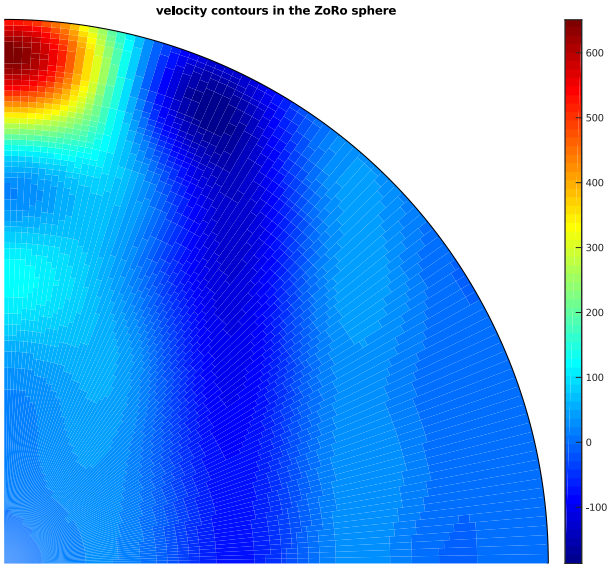

Figure 4.17: Adimensionned angular velocity map obtained from a spherical inversion on (r, θ) with the latitudinal component projected onto spherical harmonics up to degree 13.

We globally retrieve the invariance along z axis, except in the central region, which is to be expected from the sensitivity kernels structure. This gives us confidence in the fact that the z-invariance assumption is not overly constraining the inversion, but only helps to reduce the number of variables, as intende. This also means that we will be able to distinguish geostrophic from non-geostrophic structures in ZoRo.

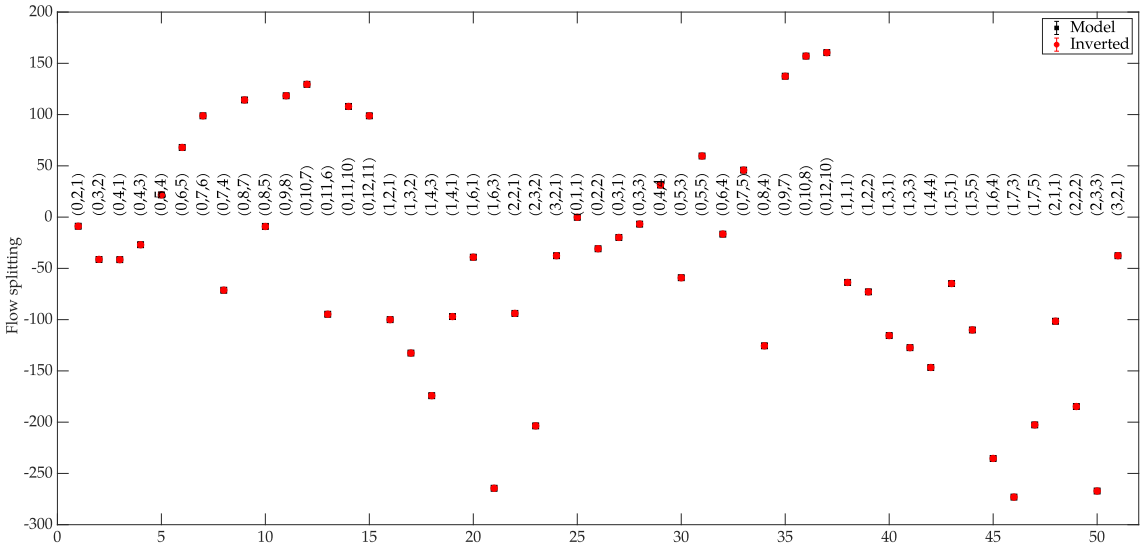

Figure 4.18: Acoustic splitting comparison between the initial splittings from geostrophic profile (in black) with the splittings obtained from inversion in (r, θ) (in red) for case (i). The selection of modes (n, l, m) used for the inversion is shown in abscissa. All splittings obtained after the inversion match the initial ones within the error bar.

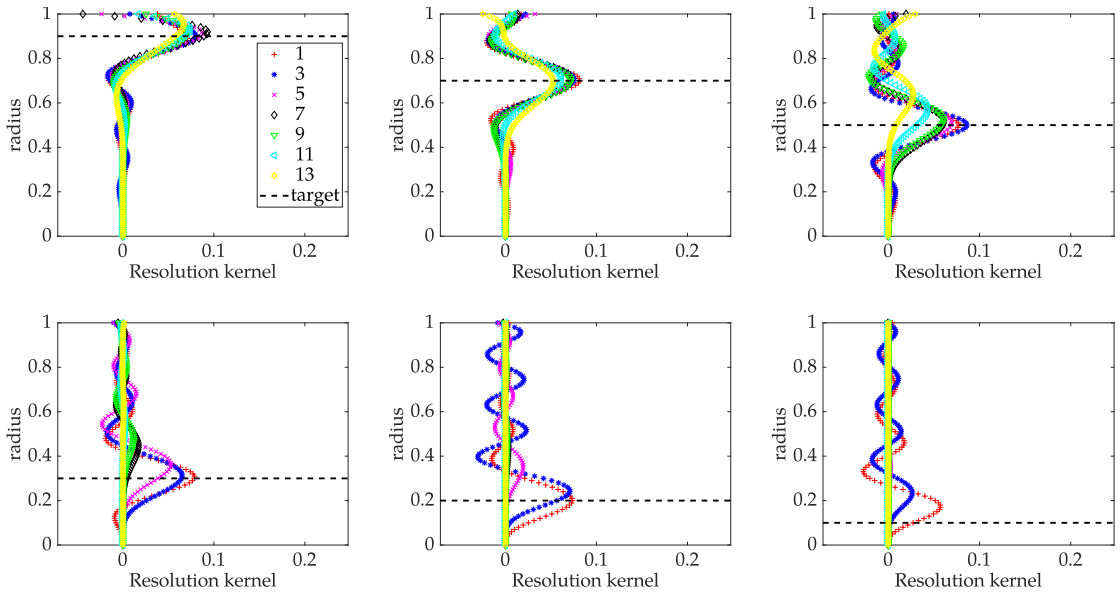

Figure 4.19: Resolution kernels for all $U_{l'}$ used for inversion (symbols), for case (i) for target radius at $s = 0.9$, 0.7, 0.5, 0.3, 0.2 and 0.1 (dimensionless spherical radius). For $s < 0.2$ the inversion is not able to retrieve the target anymore.

4.4.2 Influence of the sign of acoustic splittings

The current data analysis on experimental data only allows to extract the absolute value of acoustic splitting. As seen in Figure 4.14, the splittings can have both signs depending on whether $+m$ or $-m$ mode has highest frequency. This introduces a measurement bias that may affect the inversion. We test this effect by performing the same inversion but with the absolute value of the splittings from Figure 4.14.

Since the flow display alternating jets such as the profiles from Guervilly and Cardin (2017), forcing all splittings to be positive might cause that no valid inversion can be found. Typically for case (i), there is no $(\sigma_p,\, \delta)$ pair that allow the misfit $\hat{\phi}$ to be less than 1. We manage to reduce $\hat{\phi}$ by increasing $e_i = 15$, but as seen in Figure 4.20, the result is not satisfactory ($\hat{\phi} = 2.5$). For strong alternating flows, which are typically expected from zonal jets, it is necessary to be able to distinguish $\pm m$ modes.

Note that for spin up flows and prograde solid-body rotation, the experimental bias has no influence as all splittings are already positive. For a globally retrograde flow (negative splittings) but without change of sign, this bias should only affect the inverted flow sign. For an example of such flow and how taking all splittings as positive would affect its inversion, see Chapter 5, §5.2.1.

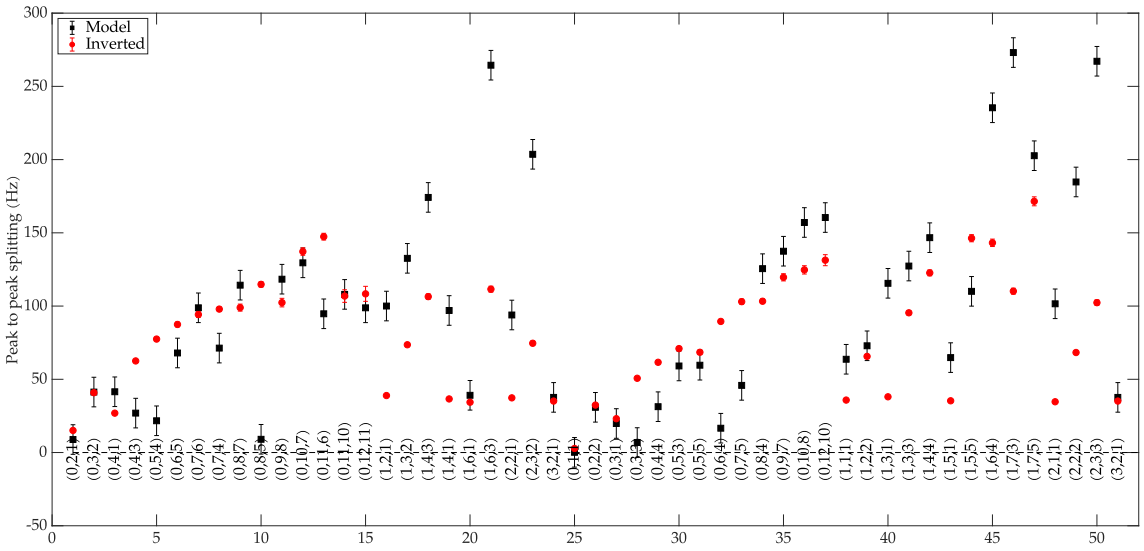

Figure 4.20: Acoustic splitting comparison between the absolute splittings (in black) with the splittings obtained from the inverted flow (in red) for case (i). The selection of modes (n, l, m) used for the inversion is shown in abscissa.

4.4.3 Determination of the inverted model errors

In a Bayesian inversion, the usual error on the model is given by Tarantola (1987), eq. (3.38), as

$$\hat{\boldsymbol{C}}_{\boldsymbol{pp}} = \left(\boldsymbol{G}^T \boldsymbol{C}_{\boldsymbol{dd}}{}^{-1} \boldsymbol{G} + \boldsymbol{C}_{\boldsymbol{pp}}{}^{-1} \right)^{-1}, \tag{4.20}$$

and corresponds to the so-called posteriori model covariance. This matrix depends on the data but also on the initial parameters of the inversion σ_p and δ through the model covariance matrix.

We reproduce in the middle panel of Figure 4.21 the inversion results (solid blue) of Guervilly and Cardin (2017), with the same parameters ($\delta = 0.01$, $\sigma_p = 1250$) as (iii) from Figure 4.16, along with the corresponding errors determined as eq. (4.20) in blue shade.

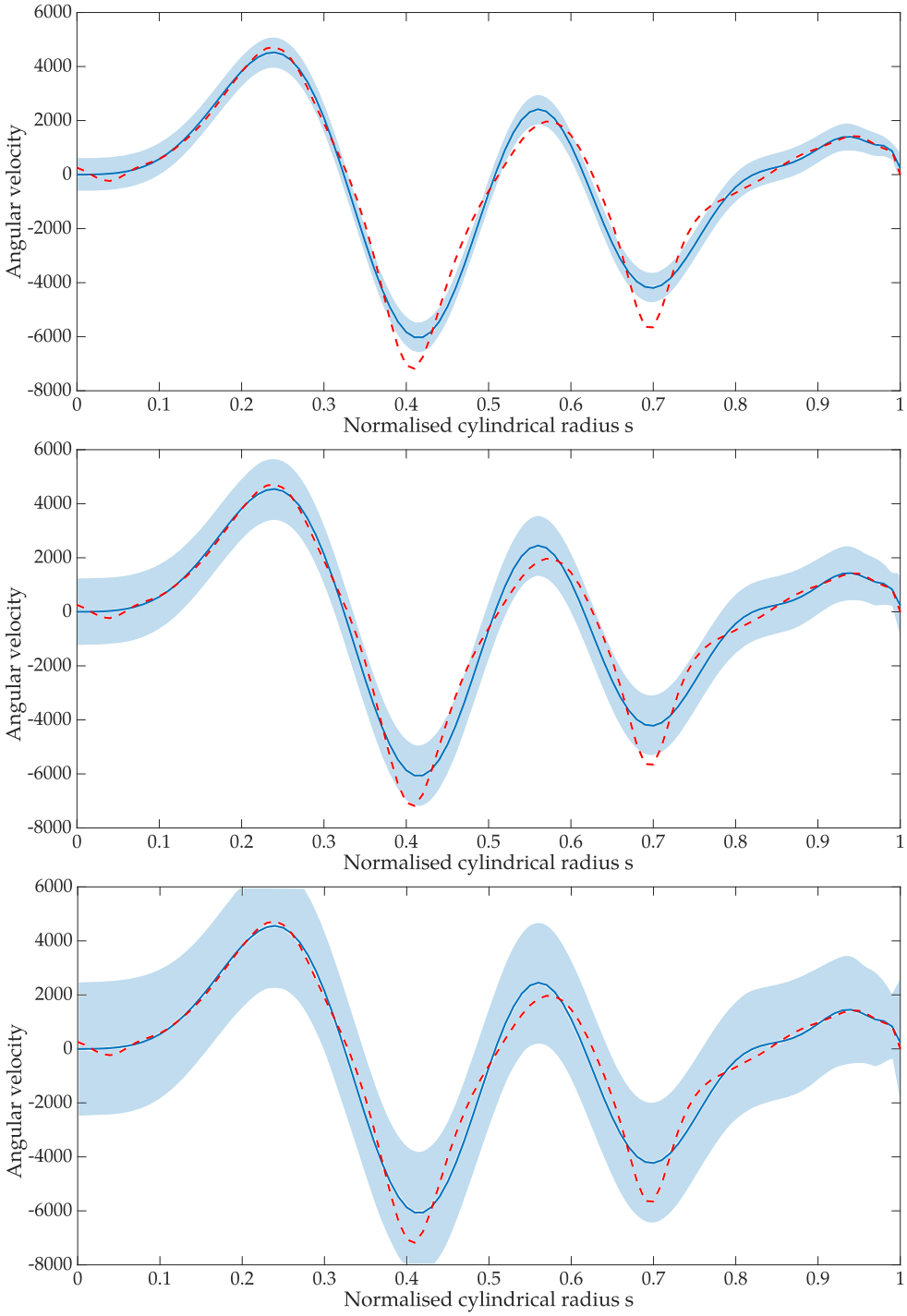

Figure 4.21: Influence of σ_p on the velocity profile (solid blue) inverted from synthetic data taken from Guervilly and Cardin (2017) (red dashed), $\sigma_p = 625$ (top), 1250 (middle) and 2500 (bottom). Estimated errors on the inversion results, as defined in eq. (4.20) are given in shaded blue.

We remark that the shaded area is slightly smaller for intermediate radii, where the data carry information and constrain the model. We then try to understand the influence of the inversion parameters, δ show no visible influence on the error, but σ_p significantly changes its value. For comparison we show in Figure 4.21, the same inverted profile from the same data and we vary σ_p, from 625 (top panel) to 2500 (bottom panel). Note that the small misfit condition is still verified by those values, and that there is not visible difference in the inversion result, even allowing the synthetic profile (red dashed line) to be outside of the estimated model error.

Recalling the inversion parameter scan maps (e.g. Figure 4.2, σ_p presents a lower bound, but there is seemingly no upper bound. It seems that for our study, the freedom allowed to the model can never be too large, as there is no influence on the inversion results even for very large values of σ_p, showing that the data give consistent constraints. However that also means that we currently have no objective measure of the model's errors, and have to rely on synthetic tests to gain insights on the confidence of each set of inversion parameters and data collection.

Key points

- Linear Bayesian inversion to retrieve flow field from acoustic splitting
- Tools to quantitatively define an accurate inversion
- Test the inversion routine on synthetic flows from simple solid-body rotation to spin-up and realistic zonal flows from numerical simulations
- Validation of the radial inversion for z-invariant flows

5

Modal acoustic velocimetry applied to experimental zonal flows

Des petits trous, des petits trous, toujours des petits trous.

- Serge Gainsbourg, *Le Poinçonneur des Lilas*

In the previous chapters we presented the experimental apparatus, as well as all the data acquisition, analysis and inversion procedure that are useful to measure a flow velocity field within ZoRo. We now want to apply our MAV routine on a realistic unknown flow that can typically be found in ZoRo. For this first confrontation with real data, we want to study a mechanically induced azimuthal flow. This allows us to apply the procedures we developed so far without further complications (that would arise from temperature gradients for example).

We choose to study the velocity field induced by centrifugal pumps. In order to induce this flow we opened some of the holes we have on the apparatus, while rotating. The openings are placed at different latitudes, hence submitted to a different centrifugal pressure, pumping the fluid and creating a flow. Using the protocol and techniques from data acquisition, analysis and inversion routines we developed, we now apply all of them to describe this centrifugally driven flow. We start from the experimental observations and study the acoustic splittings. We then invert those data to retrieve an azimuthal flow. In order to check whether the inverted velocity is realistic, we compare it with results from finite-element numerical simulations.

There is a good agreement between the velocity profiles obtained from finite-element simulation and experimental data. This allows us to be confident in the MAV method applied on experimental data. We then try to propose a physical mechanism to explain the measured flow. This is still work in progress but preliminary force balances show that this centrifugally driven flow might be a large scale geostrophic flow formed from many small scale quasi-geostrophic vortices.

We managed to image a non-trivial geostrophic flow, with similar mechanisms as zonal flows, using modal acoustic velocimetry in ZoRo.

5.1 Experimental observation

We first present how we induce the centrifugally driven flow we want to study, and its signature on the acoustic data. We then deduct the corresponding velocity profile using the inversion procedure described in Chapter 4.

5.1.1 Description of the experimental protocol

We make use of the through holes initially provided for thermal sensors. They are disposed in groups of seven, equally spaced in longitude (separated by 6.67° from each other) on two co-latitudes (27° and 60°). The holes are 8-mm long threaded cylinders of 4 mm in diameter, narrowing into a 2 mm-diameter cylinder 2 mm before reaching the cavitiy. Figure 5.1 shows a sketch of the holes' geometry and their disposition on the spheroidal shell. Excerpts of technical drawings with exact positions of each hole and their geometry are given in Appendix C.

The open holes are symmetric both with respect to the equator and the meridian plane. When we open one hole in a series, all corresponding holes on all other series are also open. In practice we studied three configurations: one hole open (in each series so in total 8 symmetric open holes) shown in green in Figure 5.1, three open holes (24 in total) in blue and all seven open holes (56 in total) in red. After opening the chosen pipes, we rotate the spheroid and wait for stationary state (equivalent of several spin-up time).

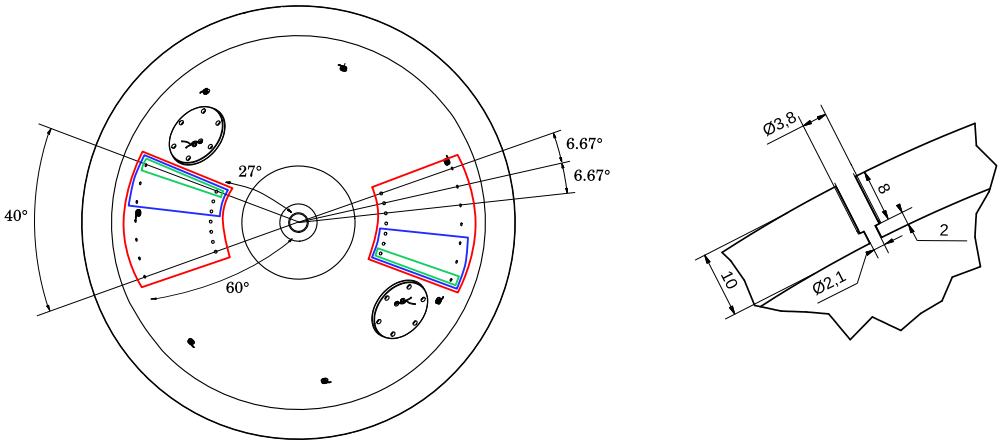

Figure 5.1: Left: Sketch of the holes positions on ZoRo, top view. In colour frame (green, blue, red) the open holes for resp. 1, 3 and 7 open holes configurations. Speakers and electrets positions are indicated for comparison. The southern hemisphere is strictly symmetric. Right: cut through view of one hole, dimensions are in mm.

5.1.2 Direct observations

We apply the data acquisition and data analysis protocol described in Chapter 3. We first note that the modes do split in frequency and that these splittings are qualitatively different from solid-body rotation. We define as residual splitting (or flow splitting), the splitting left after subtracting the splitting due to solid-body rotation as predicted by the spherical Ledoux coefficients given in eq. (2.70).

In Figure 5.2, we compile the flow splittings for a chosen collection of modes for increasing rotation rates when all holes are open (7 open holes configuration). The open holes clearly induce a flow, which is different from solid-body rotation (retrieved when all flow splittings are zero). The flow splittings increase with the rotation rate. At first glance they seem proportional to the rotation rate, except for the fundamental ${}_0\mathcal{S}_1^1$ mode which stays close to zero (solid-body rotation). Larger m modes also seem to display steeper slopes, with the exception of ${}_0\mathcal{S}_1^1$ again.

All these observations give us some first insights on the expected velocity profile. Indeed the seemingly proportionality with m and f_Ω hints towards a profile with a constant velocity, different from the container rotation rate. But the presence of few modes for which this is not verified shows that the open holes driven flow is more complicated and motivates the inversion.

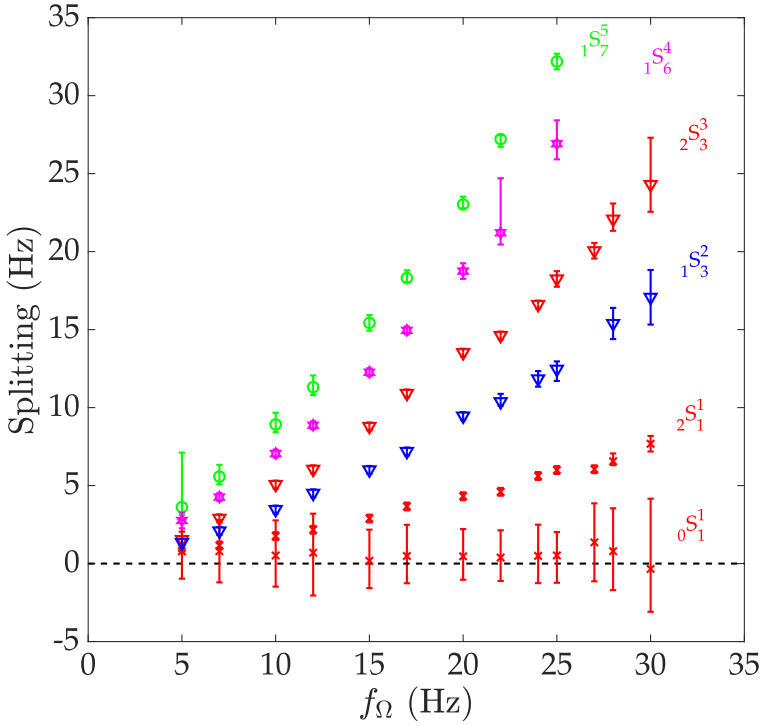

Figure 5.2: Flow splitting for increasing rotation rates for 7 open holes configuration. The flow splitting is zero for solid-body rotation at the container rotation rate.

5.1.3 Real data inversion

For each rotation rate, we apply the inversion routine developed in Chapter 4 to retrieve a velocity profile in the cavity. Note that since we now work with real data, the modes we are able to extract vary from one run to another, as seen in Figure 5.2 where some modes are missing for several rotation rates. This directly implies that the inversion is based on one specific dataset that is potentially different for each run. Due to the variable data collection, we have different inversion parameters σ_p and δ for each run, chosen as the best pair for each specific dataset, determined with the systematic grid search described in Chapter 4. A typical set of parameters is $\sigma_p = 1$ Hz, $\delta = 0.2$.

In Figure 5.3 we show the normalised misfit and number of accurate splittings for real data collection extracted for 25 Hz with all holes open. The corresponding best inversion parameters is $\sigma_p = 2$ Hz, $\delta = 0.1$. The corresponding inversion results is shown in Figure 5.4, with the associated resolution kernels in Figure 5.6.

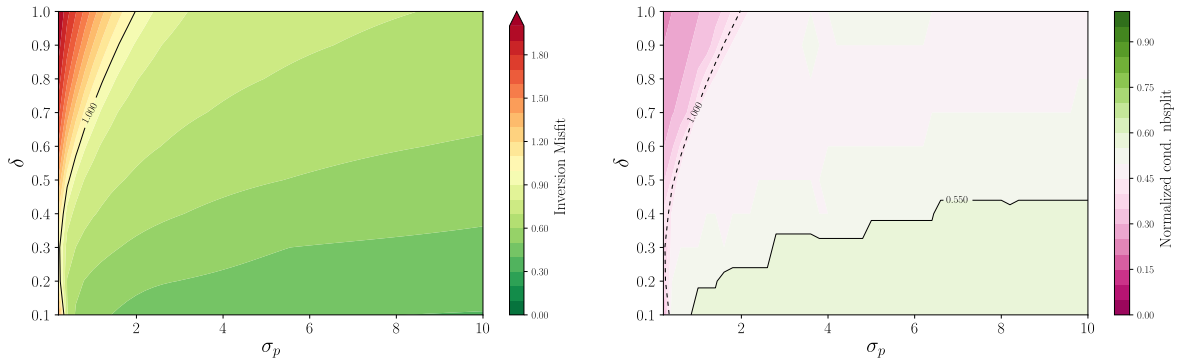

Figure 5.3: Left: Splitting misfit between model and inverted splittings (in Hz) for different parameters σ_p and δ. Right: Normalised number of inverted splittings within error bars of the data. The inversion is considered accurate for misfit < 1 and normalised number of splittings > 0.5.

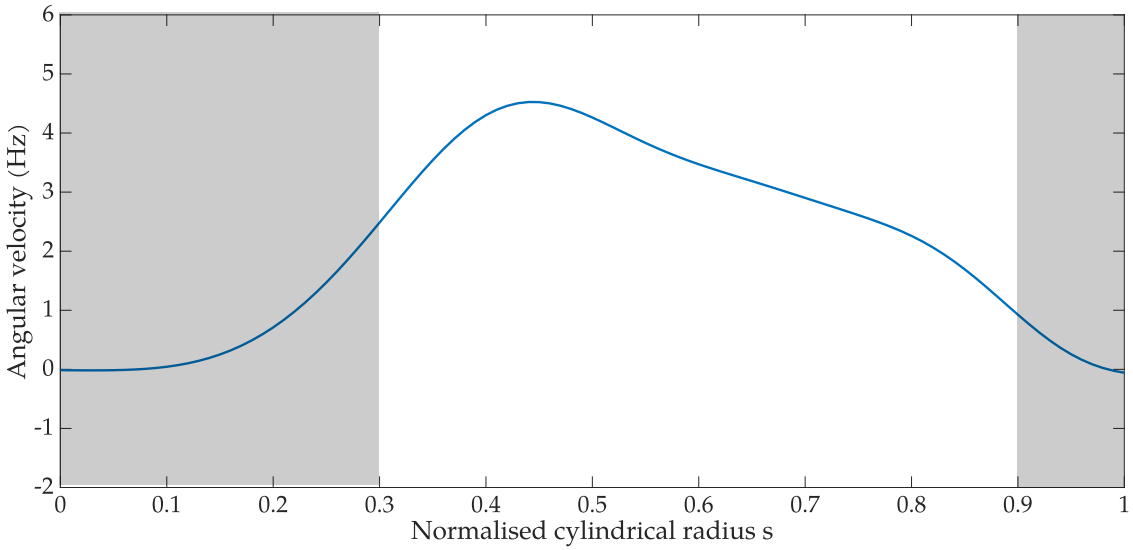

Figure 5.4: Fluid angular velocity in the frame rotating with the container for 7 open holes at $\Omega = 25$ Hz against adimensioned cylindrical radius. The mode collection used for inversion are given in Figure 5.5.

We recall from Chapter 4 that regions near the center and the boundary should not be taken into account, as confirmed by the poor resolution kernels in those areas. A compilation of the inverted velocity profiles for various rotation rates are shown in Figure 5.7, for the 7 open holes configuration. Note that since each dataset is comprised of a different mode collection, the areas where the inversion is not accurate anymore are slightly different for each profile. We represented in grey the regions where the inversion is typically not accurate for these collections.

We retrieve that the velocity is larger when the rotation rate increases. The profiles seem relatively homogeneous in the center of the cavity (where the inversion is accurate), with a slightly higher value at small radius (near the rotating axis). This is qualitatively consistent with the observations we had on the acoustic splittings themselves, when we predicted a mostly flat profile.

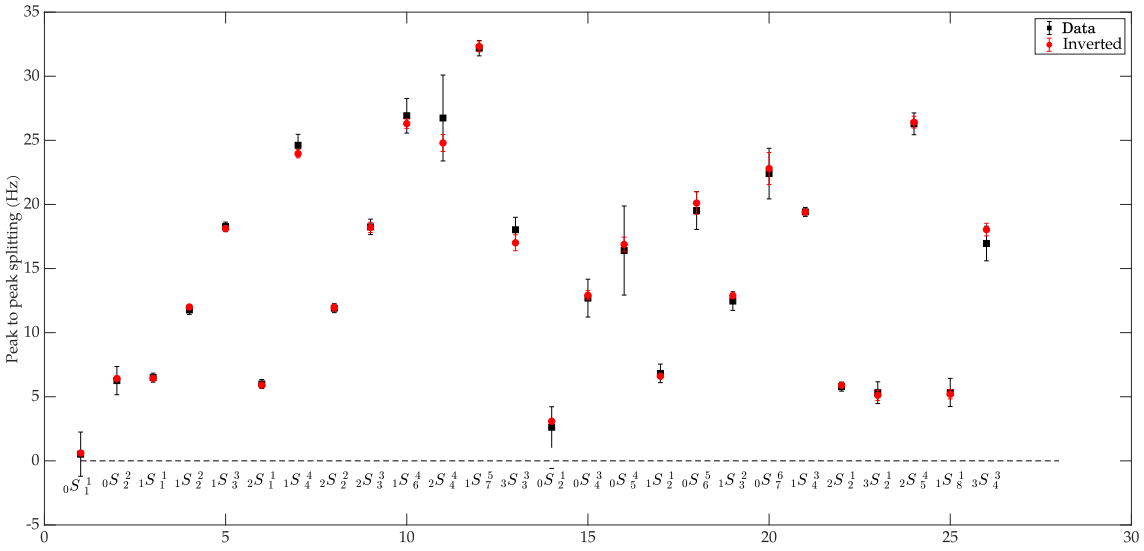

Figure 5.5: Acoustic splitting comparison between the experimental splittings (in black) with the splittings obtained from the inverted flow (in red). The selection of modes ${}_n\mathcal{S}_l^m$ used for the inversion is shown in abscissa. All splittings obtained after the inversion match the initial ones within their error bar.

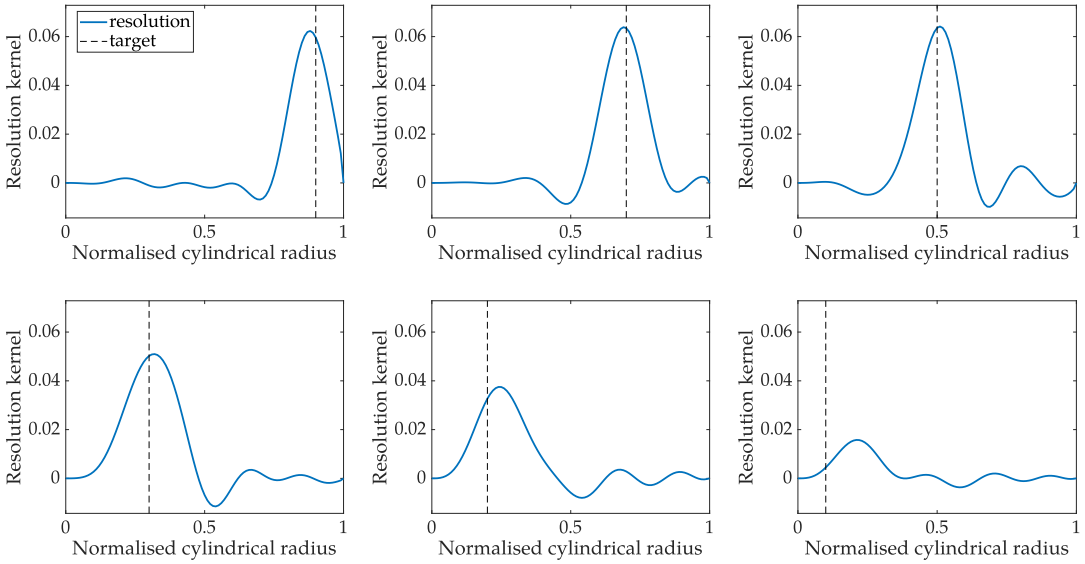

Figure 5.6: Resolution kernels for target radius at $s = 0.9$, 0.7, 0.5, 0.3, 0.2 and 0.1 (dimensionless cylindrical radius), for inversion of 7 open holes, 25 Hz. For radius $s < 0.2$ the inversion is not able to retrieve the target anymore.

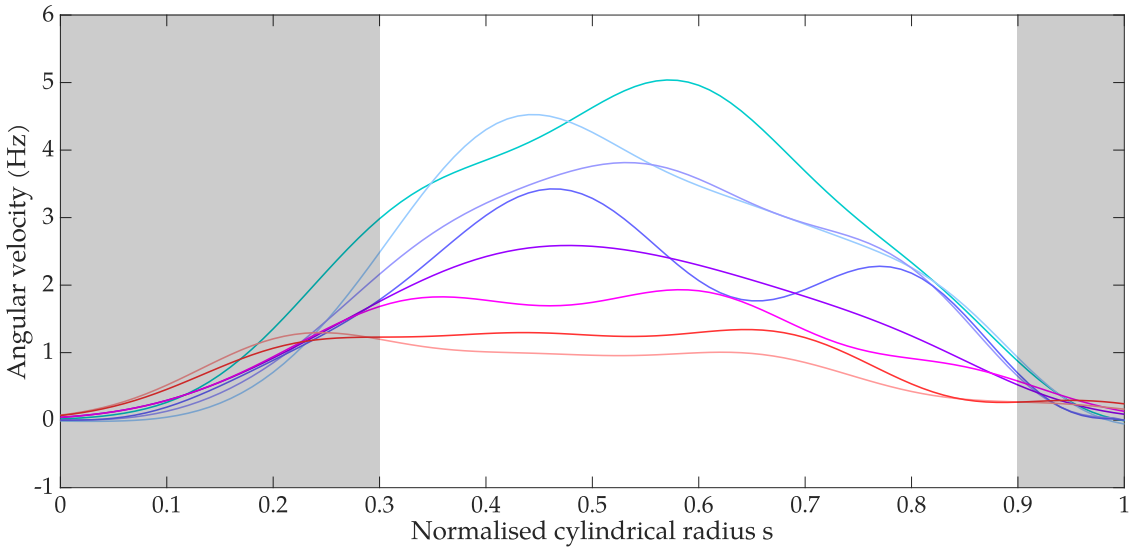

Figure 5.7: Inverted velocity profiles for 7 open holes configuration at rotation rates: 28, 25, 24, 18, 15, 12, 10 and 7 Hz in solid lines (from cold to hot colours). The grey regions are indicative of where the inversions are not accurate anymore.

5.2 Finite-element simulations

5.2.1 Axisymmetric simulations

To reduce the calculation cost, we take the axisymmetric assumption again, so the series of holes become hollow torii in the container. This may lead to important changes in the amplitude of the flow but we expect the geometry of the flow to be quite similar to the one in the experiment. The angular velocity obtained for rotation rate 20 Hz is shown in Figure 5.8 (dashed red), along with the inverted profile using a realistic collection of modes (blue). In the simulations, the toric hole is $D = 1$ mm wide and $L = 1$ cm long.

Firstly we verify that we should be able to retrieve this type of profile using MAV. The flow structure is pretty similar to the inverted flows from real splitting data. However one striking fact is that the simulations predicts a global retrograde (negative) flow while the real data inversions give the opposite sign. Note that the maximum (absolute) amplitude of the angular velocity is significantly higher than the value obtained from experimental data. This can be linked with the fact that the total surface of pipe is much larger in the simulation than the experiment. However no easy scaling are available at first sight.

As discussed in Chapter 3 and Chapter 4, in the experiment, we are only able to retrieve the absolute splitting. Since we are not able to distinguish the two $\pm m$ modes, we may lose relevant information needed to correctly invert the flow. We can verify the splittings' sign importance on this inversion, where we know the velocity profile we should retrieve. Figure 5.8 clearly shows a retrograde flow, which is associated with negative splittings. We try to retrieve the same profile by taking the absolute values of all splittings. We compare the inverted flow obtained as such with the (absolute) profile from simulations in Figure 5.9.

We again retrieve the correct structure, which was expected since the velocity profile is globally smooth, and stays retrograde (no alternating jets). This also successfully explains the sign difference between the experimental and numerical velocity profiles. However the amplitude of the flow velocity obtained with such simulations are pretty far from the measured ones, leading us to reconsider the validity of the axisymmetry assumption.

Note that we are confident in having a retrograde flow since the flow splitting increases the Ledoux splittings. This means that the additional flow has the same sign as the Coriolis effect, which induces a retrograde drift of the acoustic waves, as showed by Backus and Gilbert (1961).

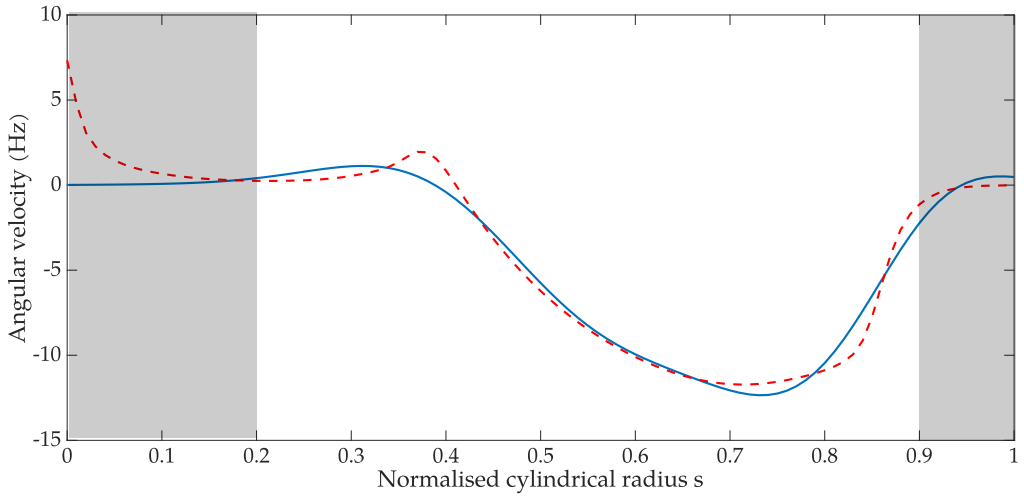

Figure 5.8: Angular velocity profile obtained with finite-element simulation for toric holes driven flow at 20 Hz (dashed red). The inversion of this known flow using mode collection from Figure 4.6 is plotted for comparison in solid blue.

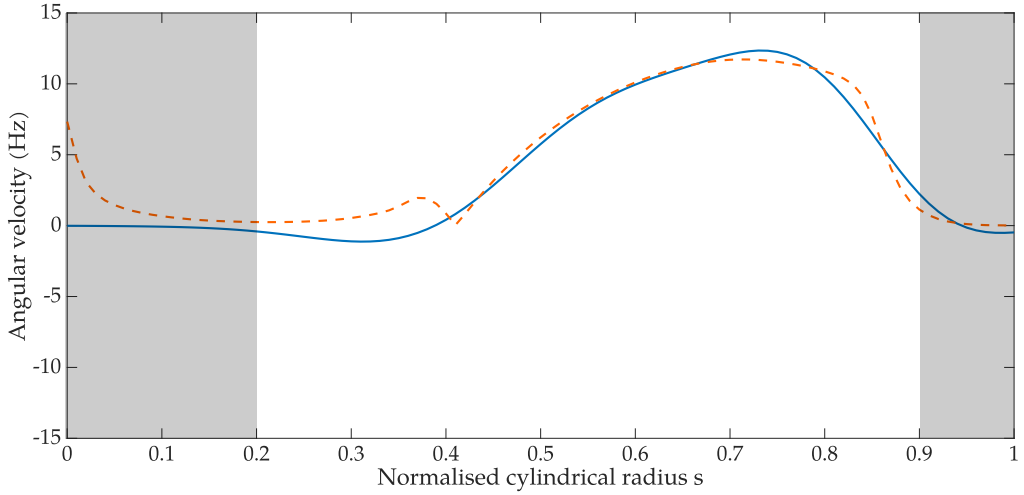

Figure 5.9: Angular velocity profile obtained with finite-element simulation in the frame rotating with the container for holes driven flow at 20 Hz against adimensioned cylindrical radius, absolute value in dashed orange. The inversion of this known flow using mode collection from Figure 4.6 is plotted for comparison in solid blue.

5.2.2 Three-dimensions (3D) simulations

The discrepancy of (absolute) amplitude between simulations and experiments is not satisfactory. In order to better reproduce the experimental conditions, we modelled each holes and ran three-dimensions (3D) equatorially symmetric simulations. A typical velocity map is plotted in Figure 5.10 for a 7 open holes configuration.

A compilation of velocity profiles obtained with 3D simulations for various rotation rates and number of open holes is grouped in Figure 5.11. We can see that the velocity amplitudes are much closer to the experimental ones. We confirm the increase of flow velocity with rotation rates. The dependence with the number of holes is not very clear. At low rotation rate (4 Hz, in blue), all 1, 3 and 7 open holes configurations (dash-dotted, dashed and solid lines respectively) have very similar profiles. But for higher rotation rates, e.g. 10 Hz (brown) and 15 Hz (yellow) we seem to able able to distinguish a linear relation between the velocity and the number of open holes.

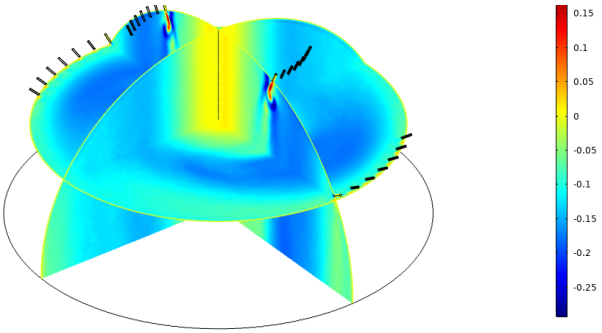

Figure 5.10: Snapshot of azimuthal velocity map (m/s) from full equatorially symmetric 3D finite-element simulation with 7 open holes, rotating at 4 Hz. The black rectangles represent the holes.

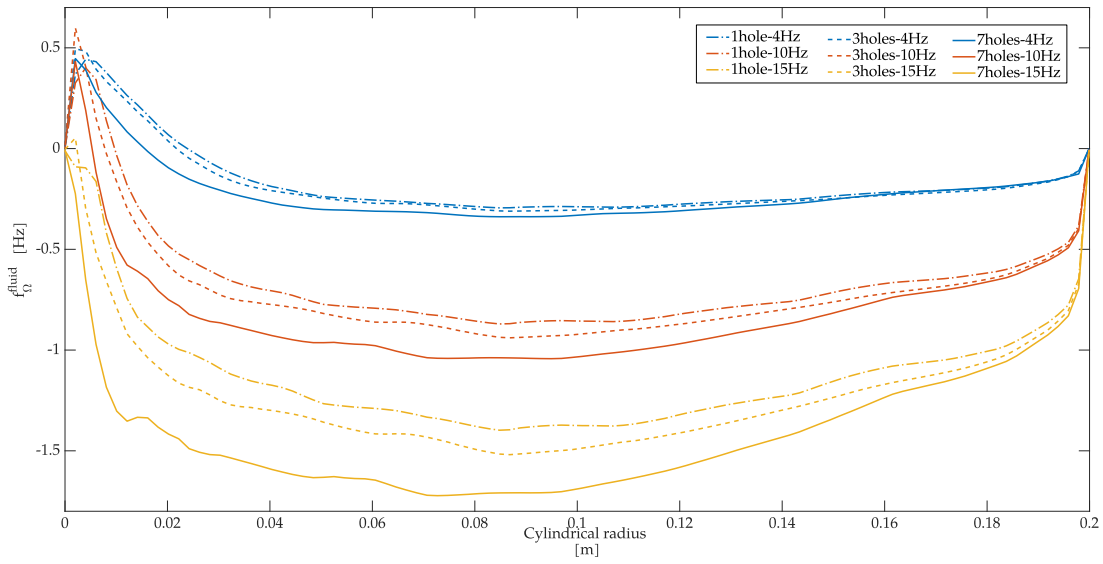

Figure 5.11: Angular velocity (absolute) profile from full 3D finite-element simulation for increasing rotation rates (colours). Different holes configurations are represented: 7 open holes (solid lines), 3 (dashed), and 1 (dash-dotted).

5.2.3 Comparison with the experiment

The (absolute) amplitude of the angular velocity from the 3D finite-element simulation is much closer to the experimental profiles. In order to compare them, we show a superposition of both profiles for the same configuration.

We focus on the effect of the shell rotation rates for a given open holes configuration. In Figure 5.12 we show velocity profiles obtained from both experimental data inversions and finite-element simulations, for 7 open holes for increasing shell rotation rates. Profiles from numerics and experimental data are overall pretty consistent, with the same amplitude and global structure. They differ significantly only in the regions where the inversion is not to be trusted, as symbolised by the grey areas in Figure 5.12.

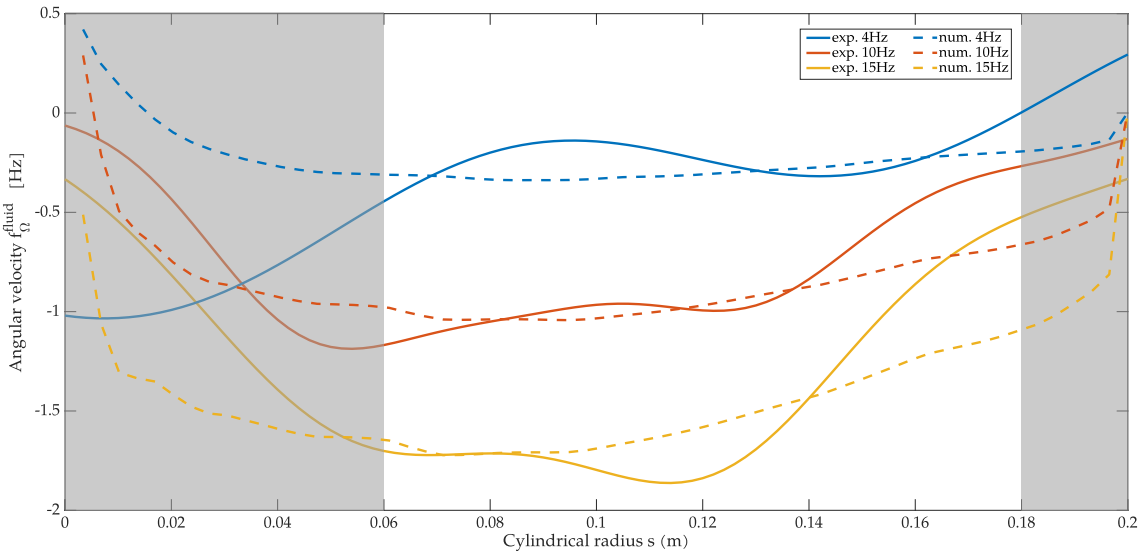

Figure 5.12: Angular velocity profiles obtained with full 3D finite-element simulation for increasing rotation rates (dashed lines) and real data inversion (solid lines) for the 7 open holes configuration and increasing rotation rates: 4 Hz (blue), 10 Hz (brown) and 15 Hz (yellow).

We seem to observe that the holes-driven flow amplitude is mostly proportional to the shell rotation rate. We also remark that the experimental profiles display some radial oscillations that are not reproduced by the simulations. Those are a signature from the mode collection again, as mentioned in Chapter 4, due to the fact that the mode collection we managed to extract does not fully constrain the inversion. This effect is especially strong on the lower 4 Hz rotation rate, where the flow splittings are rather small, hence difficult to accurately extract (and separate from the rotational splittings).

We started to investigate the influence of the number of open holes. We remarked that the flow amplitude decreases with the number of open holes, as predicted by the finite-element simulations. However this leads to small flow splittings that are in turn more difficult to accurately extract. This is still work in progress and we currently have too few reliable inverted velocity profiles to be able to deduct a clear trend on the influence of the number of open holes.

5.3 Physical description of the flow

We now try to understand the physical mechanisms at play to interpret the observations. The difference in pressure caused by centrifugal effect is expected to induce a flow in the holes, which in turn causes a global zonal flow.

We first consider the relation between the pressure gradient and the flow it can produce in the holes. Then we will consider the balance with the bulk to try and recover a relation with the global zonal flow velocity.

5.3.1 In the hole

In presence of rotation, a pressure gradient due to centrifugal effects appear. When there are several openings in the container, at positions with different pressure, a circulation can take place. This is the principle of centrifugal pumps (Shah et al., 2013). The hole we open to induce the centrifugal zonal flow can be considered as a pipe, where the general Bernoulli equation reads (Guyon et al., 2001)

$$(\mathfrak{a}+\mathfrak{K})\frac{1}{2}\rho v_{\text{hole}}^2+\mathfrak{L}\frac{L}{D}\frac{1}{2}\rho v_{\text{hole}}^2=p_{\text{in}}-p_0=p_{\text{cent}}, \tag{5.1}$$

where $D=2$ mm, $L=1$ cm are the diameter and length of the pipe, p_0 and p_{in} are the ambient pressure and the pressure in the cavity respectively.

In this equation, the energy related to advection is proportional to $\mathfrak{a}$ which is the energy coefficient (or kinetic energy correction factor) of the flow. For a uniform flow $\mathfrak{a}=1$ and $\mathfrak{a}=2$ for a Poiseuille flow. $\mathfrak{K}$ is the coefficient of the singular head loss,which may depend on D, and is typically around 1 for an outlet or an inlet. Finally $\mathfrak{L}$ is the regular head loss coefficient (or Darcy-Weisbach friction coefficient), usually given by the Colebrook equation (Brkić, 2011) or Moody diagrams (Darcy, 1857; Moody, 1944).

Typically, for a Reynolds number $Re=v_{hole}D/\nu<10^3$, the flow is a Poiseuille flow, leading to $\mathfrak{L}=64/Re$, whereas $\mathfrak{L}$ is a rugosity-dependent constant for $Re>10^3$, around $\mathfrak{L}=0.01-0.1$. In this equation,

$$p_{\text{cent}}=\frac{\rho(\Omega a)^2}{2}\left(\sin^2\theta_{\text{out}}-\sin^2\theta_{\text{in}}\right)=\frac{\rho(\delta_s\Omega a)^2}{2} \tag{5.2}$$

is the driving pressure due to the centrifugal force, with a the radius of the container and $\delta_s^2=\sin^2\theta_{\text{out}}-\sin^2\theta_{\text{in}}$ with the inlet and outlet holes at θ_{in} and θ_{out} respectively. For $\theta_{\text{out}}=2\theta_{\text{in}}=\pi/3$, which is typically the case for ZoRo, we have $\delta_s^2=1/2$.

The velocity in the hole (or pipe) is thus controlled by a local balance, and can be solved analytically (quadratic polynomial). Using e.g. $\mathfrak{L}=64/Re$, we obtain

$$v_{\text{hole}} = \frac{32L\nu}{D^2(\mathfrak{a}+\mathfrak{K})}\left[\sqrt{1+\left(\frac{\delta_s a\Omega D^2\sqrt{\mathfrak{a}+\mathfrak{K}}}{32L\nu}\right)^2}-1\right] \tag{5.3}$$

$$= 0.4\left[\sqrt{1+\Omega^2/32}-1\right], \tag{5.4}$$

with $a=0.2$ m, $\nu=2.10^{-5}$ m^2/s and $\mathfrak{a}=\mathfrak{K}=2$.

This equation corresponds to a Poiseuille profile in presence of an inlet and an outlet. We recover that $v_{hole} \propto \Omega$ in the regime of large Ω where the regular head loss is negligible, i.e. when $\mathfrak{a}+\mathfrak{K} \gg \mathfrak{L}L/D$ or $Re > 160$. Note that this assumption will also give the correct order of magnitude when $\mathfrak{L}L/D = 0.05 - 0.5 < \mathfrak{a}+\mathfrak{K} = 4$ for $Re > 10^3$. We also verified with finite-elements simulations that this it the correct order of magnitude of v_{hole}.

In this regime, p_{cent} is mainly balanced by $(\mathfrak{a}+\mathfrak{K})\frac{1}{2}\rho v_{\text{hole}}^2$, and the exact solution gives

$$v_{\text{hole}} \approx \frac{\delta_s \Omega a}{\sqrt{\mathfrak{a}+\mathfrak{K}}} - \frac{32L\nu}{D^2(\mathfrak{a}+\mathfrak{K})} \approx \frac{\delta_s \Omega a}{\sqrt{\mathfrak{a}+\mathfrak{K}}}, \tag{5.5}$$

for large Ω, i.e. a constant Rossby number

$$Ro = \frac{v_{\text{hole}}}{\Omega a} \approx \frac{\delta_s}{\sqrt{\mathfrak{a}+\mathfrak{K}}} \sim \frac{1}{4}. \tag{5.6}$$

5.3.2 In the bulk

In the bulk, the inviscid linearised fluid equations govern the flow. They write as (Blackstock, 2000)

$$\partial_t v_s - 2\Omega v_\phi = -\partial_r p \tag{5.7}$$
$$\partial_t v_\phi + 2\Omega v_s = 0. \tag{5.8}$$

At the inlet, the flow goes away from the rotation axis (in the s direction), leading to retrograde columnar vortex, whereas the flow converge towards the outlet, leading to prograde columnar vortex (Aubert et al., 2002), similar to cyclones and anti-cyclones seen in the atmosphere. Due to the positions of the holes, the quasi-geostrophic vortices are aligned and then create a large scale geostrophic flow in the bulk (conveyor belt), a drawing of the flows created by such a mechanism is shown in Figure 5.13.

In the experiments, the size ℓ of these vortices is given by

$$\ell = \max(D, hE^{1/3}), \tag{5.9}$$

where h is the height of the geostrophic column. We may thus expect a change of trend for $D = hE^{1/3}$, i.e. 10 Hz using $D = 2$ mm and $h = 10$ cm. One can thus expect a retrograde bulk flow between the cylindrical radii of the inlet and the outlet. The columnar vortex are balanced by the Ekman drag, leading to a local vorticity

$$\widetilde{\omega} = -v_{\text{hole}}\sqrt{\Omega/\nu}, \tag{5.10}$$

and $v_{\text{hole}} \propto \Omega$, as explicited in eq. (5.5). So this gives for large enough rotation rates (typically > 10 Hz in the experiment),

$$v_\phi^{\text{bulk}} \propto f_\Omega^{3/2}. \tag{5.11}$$

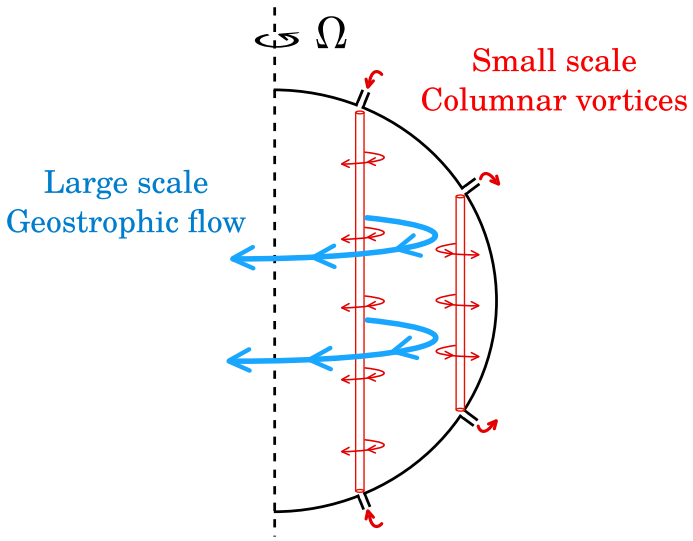

Figure 5.13: Drawing of the expected flow structure. Each hole behave like a centrifugal pump creating columnar quasi-geostrophic vortices, which in turn create a large scale geostrophic flow (Aubert et al., 2002).

5.3.3 Comparison with the experiment

From the inverted velocity profile it is difficult to discriminate the variations due to the inversion itself (limited and influenced by its spatial resolution) and actual physically relevant variations. So we decided to consider the maximum angular velocity within each profile. We compile the (experimental) maximum inverted angular velocity for increasing rotation rates and 7 open holes configuration in Figure 5.14 (in log-scale). The predicted $f_\Omega^{3/2}$ law is added in dashed line for comparison. Here the pre-factor used is 0.04.

The experimental inverted velocity can be explained with this law for rotation rates, above 10 Hz. However more experimental data would be welcomed to complete the dataset and be more confident in whether we verify the predicted scaling.

We can consider a more precise force balance by supposing that the azimuthal velocity $v_\phi^{col} \approx \omega \ell_\phi$ of the columnar vortex exerts a viscous drag on the bulk of the fluid: a bulk column of area $\sim ah$ is put in rotation by the vortex surface, of $\sim N\ell_\phi h$ in the experiments (with N the number of columns, i.e. of opened holes), and of $\sim ah$ in the COMSOL axisymmetric simulations. Using the surface area ratio as an estimate of the coupling efficiency, one can thus expect a bulk azimuthal velocity of

$$v_\phi^{bulk} \approx \frac{N\ell_\phi}{a} v_\phi^{col} \approx -\frac{N\ell_\phi^2}{a} v_{hole} \sqrt{\Omega/\nu}, \tag{5.12}$$

where $N = a/\ell_\phi$ allows to retrieve the case of COMSOL axisymmetric simulations. In the experiments, this gives, for large enough rotation rates (typically > 10 Hz),

$$v_\phi^{bulk} \approx -\frac{N\,\delta_s\,\Omega^{3/2}\ell^2}{\sqrt{\nu(\mathfrak{a}+\mathfrak{K})}} = -3.5\cdot 10^{-3}\, N\, f_\Omega^{3/2} \tag{5.13}$$

with $\ell = D$ and $f_\Omega = \Omega/(2\pi)$ is the rotation rate in Hz.

For the experimental values with 7 open holes, the pre-factor is 0.03, very close to the experimental value of 0.04.

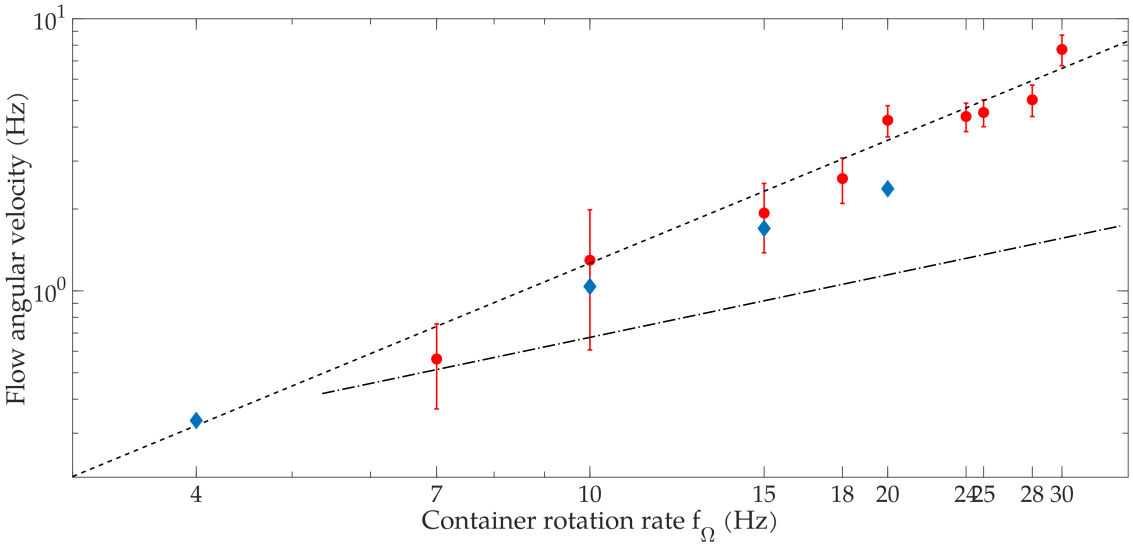

Figure 5.14: Experimental absolute angular velocity (averaged in obtained with inversion of data at increasing rotation rates, for 7 open holes configurations (red circles). Finite-element solutions for same configuration are shown in blue diamonds for comparison. The predicted relation with $f_\Omega^{3/2}$ is given in dashed black line, here with prefactor 0.04. For comparison the f_Ω slope is given in dash-dotted black line.

5.4 Discussion

Flows driven by the centrifugal force through numerous narrow holes are very rich both by the parameters we can vary and its physical mechanisms that is close to convective zonal flows. We have reproduced a zonal flow induced by mechanical energy injection at small scale, which is comparable to e.g. Cabanes et al. (2017).

However the open holes change the boundary condition from a no-slip to a no-stress boundary, and this is expected to affect the acoustic modes. Indeed when we consider low rotation rates, the splittings do not seem to follow a clear slope anymore. As seen in Figure 5.15, the flow splitting seem to hit a plateau around 5 Hz for several mode. In particular for the fundamental mode ${}_0\mathcal{S}_1$, the flow splitting is minimum at 5 Hz and goes up again at lower rotation rates.

In order to investigate this effect, we looked at the splitting at rest (no flows, no rotation) but with the holes open. In Figure 5.16, we show a comparison between acoustic spectra at rest for all closed holes (top) and all open holes (bottom). The splitting at rest (around 4 Hz) for all open holes is consistent with the observed trend from 5 Hz downwards. Note that this effect is most important for $n = 0$ modes and almost negligible for $n > 0$ modes.

It is now clear that this splitting is purely due to the change of boundary conditions, and is not to be attributed on actual flow velocity in the cavity. In order to investigate this issue further, we ran full 3D finite-element simulations both at rest and with rotation, and retrieve the same results.

One particular fact is that the influence of the hole dimension (diameter D and length L). Indeed the influence of the opening depends on the hole geometry, and in particular the D/L ratio. When the ratio is large the hole is closer to a simple opening

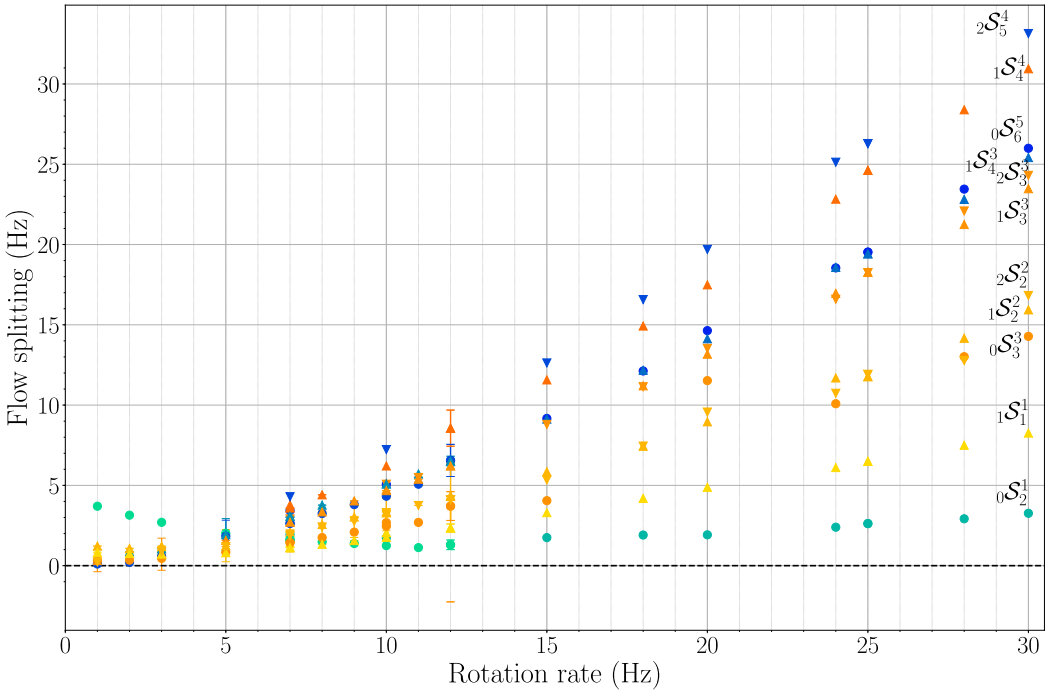

Figure 5.15: Flow splitting for increasing rotation rates for 7 open holes configuration. Symbols give the n number, colour the m number. The flow splitting is zero for solid-body rotation at the container rotation rate.

and when it is large, it verifies the asymptotic relations valid for pipes. We plotted in Figure 5.17 the evolution of the acoustic eigen frequencies with the length of the pipe L for different open holes configurations. We can see that the free boundary condition is the key element here as there is no significant difference between closed holes (closed at the end of the hole), dashed red, and no holes at all, black line. At rest the frequency shift seem proportional to the number of holes. We also remark the steep slope near $L = 0$, where the cavity is almost in contact with the outside fluid, and the change of slope seems to be around $L = 0.2$ cm, which corresponds to the experimental hole diameter.

We are now convinced that the local change of boundary condition has a non-negligible effect on acoustic frequencies. It is possible to take this effect into account using the theory developed by Moldover et al. (1986). We started to implement his theory, but it is still work in progress. We show some values of splitting due to open holes (at rest) obtained with the two methods, finite-element simulations and Moldover et al. (1986)'s theory in Table 5.1, along with the splittings measured in the experiment.

As we can see the theorerical implementation still needs improvement, although it retrieves the correct relative splittings. The finite-element calculations values are quite close to the experiment, once again validating its relevance for the experimental apparatus.

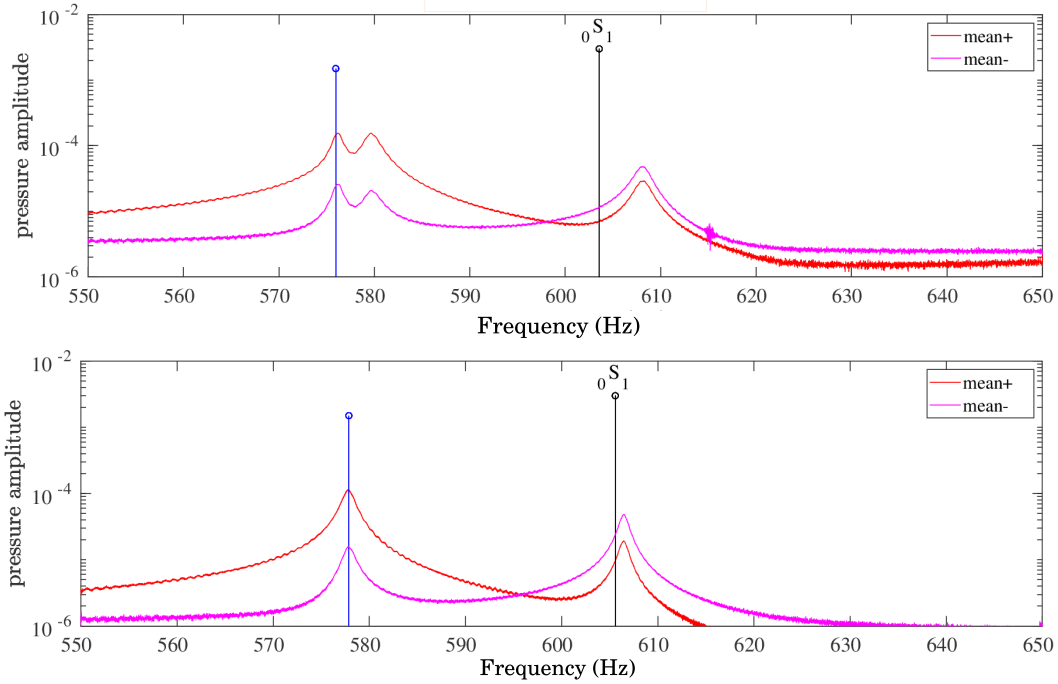

Figure 5.16: Experimental acoustic spectra centred around ${}_0\mathcal{S}_1$ at rest with 7 open holes configuration (top) and all closed holes (bottom). The predicted frequencies for a closed container are shown in vertical lines.

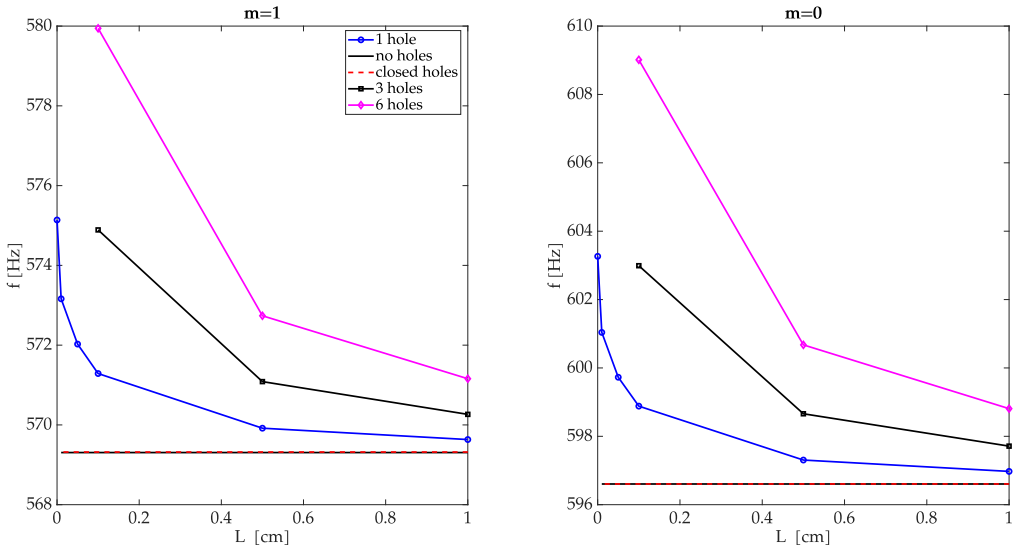

Figure 5.17: Evolution of acoustic mode frequency for the fundamental multiplet ${}_0\mathcal{S}_1$, left $m = 1$, right $m = 0$. The colours correspond to different number of open holes (0 up to 6), and no holes (smooth container).

	Mode	Exp.	COMSOL	Theory
7 open holes	${}_0\mathcal{S}_1^1$	3.47	2.00	0.52
	${}_0\mathcal{S}_2^1$	4.5	2.6	0.69
	${}_0\mathcal{S}_2^2$	1.59	0.79	0.20
3 open holes	${}_0\mathcal{S}_1^1$	1.75	0.95	
	${}_0\mathcal{S}_2^1$	2.74	1.23	
	${}_0\mathcal{S}_2^2$	1.15	0.51	

Table 5.1: Acoustic splitting (Hz) at rest for 7 and 3 open holes, values from the experimental measures, finite-element calculations and theory from Moldover et al. (1986).

Key points

We presented some preliminary results we have on a zonal flow driven by centrifugal pumps. So far we did the following:

Successful imaging of centrifugal pumps driven flow using MAV

Verification with finite-element simulation (axisymmetric and 3D)

First insights on theoretical scalings

Discussion around the influence of the boundary condition modification in presence of holes

6

Conclusions and Perspectives

The more I learn, the more I know that I don't know.

- Plato, *Apology*

6.1 Conclusions

We implemented a new velocimetry technique called modal acoustic velocimetry (MAV). This technique relies on the acoustic resonances of the fluid cavity. The resonance frequencies are sensitive to the resonating medium internal properties but also to its velocity. In particular azimuthal flows can be linked to a splitting in mode frequency. This feature has been used in helio-seismology to image the Sun's internal flows. Recently a laboratory equivalent was proposed by Triana et al. (2014). Following this pioneering work, we build a new experimental apparatus with the long term goal of studying thermally driven zonal flows using MAV. The new ZoRo experiment is an air-filled oblate spheroid rotating around its symmetry axis. We conceived, manufactured and built the ZoRo experiment, and implemented the measurements chain needed to apply MAV on it.

In order to isolate the flow velocity influence on the acoustic spectra we have used theoretical developments to predict the main relevant effects that influence the acoustic spectrum. We use the perturbation theory approach and linearly superpose the deviations from the initial reference model, the diffusionless gaseous sphere at rest. To do so we followed the existing work from various domains that have used normal modes. We considered the flow influence with the framework used by astero-seismologists (Aerts et al., 2010), the diffusion effects (thermal and viscous) are taken into account thanks to the metrologist's framework (Moldover et al., 1986) and finally the expression of the geometrical effect comes from both seismologists (Dahlen and Tromp, 1998) and metrologists (Mehl, 2007). Combining all those different theories allowed us to fully describe the acoustic spectrum corresponding to the experimental set-up and better understand the spectra measured in the experiment. We also compared those results to finite-element simulations, using the commercial software COMSOL. We managed to create realistic theoretical synthetic spectra that correspond well to the data obtained from the ZoRo measurements.

Having the theoretical description is needed to solve the inverse problem, where we measure the acoustic splittings and try to retrieve the flow field. We then test the inversion routine against synthetic cases. We choose realistic and relevant flows with increasing complexity, and try to retrieve the given velocity profile with acoustic modes inversion. We first invert solid-body rotation of the fluid, then spin up using velocity profiles predicted with theoretical calculations. Then we confront the inversion against realistic profiles of zonal flows driven by thermal convection, obtained with numerical simulations by Guervilly and Cardin (2017). We verified that MAV is a suitable measurement technique to retrieve zonal flows, even those that display complicated velocity profiles with multiple jets.

Finally we apply the routines we developed on an experimental flow. We choose to study a centrifugally driven zonal flow, obtained by opening small holes in the container while in rotation. It is a mechanically induced flow where energy is injected as small-scale and back-cascaded toward global zonal flow, similar to what we expect would happen with a thermally driven flow. We successfully retrieved relevant velocity profiles using MAV, with spatial resolution down to a few centimeters. We are able to discuss some of the mechanisms driving the zonal flow structures and the different regimes we can attain.

In conclusion, we showed that MAV is a well-suited measurement technique to study zonal flows. MAV allows to retrieve a global velocity profile with relatively high spatial resolution, while being non-intrusive and without needing to seed the fluid. We fully developed both the experimental, theoretical and numerical tools to apply MAV on ZoRo. This forms the first step towards the study of zonal flows driven by thermal convection in a regime closer to that of natural systems than existing experiments.

6.2 Perspectives

We present some possible perspective of future work, including some unfinished applications that were not included in this manuscript. We then suggest some ideas for further possible experiments and application of MAV.

6.2.1 Improvements on MAV technique

Splitting extraction improvements

In the continuity of the present work, we can use mechanically driven flows that we mentioned to further improve the MAV technique. We showed in Chapter 4 synthetic cases of spin up. We would like to reproduce the synthetic spectra and velocity profile using real experimental data, on both spin up and down. In order to do so, we need a precise synchronisation between the motor jerk and the acoustic signal. We recently implemented this on the experimental apparatus, which should allow us to investigate those flows.

A second limitation is the frequency resolution of the acoustic spectra. Since the flow is time-dependent, in order to capture its time variation, the acquisition time needs to be short (compared to the flow variation). However the frequency resolution is inversely proportional to the acquisition time: 10 s of signal allows a resolution down to 0.1 Hz while 1 s gives only one data point every 1 Hz, which is the typical half-width of the acoustic resonance peak. In order to tackle this issue, we previously used an equivalent technique on the spectrum, stacking several iteration of the same flow moment to cancel out the noise. But in order to significantly improve the frequency resolution, some sort of

interpolation is needed which is not satisfactory. In order to solve this issue, we plan to rely on the phase of the Fourier transform. The phase is not affected by the noise so can easily be averaged over many iteration to improve the peak frequency determination.

We are currently investigating how the study of the signal phase can bring additional information for data analysis. We have 7 electrets uniformly distributed on each latitude, so we should be able to fully discriminate the m of any mode up to 3 by performing a Laplace transform. This would further help mode identification and could significantly increase the number of available modes. This is of particular interest since the small m modes are very close to each other (geometry splitting in m^2 at first-order), so they are currently difficult to extract.

More accurate synthetic predictions of acoustic spectra

In particular we would like to take into account the coupled terms between ellipticity and rotation that we saw can make a difference when rotation rate starts to get faster. To do so we can use the eigenfunctions corresponding to the spheroid up to second-order (instead of the spherical functions). This would define spheroidal Ledoux coefficients and the spheroidal sensitivity kernels, allowing more accurate flow inversions.

We would also like to include second-order perturbation in rotation, as Vidal et al. (2020) shows that second-order Coriolis terms should be visible at ZoRo's rotation rate range (starting from 20 Hz). We would also like to include centrifugal effects that is also second-order in rotation. Expression of both of these additional terms have been proposed by Dahlen and Tromp (1998), but some theoretical considerations are needed to adapt it for ZoRo.

Change of working fluid

From the experimental side, it would be interesting to try and change the working fluid. Preliminary studies showed that different gases may have very different attenuation process when the bulk contribution can be larger than the boundary's. A gas of particular interest would be SF_6 which has a very small dissipation, hence would display thinner peaks in its acoustic spectra than air. This feature could allow more precise mode identification and frequency measurements.

MAV would also be of particular interest for experiments using liquid metals, since they are opaque (in the visible wavelength). However attempts to use MAV on liquid sodium have been unsuccessful so far. The main concern would be the ratio of acoustic impedances ($\propto \rho c^2$) between the container and the fluid. It is very large for gases enclosed in metal shells ($\sim 10^6$ for air in aluminium, as in ZoRo), but not for liquids (~ 4 for water in plexiglas and ~ 50 for liquid sodium in aluminium, which was tested so far). The container impedance is still larger so the method should be able to work but we expect the resonances to be much more difficult to measure. It would thus be interesting to start by trying to apply MAV on simpler liquids such as water. Acousticians recently managed to efficiently excite acoustic waves in a water tank (Novak et al., 2018) that could help to implement MAV in such conditions. Such change of working fluid is possible thanks to the gas-tightness of ZoRo apparatus, and it would generalise MAV to be usable in both gases and liquids.

6.2.2 Geophysical applications

Centrifugal holes driven flows

We presented a first set of data along with their inverted velocity profiles. However as discussed in Chapter 5, we have not fully exploited the parameters available in the experimental conditions. We aim to further investigate the influence of the number of open holes to see if the data agree with the theoretical predicted evolution.

Additionally, the open holes induce a splitting at rest by changing the boundary conditions locally. This caused the acoustic splittings to be intricate at low rotation rates. In order to separate the two effects, it would be useful to differentiate the two $\pm m$ modes. In order to do that we tried to track each peak based on its amplitude. This method was not very successful as the amplitudes tend to vary from on rotation rate to another.

We are currently investigating the phase of the Fourier transform of the acoustic signal. So far we only used its module to extract the acoustic spectrum (and marginally the dissipation to help distinguish the overtones). But the phase changes depending on the mode, and in particular depending on its sign (Ecotiere et al., 2004). The phase could also serve to improve the spectral resolution of the mode eigenfrequency.

Longitudinal librations

Longitudinal librations are a relevant type of geophysical forcings that mechanically induce zonal flows. And it is a type of flow that we can easily implement with the ZoRo experimental set-up. They consist in having the container rotation rate oscillate in time (while keeping the same rotation axis). They are characterized by the mean rotation rate Ω_0 (or offset), the amplitude $A_{\rm lib}$ and frequency $\omega_{\rm lib}$ of the oscillations. The flow induced in the bulk by such container movements can be theoretically predicted for small amplitude flows (small Rossby number) in the frame rotating at Ω_0, by (Deleplace, 2005)

$$v_\phi(r,\theta,t) = A_{\rm lib} r \sin\theta \frac{Ek^{1/2}}{(Ek+\omega_{\rm lib}^2 L^3)^{1/2}} \sin\left[\omega_{\rm lib} t + \arctan\left(-\frac{\omega_{\rm lib} L^{3/2}}{Ek^{1/2}}\right)\right] \tag{6.1}$$

where $L = \sqrt{a - r^2\sin^2\theta}$ is the column height and Ek is the Ekman number.

An example of longitudinal libration flow is represented in the left panel of Figure 6.1 against time. It corresponds to $A_{\rm lib} = 1$ Hz and the period $T_{\rm lib} = 7$ s. Longitudinal librations are interesting because of the very large variation of flows they can induce depending on the regime. Depending on the libration parameters ratio, it can be considered as a succession of spins up and down, create inertial waves (Aldridge and Toomre, 1969; Sauret et al., 2013), or even instabilities (Cébron et al., 2012, 2014) that can be turbulent and create large scale zonal mean flows (Noir et al., 2010; Sauret et al., 2010; Busse, 2010; Le Dizès, 2015). Librations are also interesting from the geophysical point of view as they are part of the mechanical forcings observed in geophysical bodies that have the potential to affect the energy transfer (Noir et al., 2009; Le Bars et al., 2015; Vidal and Cébron, 2017). We show in the right panel of Figure 6.1, the regimes we can attain within ZoRo experimental conditions (in green) along with the predicted values for the regime change.

It would be interesting to try to recover the different predicted regimes, and measure the full flow as existing experimental study of longitudinal libration only acquire data on bi-dimensional plane at the time (mostly due to the laser sheet geometry in the PIV technique they use).

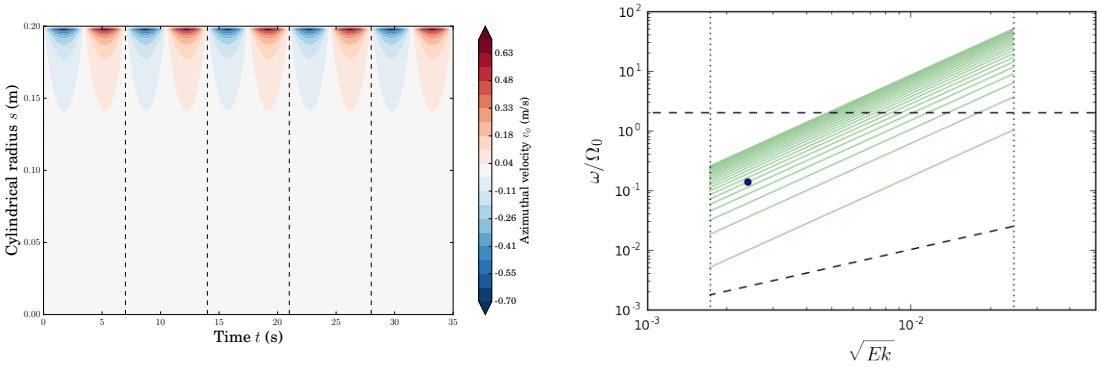

Figure 6.1: Left: Azimuthal velocity in the frame rotating at Ω_0 for longitudinal libration of amplitude $A_{\text{lib}} = 1$ Hz, period $T = 7$ s against cylindrical radius s and time. The start of each libration period is indicated by dashed lines. Within a period the fluid goes through a retrograde and prograde phase where it is slower (resp. faster) rotating than the average rate Ω_0. Right: Librations regimes separated by dashed lines, in green the attainable regimes within ZoRo. The parameters corresponding to the left panel velocity field is indicated by the blue circle.

Thermal gradients

The next step towards realistic zonal flows is to add the thermal ingredient into the experiment. This comes with several challenges, some that we already started to tackle.

Experimental adjustments ZoRo was conceived with this goal in mind, so it can accommodate all additional thermal sources and sensors. The thermal gradient is imposed from the outside of the container using infra-red radiants (ref. 198-8529 from RadioSpare) mounted on the frame (see Appendix C for details). The container presents two types of pre-drilled holes intended for temperature sensors. The first kind are non-through holes where we mounted digital temperature sensors (ref. D18B20 from Maxim Arduino) in contact with the container. They are distributed at three latitudes on each hemisphere (see Appendix C for detailed positions). The role of these sensors is to measure the overall container temperature with a twofold purpose, first to know what is the surface temperature in contact with the fluid cavity, and second to monitor this temperature in order to ensure that the container temperature is below the maximum working temperature of the instrumentation in contact with it (speakers, electrets, wires...). Both the infra-red heating and container temperature sensors have been successfully tested on ZoRo.

The second kind of temperature sensors are NTC thermistors (ref. TT5-10KC3-70 from TEWA Thermico Ltd), mounted in through holes (the holes used to induced the centrifugal flow) and they have the sensitive component in contact with the gas inside the cavity. We aim to use the thermistors to track the temperature anomalies that are expected to be carried by the large scale zonal flow (Guervilly and Cardin, 2017), in order to have a complementary velocity measurements as well as an insight on the temperature in the cavity. This is the reason why a lot of sensors are needed (56 can be mounted on the container at the same time). One challenge arises from the fact that the acquisition wires need to go through a slip ring with limited entries (36 at most). In order to solve this problem we choose to multiplex the thermistors' signals. The idea is to successively measure the N wanted channels during a period T each, creating only one (longer) data

signal of length NT that would contain all the data from all the channels depending on the time: from 0 to T is the data from channel 1, T to $2T$ from channel 2, etc. We adapted and manufactured an electronic card for this purpose (original electronic card design by Yoann Corre, Menaut (2019)). Our design is given in Appendix E, we successfully tested it in "desk" conditions and plan to mount it on ZoRo to test it in experimental conditions.

Theoretical developments One of the major difficulty of adding thermal gradient is the sensitivity of sound speed with temperature, as observed in Chapter 3.

The theoretical influence of local change of temperature on normal modes has been explicitly proposed only recently by Koulakis et al. (2018). Dahlen and Tromp (1998)'s formalism allow local changes of density and elastic parameters, and we plan to apply it to our acoustic case.

This was one of the objective of Arnaud Piet's Master thesis (Piet, 2019), partly reproduced in Appendix F. We do not fully understand how to predict acoustic spectra in presence of any temperature profile yet. One of the upcoming work is to tackle this problem again building on Piet (2019)'s preliminary work.

We already ran some preliminary finite-element simulations that gave us some insights on the expected results. We would also like to extend the method used in Vidal et al. (2020) to include thermal gradients and compare it with future experimental results.

Thermal wind experiment Thermal winds present the advantage of including the thermal ingredient we were missing while being a well-known stable flow with analytical solutions (Vallis, 2017).

We ran some preliminary experiments of thermal winds and measured the corresponding spectral acoustic response. This was part of the Master thesis of Piet (2019). An example of acoustic spectra with both rotation and thermal gradient, is plotted in Figure 6.2.

While doing so, we ran into several difficulties. First since the experimental system allows only either heating or cooling (not both at the same time), the experiment must be conducted in a transient regime where the average temperature either goes up or down. As already discussed in Chapter 3, this causes the spectrum to drift in frequency, which can be observed on Figure 6.2. This drift complicates the spectrum interpretation, enforcing the need to have a reliable theoretical model for local changes in the fluid's temperature.

Those preliminary qualitative observations are nonetheless very encouraging as we can clearly see a signature of those thermally driven flows compared to a simple solid-body rotation.

Change of pressure

ZoRo is capable of supporting over and under pressure in its cavity, which allows change of fluid but also controlled pressure variations in the cavity.

This feature is of great interest because in gases a change in pressure only change the gas density (at first order). This means that a change of pressure is directly linked (mainly proportional) to a change of Ekman number. To double the pressure is equivalent to dividing the Ekman number by 2. This would allow even smaller Ekman number, allowing us to study regimes even closer to what can be seen in the natural systems.

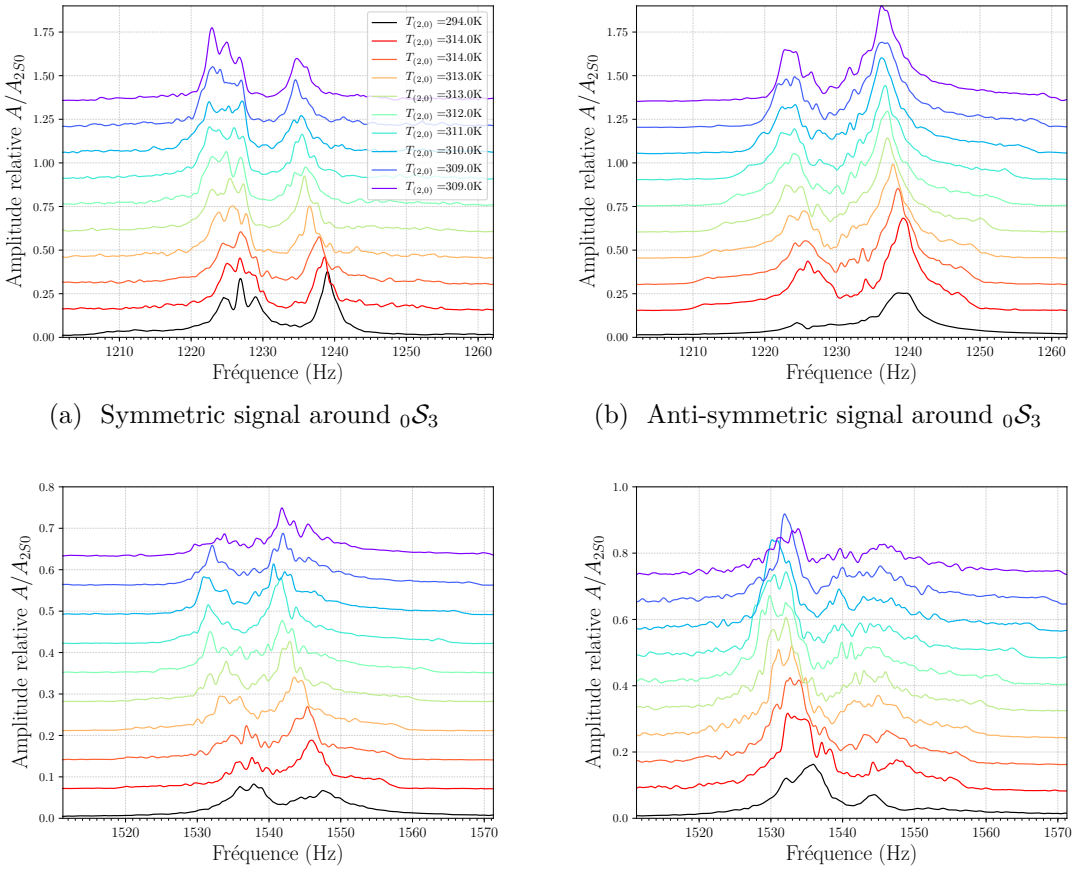

(a) Symmetric signal around ${}_0\mathcal{S}_3$

(b) Anti-symmetric signal around ${}_0\mathcal{S}_3$

(c) Symmetric signal around ${}_0\mathcal{S}_4$

(d) Anti-symmetric signal around ${}_0\mathcal{S}_4$

Figure 6.2: Acoustic spectra for a selection of modes for a solid-body rotation (black) and a equatorial cooling with rotation (colours). Left (right) column are the sum (difference) of acoustic signal respectively. During the cooling, the apparent temperature deduced from the ${}_2\mathcal{S}_0$ modes frequency goes from 314 K (red) down to 309 K (dark blue). From Piet (2019).

Change of geometry

We chose spheroidal geometry with the idea of only partially lifting the degeneracy at rest, in order to have a clear distinction when there is a velocity involved (apparition of peaks). However we are now confident in all the mode identification and extraction routines, and the experimental acoustic spectra have proven to be strikingly well predicted by theory and numericals.

It would be interesting to consider a non-axisymmetric container this time such as a triaxial ellipsoid. This would lift all degeneracy at rest, and would help distinguish the $\pm m$ of a multiplet, hence bring additional information on the flow direction.

Ellipsoids are also relevant from a planetary point of view, since they allow even more instabilities than an axisymmetric body (Noir et al., 2012; Grannan et al., 2014; Le Bars et al., 2015; Vidal and Cébron, 2017).

Acoustic spectra carry a lot of information on both the cavity where they resonate and on the medium they propagate in. They are a very sensitive and completely measurable quantity, while requiring very little instrumentation. In that sense they are the perfect observational technique. However this quality is also what makes this technique so difficult to use, as a lot of parameters influence the acoustic spectra sometimes even interacting with each other. Retrieving only one effect and isolating its signature in the acoustic spectrum is the challenge of MAV. I believe we started to make a dent on this problem, explaining one effect after another, hopefully paving the way for even more interesting applications of this technique.

Bibliography

Aerts, C., Christensen-Dalsgaard, J., and Kurtz, D. W. (2010). *Asteroseismology*. Springer Science & Business Media.

Afanasyev, Y. D. and Wells, J. (2005). Quasi-two-dimensional turbulence on the polar beta-plane: Laboratory experiments. *Geophysical & Astrophysical Fluid Dynamics*, 99(1):1–17.

Albrecht, H.-E., Damaschke, N., Borys, M., and Tropea, C. (2013). *Laser Doppler and Phase Doppler Measurement Techniques*. Springer Science & Business Media.

Aldridge, K. D. and Toomre, A. (1969). Axisymmetric inertial oscillations of a fluid in a rotating spherical container. *Journal of Fluid Mechanics*, 37(2):307–323.

Aubert, J., Jung, S., and Swinney, H. L. (2002). Observations of zonal flow created by potential vorticity mixing in a rotating fluid. *Geophysical Research Letters*, 29(18):23–1–23–4.

Aurnou, J. M., Calkins, M. A., Cheng, J. S., Julien, K., King, E. M., Nieves, D., Soderlund, K. M., and Stellmach, S. (2015). Rotating convective turbulence in Earth and planetary cores. *Physics of the Earth and Planetary Interiors*, 246:52–71.

Aurnou, J. M. and Olson, P. L. (2001). Experiments on Rayleigh–Bénard convection, magnetoconvection and rotating magnetoconvection in liquid gallium. *Journal of Fluid Mechanics*, 430:283–307.

Backus, G. and Gilbert, F. (1961). The Rotational splitting of the free Oscillations of the Earth. *Proceedings of the National Academy of Sciences of the United States of America*, 47(3):362–371.

Bayes, T. and Price, n. (1763). LII. An essay towards solving a problem in the doctrine of chances. By the late Rev. Mr. Bayes, F. R. S. communicated by Mr. Price, in a letter to John Canton, A. M. F. R. S. *Philosophical Transactions of the Royal Society of London*, 53:370–418.

Bender, C. M. and Orszag, S. A. (1978). *Advanced Mathematical Methods for Scientists and Engineers*. New York, Nouvelle-Zélande, France, Pays multiples.

Benton, E. R. and Clark, A. (1974). Spin-Up. *Annual Review of Fluid Mechanics*, 6(1):257–280.

Bergliaffa, S. E. P., Hibberd, K., Stone, M., and Visser, M. (2004). Wave equation for sound in fluids with vorticity. *Physica D: Nonlinear Phenomena*, 191(1):121–136.

Bertero, M. (1986). Regularization methods for linear inverse problems. In Talenti, G., editor, *Inverse Problems*, Lecture Notes in Mathematics, pages 52–112, Berlin, Heidelberg. Springer.

Blackstock, D. T. (2000). *Fundamentals of Physical Acoustics*. John Wiley & Sons.

Bolton, S. J. and Team, t. J. S. (2010). The Juno Mission. *Proceedings of the International Astronomical Union*, 6(S269):92–100.

Bourouina, T., Exertier, A., Spirkovitch, S., Chaumet, B., and Pleska, E. (1997). Preliminary results on a silicon gyrometer based on acoustic mode coupling in small cavities. *Journal of Microelectromechanical Systems*, 6(4):347–354.

Brito, D., Nataf, H.-C., Cardin, P., Aubert, J., and Masson, J.-P. (2001). Ultrasonic Doppler velocimetry in liquid gallium. *Experiments in Fluids*, 31(6):653–663.

Brkić, D. (2011). Review of explicit approximations to the Colebrook relation for flow friction. *Journal of Petroleum Science and Engineering*, 77(1):34–48.

Bruneau, M., Garing, C., and Leblond, H. (1986). A rate gyro based on acoustic mode coupling. *The Journal of the Acoustical Society of America*, 80(2):672–680.

Busse, F. H. (1994). Convection driven zonal flows and vortices in the major planets. *Chaos: An Interdisciplinary Journal of Nonlinear Science*, 4(2):123–134.

Busse, F. H. (2010). Mean zonal flows generated by librations of a rotating spherical cavity. *Journal of Fluid Mechanics*, 650:505.

Byrd, R. H., Schnabel, R. B., and Shultz, G. A. (1988). Approximate solution of the trust region problem by minimization over two-dimensional subspaces. *Mathematical Programming*, 40(1):247–263.

Cabanes, S., Aurnou, J., Favier, B., and Le Bars, M. (2017). A laboratory model for deep-seated jets on the gas giants. *Nature Physics*, 13(4):387–390.

Cao, H. and Stevenson, D. J. (2017). Zonal flow magnetic field interaction in the semi-conducting region of giant planets. *Icarus*, 296:59–72.

Cébron, D., Le Bars, M., Noir, J., and Aurnou, J. M. (2012). Libration driven elliptical instability. *Physics of Fluids*, 24(6):061703.

Cébron, D., Vantieghem, S., and Herreman, W. (2014). Libration-driven multipolar instabilities. *Journal of Fluid Mechanics*, 739:502–543.

Chandrasekhar, S. (1964). A General Variational Principle Governing the Radial and the Non-Radial Oscillations of Gaseous Masses. *ApJ*, 139:664.

Chang, C. T. M. (1971). Natural Resonant Frequency of a Prolate Acoustical Resonator. *The Journal of the Acoustical Society of America*, 49(3A):611–614.

Chang, C. T. M. (1972). Natural Resonant Frequencies of an Oblate Acoustical Resonator. *The Journal of the Acoustical Society of America*, 51(1A):1–5.

Chaplin, W. J. and Basu, S. (2008). Perspectives in Global Helioseismology and the Road Ahead. *Solar Physics*, 251(1):53–75.

Christensen, U. R. (2002). Zonal flow driven by strongly supercritical convection in rotating spherical shells. *Journal of Fluid Mechanics*, 470:115–133.

Christensen-Dalsgaard, J. (2002). Helioseismology. *Reviews of Modern Physics*, 74(4):1073–1129.

Christensen-Dalsgaard, J., Dilke, F. W. W., and Gough, D. O. (1974). The Stability of a Solar Model to Non-Radial Oscillations. *Monthly Notices of the Royal Astronomical Society*, 169(3):429–445.

Christensen-Dalsgaard, J. and Gough, D. O. (1976). Towards a heliological inverse problem. *Nature*, 259(5539):89–92.

Cohen-Tannoudji, C., Diu, B., and Laloë, F. (2018). *Mécanique quantique. Tome I.* EDP sciences, Les Ulis, France.

Condie, S. A. and Rhines, P. B. (1994). A convective model for the zonal jets in the atmospheres of Jupiter and Saturn. *Nature*, 367(6465):711–713.

Cowell, W. R. (1984). *Sources and Development of Mathematical Software*. Prentice-Hall, Englewood Cliffs, N.J. OCLC: 10300381.

Cowling, T. G. (1941). The Non-radial Oscillations of Polytropic Stars. *Monthly Notices of the Royal Astronomical Society*, 101(8):367–375.

Cowling, T. G. and Newing, R. A. (1949). The Oscillations of a Rotating Star. *ApJ*, 109:149.

Dahlen, F. A. (1968). The Normal Modes of a Rotating, Elliptical Earth. *Geophysical Journal International*, 16(4):329–367.

Dahlen, F. A. (1976). Reply [to "Comments on 'The correction of great circular surface wave phase velocity measurements from the rotation and ellipticity of the Earth' by F. A. Dahlen"]. *Journal of Geophysical Research (1896-1977)*, 81(26):4951–4956.

Dahlen, F. A. and Tromp, J. (cop. 1998). *Theoretical Global Seismology*. Princeton University Press, Princeton, N.J., Etats-Unis d'Amérique.

Darcy, H. (1857). *Recherches expérimentales relatives au mouvement de l'eau dans les tuyaux*. Imprimerie impériale, Paris, France.

Deleplace, B. (2005). *Approche expérimentale de la turbulence par mesures de viscosité apparente dans les fluides en rotation: application au couplage visco-magnétique de l'interface noyau-manteau*. PhD thesis, Atelier national de reproduction des thèses„ Grenoble, France.

Diu, B., Guthmann, C., Lederer, D., and Roulet, B. (1989). *Éléments de physique statistique*. Hermann, Paris, France.

Dowling, T. E. (1995). Dynamics of Jovian Atmospheres. *Annual Review of Fluid Mechanics*, 27(1):293–334.

Duck, P. and Foster, M. (2001). Spin-up of Homogeneous and Stratified Fluids. *Annual Review of Fluid Mechanics*, 33(1):231–263.

Dupire, P. and Bruneau, M. (1998). TRANSIENT BEHAVIOUR OF ACOUSTIC GYROMETERS. *Journal of Sound and Vibration*, 212(1):37–59.

Dziewonski, A. M. and Anderson, D. L. (1981). Preliminary reference Earth model. *Physics of the Earth and Planetary Interiors*, 25(4):297–356.

Ecotiere, D., Tahani, N., and Bruneau, M. (2004). Inertial Coupling of Resonant Normal Modes in Rotating Cavities: Acoustic Gyrometers for High Rotation Rates. *ACTA ACUSTICA UNITED WITH ACUSTICA*, 90:8.

Espa, S., Nitto, G. D., and Cenedese, A. (2010). The emergence of zonal jets in forced rotating shallow water turbulence: A laboratory study. *EPL (Europhysics Letters)*, 92(3):34006.

Galperin, B. and Read, P. L. (2016). *Zonal Jets: Phenomenology, Genesis, and Physics*. Cambridge University Press.

Gastine, T., Heimpel, M., and Wicht, J. (2014). Zonal flow scaling in rapidly-rotating compressible convection. *Physics of the Earth and Planetary Interiors*, 232:36–50.

Gillet, N., Brito, D., Jault, D., and Nataf, H. C. (2007). Experimental and numerical studies of convection in a rapidly rotating spherical shell. *Journal of Fluid Mechanics*, 580:83–121.

Golub, G. H., Hansen, P. C., and O'Leary, D. P. (1999). Tikhonov Regularization and Total Least Squares. *SIAM Journal on Matrix Analysis and Applications*, 21(1):185–194.

Goupil, M.-j. (2011). Effects of Rotation on Stellar p-Mode Frequencies. *arXiv:1102.1884 [astro-ph]*.

Grannan, A. M., Le Bars, M., Cébron, D., and Aurnou, J. M. (2014). Experimental study of global-scale turbulence in a librating ellipsoid. *Physics of Fluids*, 26(12):126601.

Greenspan, H. P. (1964). On the transient motion of a contained rotating fluid. *Journal of Fluid Mechanics*, 20(4):673–696.

Greenspan, H. P. (1965). On the general theory of contained rotating fluid motions. *Journal of Fluid Mechanics*, 22(3):449–462.

Greenspan, H. P. (1968). *The Theory of Rotating Fluids*. Breukelen Press.

Greenspan, H. P. and Howard, L. N. (1963). On a time-dependent motion of a rotating fluid. *Journal of Fluid Mechanics*, 17(03):385.

Guervilly, C. and Cardin, P. (2017). Multiple zonal jets and convective heat transport barriers in a quasi-geostrophic model of planetary cores. *Geophysical Journal International*, 211(1):455–471.

Guianvarc'h, C., Pitre, L., Bruneau, M., and Bruneau, A.-M. (2009). Acoustic field in a quasi-spherical resonator: Unified perturbation model. *The Journal of the Acoustical Society of America*, 125(3):1416–1425.

Guyon, É., Hulin, J.-P., and Petit, L. (impr. 2001). *Physical Hydrodynamics*. Oxford University Press, Oxford, Royaume-Uni de Grande-Bretagne et d'Irlande du Nord.

Heimpel, M. and Pérez, N. G. (2011). On the relationship between zonal jets and dynamo action in giant planets. *Geophysical Research Letters*, 38(14).

Heimpel, M. H., Aurnou, J. M., Al-Shamali, F. M., and Gomez Perez, N. (2005). A numerical study of dynamo action as a function of spherical shell geometry. *Earth and Planetary Science Letters*, 236(1):542–557.

Herzfeld, K. F. (1938). Reflection of Sound. *Physical Review*, 53(11):899–906.

Herzog, P. and Bruneau, M. (1989). Shape perturbation and inertial mode coupling in cavities. *The Journal of the Acoustical Society of America*, 86(6):2377–2384.

Hishida, K. and Sakakibara, J. (2000). Combined planar laser-induced fluorescence–particle image velocimetry technique for velocity and temperature fields. *Experiments in Fluids*, 29(1):S129–S140.

Hunt, F. V. (1955). Notes on the Exact Equations Governing the Propagation of Sound in Fluids. *The Journal of the Acoustical Society of America*, 27(6):1019–1039.

Hurly, J. J., Gillis, K. A., Mehl, J. B., and Moldover, M. R. (2003). The Viscosity of Seven Gases Measured with a Greenspan Viscometer. *International Journal of Thermophysics*, 24(6):1441–1474.

Iess, L., Folkner, W. M., Durante, D., Parisi, M., Kaspi, Y., Galanti, E., Guillot, T., Hubbard, W. B., Stevenson, D. J., Anderson, J. D., Buccino, D. R., Casajus, L. G., Milani, A., Park, R., Racioppa, P., Serra, D., Tortora, P., Zannoni, M., Cao, H., Helled, R., Lunine, J. I., Miguel, Y., Militzer, B., Wahl, S., Connerney, J. E. P., Levin, S. M., and Bolton, S. J. (2018). Measurement of Jupiter's asymmetric gravity field. *Nature*, 555(7695):220–222.

Ingersoll, A. P. (1990). Atmospheric Dynamics of the Outer Planets. *Science*, 248(4953):308–315.

Jordan, P. M. and Keiffer, R. S. (2016). Comments on: "On the sound attenuation in fluid due to the thermal diffusion and viscous dissipation" [Phys. Lett. A 379 (2015) 1799–1801]. *Physics Letters A*, 380(14):1392–1393.

Jougla, T. (2019). *On the Emergence and Evolution of Jets and Vortices in Turbulent Planetary Atmospheres*. Ph.D., University of St Andrews and Universite de Genoble Alpes.

Kaspi, Y., Flierl, G. R., and Showman, A. P. (2009). The deep wind structure of the giant planets: Results from an anelastic general circulation model. *Icarus*, 202(2):525–542.

Kaspi, Y., Galanti, E., Hubbard, W. B., Stevenson, D. J., Bolton, S. J., Iess, L., Guillot, T., Bloxham, J., Connerney, J. E. P., Cao, H., Durante, D., Folkner, W. M., Helled, R., Ingersoll, A. P., Levin, S. M., Lunine, J. I., Miguel, Y., Militzer, B., Parisi, M., and Wahl, S. M. (2018). Jupiter's atmospheric jet streams extend thousands of kilometres deep. *Nature*, 555(7695):223–226.

Kinsey, J. L. (1977). Laser-Induced Fluorescence. *Annual Review of Physical Chemistry*, 28(1):349–372.

Kirchhoff, G. (1868). Ueber den Einfluss der Wärmeleitung in einem Gase auf die Schallbewegung. *Annalen der Physik*, 210(6):177–193.

Kong, D., Liao, X., Zhang, K., and Schubert, G. (2013). Gravitational signature of rotationally distorted Jupiter caused by deep zonal winds. *Icarus*, 226(2):1425–1430.

Kong, D., Zhang, K., and Schubert, G. (2015). Wind-induced odd gravitational harmonics of Jupiter. *Monthly Notices of the Royal Astronomical Society: Letters*, 450(1):L11–L15.

Kong, D., Zhang, K., Schubert, G., and Anderson, J. D. (2018). Origin of Jupiter's cloud-level zonal winds remains a puzzle even after Juno. *Proceedings of the National Academy of Sciences*, 115(34):8499–8504.

Korzennik, S. G. and Eff-Darwich, A. (2011). The rotation rate and its evolution derived from improved mode fitting and inversion methodology. *Journal of Physics: Conference Series*, 271:012067.

Koulakis, J. P., Pree, S., and Putterman, S. (2018). Acoustic resonances in gas-filled spherical bulb with parabolic temperature profile. *The Journal of the Acoustical Society of America*, 144(5):2847–2851.

Lamb, H. (1881). On the Vibrations of an Elastic Sphere. *Proceedings of the London Mathematical Society*, s1-13(1):189–212.

Landau, L. D., Lifshits, E. M., and Pitaevskij, L. P. (1977). *Quantum Mechanics: Non-Relativistic Theory*. Oxford, Royaume-Uni de Grande-Bretagne et d'Irlande du Nord.

Le Bars, M., Cébron, D., and Le Gal, P. (2015). Flows Driven by Libration, Precession, and Tides. *Annual Review of Fluid Mechanics*, 47(1):163–193.

Le Dizès, S. (2015). Wave field and zonal flow of a librating disk. *Journal of Fluid Mechanics*, 782:178–208.

Le Dizès, S. and Le Bars, M. (2017). Internal shear layers from librating objects. *Journal of Fluid Mechanics*, 826:653–675.

LeBlond, H., Herzog, P., and Bruneau, M. (1990). Acoustic gyrometer.

Ledoux, P. (1951). The Nonradial Oscillations of Gaseous Stars and the Problem of Beta Canis Majoris. *Astrophysical Journal*, 114.

Livermore, P. W., Hollerbach, R., and Finlay, C. C. (2017). An accelerating high-latitude jet in Earth's core. *Nature Geoscience*, 10(1):62–68.

Lonzaga, J. B., Mobley, J., and Gaitan, D. F. (2011). Modal exchange between an elastic mode and an acoustic mode of a fluid-filled spherical shell resonator at an avoided crossing. *The Journal of the Acoustical Society of America*, 129(4):2381–2381.

Lynden-Bell, D. and Ostriker, J. P. (1967). On the Stability of Differentially Rotating Bodies. *Monthly Notices of the Royal Astronomical Society*, 136(3):293–310.

Manneville, J.-B. and Olson, P. (1996). Banded Convection in Rotating Fluid Spheres and the Circulation of the Jovian Atmosphere. *Icarus*, 122(2):242–250.

Mehl, J. B. (1978). Analysis of resonance standing-wave measurements. *The Journal of the Acoustical Society of America*, 64(5):1523–1525.

Mehl, J. B. (1982). Acoustic resonance frequencies of deformed spherical resonators. *The Journal of the Acoustical Society of America*, 71(5):1109–1113.

Mehl, J. B. (1985). Spherical acoustic resonator: Effects of shell motion. *The Journal of the Acoustical Society of America*, 78(2):782–788.

Mehl, J. B. (1986). Acoustic resonance frequencies of deformed spherical resonators. II. *The Journal of the Acoustical Society of America*, 79(2):278–285.

Mehl, J. B. (2007). Acoustic Eigenvalues of a Quasispherical Resonator: Second Order Shape Perturbation Theory for Arbitrary Modes. *Journal of Research of the National Institute of Standards and Technology*, 112(3):163–173.

Mehl, J. B. (2010). Acoustic Eigenvalues of Quasispherical Resonators: Beyond the Triaxial Ellipsoid Approximation. *International Journal of Thermophysics*, 31(7):1259–1272.

Mehl, J. B. (2015). Second-order electromagnetic eigenfrequencies of a triaxial ellipsoid II. *Metrologia*, 52(5):S227–S232.

Mehl, J. B. and Moldover, M. R. (1989). Spherical Acoustic Resonators. In Hess, P., editor, *Photoacoustic, Photothermal and Photochemical Processes in Gases*, Topics in Current Physics, pages 61–83. Springer Berlin Heidelberg, Berlin, Heidelberg.

Mehl, J. B., Moldover, M. R., and Pitre, L. (2004). Designing quasi-spherical resonators for acoustic thermometry. *Metrologia*, 41(4):295–304.

Melling, A. (1997). Tracer particles and seeding for particle image velocimetry. *Measurement Science and Technology*, 8(12):1406–1416.

Menaut, R. (2019). *Convection compressible : expériences en hypergravité et modélisation anélastique quasi-géostrophique*. PhD thesis.

Menaut, R., Corre, Y., Huguet, L., Le Reun, T., Alboussière, T., Bergman, M., Deguen, R., Labrosse, S., and Moulin, M. (2019). Experimental study of convection in the compressible regime. *Physical Review Fluids*, 4(3):033502.

Menke, W. and Eilon, Z. (2015). Relationship Between Data Smoothing and the Regularization of Inverse Problems. *Pure and Applied Geophysics*, 172(10):2711–2726.

Michelsen, H., Liu, F., Kock, B., Bladh, H., Boiarciuc, A., Charwath, M., Dreier, T., Hadef, R., Hofmann, M., Reimann, J., Will, S., Bengtsson, P.-E., Bockhorn, H., Foucher, F., Geigle, K.-P., Mounaïm-Rousselle, C., Schulz, C., Stirn, R., Tribalet, B., and Suntz, R. (2007). Modeling laser-induced incandescence of soot: A summary and comparison of LII models. *Applied Physics B*, 87(3):503–521.

Moldover, M. R., Gavioso, R. M., Mehl, J. B., Pitre, L., de Podesta, M., and Zhang, J. T. (2014). Acoustic gas thermometry. *Metrologia*, 51(1):R1–R19.

Moldover, M. R., Mehl, J. B., and Greenspan, M. (1986). Gas-filled spherical resonators: Theory and experiment. *The Journal of the Acoustical Society of America*, 79(2):253–272.

Moldover, M. R., Trusler, J. P. M., Mehl, J. B., and Davin, R. S. (1988). Measurement of the universal gas-constant R using a spherical acoustic resonator. *Journal of Research of the National Bureau of Standards*, 93(2):60.

Moody, L. F. (1944). Friction factors for pipe flow. *Trans. ASME*, 66:671–684.

Morse, P. M. and Feshbach, H. (1953a). *Methods of Theoretical Physics. Part I, Chapters 1 to 8*. New York, Etats-Unis d'Amérique, Canada, Royaume-Uni de Grande-Bretagne et d'Irlande du Nord.

Morse, P. M. and Feshbach, H. (1953b). *Methods of Theoretical Physics, Part II*. McGraw-Hill, New York. OCLC: 25619175.

Morse, P. M. and Ingard, K. U. (1986). *Theoretical Acoustics*. Princeton university press, Princeton, New Jersey, Etats-Unis d'Amérique.

Nataf, H.-C. (2013). Magnetic induction maps in a magnetized spherical Couette flow experiment. *Comptes Rendus Physique*, 14(2-3):248–267.

Noir, J., Calkins, M. A., Lasbleis, M., Cantwell, J., and Aurnou, J. M. (2010). Experimental study of libration-driven zonal flows in a straight cylinder. *Physics of the Earth and Planetary Interiors*, 182(1):98–106.

Noir, J. and Cébron, D. (2013). Precession-driven flows in non-axisymmetric ellipsoids. *Journal of Fluid Mechanics*, 737:412–439.

Noir, J., Cébron, D., Le Bars, M., Sauret, A., and Aurnou, J. M. (2012). Experimental study of libration-driven zonal flows in non-axisymmetric containers. *Physics of the Earth and Planetary Interiors*, 204-205:1–10.

Noir, J., Hemmerlin, F., Wicht, J., Baca, S. M., and Aurnou, J. M. (2009). An experimental and numerical study of librationally driven flow in planetary cores and subsurface oceans. *Physics of the Earth and Planetary Interiors*, 173(1):141–152.

Novak, A., Bruneau, M., and Lotton, P. (July/August 2018). Small-Sized Rectangular Liquid-Filled Acoustical Tank Excitation: A Modal Approach Including Leakage Through the Walls.

Park, J. (2005). Earth's Free Oscillations Excited by the 26 December 2004 Sumatra-Andaman Earthquake. *Science*, 308(5725):1139–1144.

Pedlosky, J. (1987). *Geophysical Fluid Dynamics*. Springer, New York, Etats-Unis d'Amérique.

Pekeris, C. L., Alterman, Z., and Jarosch, H. (1961). Rotational Multiplets in the Spectrum of the Earth. *Physical Review*, 122(6):1692–1700.

Pentland, A. P. (1987). A New Sense for Depth of Field. *IEEE Transactions on Pattern Analysis and Machine Intelligence*, PAMI-9(4):523–531.

Pierce, A. D. (1990). Wave equation for sound in fluids with unsteady inhomogeneous flow. *The Journal of the Acoustical Society of America*, 87(6):2292–2299.

Piet, A. (2019). Signature acoustique de vents thermiques dans une sphère en rotation rapide (Master Thesis). *Grenoble, France*.

Pitre, L., Guianvarc'h, C., Sparasci, F., Guillou, A., Truong, D., Hermier, Y., and Himbert, M. E. (2009). An improved acoustic method for the determination of the Boltzmann constant at LNE-INM/CNAM. *Comptes Rendus Physique*, 10(9):835–848.

Porco, C. C., West, R. A., McEwen, A., Del Genio, A. D., Ingersoll, A. P., Thomas, P., Squyres, S., Dones, L., Murray, C. D., Johnson, T. V., Burns, J. A., Brahic, A., Neukum, G., Veverka, J., Barbara, J. M., Denk, T., Evans, M., Ferrier, J. J., Geissler, P., Helfenstein, P., Roatsch, T., Throop, H., Tiscareno, M., and Vasavada, A. R. (2003). Cassini imaging of jupiters atmosphere, satellites, and rings. *Science*, 299(5612):1541–1547.

Rand, R. and DiMaggio, F. (1967). Vibrations of Fluid-Filled Spherical and Spheroidal Shells. *The Journal of the Acoustical Society of America*, 42(6):1278–1286.

Rayleigh, J. W. S. (1894). *The Theory of Sound*. Macmillan, London, Royaume-Uni de Grande-Bretagne et d'Irlande du Nord.

Read, P. L., Jacoby, T. N. L., Rogberg, P. H. T., Wordsworth, R. D., Yamazaki, Y. H., Miki-Yamazaki, K., Young, R. M. B., Sommeria, J., Didelle, H., and Viboud, S. (2015). An experimental study of multiple zonal jet formation in rotating, thermally driven convective flows on a topographic beta-plane. *Physics of Fluids*, 27(8):085111.

Read, P. L., Yamazaki, Y. H., Lewis, S. R., Williams, P. D., Miki-Yamazaki, K., Sommeria, J., Didelle, H., and Fincham, A. (2004). Jupiter's and Saturn's convectively driven banded jets in the laboratory. *Geophysical Research Letters*, 31(22).

Rhines, P. B. (1975). Waves and turbulence on a beta-plane. *Journal of Fluid Mechanics*, 69(3):417–443.

Rieutord, M., Espinosa Lara, F., and Putigny, B. (2016). An algorithm for computing the 2D structure of fast rotating stars. *Journal of Computational Physics*, 318:277–304.

Russell, D. A. (2010). Basketballs as spherical acoustic cavities. *American Journal of Physics*, 78(6):549–554.

Sauret, A., Cébron, D., and Le Bars, M. (2013). Spontaneous generation of inertial waves from boundary turbulence in a librating sphere. *Journal of Fluid Mechanics*, 728.

Sauret, A., Cébron, D., Morize, C., and Bars, M. L. (2010). Experimental and numerical study of mean zonal flows generated by librations of a rotating spherical cavity. *Journal of Fluid Mechanics*, 662:260–268.

Schaeffer, N., Jault, D., Nataf, H.-C., and Fournier, A. (2017). Turbulent geodynamo simulations: A leap towards Earth's core. *Geophysical Journal International*, 211(1):1–29.

Schiff, L. I. (1969). *Quantum Mechanics*.

Schou, J., Antia, H. M., Basu, S., Bogart, R. S., Bush, R. I., Chitre, S. M., Christensen-Dalsgaard, J., Mauro, M. P. D., Dziembowski, W. A., Eff-Darwich, A., Gough, D. O., Haber, D. A., Hoeksema, J. T., Howe, R., Korzennik, S. G., Kosovichev, A. G., Larsen, R. M., Pijpers, F. P., Scherrer, P. H., Sekii, T., Tarbell, T. D., Title, A. M., Thompson, M. J., and Toomre, J. (1998). Helioseismic Studies of Differential Rotation in the Solar Envelope by the Solar Oscillations Investigation Using the Michelson Doppler Imager. *The Astrophysical Journal*, 505(1):390.

Shah, S. R., Jain, S. V., Patel, R. N., and Lakhera, V. J. (2013). CFD for Centrifugal Pumps: A Review of the State-of-the-Art. *Procedia Engineering*, 51:715–720.

Smith, C. A., Speer, K. G., and Griffiths, R. W. (2014). Multiple Zonal Jets in a Differentially Heated Rotating Annulus. *Journal of Physical Oceanography*, 44(9):2273–2291.

Stanley, S. and Glatzmaier, G. A. (2010). Dynamo Models for Planets Other Than Earth. *Space Science Reviews*, 152(1):617–649.

Tarantola, A. (cop. 1987). *Inverse Problem Theory: Methods for Data Fitting and Model Parameter Estimation*. Elsevier, Amsterdam, Pays-Bas.

Tarantola, A. and Valette, B. (1982a). Generalized nonlinear inverse problems solved using the least squares criterion. *Reviews of Geophysics*, 20(2):219.

Tarantola, A. and Valette, B. (1982b). Inverse Problems = Quest for Information. *Journal of Geophysics*, page 16.

Tollefson, J., Wong, M. H., de Pater, I., Simon, A. A., Orton, G. S., Rogers, J. H., Atreya, S. K., Cosentino, R. G., Januszewski, W., Morales-Juberías, R., and Marcus, P. S. (2017). Changes in Jupiter's Zonal Wind Profile preceding and during the Juno mission. *Icarus*, 296:163–178.

Triana, S. A., Zimmerman, D. S., Nataf, H.-C., Thorette, A., Lekic, V., and Lathrop, D. P. (2014). Helioseismology in a bottle: Modal acoustic velocimetry. *New Journal of Physics*, 16(11):113005.

Trusler, J. P. M. (cop. 1991). *Physical Acoustics and Metrology of Fluids*. A. Hilger, Bristol etc., Royaume-Uni de Grande-Bretagne et d'Irlande du Nord.

Vallis, G. K. (2017). *Atmospheric and Oceanic Fluid Dynamics*. Cambridge University Press.

Vallis, G. K. and Maltrud, M. E. (1993). Generation of Mean Flows and Jets on a Beta Plane and over Topography. *Journal of Physical Oceanography*, 23(7):1346–1362.

Vander Wal, R. L. and Weiland, K. J. (1994). Laser-induced incandescence: Development and characterization towards a measurement of soot-volume fraction. *Applied Physics B*, 59(4):445–452.

Vasavada, A. R. and Showman, A. P. (2005). Jovian atmospheric dynamics: An update after Galileo and Cassini. *Reports on Progress in Physics*, 68(8):1935–1996.

Vidal, J. and Cébron, D. (2017). Inviscid instabilities in rotating ellipsoids on eccentric Kepler orbits. *Journal of Fluid Mechanics*, 833:469–511.

Vidal, J., Su, S., and Cébron, D. (2020). Compressible fluid modes in rigid ellipsoids: towards modal acoustic velocimetry. *Journal of Fluid Mechanics*, 885.

Wereley, S. T. and Meinhart, C. D. (2010). Recent Advances in Micro-Particle Image Velocimetry. *Annual Review of Fluid Mechanics*, 42(1):557–576.

Woodhouse, J. H. and Dahlen, F. A. (1978). The Effect of A General Aspherical Perturbation on the Free Oscillations of the Earth. *Geophysical Journal International*, 53(2):335–354.

Yarom, E. and Sharon, E. (2014). Experimental observation of steady inertial wave turbulence in deep rotating flows. *Nature Physics*, 10(7):510–514.

Yarom, E., Vardi, Y., and Sharon, E. (2013). Experimental quantification of inverse energy cascade in deep rotating turbulence. *Physics of Fluids*, 25(8):085105.

Zeeman, P. (1897). Xxxii. on the influence of magnetism on the nature of the light emitted by a substance. *The London, Edinburgh, and Dublin Philosophical Magazine and Journal of Science*, 43(262):226–239.

Zhang, K., Kong, D., and Schubert, G. (2015). Thermal-gravitational wind equation for the wind-induced gravitational signature of giant gaseous planets: Mathematical derivation, numerical method, and illustrative solutions. *The Astrophysical Journal*, 806(2):270.

Zhang, Y. and Afanasyev, Y. D. (2014). Beta-plane turbulence: Experiments with altimetry. *Physics of Fluids*, 26(2):026602.

Zuckerwar, A. J. (1996). Speed of sound in real gases. I. Theory. *The Journal of the Acoustical Society of America*, 100(4):2747–2747.

Appendices

A

Rotational sensitivity kernels

Rotational sensitivity kernels K_{nlm} as defined in eq. (2.62). We show a more complete set of kernels than in the main text, one page per n ($n = 0$, $n = 1$, $n = 2$).

Please note that we show here the adimensional kernel (computed with adimensionned radius of the sphere $a = 1$). The structures remain unchanged, and the amplitude of the dimensionned K_{nlm} from main text can be retrieved by simply multiply the admensional kernels by $1/a_{ZoRo} = 1/0.2 = 8$ (with 0.2 m the dimensional ZoRo radius).

Adimensionnal Rotational sensitivity kernels, n = 0

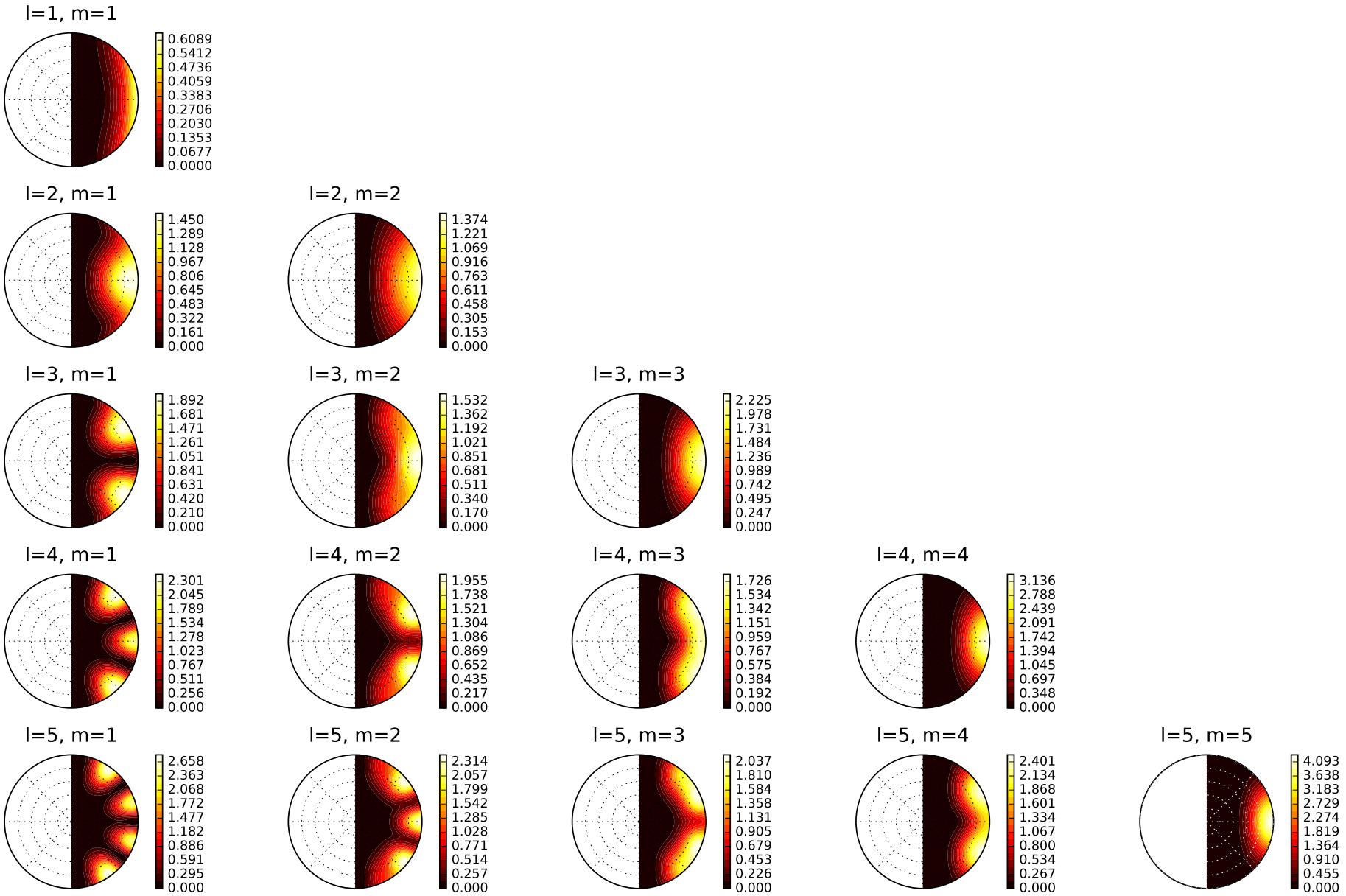

Adimensional Rotational sensitivity kernels, n = 1

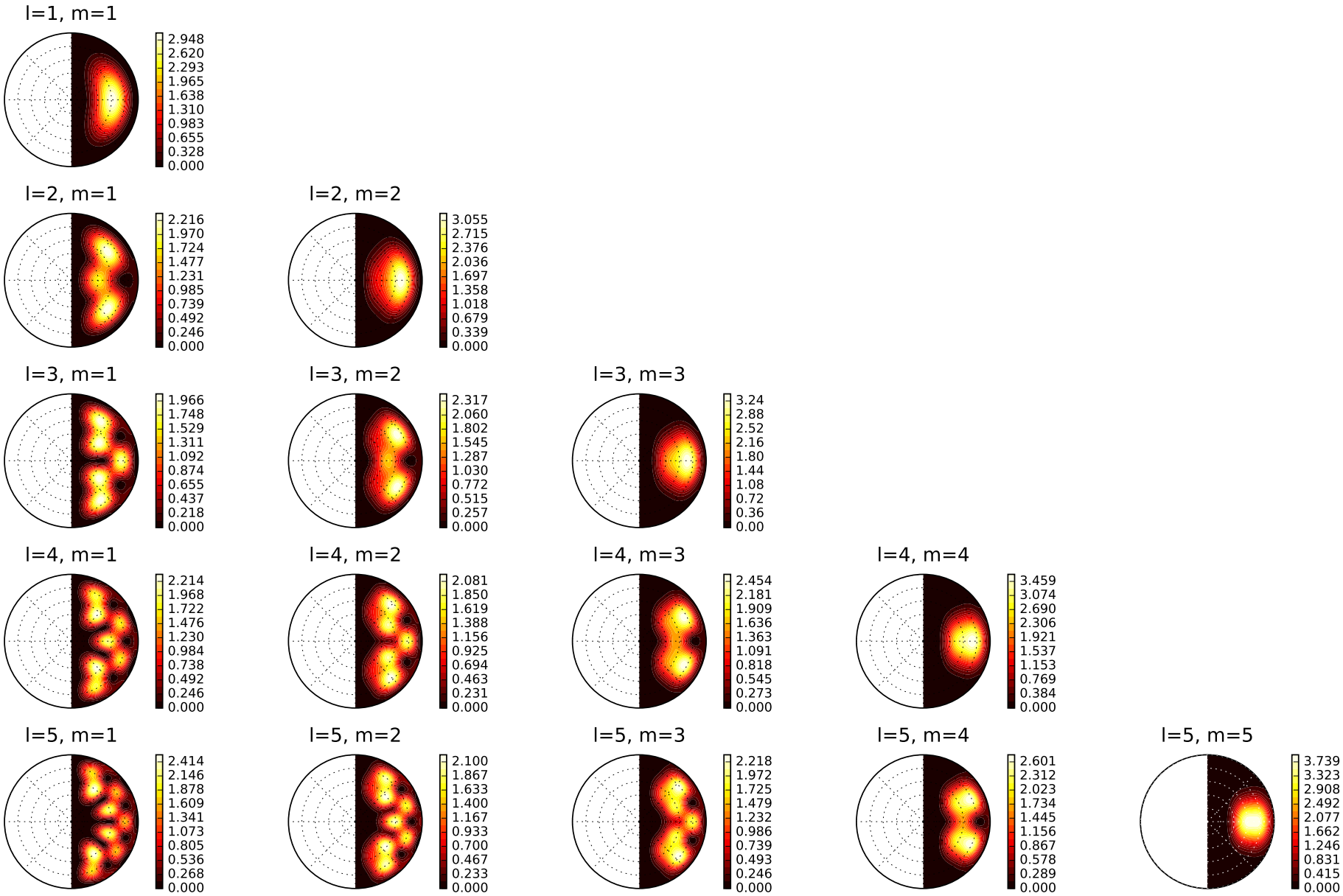

Adimensional Rotational sensitivity kernels, n = 2

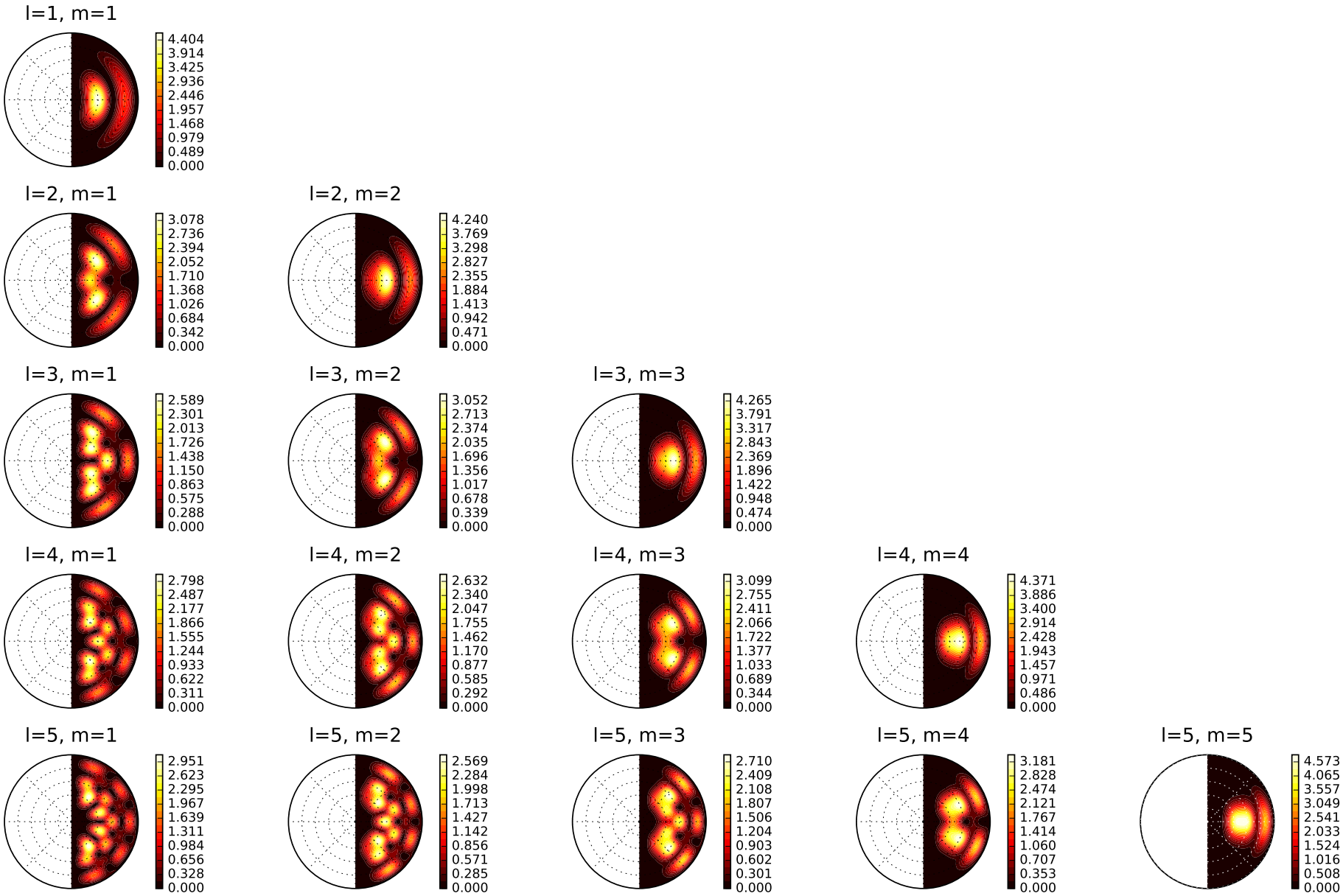

B

Finite-element calculations with COMSOL Multiphysics

All finite-element simulations were carried out with the commercial software COMSOL. We present here an overview of the numerical procedures we used, some of the difficulties we came across and how we solved them.

B.1 Built-in COMSOL (version 5.4) capabilities and limitations

Finite-element calculations, on which relies the commercial software COMSOL Multiphysics, allow calculating acoustic modes in arbitrary geometries, in particular in the exact geometry of ZoRo. In this section, we show how one can determine accurately the effects, on modes, of rotation and thermo-viscous diffusion with COMSOL. Indeed, these effects cannot be simply calculated using the acoustic (scalar) equation governing the pressure p, and require thus to consider the more complex (vectorial) Navier-Stokes equations governing the velocity field $\boldsymbol{u}$. This can be done using the aeroacoustics interface of COMSOL, but three-dimensional (3D) calculations are too costly to resolve the thin acoustic boundary layers, and the built-in axisymmetric interface discard any possible azimuthal dependency of the fields.

In order to perform efficient axisymmetric calculations with a 2D mesh and a possible azimuthal dependency, we have thus exploited the axisymmetry of our spheroidal geometry by assuming a periodic dependency $\exp[\mathrm{i}(\omega t + m\phi)]$, with the imaginary unit i, the cylindrical coordinates (r, ϕ, z), the azimuthal wavenumber m, the time t and the angular eigenfrequency ω. Built-in COMSOL interfaces allow such 2D calculations for the acoustic equation but not for the Navier-Stokes equations, for which the built-in interface is limited to $m = 0$.

The scripts taking into account the following modified equations are available at `https://www.isterre.fr/annuaire/member-web-pages/david-cebron/`.

B.2 How to calculate COMSOL axisymmetric aero-acoustic modes with $m \neq 0$?

To consider a possible azimuthal flow v using the built-in COMSOL axisymmetric interface for aeroacoustics, we need an additional equation governing v, and the ansatz $\exp[\mathrm{i}(\omega t + m\varphi)]$ will add supplementary terms in every equation. Note also that additional terms are also required to take into account the rotation of the frame.

In practice, we have used two sets of axisymmetric COMSOL aero-acoustics interfaces in the frequency domain, such that equations (2.21)-(2.23) are solved for two sets of unknowns named $(\boldsymbol{u}, T, p)$ and $(\boldsymbol{u_2}, T_2, p_2)$, where $\boldsymbol{u} = (u, w)$ is the built-in unknown velocity field in the cylindrical coordinates, with the cylindrico-radial velocity component u, and the axial velocity w along the z axis. Note that the interface 'Heat transfer in Fluids' is not well suited since eigensolvers are not built-in COMSOL for this interface, while using the PDE interface is difficult since the axisymmetric interface is not built-in (r and z are surprisingly treated as Cartesian coordinates in the built-in PDE interface). Then, noting with a subscript 2 the quantities associated with the set of equations governing $(\boldsymbol{u_2}, T_2, p_2)$, the required additional equation is given by the equation governing the unknown T_2, which is formally the same as equation (2.23). Indeed, the (scalar) equation governing v is the same as the one governing T_2 provided that (i) the velocity $\boldsymbol{u_2}$ is replaced by $\boldsymbol{u}$, (ii) the density ρ_2 is replaced by ρ, (iii) we set $\lambda_2 = \mu_2 = 0$, such that the velocity $\boldsymbol{u_2}$ does not contribute to the eigenmode damping calculation, and $\lambda_2 = \mu$, $\alpha_2 = 0$, $C_{p_2} = 1$, $T_{02} = v_0$, with the basic state $\boldsymbol{u_0} = (u_0, w_0)$. Then, in the frame rotating at $\boldsymbol{\Omega} = \Omega\hat{\boldsymbol{z}} = 2\pi f_\Omega \hat{\boldsymbol{z}}$, the following source terms (due to $m \neq 0$ and rotation) have been calculated using the commercial software MAPLE (symbolic computations) and added in the COMSOL built-in equations. In cylindrical coordinates (r, ϕ, z), these source terms read

$$M = -\frac{\mathrm{i}\rho_0 m v}{r} - \frac{\mathrm{i}\rho m v_0}{r}, \tag{B.1}$$

$$F_r = -\rho_0\left[\frac{v_0}{r}(\mathrm{i}mu - 2v) - 2\Omega v\right] + \rho\left[\frac{v_0^2}{r} + 2\Omega v_0 + \Omega^2 r\right] - \frac{\mu}{r^2}\left(2\mathrm{i}mv + m^2 u\right) + \mathrm{i}m\left(\mu_B + \frac{\mu}{3}\right)\left(\frac{\partial_r v}{r} - \frac{v}{r^2}\right), \tag{B.2}$$

$$F_z = -\frac{\mathrm{i}\rho_0 m v_0 w}{r} - \mu\frac{m^2}{r^2}w + \left(\mu_B + \frac{\mu}{3}\right)\frac{\mathrm{i}m\partial_z v}{r}, \tag{B.3}$$

and

$$Q = -C_p\frac{\mathrm{i}}{r}\rho_0 m v_0 T + \alpha\frac{\mathrm{i}}{r}T_0 m v_0 p - \lambda\frac{m^2}{r^2}T, \tag{B.4}$$

$$Q_2 = -\rho_0\left[\frac{v_0(\mathrm{i}mv + u) + u_0 v}{r} + 2\Omega u\right] - \rho\left[\frac{u_0 v_0}{r} + 2\Omega u_0\right] - \frac{\mathrm{i}m}{r}p + \frac{\mu}{r^2}\left[2\mathrm{i}mu - (1+m^2)v\right] + \left(\mu_B + \frac{\mu}{3}\right)\left[\frac{\mathrm{i}m(\partial_r u + \partial_z w)}{r} + \frac{\mathrm{i}mu - m^2 v}{r^2}\right], \tag{B.5}$$

where the azimuthal velocity v is actually governed by the built-in temperature equation of COMSOL for T_2, and where Q_2 is the source term to add in the set of equations governing $(\boldsymbol{u_2}, T_2, p_2)$. Note that these supplementary terms have been simply obtained

by subtracting, from the full equations, the equations in the particular case $v = m = \Omega = 0$ corresponding to the COMSOL built-in equations.

In all our calculations, we have actually considered a homogeneous basic state (we have checked that the centrifugal forces are negligible in the context of the ZoRo experiment) at 20°C, using the parameters of table B.1. Note also that global rotation, via the Coriolis force, adds a supplementary family of eigenmodes named inertial modes (Greenspan, 1968). However, since the global rotation rate for ZoRo is small compared to the sound speed, there is no hybridization between acoustic and inertial modes (Vidal et al., 2020).

Table B.1: Parameter values used in the COMSOL calculations, for homogeneous ambient pressure $p_0 = 1$ atm and temperature $T_0 = 20°$ (see p. 315 of Blackstock, 2000, for the chosen value of μ_B).

ρ_0	μ	μ_B	C_p	α	λ	β_T	γ	c
kg.m^{-3}	Pa.s	Pa.s	J.kg^{-1}.K^{-1}	K^{-1}	W.K^{-1}.m^{-1}	Pa^{-1}		m.s^{-1}
1.204	$1.81 \cdot 10^{-5}$	0.6 μ	1005.42	$3.41 \cdot 10^{-3}$	$2.58 \cdot 10^{-2}$	$9.87 \cdot 10^{-6}$	1.4	343.194

B.3 Boundary conditions and details on the numerics

To be as close as possible to the experiment, we impose at the fluid boundary a no-slip condition, i.e. $(u, v, w) = (0, 0, 0)$ in the frame attached to the rigid container, and a constant temperature. These conditions leads to a modification of the (complex) eigenvalue due to respectively the viscous and thermal boundary layers. Because of the large thermal conductivity of the metallic container of ZoRo compared to the one of air, the COMSOL calculations neglect the finite thermal conductivity of the container (which would modify the boundary heat loss and thus the thermal damping of acoustic modes). In the main calculations shown in the article, the finite elasticity of the boundary is also neglected (the boundary is assumed to be perfectly rigid, preventing any radiation of sound in the surrounding fluid). However, calculations with an elastic boundary (with and without a sound radiation in a surrounding fluid) have also been performed in order to validate the elasto-acoustic estimates of the theoretical perturbative calculation (see section B.4 for details on these calculations).

In addition to eigenvalue calculations, COMSOL also allows us to calculate, in the frequency domain, the fluid response for a given excitation source. At the locations of the experiment audio speakers and taking into account the finite size of the audio speaker, we have thus prescribed a velocity $i\omega$ at the boundary, both in the normal and tangential directions. Then, the pressure is recorded, in the COMSOL calculation, at the point where the electrets are positioned in the experiment (the finite size of electrets is neglected in COMSOL calculations). Finally, the fluid response is calculated for a large number of m, and the complete response is then simply obtained by summing the results obtained for each m.

In order to give an idea of the CPU time required for such calculations, one can consider the numerical calculations we have done to reproduce the acoustic spectrum measured experimentally between 500 Hz and 2335 Hz. For this calculation, the fluid response has been calculated for each m between 0 and 6 for $\sim$ 3000 well-chosen frequencies, with

a step of 0.2 Hz near the resonance peaks and with typically 15 calculated frequencies between the acoustics peaks. To capture correctly the thin boundary layers, we have used a fine mesh model with $\sim 160\,000$ degrees of freedom. Even if the calculation of a unique fluid response takes only $\sim$ 12s on a 6 cores desktop computer, we had to do $\sim 20\,000$ calculations, leading to a CPU time of 3 days on this computer. Thus, the calculation of the complete spectrum between 500 Hz and 3000 Hz (typical resolution of 0.2 Hz near the resonances), which requires to consider all the values of m between 0 and 8, has taken a full week of calculation (or 1 day using a 64 cores cluster).

Note finally that careful tests of numerical convergence have been systematically performed. We have checked that the boundary layers are well resolved, with several mesh points within the boundary layer thickness $\sqrt{\nu/f_t} = 100\,\mu$m, with $f_t = 2$ kHz the typical acoustic frequency and $\nu = \mu/\rho_0 = 2 \cdot 10^{-5}\,\mathrm{m}^2.\mathrm{s}^{-1}$ the typical air kinematic viscosity in experiments (the thermal boundary layer thickness is similar since the air Prandtl number is $Pr = \rho C_p \nu/\lambda = 0.7$). Our tests of numerical convergence (see appendix C of Vidal et al., 2020) show that, for a given number of degrees of freedom, increasing the elements order decreases (respectively increases) the accuracy of the calculated eigenfrequency (respectively damping). We have thus used systematically Lagrange elements of order 3 for the pressure and order 4 for the velocity and temperature.

B.4 Elastic container, boundary coupling and sound radiation in the surrounding outer fluid

COMSOL also allows built-in calculations of pure elastic modes of the container. Even without any shell model approximation, such calculations are not costly, which allows 3D calculations. Considering a linear elastic container with completely free boundaries, such 3D calculations give a (degenerate) fundamental mode at 2853 Hz for a 1 cm thick sphere of internal radius 0.2 m, with a Young modulus of 71 GPa, a Poisson's ratio of 0.33 and a density of $2810\,\mathrm{kg.m}^{-3}$. Considering now the 1 cm thick spheroidal geometry of ZoRo, of internal semi-axes 0.2 m and 0.19 m, this mode is split into a mode at 2807 Hz and another (degenerate) mode at 2854 Hz.

Now, if we consider the COMSOL built-in axisymmetric calculations of elastic modes with arbitrary m and the previously developed axisymmetric model for acoustic modes, one can modify the boundary condition to take into account the two-way coupling between elastic and acoustic modes. However, built-in axisymmetric models do not allow any axial boundary displacement on the symmetry axis. While this is not a problem for acoustic modes with a rigid boundary, this axial displacement constraint only allows us to recover the 3D elastic modes verifying this condition, but also leads to additional elastic modes (e.g. $m = 1$ additional modes). Having this issue in mind, we have performed axisymmetric calculations of elasto-acoustic (diffusive) modes to obtain insights and order of magnitude estimates, but we have also done 3D calculations of the diffusionless counterparts of these modes by considering the cheaper scalar acoustic equation (which neglects diffusion and rotation). For instance, both approaches give that, for a 1 cm thick sphere of internal radius 0.2 m, the elastic coupling leads to a 0.1% increase of the fundamental acoustic frequency (around 568 Hz), while the next acoustic eigenfrequency (around 912 Hz) is decreased by 0.01%. Calculations in the spheroidal geometry of ZoRo give similar results.

Finally, one can also add a surrounding fluid in order to allow sound radiation in the

outer fluid. To do so, we have solved the scalar acoustic equation in the outer fluid, coupled to the outer boundary of the elastic container. In order to mimic a sound radiation in an infinite domain, we have to prevent any sound reflection at the outer (computational) boundary of the outer fluid domain. To do so, we have used the built-in perfectly matched layer (PML) of COMSOL, which is an additional surrounding domain where the acoustic waves are absorbed. Using the advised structured mesh for the PML region, we have thus performed elasto-acoustic calculations with sound radiation. These calculations have confirmed that the sound radiation can be largely neglected in the discussion of the experimental results of ZoRo.

C

Excerpts of ZoRo's technical drawings

The mechanical design and realisation of ZoRo is the work of Max Solazzo, mechanical engineer at ISTerre (IE, CNRS). Instrumentation implementation, user interface for controlling the set-up and acquire the data were done with help from Yann Do, instrumentation engineer (AI, CNRS). Both are part of the Geophysical Instrumentation Team (SIG) of ISTerre.

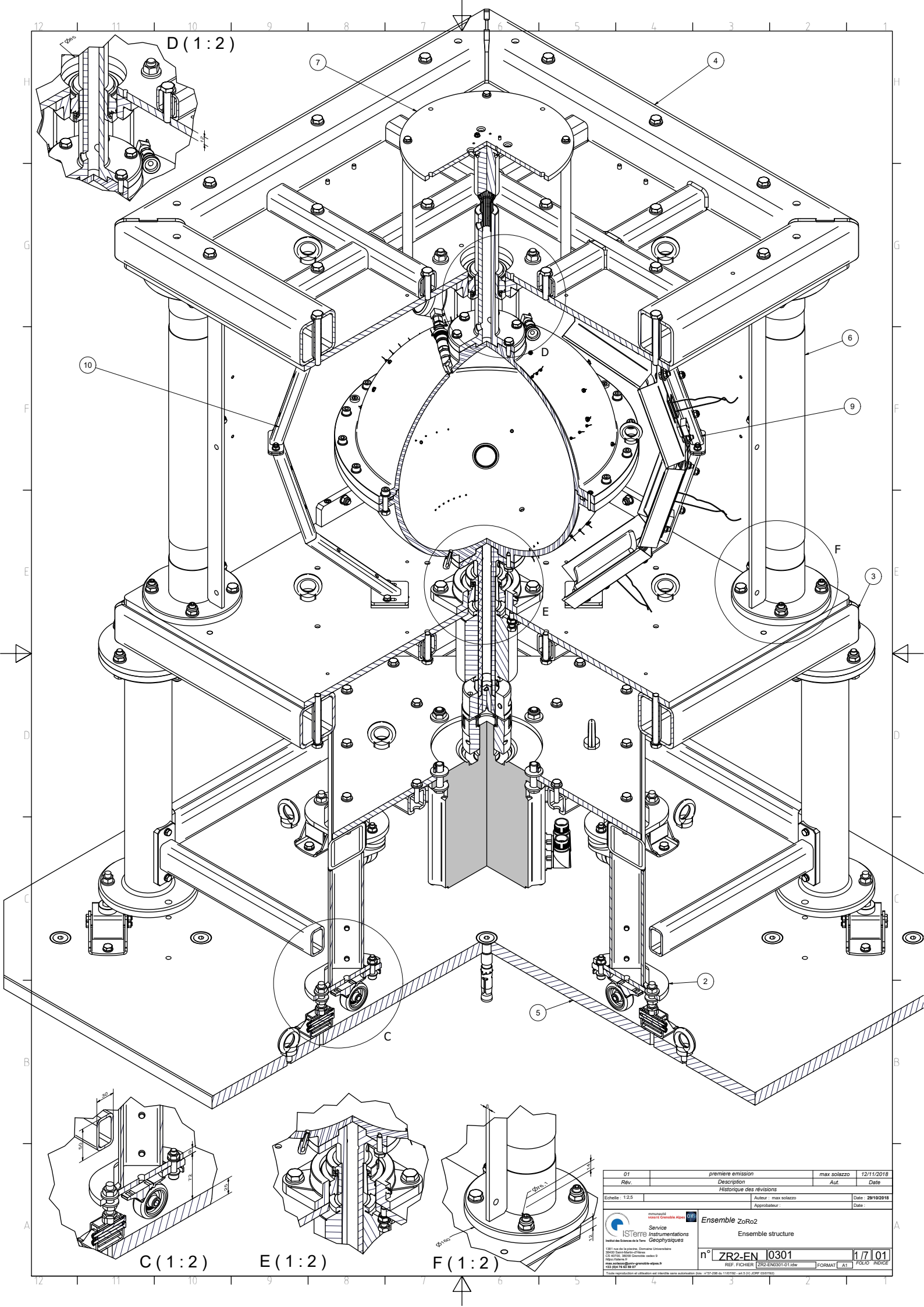

Rév.	Description	Aut.	Date
01	premiere emission	max solazzo	12/11/2018

Historique des révisions

Echelle : 1:2,5 | Auteur : max solazzo | Date : 29/10/2018 | Approbateur : | Date :

Université Grenoble Alpes
ISTerre Institut des Sciences de la Terre
Service Instrumentations Geophysiques
1381 rue de la piscine, Domaine Universitaire
38400 Saint-Martin-d'Hères
CS 40700, 38058 Grenoble cedex 9
https://isterre.fr
max.solazzo@univ-grenoble-alpes.fr
+33 (0)4 76 63 59 97

Ensemble ZoRo2

Ensemble structure

n° ZR2-EN 0301 | 1/7 FOLIO | 01 INDICE

REF. FICHIER ZR2-EN0301-01.idw | FORMAT A1

Liste de pièces

ARTICLE	QTE	N° DE PIECE	DESCRIPTION	MATIERE
1	1	ZR20102-01	demi-sphere basse	mecalu+
2	1	ZR20102-02	demi-sphere haute	mecalu+
3	1	JTR188668	joint torique DF 801 412,48x6,94	FKM
4	18	ISO 4032 - M8	Ecrou hexagonal. Produit de classe A et B	A2
5	18	ISO 7089 - 8	Rondelles plates - Série standard - Produit de classe A	A2
6	18	ISO 4762 - M8 x 40	Vis cylindrique à six pans creux	A2
7	2	ISO 8735 - 8 x 35 - A	Goupille avec couronne et taraudage interne, acier inoxydable martensitique	Acier

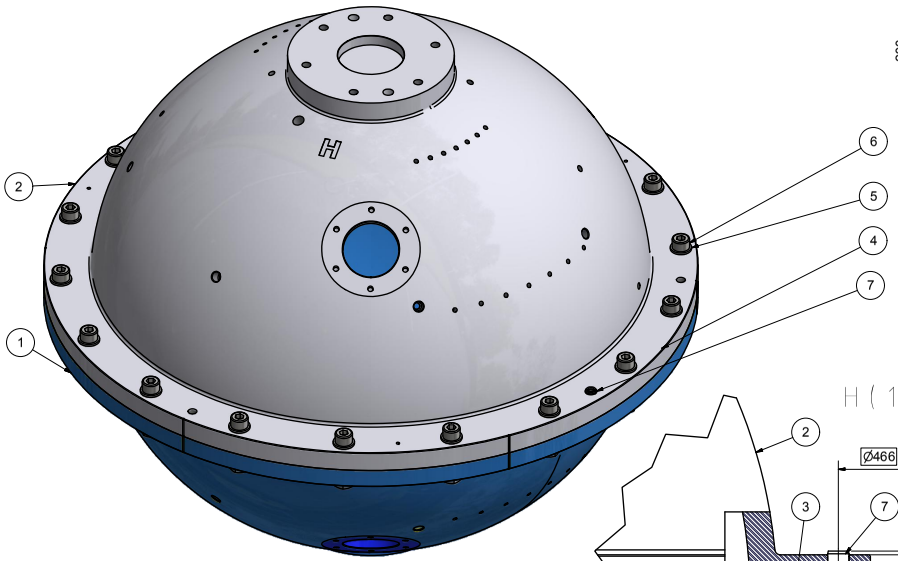

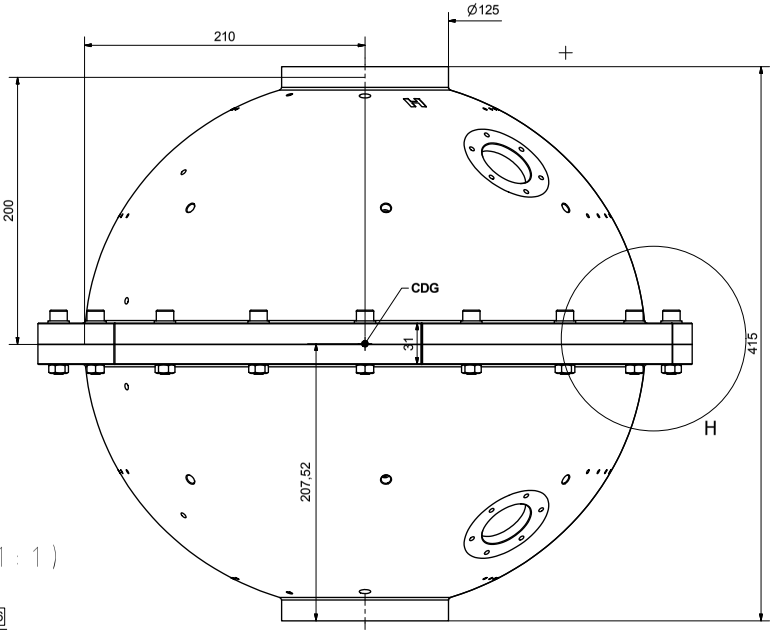

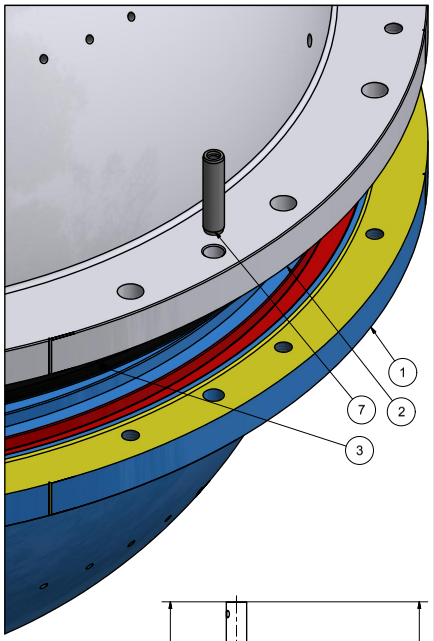

H (1 : 1)

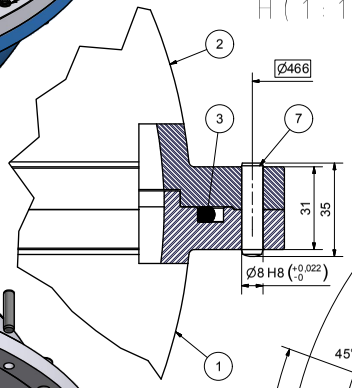

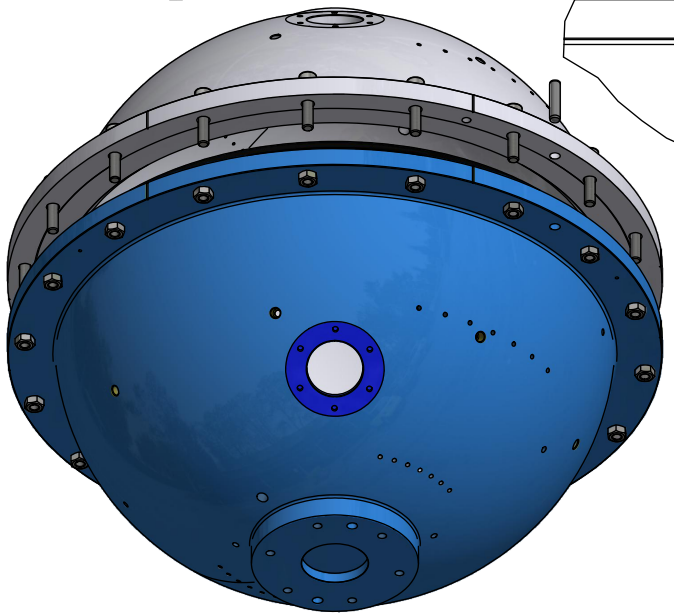

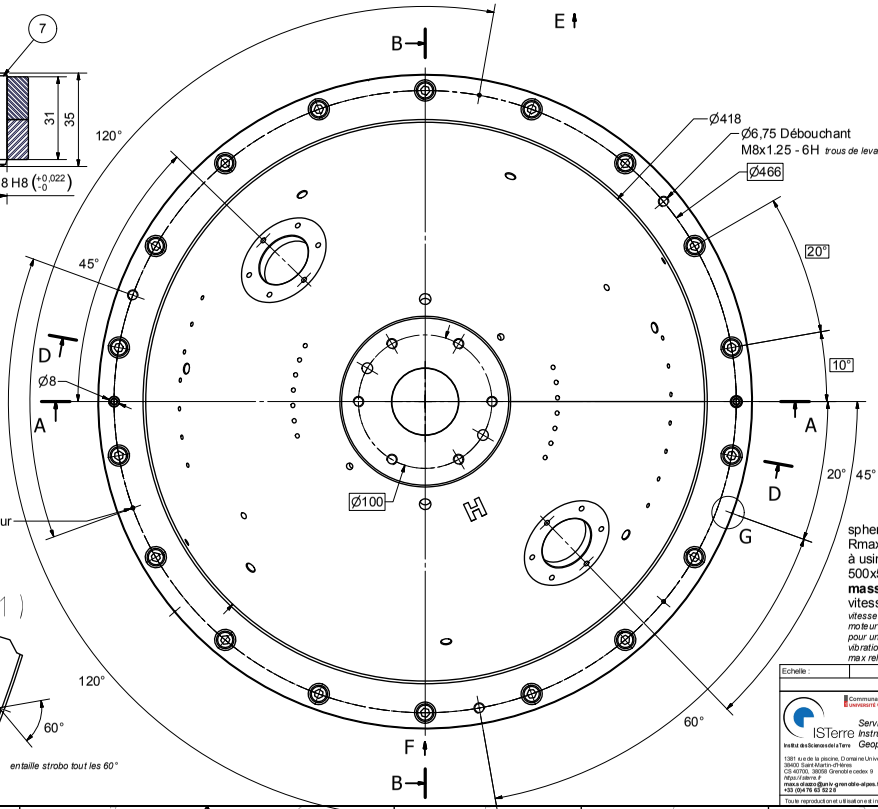

G (2 : 1)

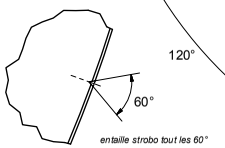

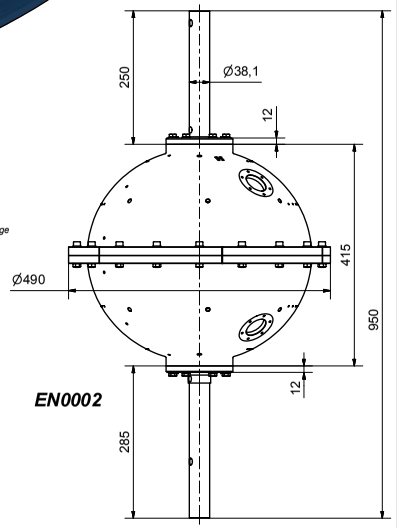

spheroide composé de 2 demisphere en mecalu+®, aluminium serie 7xxx
Rmax480MPa, Re0.2 430MPa, A 2.8%, 150HB, Young 71GPa
à usiner dans 2 blocs scié de tole tractionné/compressé T651/6522
500x500x225 fraisée 2 faces 225mm (0+0.2)
masse calculée ensemble 21.050kg (avec visserie)
vitesse de rotation 2500 t/min = 15000 deg/s = 41.7 Hz
vitesse limite moteur 3000 t/min = 18000 deg/s = 50hz
moteur kollmorgen AKM73Q vibration classe A (EN60034-14)
pour une plage de vitesse de 600 à 3600 tr / min et un centre d'arbre entre 53-132 mm, la valeur de vibration autorisée est de 1,6 mm / s
max rel vibration displacement 65µm, max run-out 16µm.

Echelle :	Auteur : max solazzo	Date : 08/11/2017
	Approbateur :	Date:

ISTerre Institut des Sciences de la Terre — Service Instrumentations Geophysiques
1381 rue de la piscine, Domaine Universitaire, 38400 Saint-Martin-d'Hères, CS 40700, 38058 Grenoble cedex 9
https://isterre.fr
maxa.solazzo@univ-grenoble-alpes.fr
+33 (0)4 76 63 52 29

Ensemble : ZoRo2
ensemble demi-spheres

n° ZR2-EN 0102 1/2 01
REF. FICHIER ZR2-EN0102.idw FORMAT A1 FOLIO INDICE

BON POUR FABRICATION

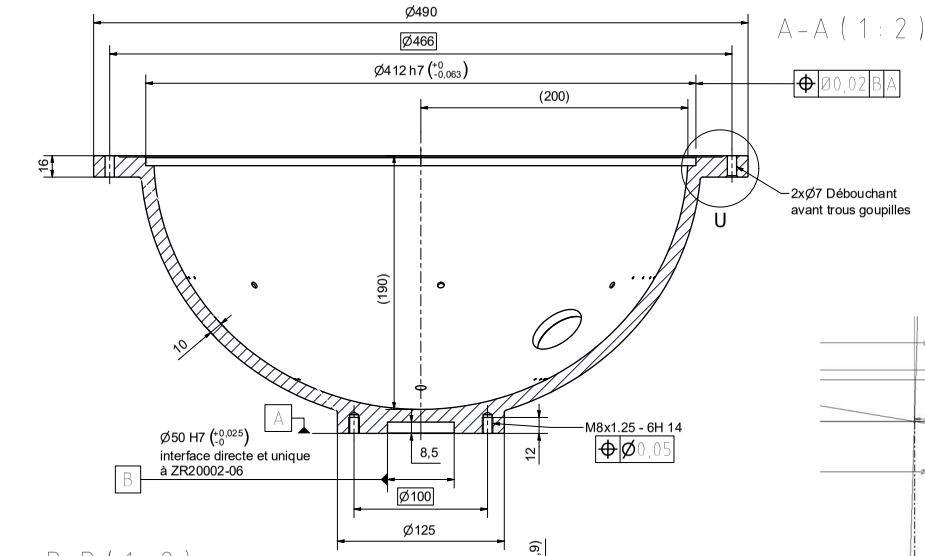

A-A (1 : 2)

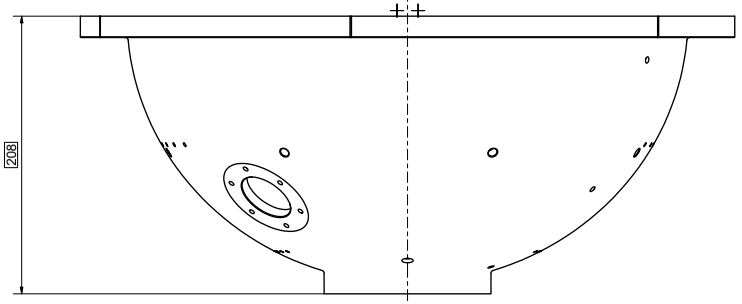

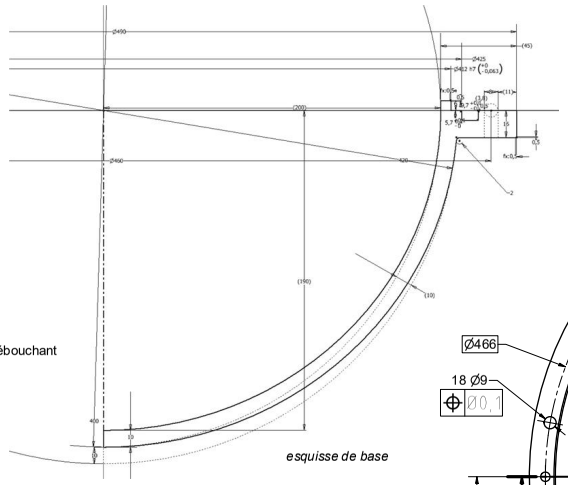

esquisse de base

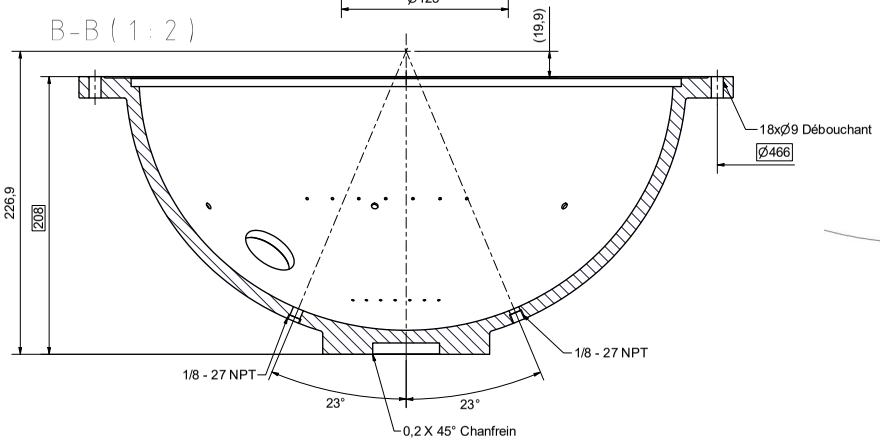

B-B (1 : 2)

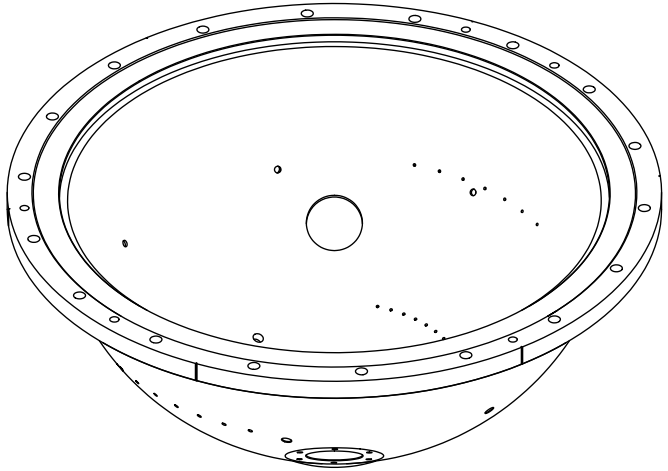

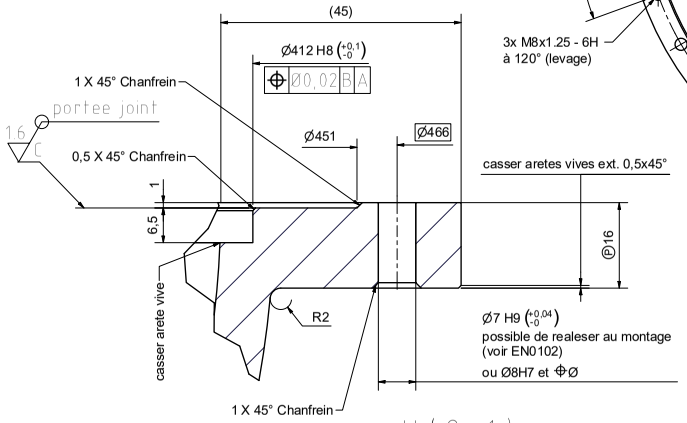

U (2 : 1)

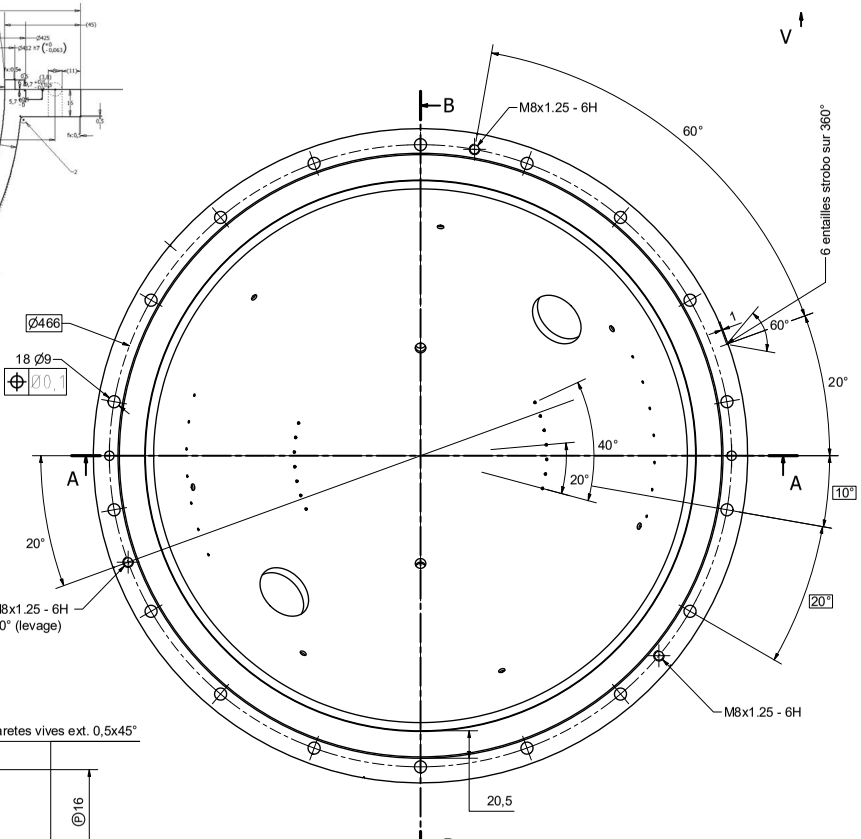

Casser les angles vifs non cotés par un rayon ou un chanfrein

Rév.	Description	Date	Aut.
01	première emission	13/10/2017	max solazzo
02	esquisse, voir ZR20102-01-03_esquisse.pdf	02/04/2018	max solazzo
03	position origine angles usinages capteurs	23/04/2018	max solazzo
04	note 50H7 + bon pour fab	30/04/2018	max solazzo
05	angle GT/8 23° (C10)	03/07/2018	max solazzo
06	notation filetage NPT + coupe U-U 60° + modif cosmetiques	12/11/2018	max solazzo

Révisions

Matière : MACAL U + (alliage de serie 7xxx)	Traitement :	Tol. générales : IH	Rugosité Ra :
Echelle : 1:2	Auteur : max solazzo	Date : 13/10/2017	Approbateur : Date :

Cotation tolérancée: Tolérances générales pour dimensions sans indications individuelles (ISO 2768-1)

Ecarts autorisés pour les cotes linéaires excepté pour les arêtes d'ébrunies												Ecarts autorisés pour cotes angulaires				
Classe de tolérance		Ecarts autorisés pour tailles de base										Rayons / chanfreins				
Désignation	Description	> 0,5 jusqu à 3	> 3 jusqu à 6	> 6 jusqu à 30	> 30 jusqu à 120	> 120 jusqu à 400	> 400 jusqu à 1000	> 1000 jusqu à 2000	> 2000 jusqu à 4000	> 4000		> 0,5 jusqu à 3	> 3 jusqu à 6	> 6		
f	fin	±0,05	±0,05	±0,1	±0,15	±0,2	±0,3	±0,5	±			±0,2	±0,5	±1		

Ecarts autorisés pour cotes angulaires					
Ecarts autorisés pour longueurs en mm du côté le plus petit de l'angle					
> 0 jusqu à 10	> 10 jusqu à 50	> 50 jusqu à 120	> 120 jusqu à 400	> 400	
±1°	±0°30'	±0°20'	±0°10'	±0°5'	

Poids calculé de la pièce: 10,410 kg

BON POUR FABRICATION

ISTerre Institut des Sciences de la Terre
Service Instrumentations Géophysiques
1381 rue de la piscine, Domaine Universitaire
38400 Saint-Martin-d'Hères
CS 40700, 38058 Grenoble cedex 9
tél +33 (0)4 76 63 52 52
max.solazzo@univ-grenoble-alpes.fr
+33 (0)4 76 63 99 07

Ensemble : ZoRo2

Elément : demi-sphere haute

n° ZR2 0102-02 1/2 06

REF. FICHIER ZR20102-02-06.idw FORMAT A1 FOLIO INDICE

V (1 : 2)

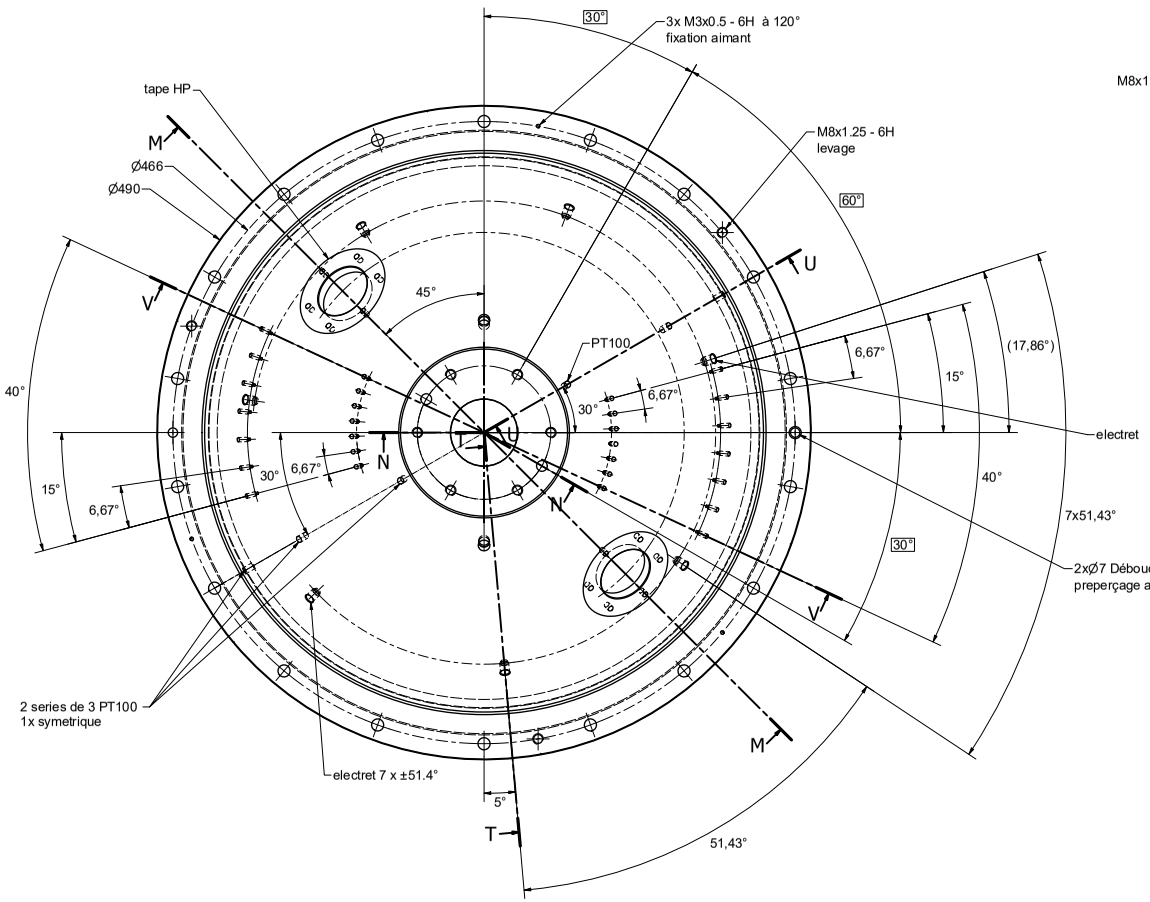

N-N (1 : 2)

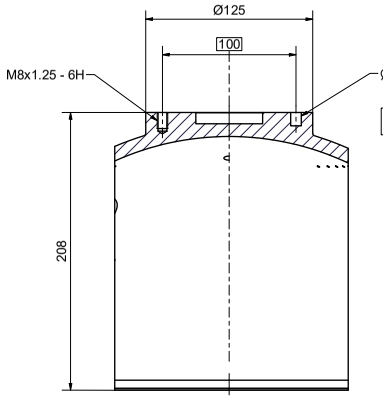

T-T (1 : 2) coupe electret

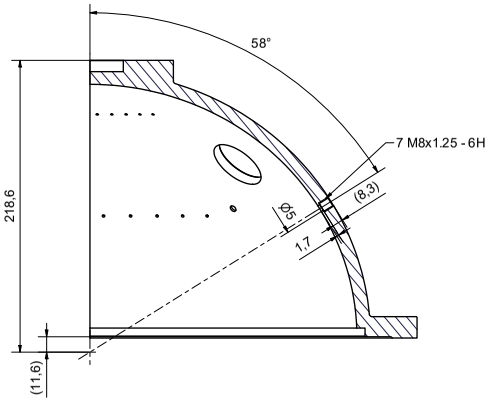

U-U (1 : 2) coupe PT100

2 series de 3 trous 1x symetriques

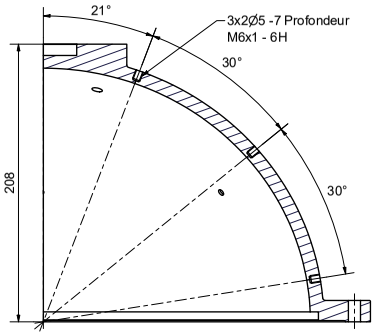

M-M (1 : 2) coupe usinage tapes HP

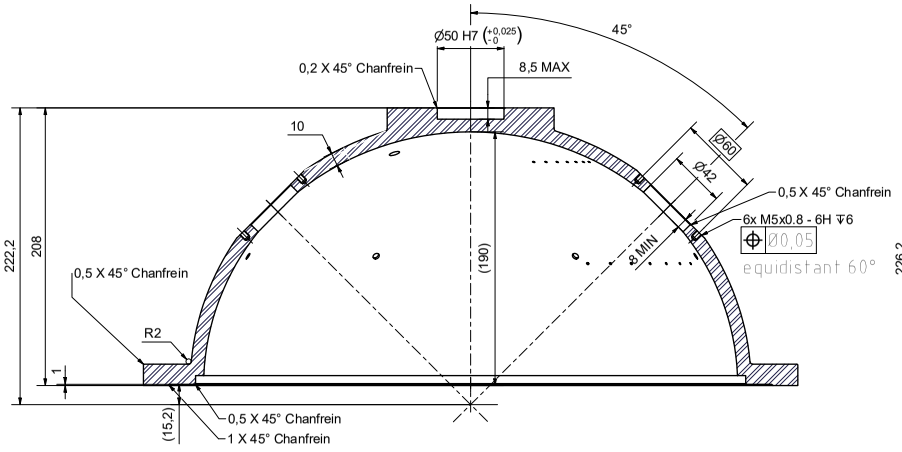

V-V (1 : 2) coupe thermistance

2 series de 7 trous 1x symetriques

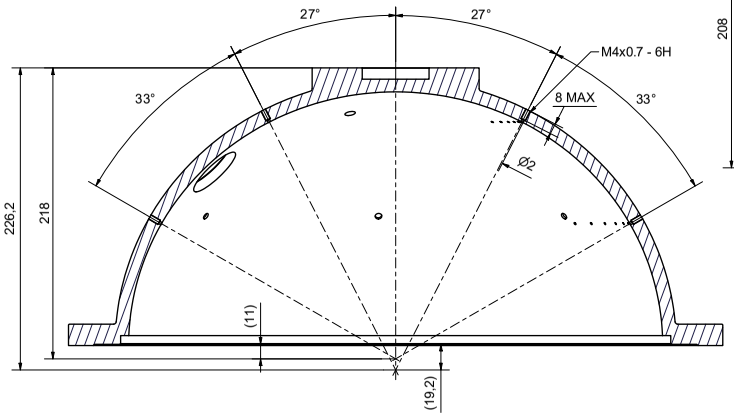

Matière : MACALU + (alliage de série 7xxx)	Traitement :	Tol. générales : IH	Rugosité Ra :
Echelle : 1:2	Auteur : max solazzo	Date : 13/10/2017 Approbateur :	Date :

ISTerre — Institut des Sciences de la Terre — Service Instrumentations Géophysiques
1381 rue de la piscine, Domaine Universitaire, 38400 Saint-Martin-d'Hères, CS 40700, 38058 Grenoble cedex 9
Tél. : +33 (0)4 76 63 52 52
max.solazzo@univ-grenoble-alpes.fr
+33 (0)4 76 63 99 07

Ensemble : ZoRo2

Elément : demi-sphere haute

n° ZR2 0102-02 2/2 06

REF. FICHIER ZR20102-02-06.idw FORMAT A1 FOLIO INDICE

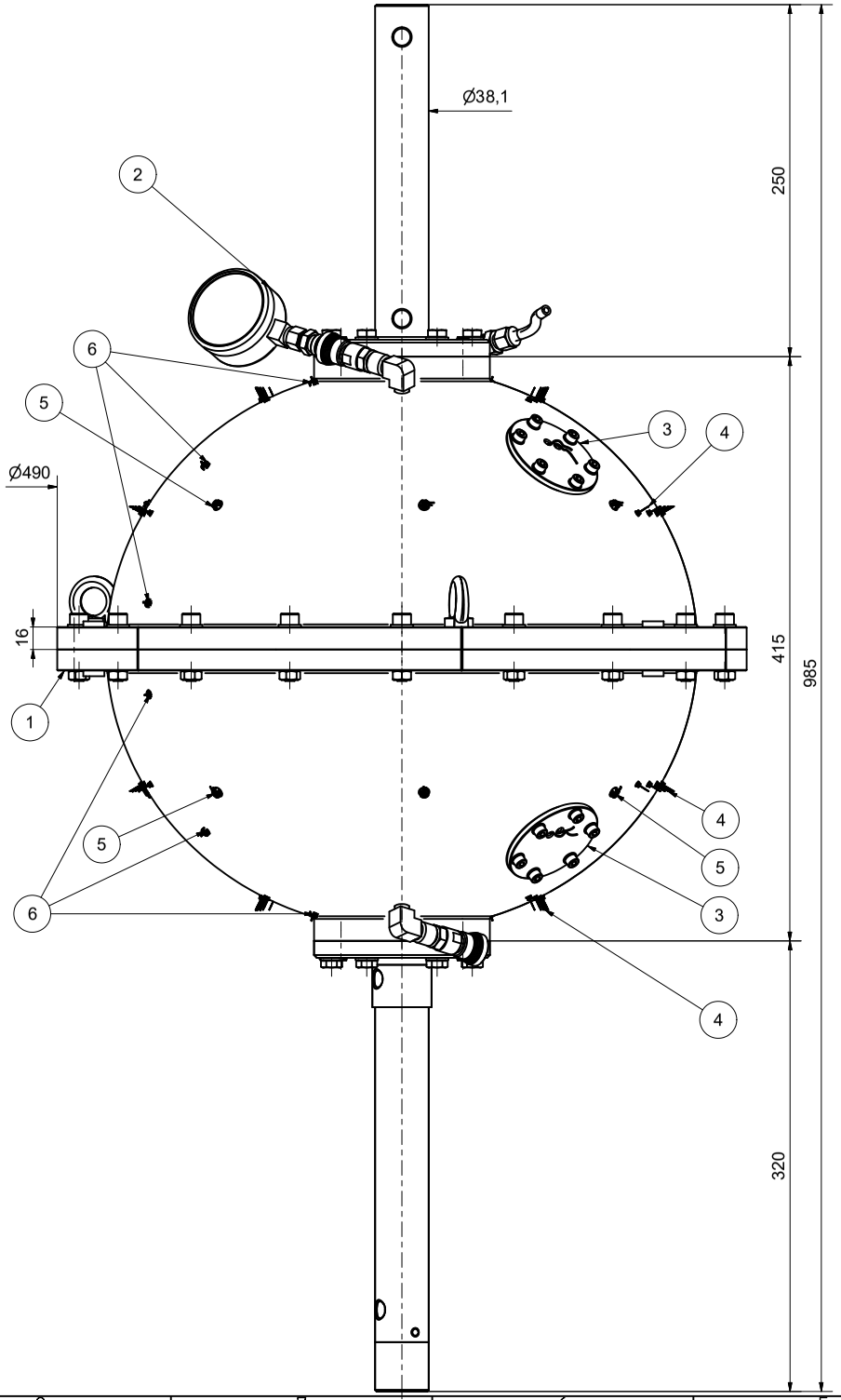

NOMENCLATURE

N°	QTE	N° DE PIECE	DESCRIPTION	MASSE	MATIERE
1	1	ZR2-EN0002	sous-ensemble en rotation	31,098 kg	
2	4	ZR2-EN1001	piquage gaz swagelok	0,231 kg	
3	4	ZR2-EN0103	ensemble HP	0,076 kg	
4	56	ZR2-EN0203	support thermistance	0,000 kg	
5	14	ZR2-EN0204	support electret	0,003 kg	
6	12	ZR2-EN0206	ensemble PT100	0,002 kg	
7	6	CSS1504N	Aimant disque CS-S-15-04-N	0,004 kg	
8	6	ISO 10642 - M4 x 8	Vis à tête fraisée à six pans creux	0,001 kg	A2

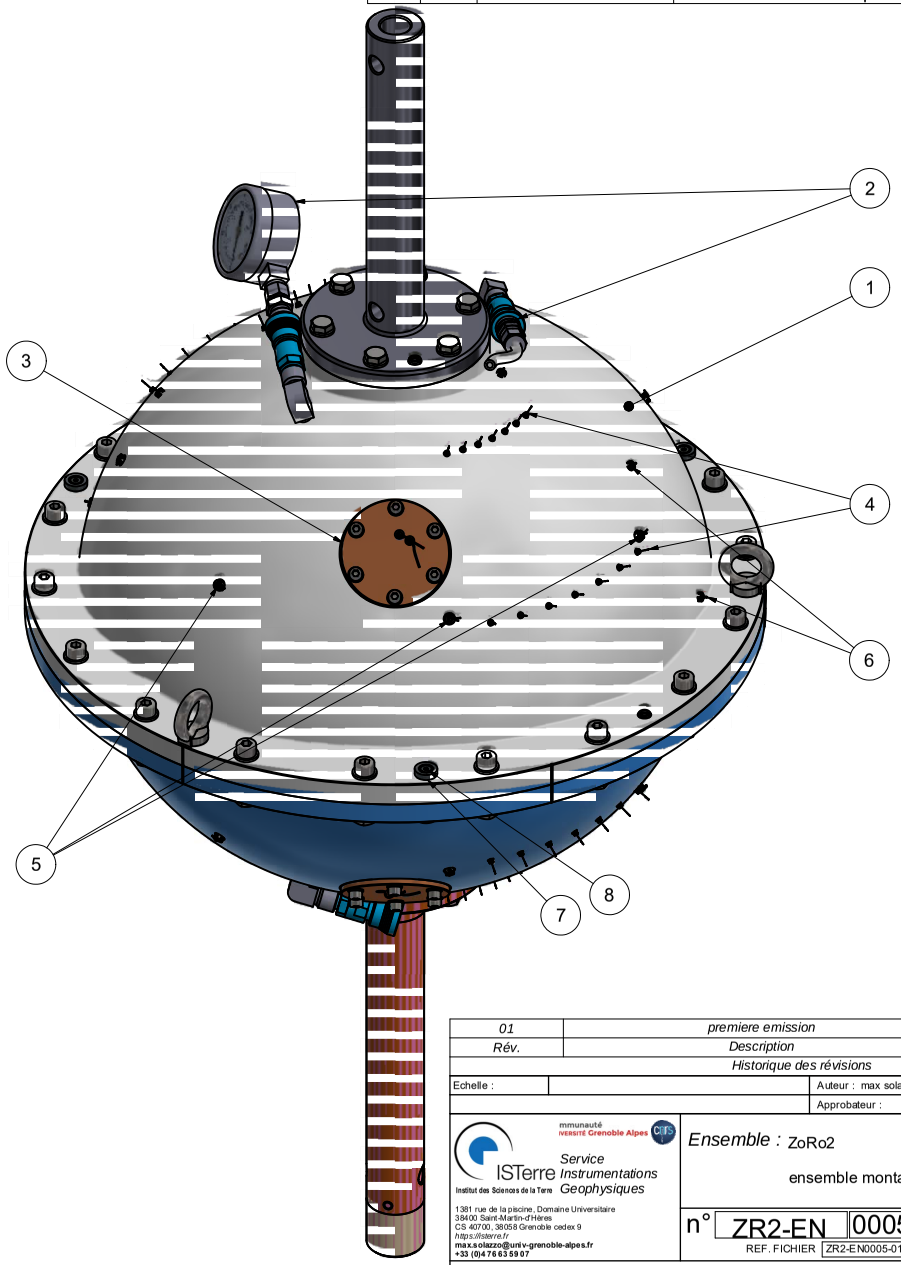

Rév.	Description	Aut.	Date
01	premiere emission	max solazzo	13/11/2018

Historique des révisions

Echelle :

Auteur : max solazzo — Date : **29/05/2018**

Approbateur : — Date :

Communauté Université Grenoble Alpes
ISTerre Institut des Sciences de la Terre
Service Instrumentations Géophysiques
1381 rue de la piscine, Domaine Universitaire
38400 Saint-Martin-d'Hères
CS 40700, 38058 Grenoble cedex 9
https://isterre.fr
max.solazzo@univ-grenoble-alpes.fr
+33 (0)4 76 63 59 07

Ensemble : ZoRo2

ensemble montage capteurs

n° ZR2-EN 0005 — 1 /2 FOLIO — 01 INDICE

REF. FICHIER ZR2-EN0005-01.idw — FORMAT A2

C (2 : 1)

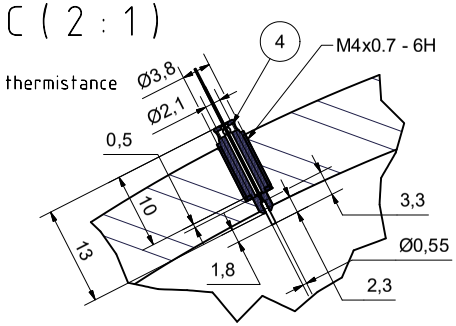

D (2 : 1)

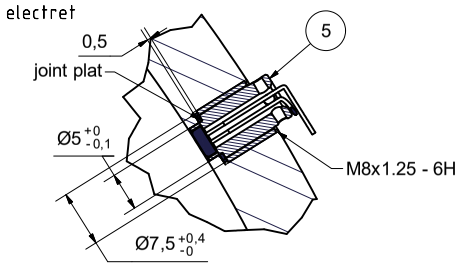

F (2 : 1)

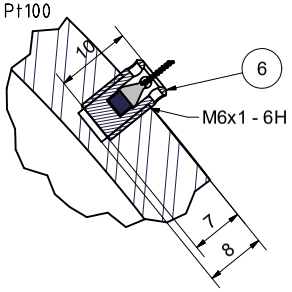

H (2 : 1)

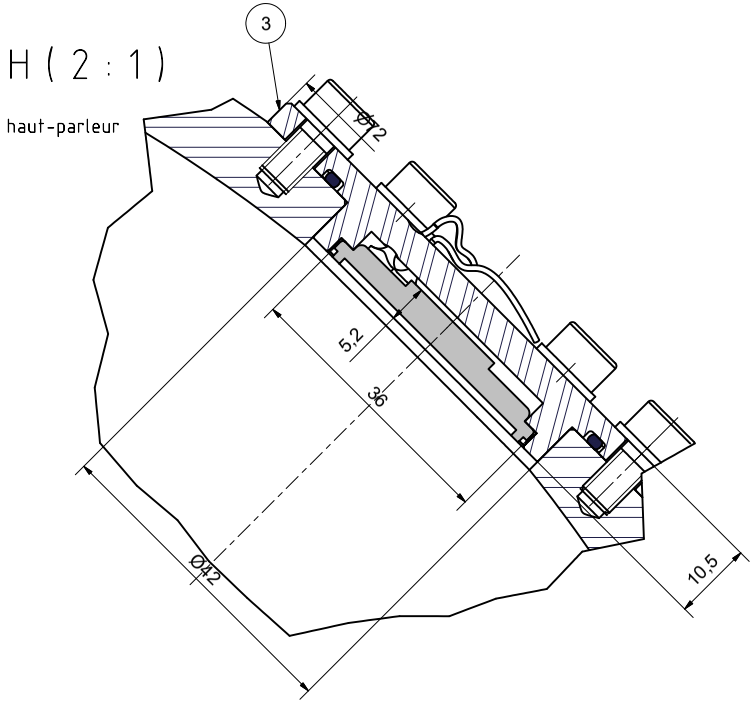

E-E (1 : 2.5)

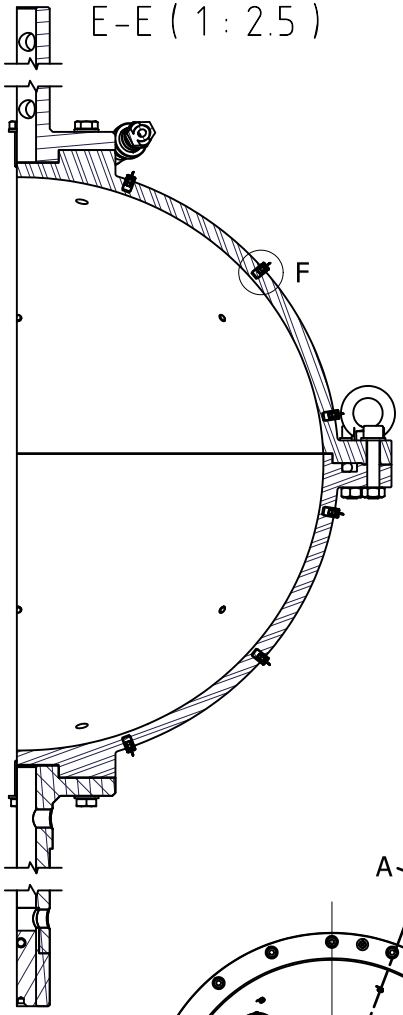

B-B (1 : 2.5)

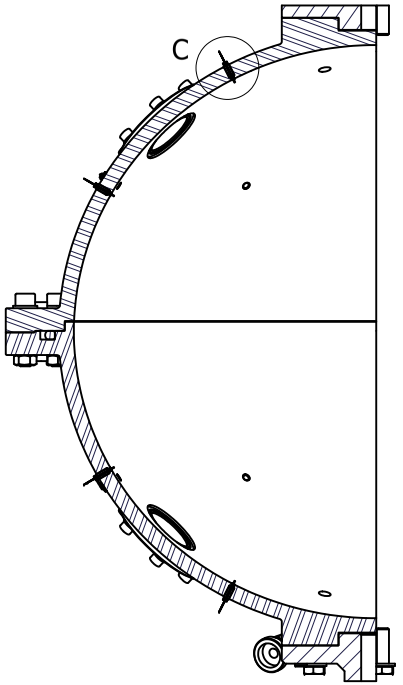

A-A (1 : 2.5)

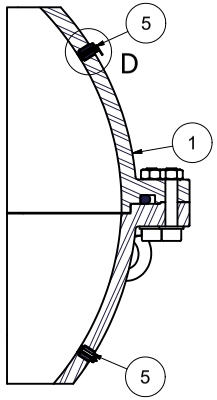

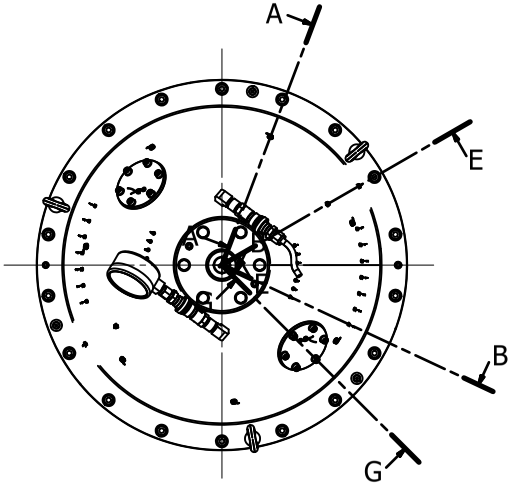

J (1 : 1)

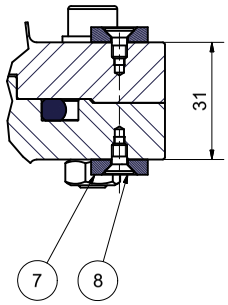

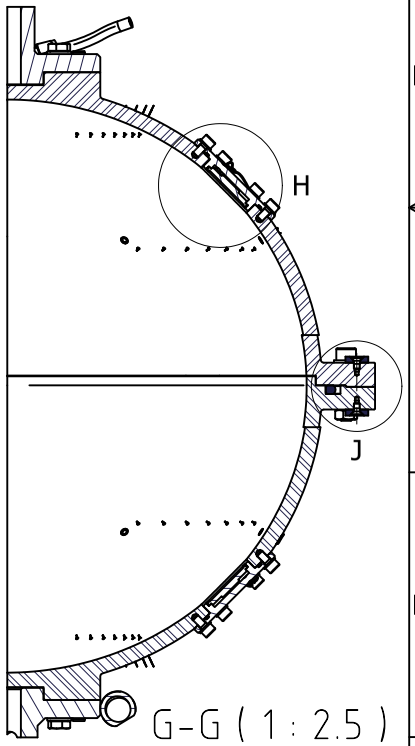

G-G (1 : 2.5)

Echelle :		Auteur : max solazzo	Date : 29/05/2018
		Approbateur :	Date :

Communauté Université Grenoble Alpes

ISTerre Institut des Sciences de la Terre — Service Instrumentations Geophysiques

1381 rue de la piscine, Domaine Universitaire
38400 Saint-Martin-d'Hères
CS 40700, 38058 Grenoble cedex 9
https://isterre.fr
max.solazzo@univ-grenoble-alpes.fr
+33 (0)4 76 63 59 07

Ensemble : ZoRo2

ensemble montage capteurs

n° ZR2-EN 0005 — 2/2 FOLIO — 01 INDICE

REF. FICHIER ZR2-EN0005-01.idw — FORMAT A2

D

Spherical prototype: ZoRo1

We briefly present the spherical prototype ZoRo1 that we built before having the current ZoRo apparatus. ZoRo1 helped us to better understand how the acoustic spectra look like, and to sharpen both numerical and theoretical tools on a slightly easier experiment (as it was spherical) before getting to the spheroid.

We have encountered difficulties in building ZoRo1, which in turn helped us better prepare for the current experiment. In particular, ZoRo1 was not perfectly spherical and presented geometrical defaults that made mode identification much more difficult that it is on ZoRo. Also, due to some manufacturing defaults, it could not rotate fast enough for relevant geophysical regimes. However we still have measured some rotating flows with ZoRo1, which made us realise how dense the acoustic spectrum was and gave us the idea to build a spheroid instead. Although ZoRo1 was a failure in the sense that it was not suitable for good MAV measurements, it was a helpful prototype that is still able to guide us for future experiments.

D.1 Experimental set-up

The experimental set-up (Figure D.1) consist of a $a = 20$ cm radius container made of a thin spherical brass shell enclosing air, the working fluid. The container is mounted on a motor shaft allowing rotation of the system and mechanical forcing of the fluid through viscous friction (same motor as ZoRo), through a rigid 1:1 coupling (discarded). For experiments with thermal gradients, forcing is done by infra-red radiants (same as ZoRo) installed on the non-rotating supported frame (ZoRo is on a different frame), 20 cm away from the sphere surface.

The container was not as spherical as expected, which proved problematic for MAV but it was also very limiting in terms of rotation rates. Since the container is not axisymmetric, it is not well balanced, hence creates many vibrations while rotating. The fastest rotation

we reached with ZoRo1 is 15 Hz (half the rate of ZoRo).

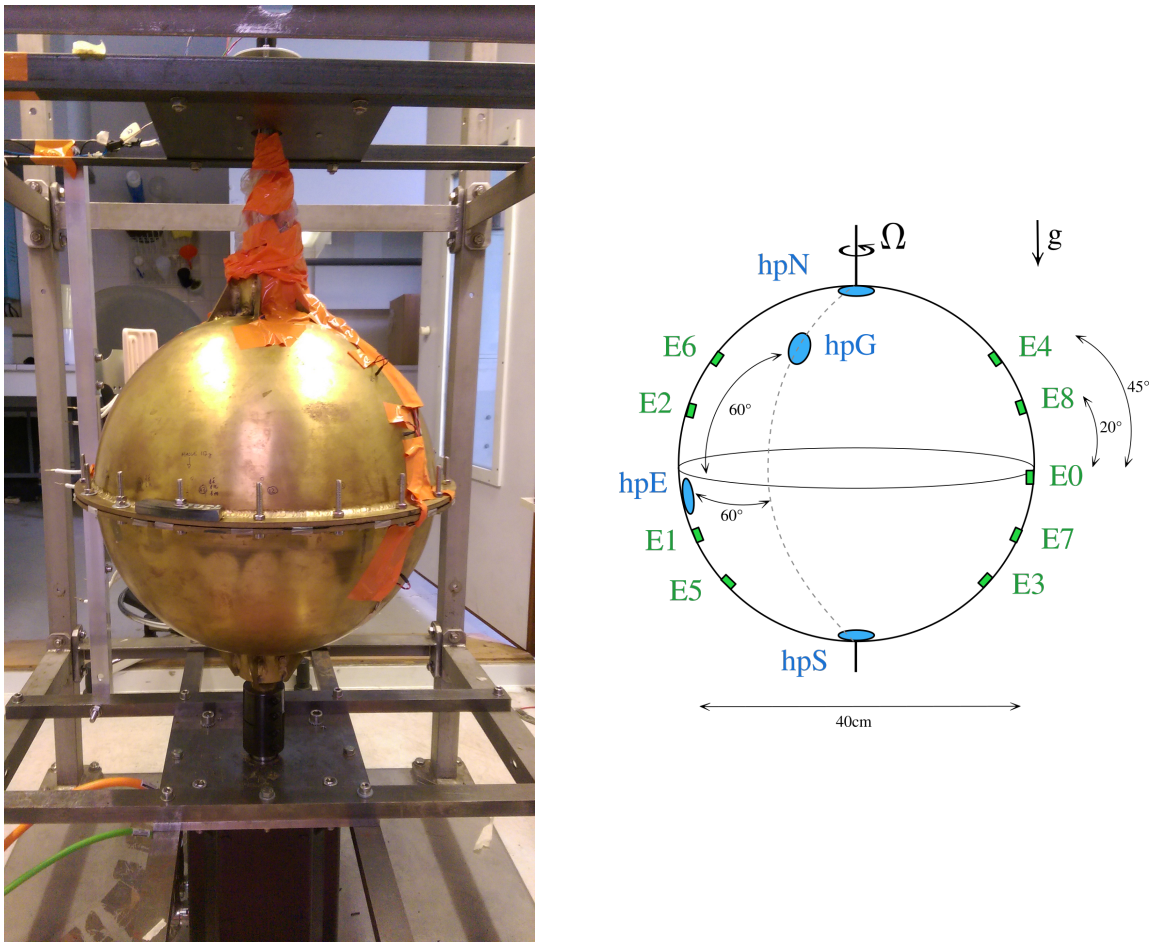

Figure D.1: Left: Photo of the experimental prototype set-up ZoRo1, mounted on its frame. Right: Schematic position of acoustic sensors.

The eigen-frequencies of ZoRo1 are close to ZoRo's. We have used the same electrets and speakers to acquire the acoustic signal. Nine electrets are installed on the inner surface of the brass shell (Figure D.1 right, in green) in contact with the air, at two facing longitudes and four latitudes symmetric with respect to the equator. One additional electret is placed at the equator. As for the speakers, four of them are fixed within the shell, at the two poles, the equator and mid-latitude (Figure D.1 right, in blue), but only two can be played at the same time (4 in ZoRo).

All sensors have been fixed to be as little protruding as possible, ideally keeping the irregularity within the Ekman layer for flows to be undisturbed by the sensors. However as we decided the sensors positions through trials and errors, the internal surface is much less smooth than ZoRo's, and both the electrets and speakers are glued (instead of screwed). This allowed us to define precisely where we wanted the acoustic sources and sensors to be on ZoRo.

The acquisition chain is mostly the same, with some improvements made for ZoRo (e.g. we added a basic electronic circuit in the electret's power supply that slightly improved the measured signal).

D.2 Theoretical acoustic spectrum

D.2.1 At rest

This time the apparatus is (supposed to be) a perfect sphere, so the theoretical prediction of the resonance frequencies is much easier, simply given by the solutions of the Helmholtz equation eq. (2.30), which are given for a sphere in eq. (2.37).

We show an experimental acoustic spectrum (at rest) with the predicted eigen frequencies in Figure D.2. Overall the theory predicts the experimental resonances well.

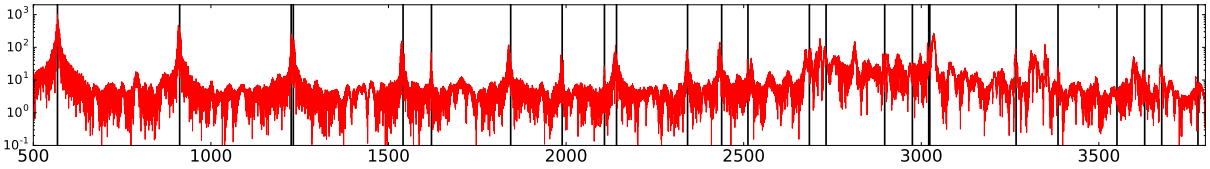

Figure D.2: Experimental acoustic spectrum (frequency in Hz) of ZoRo1 first resonances (in red), compared with theoretically predicted frequencies from eq. (2.37) (in black).

By comparing observed frequency spectrum with the predicted frequency we can identify a number of modes in the experimental spectrum. However this method reaches its limit for higher frequency (in our configuration around 2500 Hz), where eigenmodes are closer together, leading to uncertainties in the mode identification.

In a perfect sphere configuration, all the m modes from a multiplet are degenerate at rest. In order to differentiate them we need to break the spherical symmetry. To do that we impose a solid-body rotation, in ZoRo1 it is the easiest way to lift the degeneracy. And the rotational splittings should follow the Ledoux coefficients, allowing a simple verification.

D.2.2 Solid-body rotation

We show in the left panel of Figure D.3 the experimental acoustic spectra around ${}_0\mathcal{S}_1$ for increasing rotation rates, from rest (red) to 9 Hz (violet). Then in Figure D.4, we plot the sum and difference of the previous signal to distinguish symmetric and anti-symmetric modes within the multiplet. We can clearly separate the ± 1 mode on the left panel and the $m = 0$ mode on the right.

ZoRo1 is overall more noisy, as it has only electrets in 2 longitudes so no average is possible to clear up the signal. The speakers are not symmetric with each other so we can only use the symmetry properties on the electrets, which is less efficient to extinguish the modes of opposite symmetry.

We are still able to globally retrieve the theoretical splitting predicted by the spherical Ledoux coefficients (red lines in Figure D.3).

Furthermore, for modes with larger l, rotational splitting is not enough to clearly separate the m with the attainable rates in our set-up, inciting us to switch to a spheroid, where the degeneracy is partially lifted at rest.

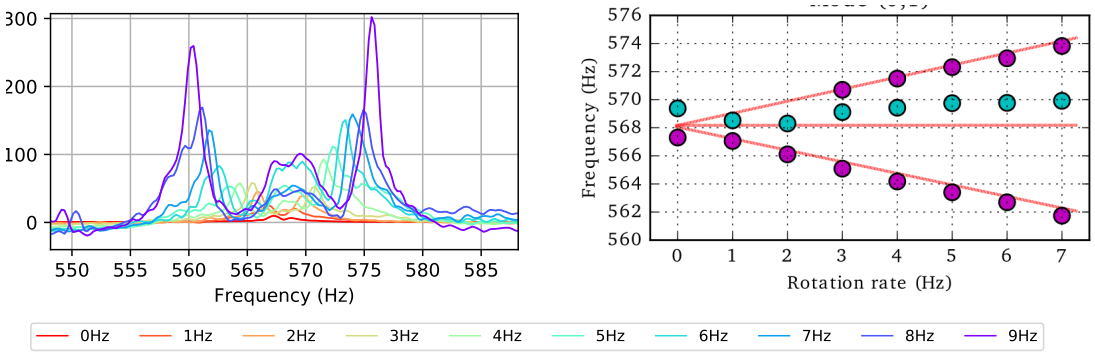

Figure D.3: Left: Spectra of fundamental mode ${}_0\mathcal{S}_1$ for increasing rotation rates (arbitrary units). Right: Extracted frequency splittings separated by symmetry, symmetric modes in purple, anti-symmetric modes in blue. Theoretical predictions using spherical Ledoux coefficient is plotted in red for comparison.

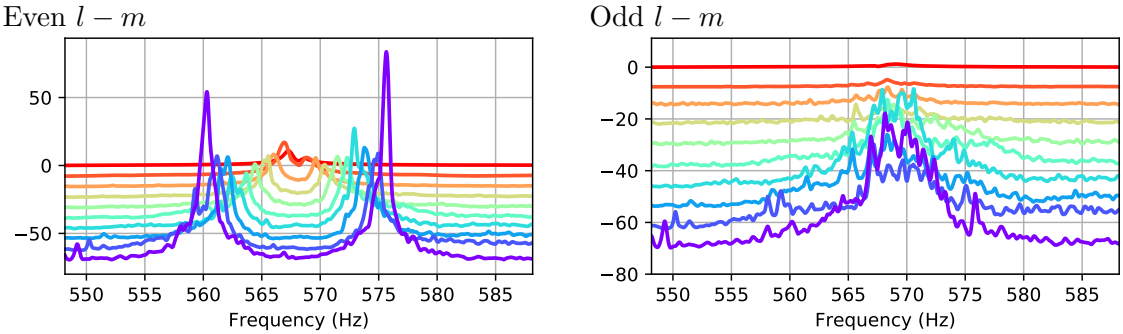

Figure D.4: Spectra of fundamental mode ${}_0\mathcal{S}_1$ for increasing rotation rates (same colour legend as Figure D.3). Left panel: summed signals enhances the modes symmetric with respect to the equator, here the odd $m = \pm 1$. Right panel: subtracted signals enhances the anti-symmtric modes, here the even $m = 0$.

D.3 Azimuthal flows measurements

We did some flow measurements with ZoRo1. We will briefly plot the corresponding acoustic spectra for a few modes.

D.3.1 Spin up

Figure D.5 shows experimental acoustic spectra for different times after spin up (change of the container rotation rate from 3 to 4 Hz). The first spectrum at the top corresponds to solid-body rotation at the initial (3 Hz) rotation rate. We can clearly retrieve the fact that some modes, e.g. ${}_0\mathcal{S}_1^1$, are almost blind to this differential flow while ${}_1\mathcal{S}_3$ shows a large signature clearly different from the solid-body rotation one. This is consistent with the observations we made from their respective sensitivity kernels spatial structures in Chapter 2, and with theoretical predictions of the splitting for spin up flow (symbols) as shown in Figure D.5. We remark, as in the synthetics in Chapter 4, that for ${}_1\mathcal{S}_3$ the biggest splitting is displayed right after the rotation changes, corresponding to Doppler

splitting.

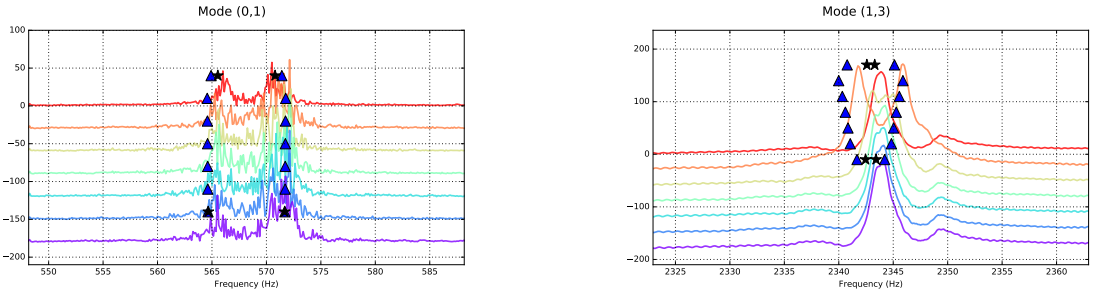

Figure D.5: Spectra of fundamental mode ${}_0\mathcal{S}_1$ left, ${}_1\mathcal{S}_3$, right, for increasing time during a spin up from 3 Hz to 4 Hz. Symbols are predicted splittings form analytical velocity profile for the successive spin up times (triangles) and solid-body rotation at starting and ending rotation rate (stars).

D.3.2 Longitudinal librations

Figure D.6 shows experimental acoustic spectra for different times within a libration period. Since the flow is periodic, we stacked several periods together to cancel out some noise. The libration shown here has the container oscillating around 4 Hz with an amplitude of 1 Hz during a 7 s period (following a sine function). Again we can clearly retrieve the fact that ${}_0\mathcal{S}_1^1$, is not affected by the oscillation (compared to solid-body rotation) to this differential flow while ${}_1\mathcal{S}_3$ shows a large signature clearly different from the solid-body rotation one.

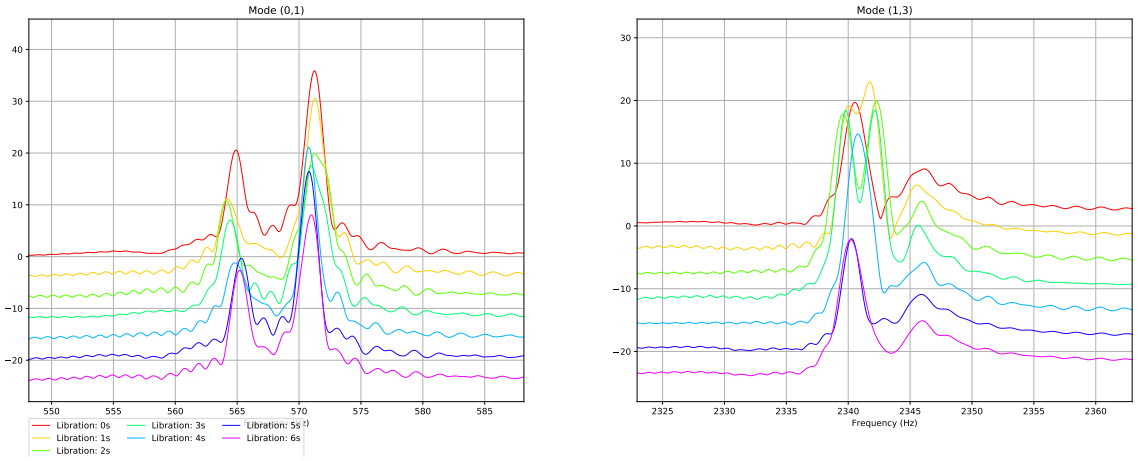

Figure D.6: Spectra of fundamental mode ${}_0\mathcal{S}_1$ left, ${}_1\mathcal{S}_3$, right, for increasing time during one libration period.

We tried to invert some of those flows. However due the unsatisfactory mode identification, very few modes are available to perform the inversion, resulting in inverted profiles that are not very physically relevant and that we do not fully trust.

E

Multiplexer electronic card design

Functional schematic and board sketch of ZoRo multiplexer electronic card, inspired by the design of Yoann Corre, with the help of Patrick La Rizza and Yann Do. This card is used to multiplex the thermistor's signal in order to reduce the number of wire passing through the slip rings.

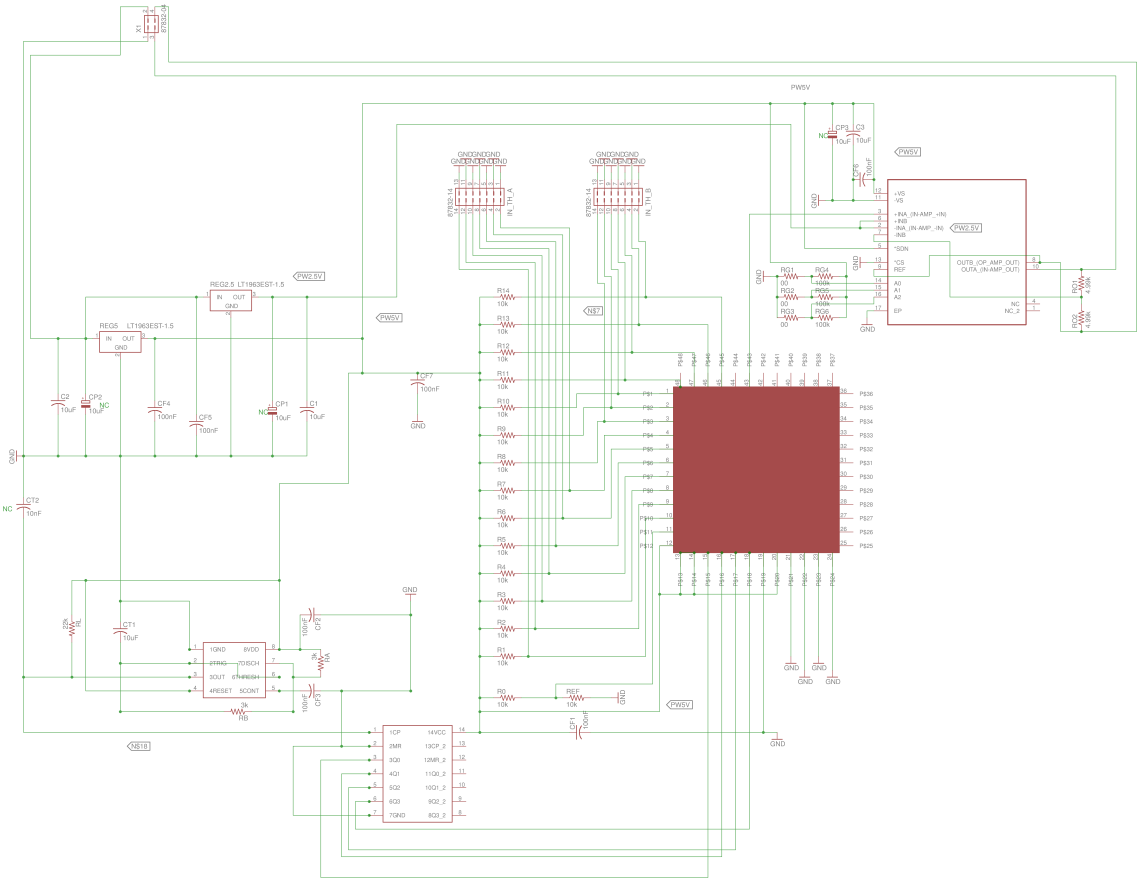

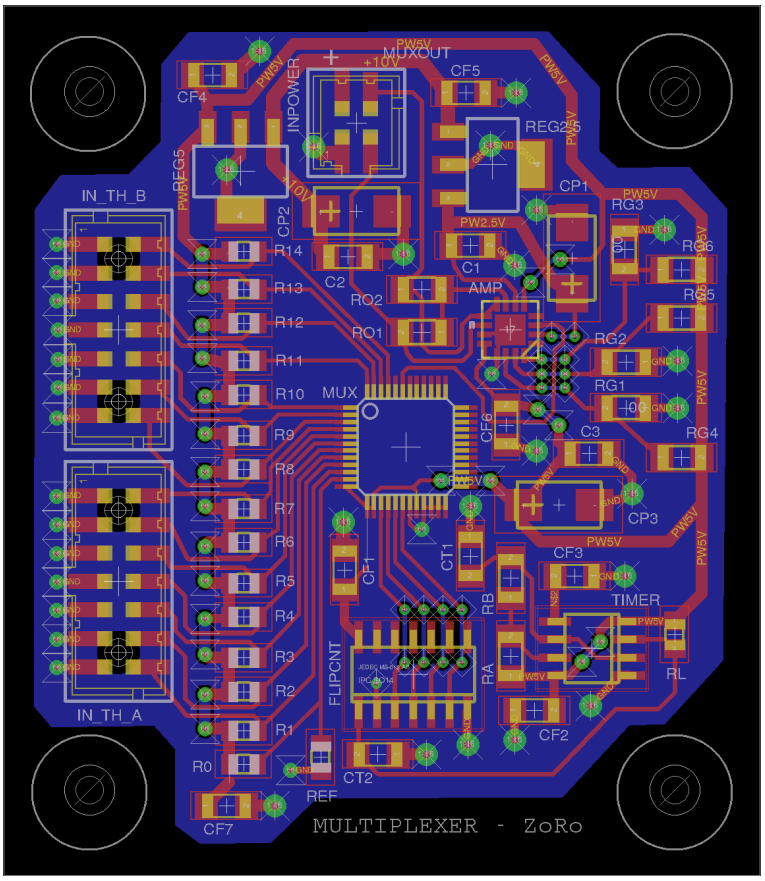
MULTIPLEXER - ZoRo
MUXOUT
INPOWER
IN_TH_B
IN_TH_A
MUX
AMP
TIMER
FLIPCNT
REF
PW5V
PW2.5V
+10V
GND

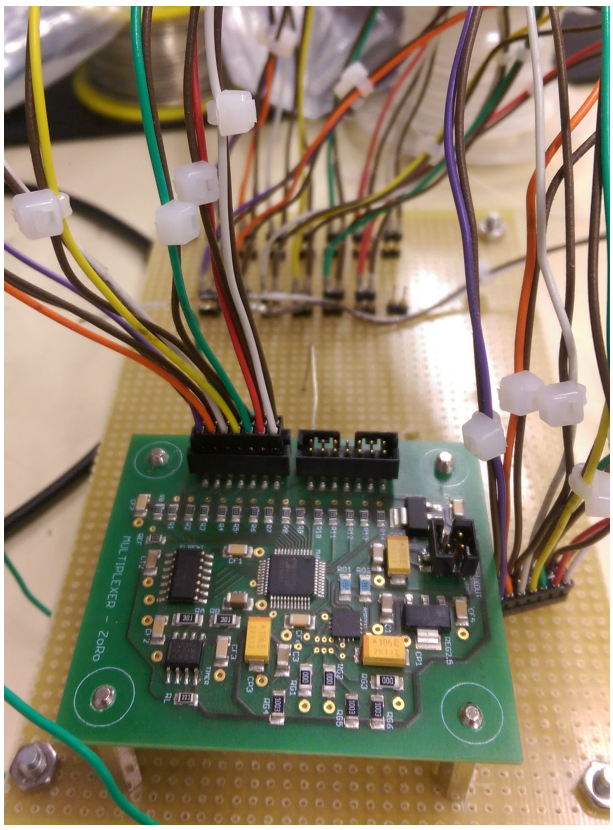

F Thermal wind equations

We reproduce some excerpts of Arnaud Piet's Master 2 Thesis (Piet, 2019), for theoretical studies of thermal winds.

F.1 Thermal wind equation

We start from the momentum energy conservation eq. (2.22), under the Boussinesq approximation

$$\frac{\partial \boldsymbol{v}}{\partial t} + 2\boldsymbol{\Omega} \times \boldsymbol{v} = -\frac{1}{\rho_0}\boldsymbol{\nabla} P + \frac{\rho'}{\rho_0}\boldsymbol{g}. \tag{F.1}$$

Taking the curl of eq. (F.1) , we get the *static* vorticity equation

$$2(\boldsymbol{\Omega} \cdot \boldsymbol{\nabla})\boldsymbol{v} = \boldsymbol{\nabla} \times [\alpha(T - T_0)\boldsymbol{g}]\,. \tag{F.2}$$

In ZoRo the rotation is along $\boldsymbol{\Omega} = \Omega \boldsymbol{e_z}$ only (and in the case of thermal wind studies, Ω will be taken as constant). Further simplification can be done by recalling that $\boldsymbol{g}$ is a potential, hence $\boldsymbol{\nabla} \times \boldsymbol{g} = 0$, and eq. (F.2) becomes

$$\frac{\partial \boldsymbol{v}}{\partial z} = \frac{\alpha \Omega s}{2}\boldsymbol{\nabla}(T - T_0) \times \boldsymbol{e_s}. \tag{F.3}$$

Focusing only on the axisymmetric variation of temperature, we get the so-called thermal wind equation (Vallis, 2017)

$$\frac{\partial v_\phi}{\partial z} = \frac{\alpha \Omega s}{2}\frac{\partial T}{\partial z}, \tag{F.4}$$

where $v_\phi = \boldsymbol{v} \cdot \boldsymbol{e_\phi}$.

F.2 The uniform internal heating full sphere

The heat conservation equation eq. (2.23) with a constant volumic internal heating Q is

$$\rho C_p \frac{\partial T}{\partial t} = \rho C_p \kappa \nabla^2 T + Q. \tag{F.5}$$

For a stationary profile, we can compute the heat flux q_0 at the outer boundary, i.e. at the aluminium shell. For simplicity, in the following, the cavity is assumed to be heated at the perfectly spherical boundary $r = r_0 = a$. At the boundary, we have

$$q_0 = \frac{r_0 Q}{3}. \tag{F.6}$$

and the temperature then becomes

$$T(r) = -\frac{Q}{2k} r^2 + T_0. \tag{F.7}$$

Injecting into the thermal wind equation eq. (F.4) gives

$$\frac{\partial v_\phi}{\partial z} = -\frac{\alpha \Omega s z}{2} \frac{Q}{\rho C_p \kappa}. \tag{F.8}$$

After integration we get

$$v_\phi(s, z) = -\frac{\alpha \Omega Q}{4 \rho C_p \kappa} s z^2 + A(s), \tag{F.9}$$

with $A(s)$ an integration constant that only varies with the cylindrical radius s.

Using the boundary condition $v_\phi(r = r_0) = 0$, we finally get

$$v_\phi(s, z) = -\frac{\alpha \Omega Q}{4 \rho C_p \kappa} s(z^2 + s^2 - r_0^2), \tag{F.10}$$

or in spherical coordinates

$$v_\phi(r, \theta) = -\frac{\alpha \Omega Q r_0^2}{4 \rho C_p \kappa} \left(\frac{r^2}{r_0^2} - 1 \right) r \sin \theta. \tag{F.11}$$

The thermal wind is maximum in the equatorial plane at $s = r_0/\sqrt{3}$ and reaches

$$\frac{\alpha \Omega Q r_0^3}{6\sqrt{3} \rho C_p \kappa} = \frac{\alpha \Omega \Phi_0 r_0^2}{2\sqrt{3} \rho C_p \kappa}. \tag{F.12}$$

Taking the variables for ZoRo rotating at 10 Hz, it gives $v_\phi = 1.98$ m/s at its maximum.

Here we want to compute the thermal wind for a stable stratified case. It corresponds to the case of a cooling on the surface, and where the external layers are colder than internal layers. If we keep in mind the idea of an inverted gravity (due to the centrifugal acceleration), heavy cold air masses will stay at the outside.

We have thus to consider an external cooling which is equivalent to an internal heating and so $Q > 0$ and $q_0 > 0$.

One can match the inviscid flow eq. (F.11) with a boundary layer. Using r_0 as the length scale and Ω^{-1} as the time scale, the flow eq. (F.11) becomes then

$$u_\phi(r, \theta) = Ro\, s(r^2 - 1) \left[1 - \exp(-\lambda \zeta) \cos(\lambda \zeta) \right], \tag{F.13}$$

with the Rossby number $Ro = \alpha q_0 r_0 / (4 \rho C_p \kappa)$, the boundary layer variable $\zeta = Ek^{-1/2}(1-r)$ and $\lambda = \sqrt{\cos \theta}$ the inverse of the characteristic thickness $\delta = 1/\lambda$ of the boundary layer. Note that a boundary layer flow in the direction $\boldsymbol{e_\theta}$ also exists, given by

$$u_\theta(r, \theta) = Ro\, s(r^2 - 1)\, \exp(-\lambda \zeta) \sin(\lambda \zeta). \tag{F.14}$$

Note that the bulk inviscid solution vanishes at the boundary, such that there is no Ekman pumping nor circulation.

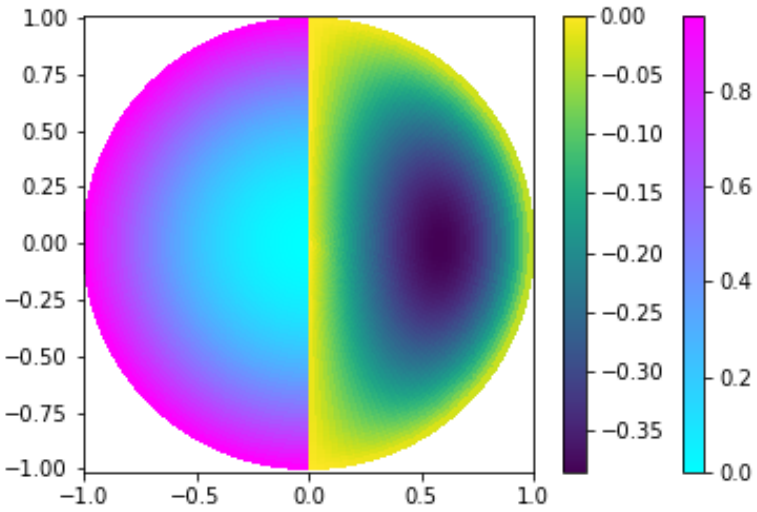

Figure F.1: Thermal wind created by constant heat flux and internal heating. Left: temperature variation (K), right: thermal wind velocity (m/s)

F.3 The heat flux latitudinal variation

We now have to consider the case without any internal heating and thus : $Q = 0$. In this case, eq. (F.5) becomes

$$\nabla^2 T = 0. \tag{F.15}$$

For a spherical geometry, the solutions of this equation are spherical harmonics. And general solutions can be written as

$$T = f(r)F(\theta, \phi). \tag{F.16}$$

By separating variables and re-writting eq. (F.15) as a system of two equations, we find

$$\frac{\mathrm{d}}{\mathrm{d}r}\left(r^2 \frac{\mathrm{d}f}{\mathrm{d}r}\right) = l(l+1) = K. \tag{F.17}$$

We obtain then $f(r) = Cr^l + \dfrac{D}{r^{l+1}}$ and $F(\theta, \phi) = \mathcal{Y}_l^0(\theta)$, where C and D are two integration constants to be determined with the boundary conditions.

The first boundary condition is given by the non-divergence of the temperature field at $r = 0$, giving $= 0$.

The second one is the heating of the shell

$$\boldsymbol{j_Q} = -\rho C_p \kappa \boldsymbol{\nabla} T(r_0). \tag{F.18}$$

The external flux is considered axisymmetric: $\Phi_l = \phi_l \mathcal{Y}_l^0$, where Y_l^0 are the spherical harmonics of degree l and order $m = 0$. Considering $\boldsymbol{n} = -\boldsymbol{u_r}$ the re -entrant normal of the sphere, we can write:

$$\boldsymbol{j_Q} \cdot \boldsymbol{n} = \Phi_l. \tag{F.19}$$

Thus we obtain

$$\phi_l \mathcal{Y}_l^0(\theta) = \rho C_p \kappa \, l \, C r_0^{l-1} \mathcal{Y}_l^0(\theta), \tag{F.20}$$

giving us the constant $C = \dfrac{\phi_l r_0}{r_0^l l \rho C_p \kappa}$.

Finally, the temperature T can be written as

$$T = \frac{\phi_l r_0}{l \rho C_p \kappa} \left(\frac{r}{r_0} \right)^l \mathcal{Y}_l^0(\theta) + T_0. \tag{F.21}$$

Injecting into the thermal wind equation the azimuthal wind is then in cylindrical coordinates

$$\begin{aligned} v_\phi(s,z) &= \int \frac{\partial u_\phi(s,z)}{\partial z} \, \mathrm{d}z = \frac{\alpha \Omega s}{2} \int \frac{\partial T(s,z)}{\partial z} \, \mathrm{d}z \\ &= \frac{\alpha \Omega s}{2} T(s,z) + C(s) \\ &= \frac{\alpha \Omega s}{2} \frac{\phi_l K_l r_0 (s^2+z^2)^{\frac{l}{2}}}{l k r_0^l} \mathcal{P}_l \left(\frac{z}{\sqrt{s^2+z^2}} \right) + C(s), \end{aligned} \tag{F.22}$$

where the K_l are the spherical harmonics' coefficients preceding the Legendre polynomials

$$\mathcal{Y}_l^0(\theta) = K_l \, \mathcal{P}_l(\cos\theta) = \sqrt{\frac{2l+1}{4\pi}} \, \mathcal{P}_l(\cos\theta),$$

or equivalently in the spherical coordinates

$$v_\phi(r,\theta) = \frac{\alpha \Omega \phi_l K_l}{2 l \rho C_p \kappa} \frac{r^l}{r_0^{l-1}} \mathcal{P}_l(\cos\theta) + C(s). \tag{F.23}$$

The explicit relations for the first few l are given in Table F.1.

l	$v_\phi(r,\theta) - C(s)$	$T(r,\theta)$
1	$\dfrac{\alpha \Omega \phi_1 K_1}{2 \rho C_p \kappa} r^2 \sin\theta \cos\theta$	$\dfrac{\phi_1 K_1}{\rho C_p \kappa} r \cos\theta$
2	$\dfrac{\alpha \Omega \phi_2 K_2 r^3}{8 \rho C_p \kappa r_0} \sin\theta [3\cos^2\theta - 1]$	$\dfrac{\phi_2 K_2 r^2}{4 \rho C_p \kappa r_0} [3\cos^2\theta - 1]$
3	$\dfrac{\alpha \Omega \phi_3 K_3 r^4}{12 \rho C_p \kappa r_0^2} \sin\theta [5\cos^3\theta - 3\cos\theta]$	$\dfrac{\phi_3 K_3 r^3}{6 \rho C_p \kappa r_0^2} [5\cos^3\theta - 3\cos\theta]$
4	$\dfrac{\alpha \Omega \phi_4 K_4 r^5}{64 \rho C_p \kappa r_0^3} \sin\theta [35\cos^4\theta - 30\cos^2\theta + 3]$	$\dfrac{\phi_4 K_4 r^4}{32 \rho C_p \kappa r_0^3} [35\cos^4\theta - 30\cos^2\theta + 3]$

Table F.1: Explicit relations for temperature and thermal wind velocity for the first degrees l, integration constant $C(s)$ to be determined.

Note that the constant $C(s)$ cannot be explicitly determined by the boundary conditions $v_\phi(s, z = \pm\sqrt{r_0^2 - s^2}) = 0$. Indeed, until now we consider the hypothesis of an inviscid fluid with the aim of computing the thermal wind velocity. The cancel of the tangential velocity at the shell is thus valid for the total velocity field and we have to add a viscous boundary layer.

In this way, for $l = 1$ we obtain

$$\widetilde{v_\phi}(r,\theta) = \frac{\alpha\Omega\phi_1 K_1}{2\rho C_p \kappa} \sin\theta\cos\theta r^2 \left[1 - \exp\left(-\frac{(r_0 - r)\cos\theta}{r_0\sqrt{Ek}}\right)\cos\left(\frac{(r_0 - r)\cos\theta}{r_0\sqrt{Ek}}\right)\right], \quad \text{(F.24)}$$

with Ek the Ekman number.

The full explicit relations for the first few l are given in Table F.2.

l	$\widetilde{v_\phi}(r,\theta)$	$T(r,\theta)$
1	$\frac{\alpha\Omega\phi_1 K_1}{2\rho C_p\kappa}\sin\theta\cos\theta r^2 \times\left[1-\exp\left(-\frac{(r_0-r)\cos\theta}{r_0\sqrt{E}}\right)\cos\left(\frac{(r_0-r)\cos\theta}{r_0\sqrt{E}}\right)\right]$	$\frac{\phi_1 K_1 r}{\rho C_p\kappa}\cos\theta$
2	$\frac{\alpha\Omega\phi_2 K_2}{4\rho C_p\kappa r_0} r\sin\theta(r^2 - r_0^2)$	$\frac{\phi_2 K_2 r^2}{4\rho C_p\kappa r_0}(3\cos^2\theta - 1)$
3	$\frac{\alpha\Omega\phi_3 K_3 r^4}{12\rho C_p\kappa r_0^2}\sin\theta(5\cos^3\theta - 3\cos\theta) \times\left[1-\exp\left(-\frac{(r_0-r)\cos\theta}{r_0 Ek^{1/2}}\right)\cos\left(\frac{(r_0-r)\cos\theta}{r_0 Ek^{1/2}}\right)\right]$	$\frac{\phi_3 K_3 r^3}{6\rho C_p\kappa r_0^2}(5\cos^3\theta - 3\cos\theta)$
4	$\frac{\alpha\Omega\phi_4 K_4}{4\rho C_p\kappa r_0^3} r\sin\theta\left[r^4 - r_0^4 - 5r^2\sin\theta(r^2 - r_0^2)\right]$	$\frac{\phi_4 K_4 r^4}{32\rho C_p\kappa r_0^3}(35\cos^4\theta - 30\cos^2\theta + 3)$

Table F.2: Explicit relations for temperature and thermal wind velocity for the first degrees l.

For a typical experiment in ZoRo, $r_0 = 0.2$ m, $f = 7$ Hz, and $\nu_{air} = 1.516\times10^{-5}$ m^{2}s^{-1}, which gives $Ek = 4.31 \times 10^{-6}$, and the thickness of the boundary layer is then $\delta = r_0 Ek^{1/2} = 4.15 \times 10^{-4}$ m. Adding an Ekman boundary layer can be done for all the odd l to match the boundary conditions. For the even l , the shape of the velocity fields satisfy the condition $v_\phi\left(s, z = \pm\sqrt{r_0^2 - s^2}\right) = 0$.

Velocity and temperature fields for thermal forcing $l = 1$, $l = 2$, $l = 3$ are represented in Figure F.2, Figure F.3 and Figure F.4 respectively.

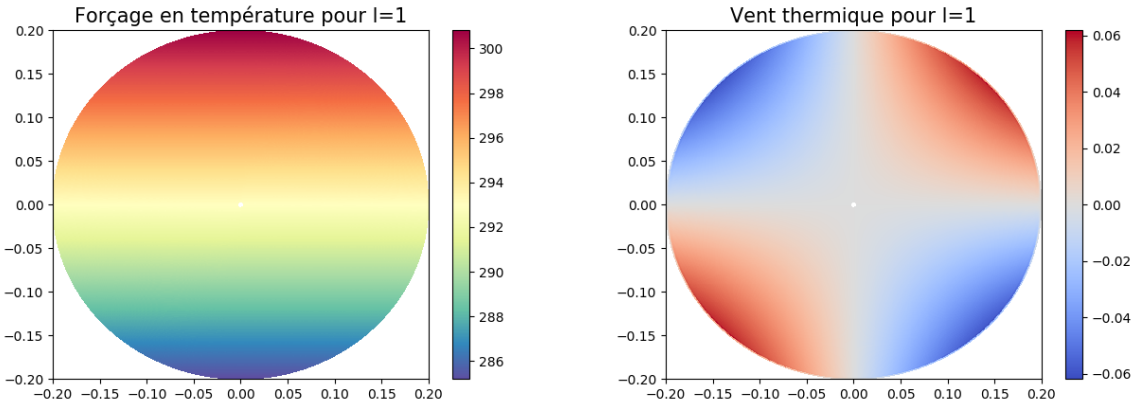

Figure F.2: Temperature (K) and thermal wind velocity (m/s) for external forcing $l = 1$.

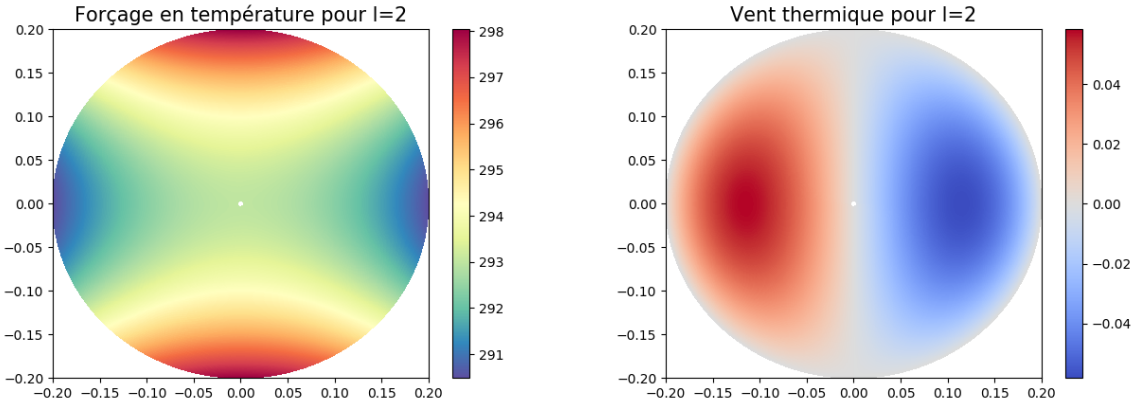

Figure F.3: Temperature (K) and thermal wind velocity (m/s) for external forcing $l = 2$.

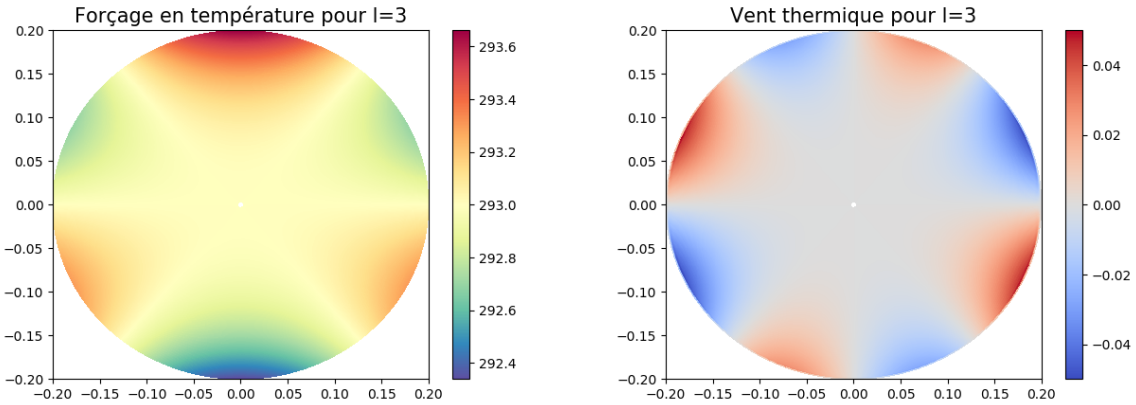

Figure F.4: Temperature (K) and thermal wind velocity (m/s) for external forcing $l = 3$.